Target Discovery and Mode of Action Studies of Dehydrodieugenol B Analogues in *Leishmania*

Hannah Asiki

University College

A thesis submitted for the degree of *Doctor of Philosophy* in the University of Oxford Trinity Term 2024

This thesis is dedicated to my family.

Abstract

Leishmaniasis is a neglected parasitic disease that places a substantial burden on endemic communities. There is an urgent need for new anti-leishmanial compounds due to the toxic side effects of current therapies and emerging drug-resistance undermining their effectiveness. Central to this is understanding a compound's mode of action (MoA) – how it interacts with the parasite at the molecular level and which target(s) it binds. The MoA is unknown for many anti-leishmanial compounds, despite well-established phenotypic, biochemical, and omics methods with proven success in this application. This thesis contributes to the ongoing search by investigating the MoA of three compound families with potent activity. Here we show that the dehydrodieugenol B (DDB) compound family (primarily using analogue **DDB-1**) localises to the mitochondrion indicating a mitochondrial MoA, **Ascididemin** carries out reactive oxygen species (ROS) generation and metal ion chelation, while the benzyltetrahydroisoquinoline (**BI**) alkaloids disrupt the cell cycle. **DDB-1** was unable to select for *in vitro* drug resistance, contrary to expectation for a drug-like compound in this often-successful method to elucidate compound MoA. **Ascididemin**, as expected, selected for specific genes in a specialist genome-wide knockdown library enabling MoA identification. Our results demonstrate that different MoA elucidation techniques are best suited to different compound families. Based on the MoA proposed here, **Ascididemin** and the **BI** compounds are rendered unsuitable hit compounds, while **DDB-1** has an unusual yet promising MoA, with the potential to become a valuable lead compound following further target identification and medicinal chemistry efforts.

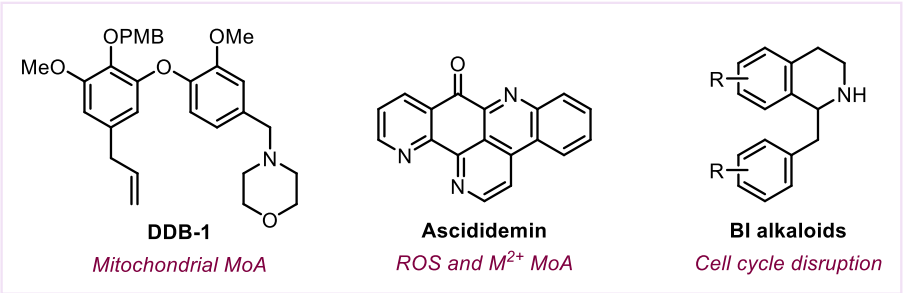

Declaration

No portion of the work referred to in this thesis has been submitted, either partially or in full, for another qualification at this or any other institute of learning.

Excluding figure captions, references, and the appendix, the text of this thesis consists of approximately 47,100 words.

Table of Contents

Abbreviations

ADMET	Absorption, distribution, metabolism, excretion, and toxicity
ADP	Adenosine diphosphate
AF488	AlexaFluor 488
AF555	AlexaFluor 555
AmB	Amphotericin B
ATP	Adenosine triphosphate
BBB	Blood-brain barrier
BSA	Bovine serum albumin
Bp	Base pairs
BSF	Bloodstream form
CC_{50}	Half maximal cytotoxic concentration
CDK	Cyclin-dependent kinase
CL	Cutaneous leishmaniasis
CoA	Coenzyme A
CRISPR-Cas9	Clustered Regularly Interspaced Short Palindromic Repeats-associated protein 9
CuAAC	Copper-catalysed azide–alkyne cycloaddition
CYP	Cytochrome P450
DDB	Dehydrodieugenol B
DMSO	Dimethyl sulfoxide
DNA	Deoxyribonucleic acid
DND*i*	Drugs for Neglected Diseases *initiative*
dNTP	Deoxyribonucleotide triphosphates
DSB	Double-stranded DNA breaks
dsDNA	Double-stranded DNA
EC_{50}	Half maximal effective concentration
EDTA	Ethylenediaminetetraacetic acid
ELISA	Enzyme-linked immunosorbent assay
EMS	ethyl methanesulfonate
ENU	*N*-ethyl-*N*-nitrosourea
ER	Endoplasmic reticulum
ETC	Electron transport chain
FAD	Flavin adenine dinucleotide
FC	Fold change
FCS	Foetal calf serum
FMN	Flavin mononucleotide
GSH	Glutathione
HEPES	4-(2-hydroxyethyl)-1-piperazineethanesulfonic acid
HIA	Human intestinal absorption
HRP	Horseradish peroxidase
HSP	Heat shock protein
IFN-γ	Interferon gamma
IL-10	Interleukin 10
LAMP	Loop-mediated isothermal amplification

L. donovani	*Leishmania donovani*
L. infantum	*Leishmania infantum*
L. mexicana	*Leishmania mexicana*
MCL	Mucocutaneous leishmaniasis
mNG	mNeonGreen
MoA	Mode of action
MS/MS	Tandem mass spectrometry
MVB	Multivesicular body
MW	Molecular weight
NGS	Next generation sequencing
NO	Nitric oxide
NTR	Nitroreductase
ORF	Open reading frame
PAINs	Pan-assay interference compounds
PAL	Photoaffinity labelling
PAM	Photospacer adjacent motif
PBS	Phosphate buffered saline
PCR	Polymerase chain reaction
PKDL	Post-kalar-azar dermal leishmaniasis
PMB	*Para*-methoxybenzyl
PSG	Promastigote secretory gel
PTU	Polycistronic transcription unit
RNA	Ribonucleic acid
RNAi	RNA interference
ROI	Region of interest
ROS	Reactive oxygen species
RPKM	Reads per kilobase per million mapped reads
r.t	Room temperature
SAR	Structure–activity relationship
SD	Standard deviation
SDS	Sodium dodecyl sulfate
sgRNA	Single guide RNA
SI	Selectivity index
SNP	Single nucleotide polymorphism
SPAAC	Strain-promoted azide–alkyne cycloaddition
TCA	Tricarboxylic acid
TEM	Transmission electron microscopy
TPEN	*N*,*N*,*N*′,*N*′-tetrakis(2-pyridinylmethyl)-1,2-ethanediamine
TPM	Transcripts per million
TPSA	Topological polar surface area
TPP	Thermal proteome profiling
T. brucei	*Trypanosoma brucei*
T. cruzi	*Trypanosoma cruzi*
UPR	Unfolded protein response
VL	Visceral Leishmaniasis
WGS	Whole genome sequencing
WT	Wildtype

1 Introduction

Leishmania is a unicellular eukaryotic parasite that causes disease. To be a parasite is to live in or on a host organism and to benefit at the host's expense. *Leishmania* exemplifies this: as early as 1903, *Leishmania donovani* amastigotes were identified in patients suffering from kala-azar, also known as black fever, a disease prevalent in India and Africa.[1-3] Since then, a substantial understanding of both the parasite and the disease has been developed: Throughout the early to mid-20th century, significant progress was made in classifying *Leishmania* species and understanding its complex life cycle, driven by its public health and economic impact on communities living in endemic regions. In the 1970s and 1980s, the development of new treatments marked significant progress in the fight against leishmaniasis.[4-6] More recently, the arrival of modern molecular biology and genetic sequencing in the 2000s has revolutionised the understanding of *Leishmania* biochemistry and how this relates to disease.

Despite over a century of research, leishmaniasis remains a huge burden on public health, particularly in developing countries. Drugs suffer from emerging resistance, and many cellular therapeutic targets remain unexplored. This thesis aims to address the need for new therapeutics by delving into mode of action and target identification for anti-leishmanial compounds.

1.1 *Leishmania* phylogeny

The *Leishmania* genus belongs to the order *Trypanosomatida* (trypanosomatids), which includes other parasitic protozoa such as *Trypanosoma brucei* and *Trypanosoma cruzi*, the causative agents of human African trypanosomiasis (sleeping sickness) and American trypanosomiasis (Chagas disease) respectively. Trypanosomatids fall into the class Kinetoplastea (kinetoplastids), owing to the presence of a kinetoplast – an organelle containing mitochondrial DNA.

Leishmania is believed to have evolved from the other trypanosomatids around 200 million years ago, diverging into over 20 recognised species pathogenic to humans.[7] Many of these are grouped

into species complexes based on genetic and pathogenic similarities,[8] which can be further classified into two branches – Old world or New world – according to geographical location and disease presentation (Table 1).

Table 1. Examples of Old and New world *Leishmania* species and their geographic location

	Complex	Common example species	Distribution
Old World	*Leishmania donovani*	*L. donovani, L. infantum*	South Asia, East Africa, the Mediterranean
	Leishmania tropica	*L. tropica, L. major*	North Africa, the Middle East, Central Asia, the Mediterranean
New World	*Leishmania braziliensis*	*L. braziliensis, L. peruviana, L. guyanensis*	Brazil, Peru, other regions of Central and South America
	Leishmania mexicana	*L. mexicana, L. amazonensis*	Mexico, Central America, parts of South America

1.2 *Leishmania* biology

1.2.1 Life cycle

Leishmaniasis is spread by over 90 different species of sandflies of the genus *Phlebotomus* (Old world) or *Lutzomyia* (New world).[9] *Leishmania* therefore exist in two major life cycle stages with distinct morphologies: flagellated promastigotes within the sandfly, and smaller, rounder, non-flagellated amastigotes within the mammalian host. Within the sandfly, extracellular procyclic promastigotes proliferate in the sandfly midgut. A mature infection of predominantly metacyclic promastigotes is then established. These secrete chitinase, a multifunctional virulence factor that promotes sandfly stomodeal valve colonisation, thereby enhancing transmission.[10] Promastigotes affect sandfly feeding habits through a promastigote secretory gel (PSG) plug composed of filamentous proteophosphoglycan;[11] this "blocks" the sandfly gut and holds open the stomodeal valve,[12, 13] leading to more frequent biting and longer feeding.[14] Thousands of promastigotes are transmitted during a sandfly blood meal within the PSG plug, which additionally promotes pathogenicity in the mammalian host.[15] In the mammalian host, *Leishmania* are phagocytosed by macrophages or other phagocytic cells such as neutrophils and monocytes.[16] This is a passive uptake;

more efficient for metacyclic promastigotes than procyclic promastigotes.[17] The changed conditions within the mammalian host of 37 °C compared to the 26–28 °C of a sandfly triggers differentiation to the immotile amastigote form, taking approximately 24 h.[18, 19] Amastigotes resist degradation by the host immune system by residing in a parasitophorous vacuole – an acidic phagolysosome-like structure developed over 2–5 days.[20] The much smaller size of intracellular amastigotes means a reduced surface-to-volume ratio, which limits exposure to the harsh parasitophorous vacuole.[20, 21] *Leishmania* modulate the host response system by impairing the ability to induce IL-12,[22-25] which inhibits the production of IFN-γ, decreasing nitric oxide production (which is crucial to *Leishmania* toxicity).[26] Additionally, they induce the production of immuno-regulatory cytokines such as IL-10 and TGF-β that deactivate macrophage functions,[27, 28] and inhibit the JAK2/STS signalling pathway which causes IFN-γ unresponsiveness.[29, 30] Proliferation of amastigotes eventually causes the infected macrophage to burst open, releasing them to perpetuate the infection in neighbouring phagocytic cells. Infected macrophages are ingested during a sandfly bloodmeal, releasing amastigotes into the sandfly midgut which differentiate into procyclic promastigotes, continuing the cycle.[31]

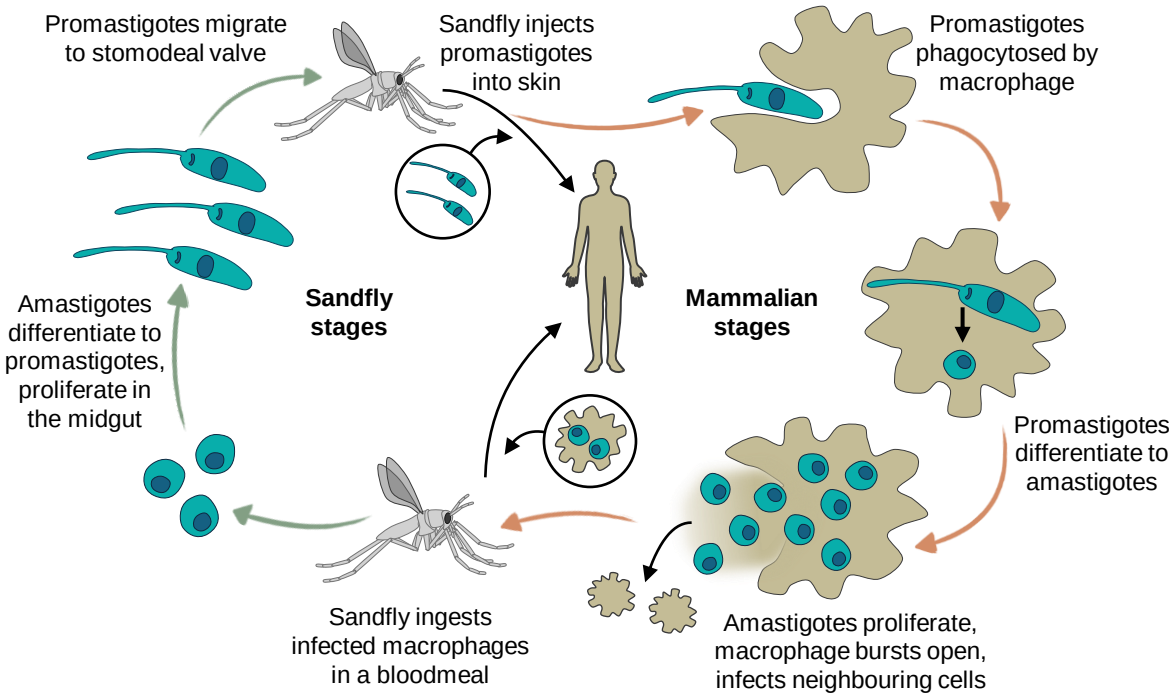

Figure 1. *Leishmania* exists in two distinct life cycle stages. A simplified overview of the *Leishmania* life cycle; In the sandfly stages the parasite proliferates as a promastigote, and in the mammalian stages as an amastigote.

1.2.2 *In vitro* culture

Leishmania have long been grown *in vitro*, first demonstrated in 1905.[32] Most species are well adapted to culture, such that the entire life cycle from promastigotes to amastigotes and back again can be completed *in vitro* without the need for a host.[33] Promastigotes can be grown in commercially available liquid cell culture medium by incubation at 24–28 °C and pH 7–7.2 as a model of sandfly conditions.[34, 35] These can be simply considered as procyclic promastigotes in exponentially growing cultures and metacyclic promastigotes at high densities in stationary phase cultures.[36] Although different from within sandflies, the axenic promastigotes are a reasonably good representative of the *in vivo* picture.[37]

Some *Leishmania* species such as *L. mexicana* and *L. donovani* can differentiate into *in vitro* axenic amastigotes in acidic culture media (pH 5.5) and high temperatures (34–37 °C).[38, 39] This is a simulation of conditions within a parasitophorous vacuole that triggers differentiation in the mammalian host. However, amastigotes of many species cannot be grown axenically and require *in vitro* infection of macrophages – a closer representation of the *in vivo* picture. Axenic and macrophage-derived amastigotes are remarkably similar: they are of comparable infectivity,[39, 40] share the same amastigote-specific markers,[41] and are morphologically indistinguishable. The metabolic profile of axenic amastigotes appears as an intermediate between intracellular amastigotes and promastigotes;[42] this is an important consideration if axenic models are used for drug discovery.

1.2.3 Cell ultrastructure

Trypanosomatids have a rigid morphology defined by a cross-linked sub-pellicular array of microtubules that is conserved throughout the life cycle stages.[43] *Leishmania* contain single copies of organelles such as the nucleus, mitochondrion and a Golgi apparatus, alongside multi-copy organelles such as lipid bodies, glycosomes and acidocalcisomes, whose localisations have been well defined by light microscopy[44] and electron microscopy.[45-47] The kinetoplast is anterior to the nucleus in *Leishmania*, and posterior in *T. brucei*. The kinetoplast directly connects to the basal body,[48, 49] from which the flagellum extends out of a cell membrane invagination called the flagellar pocket.

The internal architecture of *Leishmania* promastigotes and amastigotes is largely conserved. A major morphological difference is the elongated flagellum in promastigotes with multifunctional roles in motility and physical attachment, while the immotile amastigote flagellum is dramatically shortened and does not protrude the flagellar pocket.[50] The promastigote is also longer than the amastigote form, being between 6–12 µm.[51] The flagellar pocket is the only site of endocytosis and exocytosis,[52] therefore it plays a key role in the cells interaction with its environment. Vesicles containing material are trafficked to the early endosomes which are located close to the flagellar pocket.[53, 54] Material can then undergo either exocytosis or progress to the terminal endocytic compartment i.e., the lysosome. The *Leishmania* lysosome differs in structure from most other eukaryotes; it is a vesicle-filled tubule that stretches from close to the flagellar pocket towards the posterior end of the cell, referred to as a multivesicular tubule lysosome.[55-57] In *T. brucei*, the lysosome is a more rounded structure than the elongated form in *Leishmania*, and is located closer to the flagellar pocket.[44, 58]

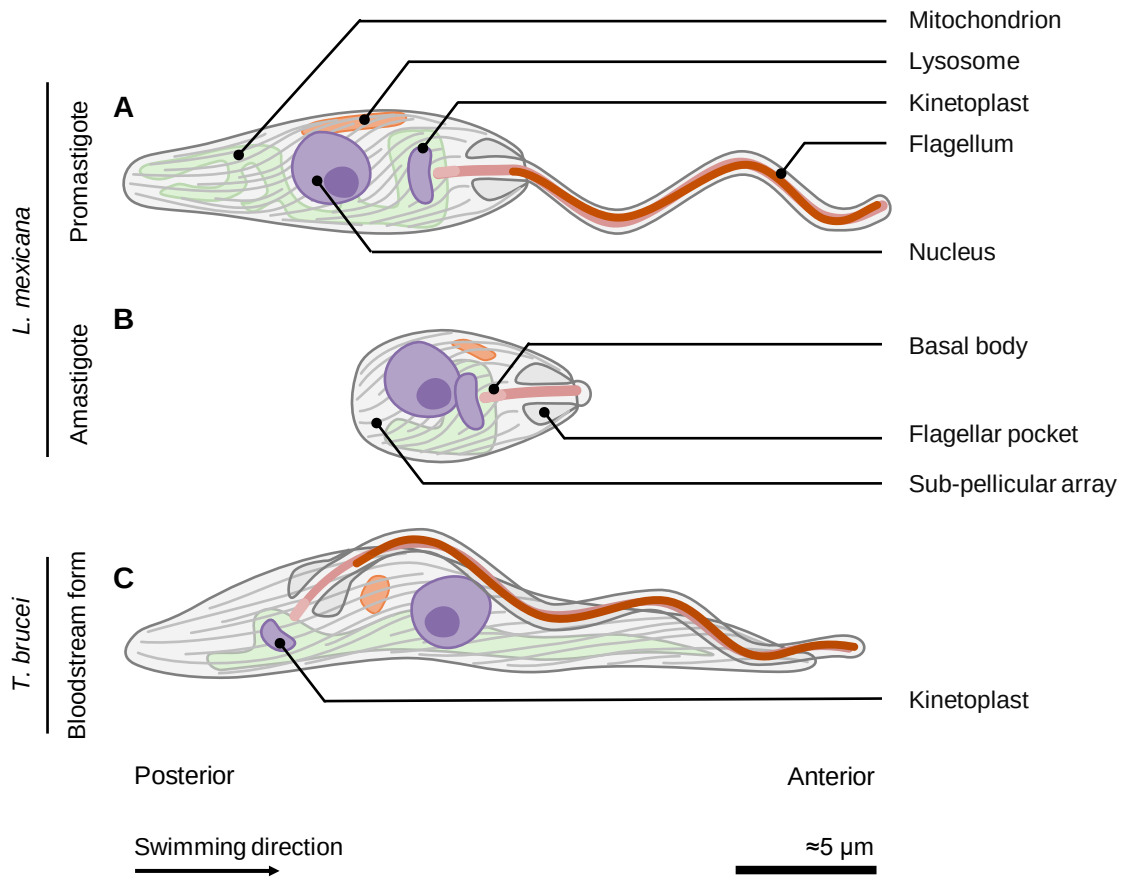

Figure 2. The morphology and ultrastructure of trypanosomatids, exemplified by *L. mexicana* and *T. brucei*. A. Promastigote; elongated cell body and flagellum, B. Amastigote; no elongated flagellum, C. Bloodstream form (trypomastigote); kinetoplast posterior to the nucleus. Figure adapted from Richard Wheeler.

1.2.3.1 Basic structure and function of the mitochondrion

The single mitochondrion of the trypanosomatids was first confirmed in the 1970s by electron microscopy, in remarkable resolution that remains relevant to modern mitochondrial studies.[59-61] In *Leishmania*, it is a large reticulated structure throughout the cell, composed of an inner and outer membrane forming the compact matrix and internal cristae.[62] *T. brucei* display mitochondrial plasticity: procyclic insect forms have an enlarged mitochondrion that contains cristae, while bloodstream forms in the mammalian host have a simplified mitochondrion lacking cristae.[63] This appears as a line along the cell body without branching or reticulation, unless it is undergoing division.[43, 63-65] Within the mitochondrial matrix is the kinetoplast – a concatenated network of circular DNA, [66] representing around 30% of the total cellular DNA.[67, 68]

Most mitochondrial proteins are synthesised in cytoplasmic ribosomes and then imported in using short mitochondrial targeting sequences.[69] The mitochondrion has roles in energy generation through the tricarboxylic acid cycle and respiratory chain, signalling, response to stress *via* reactive oxygen species (ROS) generation, and lipid metabolism. The *Leishmania* mitochondrion carries out ATP metabolism *via* oxidative phosphorylation; making use of an electron transport chain (ETC) containing Complex I to IV and an ATP synthase Complex V, canonical of eukaryotes.[70, 71] The presence of Complex I, however, is species and strain dependent. *T. brucei* procyclic forms have a similar ETC additionally incorporating the trypanosoma alternative oxidase (TAO) which presents a competing pathway for electron carrier ubiquinone.[70, 72] Conversely, the simplified mitochondrion of *T. brucei* bloodstream forms has dispensed completely with oxidative phosphorylation as an energy source. This life cycle stage relies on glycolysis to generate ATP, while the mitochondrion is an ATP consumer unless under specific environmental or genetic conditions.[73, 74]

1.2.4 *Leishmania* cell cycle

Trypanosomatids follow the canonical eukaryotic cell cycle phases: G_1, S, G_2, mitosis and cytokinesis. The size, shape, and positioning of the DNA organelles during *L. mexicana* promastigote cell division is well defined.[51] During G_1, cells grow from approximately 6 µm to

12 µm with a fixed quantity of DNA. Cell size is maintained during S phase while DNA synthesis occurs, followed by a brief G_2 phase involving cell shortening back to 6 µm and a new flagellum emerging. The cells duplicate their nucleus before their kinetoplast, leading to the existence of cells with two nuclei and one kinetoplast. Throughout, the kinetoplast is located at a fixed distance from the anterior end of the cell body while the nucleus positioning is variable depending on cell length. Mitosis is asymmetric: the old nucleus is positioned on the same side as the old flagellum, the new nucleus is positioned on the side of the new flagellum, and the new kinetoplast moves to join the new nucleus. Cytokinesis is longitudinally symmetric, hence the requirement for precise positioning of the duplicated organelles. The cell cycle of *T. brucei* is more widely studied and understood, and follows a similar pattern to *Leishmania*.[75] The timing of kinetoplast segregation is earlier than in *L. mexicana*, occurring before the completion of mitosis which leads to cells with two kinetoplasts and one nucleus, differing from *Leishmania*.[76, 77]

1.2.5 Genomic organisation

The first trypanosomatid reference genomes were sequenced and published in 2005 for *L. major*,[78] *T. brucei*,[79] and *T. cruzi*.[80] This was soon followed by whole genome sequencing for many others including *L. infantum, L. braziliensis*,[81] and *L. mexicana*.[82] These have allowed detailed analyses of gene expression, comparative genomics, functional genomics, and host or drug interactions.[83, 84]

1.2.5.1 Gene expression in trypanosomatids

The *Leishmania* genome is diploid, arranged into a species-dependent number of chromosomes (34 in *L. mexicana*, 36 in *L. donovani*)[85, 86] of approximately 32 megabases coding for around 8000 proteins.[81] The genome has a high level of plasticity and is prone to gene and chromosome copy number variations, and mosaic aneuploidy.[82, 87-89] *Leishmania* genome regulation is quite distinct from other eukaryotes. Genes are made up of protein-coding regions arranged into long polycistronic transcription units (PTUs).[90, 91] These PTUs are made up of multiple genes that are transcribed together to form a polycistronic pre-mRNA. *Leishmania* do not have traditional RNA polymerase II promoters, instead transcription occurs in both directions from regions between the PTUs.[90, 91]

Pre-mRNAs undergo trans-splicing to form individual translatable mRNAs with a 5' spliced leader sequence which is important for mRNA stability.[92, 93] Due to the polycistronic transcription mechanism, gene expression regulation happens at the post-transcriptional level involving mRNA degradation and translation control; it is not controlled by promotors on individual genes as is the case for most eukaryotes.[94-97] The *T. brucei* genome is made up of 11 pairs of chromosomes and is controlled in a very similar manner to *Leishmania.*[79, 98, 99]

1.2.5.2 RNA interference in trypanosomatids

African trypanosomes additionally make use of RNA interference (RNAi), the machinery for which is lacking in *Leishmania* (apart from *L. braziliensis*).[100-102] RNAi involves exogenous double stranded RNA (dsRNA) which can create sequence-specific small interfering RNA (siRNA). This siRNA can bind to complementary target mRNA bringing about silencing by triggering nuclease-mediated cleavage and degradation, acting as a defence mechanism.[103]

1.3 Leishmaniasis

Trypanosomatids account for the top two most deadly neglected tropical diseases: human African trypanosomiasis and leishmaniasis. *Leishmania* infections can be both zoonotic and anthroponotic in animal or human reservoirs. *L. infantum* in particular uses dogs as a reservoir, playing a crucial role in the spread of disease.[104, 105] An estimated 12 million people suffer from leishmaniasis at any given time, with a further 350 million people at risk of infection and a million new cases reported each year.[106, 107] Leishmaniasis has three major clinical manifestations: visceral leishmaniasis (VL, also known as kala-azar), cutaneous leishmaniasis (CL) and mucocutaneous leishmaniasis (MCL).

1.3.1 Epidemiology and clinical features

VL is the most severe form of the disease, and is generally fatal unless treated.[108] It is caused exclusively by *L. donovani* and *L. infantum*, with over 90% of cases occurring in only seven countries in 2015: Brazil, Ethiopia, India, Kenya, South Sudan, Sudan and Somalia.[106] VL occurs when parasites migrate to internal organs such as the liver, spleen, and bone marrow. Characteristic

symptoms are non-specific, including sporadic fever, weight loss, splenomegaly, hepatomegaly, and anaemia. Disease severity can be exacerbated by co-infection with HIV/AIDS due to synergistic action on the immune system increasing disease progression.[109, 110] Post-kala-azar dermal leishmaniasis (PKDL) is a complication that arises in up to 60% of patients after recovery from VL, particularly with *L. donovani* infections.[111] PKDL is a maculopapular and nodular rash, often spontaneously healing and with good cure rates. It has a significant epidemiological role acting as a parasite reservoir within the lesions.[112]

CL is the most common form of the disease, causing skin lesions, nodules, papules, and ulcers, generally at the site of the sandfly bite.[106, 113] While not life-threatening, the painful lesions often leave permanent scars and disfigurement which leads to social stigmatism. It has multiple causative species, a dispersed geographical distribution, and varied clinical manifestations. This leads to difficulties in diagnosis and treatment, while the low mortality rate means a low financial incentive to cure or control CL. It therefore remains a major neglected tropical disease affecting millions of people worldwide.

MCL is a potentially life-threatening complication of CL in which lesions develop in the mucosal surfaces of the upper airways. MCL can lead to severe, permanent facial disfigurement with complete destruction of the nose and mouth. It is particularly associated with infection by the *L. braziliensis* complex and is therefore observed predominantly in Bolivia, Brazil and Peru.[114, 115] The destruction caused by leishmaniasis and MCL in particular accounts for the loss of an estimated 1 million disability-adjusted life years (DALYs)[116] – calculated to factor-in years lived with disability [117] – and highlights the scale of impact on affected communities.

1.3.2 Diagnosis

The diagnostic gold standard for leishmaniasis is the microscopic observation of amastigotes in tissue samples. This has a sensitivity of over 90% from splenic aspirates but is a technically challenging procedure.[106] Serological antibody detection assays account for most of the rapid diagnostic tests (RDTs) for VL, often commercially available as dipsticks. The rK39-RDT is

particularly effective in South Asia with a high sensitivity of 97% (and is therefore the recommended diagnostic tool in the Indian subcontinent), but suffers an unexplained drop in sensitivity to only 85% in East Africa.[118] Alternatively, a semi-quantitative direct agglutination test can be used, which has a sensitivity of 95%.[119] Dilutions of patient blood/serum are mixed with fixed and stained promastigotes, causing a visible agglutination if parasite antibodies are present.[120]

ELISA, immunoblotting, and immunofluorescence antibody tests are too expensive and time consuming to use routinely in the field. Diagnostic tests in development include PCR-based LAMP targeting a region of the rRNA gene,[121] or minimally invasive ELISA detection of urinary antigens;[122] it remains to be seen if these will perform with the required sensitivity and specificity in the field. CL and MCL cannot be detected with serological assays and rely solely on microscopy and/or LAMP detection.

1.3.3 Therapeutics

Treatment of leishmaniasis is entirely reliant on chemotherapy; there is no vaccine although there are multiple in development.[123, 124] A limited arsenal of five drugs are routinely used for treatment (Figure 3), all of which suffer major drawbacks. These include but are not limited to: severely toxic side effects, lengthy treatment, invasive administration, storage difficulties and high production cost.

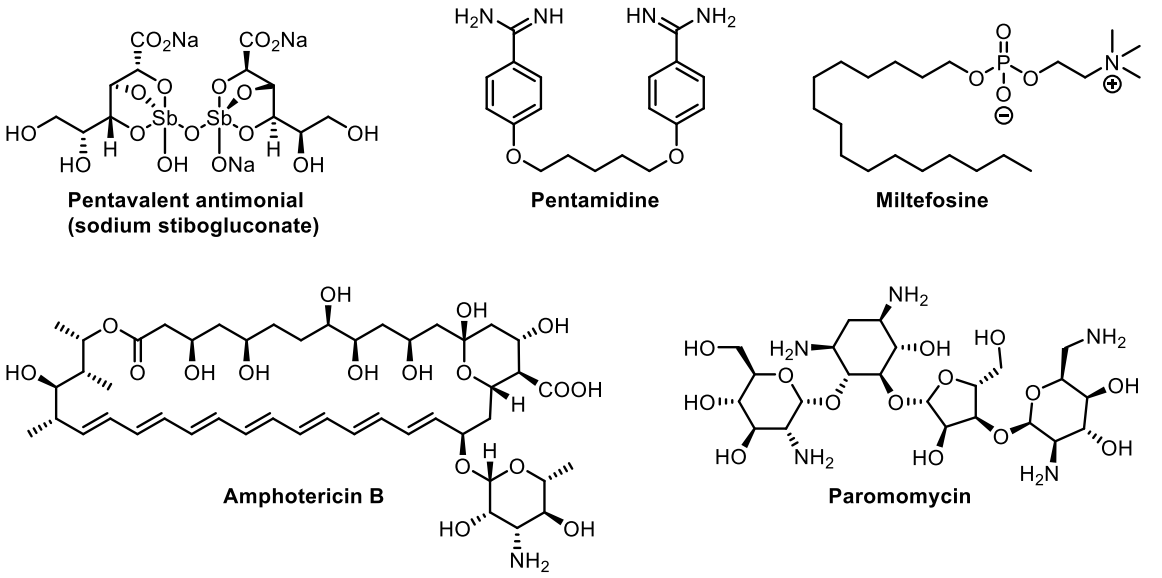

Figure 3. Structure of drugs currently in clinical use for leishmaniasis.

Table 2. The clinical drugs for leishmaniasis, their geographic areas for recommended use, and indications of negative side effects or undesirable considerations.

Drug	Clinical form and geographic location of use (% efficacy where known)	Side effects and other considerations
Pentavalent antimonials	**VL**- East Africa (94%), South America **PKDL**- East Africa **CL**- Central and South America	Cardiotoxicity, arrhythmias, pancreatitis, hepatotoxicity. Painful administration.
Amphotericin B	**VL**- East Africa (> 90%), South Asia (96%) **PKDL**- East Africa, South Asia **CL**- South America **MCL**- South America	Shivering, back pain, nephrotoxicity, hypokalaemia. Expensive, cold storage required, complex preparation.
Miltefosine	**VL**- East Africa (90%), South Asia (90%), Central and South America **PKDL**- South Asia **CL**- South Asia, Central and South America **MCL**- South Asia, Central and South America	Gastric irritation, nephrotoxicity, hepatotoxicity, teratogenic. Expensive, long treatment.
Pentamidine	**CL**- Central and South America	Gastric irritation, cytopenias, irreversible diabetes, pancreatitis, nephrotoxicity. Painful administration.
Paromomycin	**VL**- East Africa (85%), South Asia (93–95%) **CL**- Middle East, Mediterranean, East Africa	Gastric irritation, nephrotoxicity (rare). Mildly painful administration.

Information combined from various references.[106, 125-127]

Several clinical trials have indicated that drug efficacy is dependent on both the parasite species and patient population features: genetic characteristics, immune status, and social context, although this is poorly understood.[128] Drugs are generally administered intramuscularly or intravenously for VL, and as a topical therapy for CL, although as CL lesions can be self-healing, treatment is mainly recommended where there is an increased risk of MCL development.[125]

Combination therapy is becoming a powerful strategy in the treatment of leishmaniasis, i.e., the prescribing of two or more drugs concomitantly to improve treatment duration, and reduce overall doses, toxic side effects, and cost. Experience with other diseases such as leprosy, tuberculosis, and malaria has demonstrated that combination therapy can prevent resistance from developing.[129] A good approach uses one very active drug with a short half-life such as amphotericin B (half-life 24 h) or paromomycin (half-life 2–3 h), and another slow-acting drug with longer half-life such as

miltefosine (half-life 7–8 days) to clear remaining parasites from the body. Recent clinical trials have shown the benefits of an amphotericin B/oral miltefosine combination, achieving a cure rate of up to 88% in HIV–VL coinfection.[130] A paromomycin/miltefosine combination also achieved 91% efficacy, comparable to a paromomycin/pentavalent antimonial combination, with improved treatment times and no cardiotoxicity risk.[131]

1.3.3.1 Emerging drug resistance

In common with other eukaryotic pathogens, *Leishmania* drug resistance is becoming a big challenge for disease management. This has evolved in the field in part due to parasites being exposed to low levels of drug from misuse, which leads to the selection of resistant strains.[132] Levels of clinical resistance vary for each drug depending on multiple factors, including *Leishmania* species. Pentavalent antimonials have suffered strikingly high levels of clinical resistance: a study in the 1990s demonstrated that over 60% of VL patients in Bihar, India, did not respond to pentavalent antimonial treatment, leading to its discontinuation in the region.[133, 134] Similarly, antimonial resistance has been observed in parasite isolates from VL patients in eastern Sudan.[135] This has led to an increased reliance on alternatives, in particular Amphotericin B and miltefosine, which are not without their own resistance concerns. Miltefosine is vulnerable to resistance due to poor compliance with the required long treatment time (typically 28 days),[125] and reports indicate that efficacy is already declining in South Asia,[136] while some *L. infantum* isolates in South America display a natural resistance.[137] Increasing numbers of *Leishmania* isolates from relapsed patients have resistance to Amphotericin B, with different species being implicated.[138-140] Paromomycin – which is often used to treat CL – has only one report of declining sensitivity: a 3 – 5 fold *in vitro* decrease in activity was observed for *Leishmania* isolates following relapse compared to pre-treatment;[141] resistance in VL has yet to be reported.[132] While resistance to pentamidine, paromomycin and amphotericin B is still relatively rare, it is expected to increase as these have now become first-line drugs.[132, 142]

There is clearly an urgent need to develop new therapies to combat rising resistance, as well as improve safety profiles. Temperature manipulation at the site of CL lesions *via* thermotherapy (preventing *Leishmania* proliferation at high temperatures) or cryotherapy (causing *Leishmania* cell death in ice crystals) have been trialled as safer alternatives.[143] Immunotherapy with IFN-γ has led to higher cure rates of VL in combination with pentavalent antimonials, this is an approach in which the immune system is modulated to fight *Leishmania* infection.[144]

1.4 Drug discovery for leishmaniasis

1.4.1 Target-based discovery

Most modern drug discovery programs favour a target-based approach to discover new pharmaceuticals by screening compounds against a validated target. Availability of genomic data for the trypanosomatids has allowed the identification of parasite-specific essential targets that are potentially druggable, including trypanothione reductase (maintains redox equilibrium),[145] distinct cysteine proteases (amastigote virulence factor),[146] and DNA topoisomerases (DNA replication).[147] However, compounds that show activity against a purified recombinant target in cell-free assays often have poor translation to mammalian systems. This is due to the requirement of any active compounds *in vivo* passing through the membranes of the macrophage, parasitophorous vacuole, and amastigote, to reach its intended target. There are also metabolising enzymes of both the parasite and the host to contend with, the acidic conditions of the parasitophorous vacuole and/or potential compartmental sequestration. *In vitro* activity against a recombinant target is a poor model for the complex *in vivo Leishmania* infection, and this approach has yet to successfully lead to a new drug. In contrast, target-based discovery has a high success rate (70% of drugs from 1999 to 2013) in mammalian disease despite similar oversimplification challenges,[148, 149] perhaps in part due to the validated target being more readily accessible such that an *in vitro* assay is not so far removed from the *in vivo* picture as with leishmaniasis.

1.4.2 Phenotypic-based discovery

Successful drugs discovered for trypanosomatids are almost entirely based on phenotypic screening approaches, which has been the most promising method for discovering novel active compounds as hits.[150] These are screens against the whole parasite to discover compounds that impact parasite viability, therefore already accounting for intracellular conditions. The digenetic *Leishmania* life cycle raises debate as to the appropriate assay for activity screening: promastigotes grow quickest but represent the insect stage, while intracellular amastigotes provide the most accurate *in vivo* picture but are least amenable to high-throughput. A compromise has been developed in which axenic amastigotes are used for initial activity results, which are then validated in an intracellular amastigote assay.[151] Once a phenotypically active compound is identified, there often follows mode of action (MoA) deconvolution and/or target identification to pin down the action of the compound. A significant effort by GlaxoSmithKline phenotypically screened 1.8 million compounds against *L. donovani*, *T. cruzi* and *T. brucei*, resulting in around 200 original compounds per species as an open resource to the parasitology community, many of which are now the subject of MoA studies.[152]

1.4.3 Drug repurposing

Drug repurposing or repositioning is a relatively "easy" strategy to find new anti-parasitic drugs by trialling those already developed for other diseases. This is due to the reduced time associated with drug development, particularly with establishing drug safety, as the drug can go straight to preclinical efficacy testing. Nearly all anti-leishmanial drugs were repurposed from other diseases: Amphotericin B (anti-fungal), miltefosine (anti-cancer), pentamidine (anti-trypanosomal), and paromomycin (anti-bacterial). There could be the potential to repurpose other anti-trypanosomatid drugs given similarities in their genomes and therefore the likelihood of possessing similar targets. However, differences in pharmacology, particularly drug uptake, have proved to be a limitation. For example, the anti-trypanosomal drug suramin is not suitable for treating leishmaniasis, which is thought to be due to its endocytic uptake mechanism that is particularly fast in bloodstream form trypanosomes.[153] Pentamidine is also 1000-fold less active against *Leishmania* than in the

Trypanosoma for which it was originally developed, due to differences in uptake.[154] The only anti-trypanosomatid drug to be licensed in the last few decades is fexinidazole (for human African trypanosomiasis), which showed excellent efficacy in mouse models against *L. donovani*,[155] although failed in clinical trials against VL.[156] It is clear that repurposing between the trypanosomatids may not be as trivial as one might expect.

1.4.4 Use of ADMET screening

An important aspect of potential hit candidates is their pharmacokinetic properties, which factor into their *in vivo* ADMET behaviour (absorption, distribution, metabolism, excretion and toxicity). There are numerous *in vitro* ADMET screens, however these can be time consuming, are not generally suitable for high throughput, and require access to large amounts of compound. Computational models have been developed to accelerate this process, allowing ADMET read-outs to be generated early in the drug discovery pipeline, thus decreasing the rate of late-stage attrition.[157, 158] These ADMET models often rely on experimental data to improve the reliability of predictions – this is a limitation as such data may not be readily available for each of the predictable parameters. Relevant physicochemical properties such as lipophilicity and solubility can be predicted with a fairly high confidence, whereas properties like clearance, volume of distribution, aspects of metabolism and toxicity are generally harder to predict from molecular structure alone.[157, 159] This is because of the reliance on many of these processes on multiple biological interactions which are difficult to satisfactorily model, for example how both P-glycoprotein (P-gp) and cytochrome P450 3A4 in the gut play a combined role in drug absorption,[160] and the interactions of a drug with transporter proteins. While *in silico* predictors can form a good starting point, these should be followed up with *in vitro* experiments to confirm the predictions.

1.4.5 Novel compounds in the drug discovery pipeline

In recent years, there has been a substantial investment in trypanosomatid drug discovery through organisations such as the Wellcome Trust, Drugs for Neglected Diseases *initiative* (DND*i*), and key partnerships with pharmaceutical companies including Novartis, GlaxoSmithKline (GSK) and

Takeda Pharmaceuticals. Coupled with the advances in understanding parasite biology, there is now a promising pipeline for novel leishmaniasis drugs: six new entities are in early clinical development (Figure 4). Of these, LXE408 developed by Novartis is the frontrunner in Phase IIa clinical trials,[161, 162] while the remaining five compounds are in Phase I studies (as of June 2024).[163] Synthetic small molecules dominate, although one oligonucleotide DNDI-2319/CpG-D35 is being trialled for CL and PKDL as a modulator of the host immune response.[164, 165] However, there are already potential issues within this pool: toxicity concerns for DNDI-0690 which caused unexplained biological abnormalities following 10-day treatment,[166] and DNDI-6148 which has pre-clinical reproductive toxicity signals,[167] mean that neither is currently scheduled to progress to Phase IIa studies. Although the analogue of DNDI-6148 – acoziborole – successfully completed Phase IIb/III clinical trials for human African trypanosomiasis,[168] toxicity remains a concern here. Two further compounds, DNDI-6174 (GSK and University of Dundee collaboration) and DNDI-8526 (S07 series, DND*i* and Takeda Pharmaceuticals collaboration) are in pre-clinical development with hopes to progress to Phase I trials soon.[163]

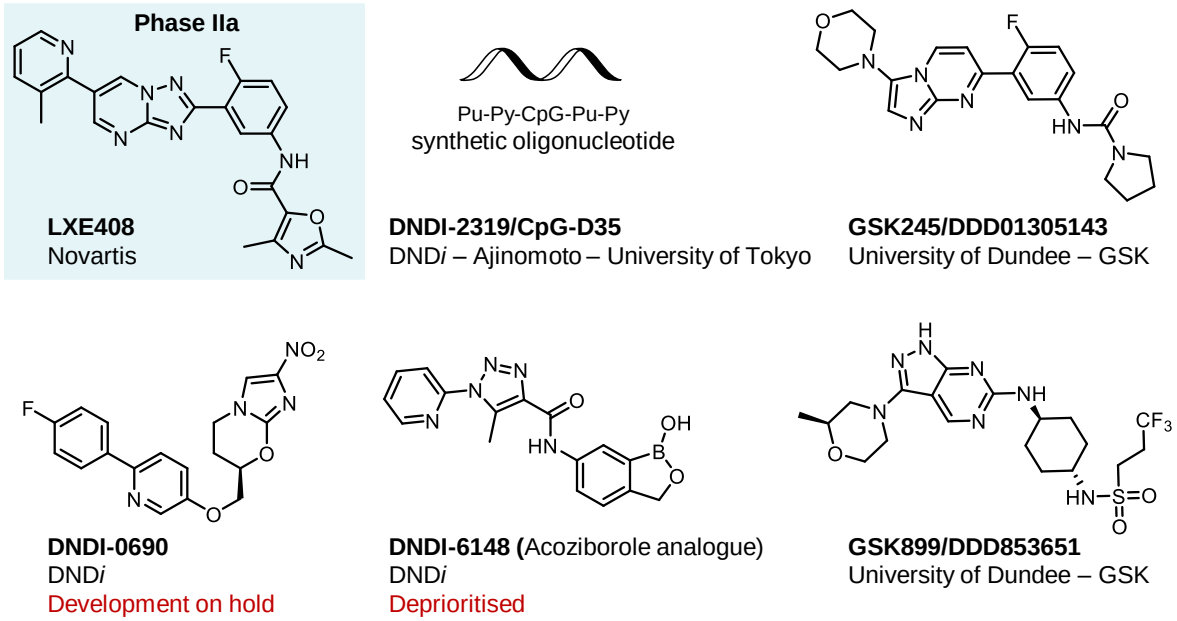

Figure 4. New chemical entities in clinical development for leishmaniasis. LXE408 is in Phase II clinical trials, all other compounds are in Phase I clinical trials (June 2024). DNDI-2319/CpG-D35 is an oligonucleotide; Pu = purine base, Py = pyrimidine base, CpG = cytosine followed by guanine, connected with a phosphate backbone.

1.5 Anti-trypanosomatid drug modes of action

Despite anti-leishmanial drugs being used for decades, it is only with the advent of modern molecular biology and genomics that the MoA of these compounds is being fully understood. There are numerous different compound MoAs proven against *Leishmania*, exemplified in Figure 5. However, target deconvolution for some clinical drugs such as paromomycin, still has not been completely elucidated. Knowledge of anti-trypanosomatid MoAs can support the development of novel drug compounds, which should have a distinct MoA from drugs already in use. This is important for two reasons: firstly, they can be used in combination therapy, and secondly, they are unlikely to display cross-resistance in the case of drug target mutation or target pathway circumvention.

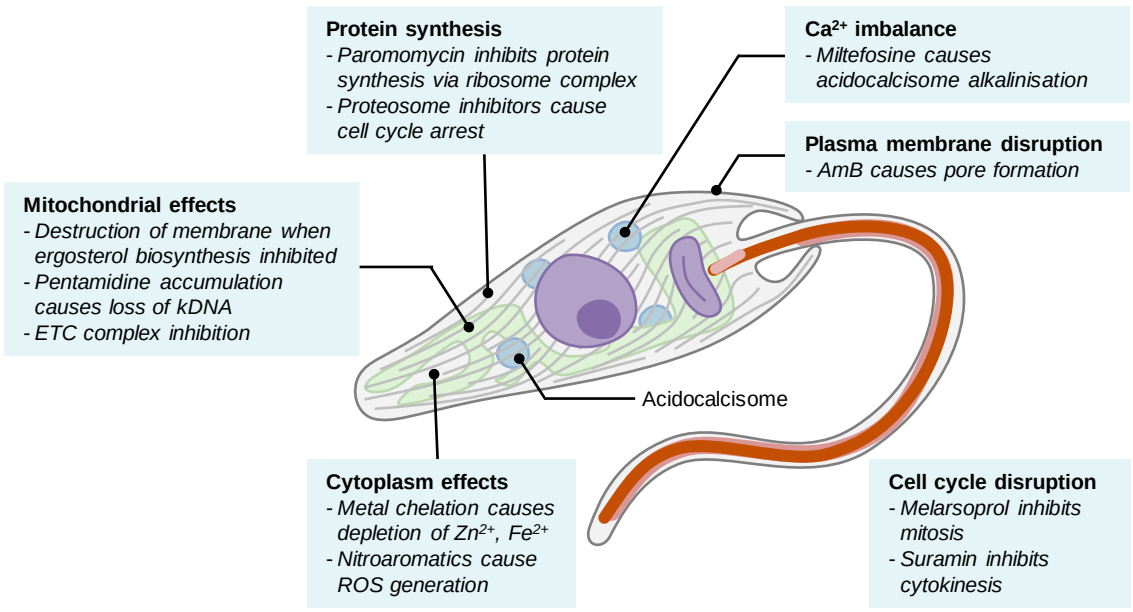

Figure 5. Numerous modes of action are known for anti-trypanosomatid compounds. A simplified overview of example modes of action of anti-trypanosomatid compounds. Figure adapted from Richard Wheeler.

1.5.1 Membrane disruption

Parasite membrane disruption presents an opportunity for drug action, either by direct interaction with the membrane or by interfering with membrane proteins. Miltefosine is an alkylphosphocholine with a varied MoA, one of which involves inhibition of phosphatidylcholine biosynthesis while stimulating membrane cholesterol uptake.[169] Amphotericin B exploits the higher ergosterol

composition in *Leishmania* membranes compared to mammalian cells by high-affinity binding to ergosterol in the plasma membrane, forming transmembrane pores that lead to ion influx and ultimately cell death.[170] Anti-microbial peptides are being considered for their activity against *Leishmania*, as these also exert their activity by insertion into the cell plasma membrane causing disruption, although non-specificity is a concern as this could cause host cytotoxicity.[171] Inhibiting squalene synthase,[172] or sterol 24-methyltransferase[173, 174] – key enzymes of ergosterol biosynthesis – results in complete destruction of the mitochondrial membrane, mitochondrial swelling and loss of matrix content.

1.5.2 Mitochondrial disruption

The mitochondrion plays an important and diverse cellular role (discussed in Section 1.2.3.1) that unsurprisingly has been implicated in the mode of action for various drugs. Pentamidine accumulates directly in the mitochondrion where it inhibits mitochondrial topoisomerase II, leading to a loss of kinetoplast DNA (kDNA).[175, 176] It also causes an imbalance in intracellular Ca^{2+} which causes the mitochondrial membrane potential to collapse.[177]

The mitochondrial electron transport chain (ETC) is a promising target for anti-leishmanials due to significant differences to mammalian ETC. Ubiquinone analogues act as competitive inhibitors of complex III (cytochrome bc_1), causing a potent inhibition of the ETC and loss of ATP production in *Leishmania* amastigotes.[178] This also generates toxic reactive oxygen species (ROS), presumably by blocking complex III activity which releases electrons to molecular oxygen. The same biochemical results were seen for tafenoquine, an anti-malarial drug approved in 2018 that also inhibits complex III in *L. donovani* promastigotes.[179] Pre-clinical candidate DNDI-6174 is another complex III targeting molecule that is showing promising results against VL.[180] Complex II is the target of bisphosphonium benzophenone analogues in *Leishmania*,[181] although interestingly in bloodstream form *T. brucei*, ATP synthase is the main target.[182]

1.5.3 Reactive oxygen species generation

The release of ROS interplays closely with mitochondrial activity, although this is not the only source of ROS in a drug context. Many anti-trypanosomatid compounds are nitro-aromatics, usually heterocycles. These act as pro-drugs, interacting with intracellular nitroreductases (NTRs) which bio-activate the compounds: this is the confirmed MoA of anti-trypanosomal drugs benznidazole, nifurtimox and fexinidazole, and is the proposed MoA of Phase I clinical candidate DNDI-0690 (Figure 4).[183] There are two classes of NTRs based on oxygen sensitivity and cofactor.[184] Type I NTRs are oxygen-insensitive and contain an FMN cofactor. They carry out a series of NAD(P)-H dependent two-electron reductions of nitro groups often to the corresponding amine, with by-products that cause DNA damage.[184, 185] They are a common feature in bacteria but have also been discovered in some lower-level eukaryotes including trypanosomatids.[186-189] Type II NTRs are oxygen-sensitive, with a FAD cofactor. They catalyse a one-electron reduction of nitro groups to produce a nitro radical anion. This then reacts with oxygen to produce superoxide and regenerate the nitro compound. [190, 191] In trypanosomes, modulation of both type I and type II NTRs directly affects the activity of nitro aromatic drugs.[192, 193] Type I NTR in *T. brucei* activates nifurtimox and benznidazole which generates an open chain nitrile with enhanced toxicity.[186, 194] For nifurtimox, this is accompanied by a redox cycling mechanism, while benznidazole is distinct from this. Fexinidazole bioactivation is catalysed by NTRs in *Leishmania*, but the exact metabolites are unknown.[155] In an alternative manner of affecting ROS, pentavalent antimonials are thought to be reduced to the trivalent species *in situ*, which can disrupt the ROS modulator trypanothione, compromising the thiol redox potential.[195]

1.5.4 Calcium ion homeostasis

Calcium ions (Ca^{2+}) have an important role in cellular homeostasis by regulating flagellar movement, exocytosis, and enzymatic activity. In trypanosomatids, Ca^{2+} is stored in the endoplasmic reticulum (ER), mitochondrion, and in contrast to mammalian cells, the largest reservoir is a dedicated acidocalcisome. Miltefosine disrupts Ca^{2+} homeostasis in *Leishmania via* two mechanisms: i)

activation of a plasma membrane Ca^{2+} channel inducing cell influx, and ii) direct alkalinisation of the acidocalcisome, releasing Ca^{2+} into the cytosol. The resulting large Ca^{2+} increase has a knock-on effect on the mitochondrion, and could be the basis of apoptosis observed upon treatment.[196]

1.5.5 Protein synthesis, degradation and the cell cycle

The paromomycin MoA is a *Leishmania*-selective inhibition of protein synthesis, presumably *via* ribosomal subunit binding as has been shown in bacteria, and which is much stronger in *Leishmania* than in mammalian cells.[197] The proteasome is a protein complex in the cytoplasm and nucleus that controls the degradation of misfolded proteins. Both VL clinical candidates GSK245/DDD01305143 and LXE408 are potent and selective proteasome inhibitors, preventing its chymotrypsin-like activity.[198, 199] These are related scaffolds so perhaps unsurprisingly are limited to a common MoA. Proteasome inhibition is linked to cell cycle arrest due to an inability to degrade G_2/M-phase control cyclins; GSK245/DDD01305143 displayed the expected accumulation of G_2/M-phase cells. Pre-clinical candidate DNDI-8526 is another compound with a proven proteasome MoA.[200] Additional factors control the cell cycle, in particular cyclin-dependent kinases (CDKs). Extensive investigation for inhibitors revealed CRK12 as a novel target for clinical candidate GSK899/DDD853651, which displays phenotypic cell cycle arrest.[201] Anti-trypanosomal drugs melarsoprol and suramin also inhibit mitosis and cytokinesis respectively.[202]

1.5.6 Metal chelation

Metals are vital to *Leishmania* homeostasis as they play key structural, catalytic, and signalling roles in cellular processes required for growth and survival. Iron is an essential redox-active metal with an important role in cell signalling such as driving promastigote differentiation to amastigotes, and cell proliferation, often through ROS generation.[203, 204] Zinc on the other hand is redox-inactive, and plays crucial antioxidant roles to modulate oxidative stress.[205] Zinc does not directly interact with ROS, and the mechanisms by which it decreases ROS are not fully understood.[206] Metal chelation is conclusively the MoA against *L. donovani* for 8-hydroxy-naphthyridines (8-HNTs) and an

aminothiazole-pyridine containing compound, proposed to be through Zn^{2+} and Fe^{2+} depletion, and not an interplay with ROS (Figure 6).[207, 208]

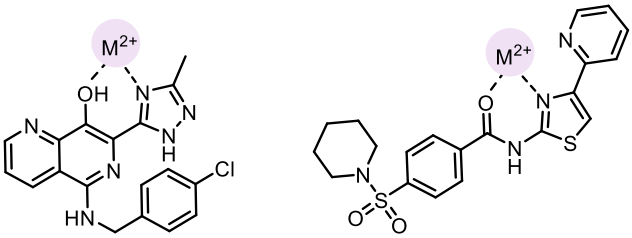

8-HNT **DDD01007886** Aminothiozole **GSK917081A**

Figure 6. Metal ion binding is a known MoA for anti-leishmanial compounds. Structures of some metal chelation compounds and their proposed sites of metal binding.

1.5.7 Modes of resistance

Complementary to understanding MoA is understanding the modes of resistance. *Leishmania* acquired resistance is associated with: i) mutation or changed expression levels of the drug target, ii) upregulation of other enzymes on the target pathway to circumvent drug action, iii) decreased drug uptake, or iv) increased drug efflux or degradation mechanisms. These modes of resistance are often identified by generating *Leishmania* resistance *in vitro*, which is readily achieved for the five main drugs.[140, 209-212] Most of the compounds described above have these modes of resistance, including downregulation of activating NTRs (nifurtimox, benznidazole),[192] decreased expression of drug transporter AQP1 (pentavalent antimonials) or LiMT (miltefosine),[213] lower mitochondrial drug loading leading to increased efflux (pentamidine),[214] overexpression of ABC transporter for drug efflux (miltefosine),[215] downregulation of enzyme sterol 24-methyltransferase (amphotericin B),[216] and mutation in targets CRK12 (GSK899/DDD853651)[201] or complex III (DNDI-6174).[180] The resistance profile for a new drug should be considered where possible: if resistance can be generated by affecting drug uptake, efflux or inactivation, this should not occur *via* routes in common with established drugs – otherwise it could suffer immediate failure.

1.6 Mode of action and target deconvolution strategies

Drug discovery for leishmaniasis has relied heavily on phenotypic and drug repurposing methods, particularly preceding recent advances in understanding *Leishmania* biology. This has produced promising leads, but comes with an unmet need for MoA elucidation and target identification. While this is not strictly necessary for drug development, knowledge of compound MoA/target(s) is useful for: i) rational hit optimisation using structure-based drug design, ii) improving selectivity, iii) prioritising targets unlikely to have mammalian toxicity, iv) increasing the breadth of targets being explored, v) monitoring potential for resistance generation, vi) guiding combination therapy, vii) revealing novel druggable targets for target-based discovery, and viii) avoiding cross-resistance. There is no roadmap to establishing the MoA of bioactive small molecules, often several complementary methods are used.

1.6.1 Utility of click chemistry for target identification

Where MoA is unknown, knowledge of the subcellular localisation of the compound could afford useful insights into the site of action. This makes use of click chemistry by attaching a reporter tag – components that can be detected such as fluorophores or biotin – to the compound. Often the compound requires modification into a small molecule probe that has a high affinity for its binding target and is compatible with click chemistry.

1.6.1.1 Click chemistry for bioorthogonal attachment

The concept of click chemistry was first introduced by Barry Sharpless in the early 2000s, referring to chemical reactions that conform to a set of guidelines: starting from simple reagents, in ambient conditions, with a wide reaction scope and high yield.[217] Since then, the use of click reactions has exploded, finding broad utility in a range of fields, with perhaps the most revolutionary being their use in biological systems. Chemical click reactions can now be carried out within cellular environments without perturbation – this is termed bioorthogonal labelling.[218, 219] The extent to which click chemistry has impacted the field is reflected with the Nobel Prize in Chemistry 2022 jointly

awarded to Carolyn Bertozzi, Morten Meldal and K. Barry Sharpless.[220] Three click reactions in particular have stood out as the most versatile, discussed below (Figure 7).

Perhaps the most famous click reaction is the copper-catalysed azide–alkyne cycloaddition (CuAAC). The azide–alkyne cycloaddition to form a 1,2,3-triazole was first proposed by Huisgen in the 1960s, although slow reaction rate at ambient temperatures coupled with mixed products at elevated temperatures hampered immediate interest in its use.[221] This was drastically changed by the introduction of a copper(I) catalyst, bringing the reaction time down to minutes in physiological conditions, which was independently developed by Sharpless and Meldal in the early 2000s.[222, 223] The main drawback of bioorthogonal CuAAC is the toxic copper catalyst which prevents its use in live cells, generally limiting applications to cell lysates.[224, 225]

In response to the toxicity issues of CuAAC, the copper-free strain-promoted azide–alkyne cycloaddition (SPAAC) was reported by Bertozzi in 2004.[226] This cycloaddition between an intrinsically reactive strained cyclooctyne and an azide proceeds rapidly under physiological conditions, enabling selective labelling in live cells without adverse toxicity effects.[227]

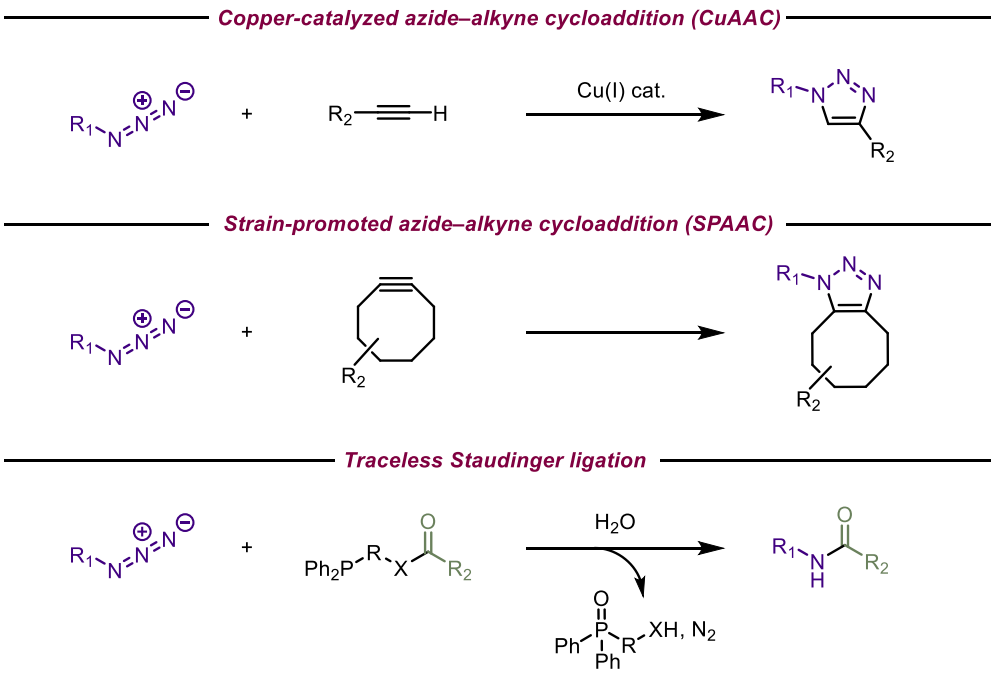

Figure 7. Click reactions commonly applied to biological systems.

Prior to the development of CuAAC, the Bertozzi group had already achieved live cell bioorthogonal labelling with the use of the Staudinger ligation.[228] Inspired by the Staudinger reaction between a phosphine and an azide *via* an aza–ylid intermediate,[229] modifications to the phosphine allowed the ylid to be trapped yielding an amide linkage. Initial Staudinger ligations incorporated a phosphine oxide within the amide backbone however this was swiftly followed by modifications which allowed the phosphine to be removed as a by-product in the traceless Staudinger ligation.[230-232] The disadvantage to the Staudinger ligation however is relatively slow reaction kinetics in comparison to the AAC methods, unwanted phosphine oxidation, and synthetic challenges with phosphine preparation.[233]

1.6.1.2 Photoaffinity labelling for small molecule attachment to proteins *in situ*

If a small molecule has a high affinity for its target and forms a direct covalent attachment then it can be directly modified for use as a probe in click chemistry. However, if the inherent target affinity of the compound is not strong enough, there is need to develop a probe with an alternative method of covalent linking to the target. Such activity probes therefore require three key features: a reactive group or warhead that covalently attaches to the protein target, a carbon chain linking region, and a handle to attach a reporter tag for detection or isolation *via* click chemistry *in situ*.[234, 235]

Cravatt and co-workers showed the first proof of principle in which a small molecule with phenotypic activity led to target identification using a photo cross-linking covalent attachment.[236] Termed photoaffinity labelling (PAL), an inert photoactivatable reactive group is incorporated into the probe that generates a highly reactive intermediate upon exposure to UV light, which allows for covalent cross-linking to nearby molecules.[237] Therefore, a probe can interrogate cells in their native state, photo cross-link upon exposure to UV forming a covalent bond to the supposed target, and then be further functionalised with click chemistry. Probes are designed with the compound of interest attached to a "linker". The chemical identity of the photoactivatable group plays a key role in the success of PAL, three of which have emerged as favourites in the field and merit further discussion (Figure 8).[238]

First, aryl azides generate a reactive nitrene that captures the target under UV light activation, and were originally popular as PAL components due to their relatively easy synthesis. However a major drawback is the requirement of cell-damaging short UV wavelengths to generate the active nitrene, which itself is prone to rearrangement instead of intermolecular capture.[239] Fluorination of the aryl ring has greatly improved the stability of the intermediate and boosted yields of labelled product over rearrangement, although this remains highly influenced by both environment and concentration and is therefore difficult to control in cellular environments.[240]

Second, benzophenones cross-link *via* a ketyl diradical when activated, and this happens at a longer wavelength than the aryl azides which is advantageous as these wavelengths are less cell-damaging.[241] Eirich *et al.* published a highly selective example in which a benzophenone–alkyne linker attached to a compound of interest was used for whole-cell fluorescent microscopy to reveal tubulin as the target in live human cells.[242] However, the authors note that the bulky nature of the benzophenone leads to a drop in activity of the probe compared to the parent compound. Benzophenones also require long activation times leading to non-specific reactivity.[243]

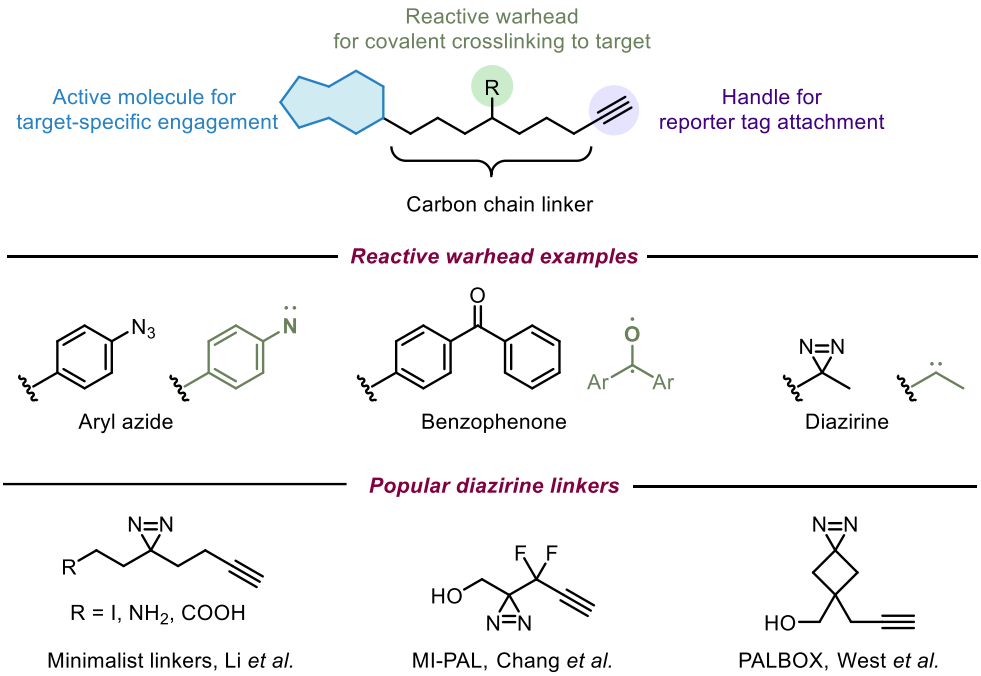

Figure 8. Probe design for a photoaffinity labelling strategy. Popular reactive warheads are aryl azide which forms a nitrene, benzophenone which forms a ketyl diradical and diazirine which forms a carbene upon UV activation to cross-link to the protein target. Popular diazirine linkers include minimalist linkers,[244] MI-PAL[245] and PALBOX.[246]

Third, diazirines have become favourites – being the most cited in the last twenty years, both in aromatic and aliphatic form, which generate a reactive carbene upon activation that carries out the cross-linking. This carbene has higher reactivity than intermediates generated by benzophenone or aryl azides which leads to higher specificity, although this comes with the associated disadvantage of fast quenching by solvent giving lower overall yields.[247, 248] In a convincing comparative study, Sakurai and colleagues investigated the effect of these three photoactivatable groups in weakly binding probes of known targets, and found that diazirines emerged as the superior choice for highest specificity in protein mixtures.[243]

Within the diazirines there are many examples of successful PAL which have been the subject of numerous reviews.[247, 249-252] The first example of a cell-permeable probe was kinase inhibitor saurosporine attached to an alkyne–diazirine handle, which underwent CuAAC with a fluorophore–azide and showed fluorescence localisation to the expected cytosolic localisation in whole cells.[253] The authors noted that the small size of the alkyl diazirine is crucial for maintaining cell permeability and probe activity. In particular, "minimalist" diazirine linkers designed by Li *et al.* show good preservation of biological activity and high labelling specificity.[244] These 7-C containing linkers are comprised of an alkyl diazirine, terminal alkyne, and either a carboxylic acid, primary amine, or iodide for conjugation to drug molecules *via* acid coupling, amine coupling or alkylation respectively. These linkers have been used for fluorescent imaging to determine cellular localisation in live cells,[254, 255] as well as profiling protein interaction partners of small molecules in a cell-wide environment.[256, 257] Small alternatives by Chang and co-workers are the minimally interfering photoaffinity label (MI-PAL),[245] and more recently, cyclobutene diazirine PALBOX,[246] both of which showed successful PAL in whole proteomes.

1.6.1.3 Click chemistry with transmission electron microscopy

In order to visualise compound targets at a high resolution, it could be possible to employ transmission electron microscopy (TEM). There are very few examples in the literature combining click chemistry with TEM, with challenges in creating sufficient contrast to be detectable in the TEM

images. One approach uses click attachment of a fluorophore to an incorporated alkyne, which photo-generates a precipitate of added diaminobenzidine reagent that is then stained with osmium tetroxide for visualisation.[258] A more direct method would be to use electron-dense gold nanoparticles, as these are TEM visible. This approach is traditionally combined with antibody recognition (termed immunogold labelling), to enable gold attachment to specific cell features. Only one report exists in the literature of combining click chemistry with gold nanoparticles for TEM. This example utilised propargylcholine as the probe, and demonstrated gold labelling in cell membranes as expected for propargylcholine phospholipids.[259]

1.6.2 Omics approaches for compound MoA

Full sequencing of the *Leishmania* genome has allowed an explosion of omics techniques: genomics, transcriptomics, proteomics and metabolomics to be exploited for drug discovery and MoA studies.[260-268] Additionally, the wealth of genome manipulation tools such as facile CRISPR-Cas9 genome editing in *Leishmania* means that targets discovered by these methods can be readily validated.[269-273]

1.6.2.1 Generation of resistant lines and whole genome sequencing

A powerful tool for target identification is the generation of cell lines resistant to a compound of interest, and then whole genome sequencing (WGS) of the resultant resistant line. This allows identification of genes that, when altered, contribute to compound resistance, which is informative to compound MoA. Resistance generation and WGS has been successful in *Leishmania* with known drugs,[209-211, 274, 275] as well as compounds in development.[180, 201, 216, 276-278] Resistance selection has been combined with chemical mutagenesis – termed MutSeq, which enhances the diversity of single nucleotide polymorphisms (SNPs) in the starting population, thus increasing the likelihood of a resistant line emerging.[263, 279] This was developed for *Leishmania* by Bhattacharya *et al.* to identify genes involved in miltefosine and paromomycin drug resistance.[280] The method is somewhat complicated by the fact that both homozygous and/or heterozygous SNPs can confer resistance, and the trypanosomatids also use aneuploidy to generate compound resistance.[281]

1.6.2.2 Genome-wide overexpression libraries

If a compound inhibits a particular target, then overexpression of the target can confer resistance. This gain-of-fitness method has been exploited in trypanosomatids using genome-wide overexpression libraries which undergo compound selection, next generation sequencing (NGS), and alignment to a reference genome to identify genes conferring a selective advantage.[282, 283] Compound selection from an overexpression library is a much quicker process than the slow incremental drug concentration normally required for resistance generation.

In *L. donovani*, an overexpression library has been created by transfection of cosmids containing genomic DNA fragments, resulting in > 15-fold coverage with 99% of genes represented.[284] After the overexpression library is enriched by a compound, the cosmids are extracted and sequenced – a method termed Cos-Seq.[283, 284] In *T. brucei*, tetracycline-inducible genomic DNA has been transfected to create an overexpression library with 8-fold coverage and > 95% genes represented.[285] The library can then be induced, put under compound selection, overexpression inserts extracted and PCR amplified, before a final sequencing and analysis.

1.6.2.3 Genome-wide knockdown library

Knockdown is an orthogonal technique to overexpression: it is a loss-of-function screen in which knockdown of a given protein could provide a selection advantage against an active compound. This can identify genes involved in drug action such as up-take mechanisms or compound activators if the compound behaves as a pro-drug, but is unlikely to directly identify a compound target.[286] RNAi can be exploited to facilitate knockdown in *T. brucei* by using tetracycline-inducible synthesis of dsRNA *in vivo*, allowing genome-wide knockdown libraries to be created.[287-289] The University of Dundee has created a *T. brucei* bloodstream form RNAi library with a 10-fold coverage and > 99% of non-redundant genes represented.[290, 291] This is combined with NGS in a technique called RIT-Seq.[290, 291]

1.6.2.4 Transcriptomics for MoA

The transcriptome has valuable information about mRNA expression levels, often correlated to protein levels. It should be noted however that gene expression in trypanosomatids relies on post-transcriptional regulation, and therefore there can be a discrepancy between mRNA expression level and protein abundance. Evaluation of trypanosomatid mRNA abundance has been widely applied to compare life cycle stages or host–pathogen interactions.[83, 292, 293] High-throughput mRNA profiling – RNA-Seq, has also contributed to the unravelling of compound MoA in *Leishmania*, *T. cruzi* and *T. brucei* by comparing transcriptome changes between compound sensitive and resistant cell lines.[210, 294-299]

1.6.2.5 Chemo-proteomics

Chemical proteomics presents a powerful tool for target identification, and can provide information on the direct interaction of a compound with its target. This approach goes beyond other omics techniques that identify genes and not target proteins directly, and has been the subject of numerous reviews.[300-303] The basic premise involves compound attachment to its interacting proteins (either directly through a covalent interaction or assisted with photoaffinity labelling), and then the proteins can be enriched from a complex mixture. Compound can either be pre-immobilised to beads and then cell lysate used for compound–target binding, or a compound–target complex can be formed (often using PAL) *in situ* in live cells, and then pulled out by a secondary attachment to beads. Following enrichment, there is often an enzymatic digest after which interacting proteins are identified with mass spectrometry. The pre-immobilisation method has been employed in kinetoplastid MoA determination to pull-down protein from a lysate,[201, 304] while the use of PAL to probe live cells has yet to be applied successfully to target identification in trypanosomatids – this is more powerful as it can probe cells in their native state. The main drawback of this technique is that it requires a compound to be synthetically modifiable and its structure–activity relationship (SAR) to be known, such that the pull-down probes can be generated.

An alternative, unbiased chemical proteomics approach is thermal proteome profiling (TPP). This is based on the biophysical principle that a compound bound to its target protein causes thermal stabilisation of the protein. Quantitative mass spectrometry can then allow identification of stabilised targets, which has been successfully developed for *Leishmania*.[264] The main benefit of TPP is that it does not require SAR understanding which may be limited for early phenotypic hits, although it is limited to soluble proteins and performs badly for stable protein complexes. Although less complete than in humans, the *Leishmania* proteome is moderately well annotated, with approximately 40% of genes annotated as "hypothetical proteins".[305-307] This can provide additional challenges in identification of proteins and their function, but is not a limitation on the use of proteomics.

1.7 Dehydrodieugenol B as an anti-parasitic natural product

Natural products are proven sources of drugs, either in their natural form, as semi-synthetic derivatives, or as analogues which retain the core framework of the natural molecule. It is well-recognised that two-thirds of small molecule drugs originate from natural bioactive leads.[308] Parasitic diseases are no exception: Amphotericin B and paromomycin were isolated from bacteria, while anti-malarials artemisinin, chloroquine and mefloquine are either natural products, or natural product-inspired.[309] Multiple different natural product families have shown activity against *Leishmania*, including alkaloids, terpenoids, saponins and flavonoids.[310-312]

A neolignan biaryl ether family of natural products was first isolated in 2015 from the Brazilian plant *Nectandra leucantha*, the parent compound of which was named dehydrodieugenol B (DDB) (Figure 9). DDB and methyl dehydrodieugenol B have promising micro-molar activity against *L. donovani* and *T. cruzi*, with low mammalian cytotoxicity.[313-316] In a collaboration between Prof. Ed Anderson (our group) and Prof. André Tempone (Instituto Adolfo Lutz, São Paolo, Brazil), a series of semi-synthetic analogues were prepared from DDB and methyl dehydrodieugenol B.[317] This resulted in compounds with improved activity against *T. cruzi*, and favourable safety profile predictions. Dr. Claire Sear (Previous PhD student) developed a concise, robust and convergent synthesis to access

these compounds *via* a copper-catalysed Ullmann cross-coupling.[318] A series of fully synthetic analogues was evaluated, with the best having low micro-molar activity against *T. cruzi* amastigotes.

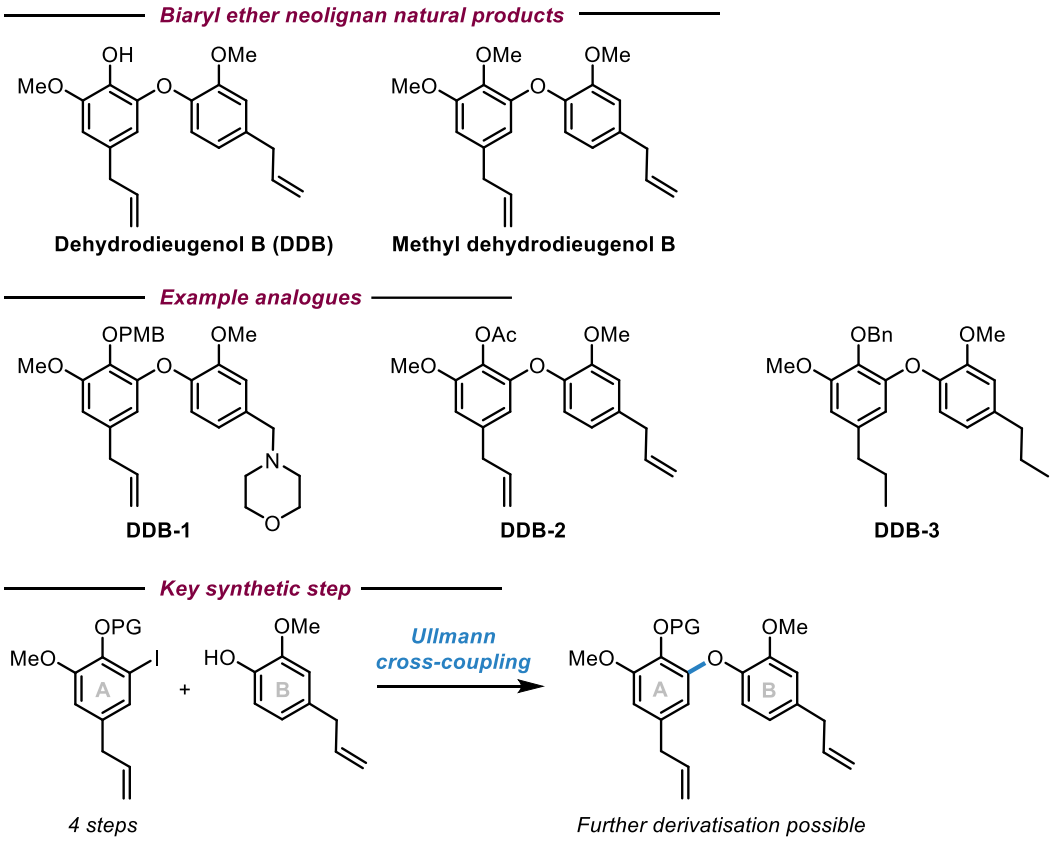

Figure 9. The dehydrodieugnol B family of natural products. Synthetic (**DDB-1**) and semi-synthetic (**DDB-2**, **DDB-3**) analogues have been prepared. Synthetic analogues are made from the corresponding A and B rings; for **DDB** these are synthesised in 4 steps (A ring) and commercially available (B ring). The key biaryl ether bond is created *via* a copper-catalysed Ullmann cross-coupling.

1.7.1 Dehydrodieugenol B SAR in *T. cruzi*

The compound family has undergone in-depth structure–activity relationship (SAR) analysis for their activity in *T. cruzi*. This analysis has included 23 semi-synthetic analogues and 21 fully synthetic analogues.[318] The analyses revealed that both allyl side chains of the compound core are important for activity although they may be saturated, while either methoxy substituent could be removed. Additionally, there is scope for further functionalisation at the phenol position as benzylic ethers were highly potent and selective.[318] It has also been established that the biaryl ether A and B ring system is necessary for activity; the monomer variant eugenol does not display any anti-parasitic

activity.[316] The SAR of the dehydrodieugenol B family of natural products in *Leishmania* is not yet known.

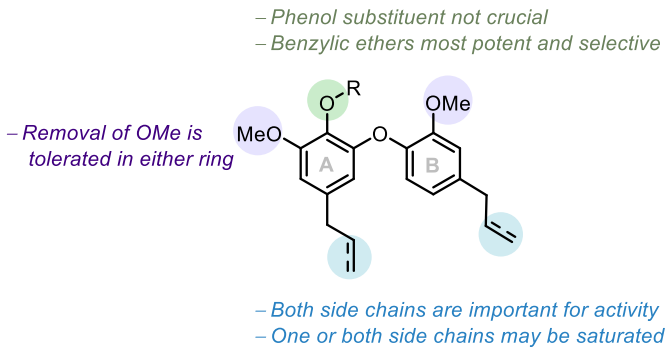

Figure 10. Structure–activity relationship trends for the dehydrodieugenol B scaffold in *T. cruzi* amastigotes.

1.7.2 Initial MoA investigations for dehydrodieugenol B analogues

Initial biochemical investigations by the Tempone group have been carried out for *L. infantum* promastigotes and *T. cruzi* trypomastigotes. Dehydrodieugenol B, methyl dehydrodieugenol B and semi-synthetic analogue **DDB-2** all caused mitochondrial membrane depolarisation and plasma membrane depolarisation in *T. cruzi*.[314, 315, 317] Similarly, semi-synthetic analogue **DDB-3** caused depolarisation of the plasma and mitochondrial membranes in *L. infantum*, with no change to the plasma membrane integrity, decreased ATP production, and dramatically increased calcium ion levels.[319] Ultrastructural TEM studies indicated mitochondrial swelling with loss of cristae after only 6 h. Fully synthetic analogue **DDB-1** caused the same effects, as well as a slight decrease in ROS and an increase in sub G_0 population in the cell cycle.[320] The compound family demonstrated activation of host cells by decreasing levels of cytokine IL-10 and IFN-γ in *L. infantum*-infected macrophages, although they do not alter NO levels. As the compounds are comparably active on both promastigote and amastigote stages, the primary MoA is likely to be through direct parasite action and not host cell modulation or action of metabolites only generated in macrophages.

1.7.3 Other natural product families with anti-parasitic activity

The natural product Ascididemin (**Asci**) is a member of the pyridoacridine alkaloids that are well established as anti-cancer compounds.[321, 322] Originally extracted from a marine ascidian,[323] **Asci** displays anti-bacterial and anti-parasitic activity against both *Plasmodium* and *Trypanosoma*, however its mechanism of action in these species is unknown.[324-326] Benzyltetrahydroisoquinoline (BI) natural products are alkaloids found in plants from tropical and subtropical regions. The family often features two of these units joined together *via* an ether linkage to form a bis-BI.[327] These compounds possess anti-microbial and anti-cancer properties,[328, 329] as well as anti-trypanosomatid activity.[330-335] Both families have been synthesised by our group, and their anti-leishmanial MoA remains to be investigated.

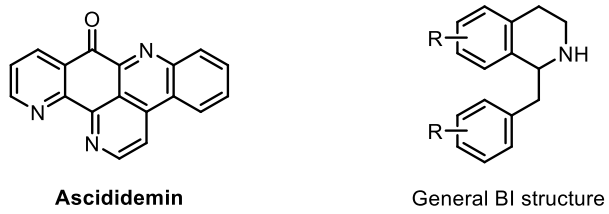

Figure 11. Ascididemin and BIs have promising anti-parasitic activity

1.8 Project aims

The merits of determining MoA early in the drug discovery process are clear with respect to safety and avoiding the likelihood of drug cross-resistance, an ever-present threat. There is also the potential monetary value of MoA projects – the GlaxoSmithKline Scientific Termination of Projects (STOP) Award in 2017 was awarded for an anti-trypanosomatid compound whose MoA predicted an unfavourable clinical outcome thus ending the project, potentially saving millions of pounds.[336]

This thesis focusses on MoA and target determination for the dehydrodieugenol B compound family. While previous investigations point towards mitochondrial disruption, an in-depth investigation of the MoA and interacting target(s) in *Leishmania* is still lacking. Identification of a target could inform further analogue development and/or contribute to target-based drug discovery efforts. There

is no "best way" to determine compound MoA and/or target(s); this project aims to use five principal approaches, each of which will be evaluated for its success in this application:

1. Changed morphology and biochemistry, addressed in Chapter 2 – This will inform on visual organelle changes that could correlate with MoA, modes of cell death, and should confirm and further elucidate the biochemical changes shown in *L. infantum*. This chapter will also evaluate the SAR for the DDB compounds as an initial step before in-depth MoA determination.

2. Compound localisation, addressed in Chapter 3 – This will establish where the compound accumulates within cells, aiding target identification.

3. Genomics, addressed in Chapter 4 – Using resistance generation, overexpression libraries, and knockdown libraries has a proven track record in establishing MoA. This is expected to be the most successful MoA identification technique used for this project.

4. Transcriptomics, addressed in Chapter 4 – This should reinforce results from the genomics experiments by looking at the whole transcriptome.

5. Chemo-proteomics, addressed in Chapter 4 – This will aim to use photoaffinity labelling pull-down techniques for successful target identification for the first time in trypanosomatids, and show compound–target engagement.

This thesis will describe the MoA deconvolution approaches applied to DDB analogues, as well as initial MoA experiments on two other natural product families; ascididemin and BIs. The compound families will additionally be assessed for their suitability as drug candidates. On paper, we expect the DDB compound family to be "good" hits, having a chemical structure amenable to modification, without obvious structural concerns. The promising anti-parasitic activity, lack of mammalian cytotoxicity and ease of synthesis makes this a particularly attractive compound family to investigate. Both the ascididemin and BI compound families are comprised of planar, aromatic structures that are common in anti-cancer applications. As they have high anti-parasitic activity, it

will be interesting to see what MoA these compounds possess in *Leishmania*, and whether these are suited to applications in parasitic diseases.

2 Structure–activity relationship studies and *Leishmania* basic cell biology

This chapter details studies of cell biology assays with *Leishmania* to investigate different aspects of exposure to anti-parasitic compounds. Compound structure–activity relationship (SAR) discussed in Section 2.2 was published in 2023: Amaral and Asiki, "Biological activity and structure–activity relationship of dehydrodieugenol B analogues against visceral leishmaniasis". *RSC Medicinal Chemistry* **2023,** *14* (7), 1344-1350.[337] Biological activity data against *L. infantum* and mammalian NCTC cells was provided by our collaborator Prof. André Tempone at the Instituto Adolfo Lutz, São Paolo, Brazil. Compounds **1**–**23**, **36**–**39** were synthesised by Dr. Claire Sear,[318] and compounds **25**, **26**, **33**–**35** were synthesised by Dr. Snigdha Singh; the SAR analysis was entirely my own. Sections of this chapter relating to compounds **BI-1** and **BI-2** were published in 2024: Sozanschi, "Synthesis and Evaluation of (Bis)benzyltetrahydroisoquinoline Alkaloids as Antiparasitic Agents". *JACS Au* **2024,** *4* (2), 847-854.[335] **BI-1** and **BI-2** were synthesised by Dr. Ana Sozanschi, **Asci** was synthesised by DPhil student Yasmine Biddick. All other experimental and analysis work in this chapter is my own.

2.1 Introduction

A structure–activity relationship (SAR) analysis of the dehydrodieugenol B (DDB) family has been carried out in *T. cruzi*, but a similar analysis has not yet been undertaken for *Leishmania*. Preliminary experiments by our collaborators in Brazil have indicated that the DDB family of compounds are likely to act *via* disruption to the *Leishmania* mitochondrion.[320] Using a combination of cell biology assays in *Leishmania infantum*, they have shown an increase in mitochondrial reactive oxygen species (ROS), decrease in ATP production, and depolarisation of the mitochondrial membrane.

Additionally, the compounds do not change the integrity of the plasma membrane, but cause an increase in cytosolic calcium ions which could be linked to mitochondrial activity.

In order to further establish the MoA of the DDB family of natural products, this chapter will investigate three aspects: First, the SAR of all synthesised analogues of this family will be established in *Leishmania*, to gain an understanding of how compound activity relates to the DDB scaffold and determine positions tolerant to modification. Second, the compound-induced cell morphology changes will be visualised, which will provide insights into the MoA and identify defects during cell death. And third, biochemical changes induced by the compound will be evaluated which should corroborate the findings in *L. infantum*, and further clarify the role of the mitochondrion. Experimental work presented in this chapter is carried out with *Leishmania mexicana* – the causative agent of cutaneous leishmaniasis. Some experiments are carried out in *Trypanosoma brucei brucei*, a related and highly conserved species – this will allow comparison to validate *Leishmania* results, as well as provide information on *T. brucei*. We will also investigate morphology and biochemical changes caused by the ascididemin and BI compound families as initial MoA determination, and for DDB comparison.

2.2 Dehydrodieugenol B analogues: SAR and *in silico* pharmacokinetic analysis

We first set out to evaluate the structure–activity relationship (SAR) for the dehydrodieugenol B family of natural products in *Leishmania*. Once the best analogues have been identified, an *in silico* pharmacokinetic analysis will be undertaken to ensure that the compounds are drug-like and therefore merit full MoA investigation.

2.2.1 Synthesis of dehydrodieugenol B analogues

SAR evaluation will take place at five key positions on the A–B biaryl ether scaffold: phenol position S1, allyl side chains S2-A and S2-B, and methoxy substituents S3-A and S3-B (Figure 12). The synthetic route to this family of natural products is well established: the biaryl ether core can be

accessed in just five relatively simple synthetic steps in a convergent manner *via* an Ullmann cross-coupling, enabling efficient analogue synthesis.[318]

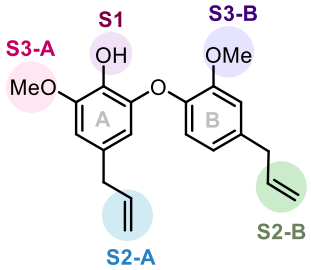

Figure 12. The dehydrodieugenol B biaryl ether scaffold. Positions to be modified for structure–activity relationship investigation are highlighted.

I proceeded with the synthesis of four novel analogues (**27**–**30**) and a re-synthesis of analogue **24** as shown in Scheme 1, these complement the 34 analogues previously synthesised by Dr. Claire Sear and Dr. Snigdha Singh.[318, 337] Analogues were designed to explore, in combination, different aspects of the biaryl ether core structure. We intended to evaluate the addition of various polar and non-polar ethers at the S1 position – and in particular investigate whether the electronic properties of a benzylic ether at this position affects compound activity. Additionally, we sought to saturate or delete the S2 allyl sidechains on the A or B ring, or replace these S2 allyl side chains with polar functionality such as a morpholine. Addition of morpholine groups often increases compound activity, including for anti-leishmanial 1,2,4-triazole derivatives and aliphatic miltefosine mimics,[338, 339] which could be due to morpholine improving the aqueous solubility of lipophilic drugs.[340] Finally, we intend to determine the essentiality of the methoxy groups at position S3 – their removal would benefit the Ullmann cross-coupling step (which is difficult for electron-rich aryls), giving an overall easier synthesis.

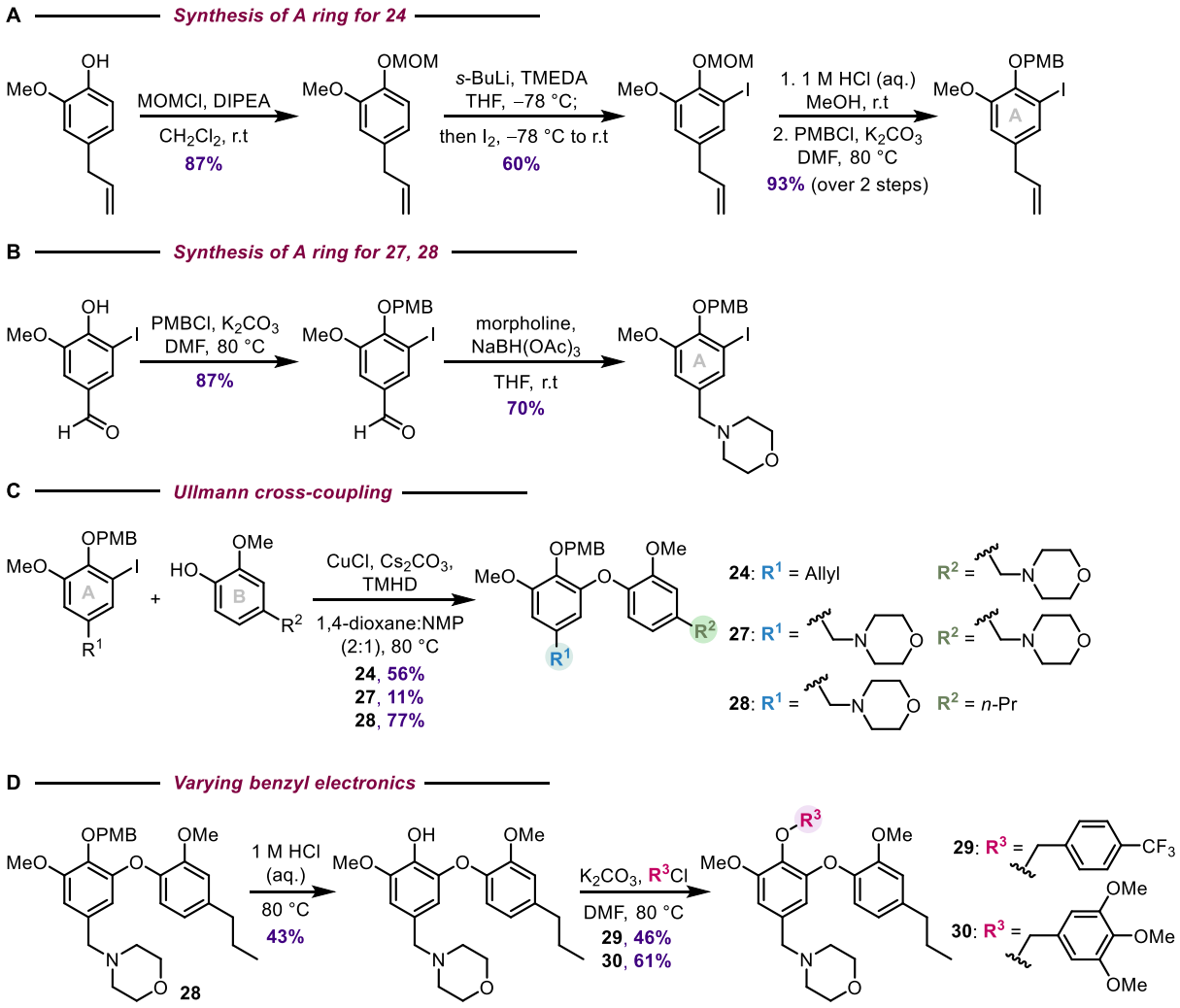

Scheme 1. Synthesis of dehydrodieugenol B analogues **24** and **27**–**30**. A. Synthesis of the A ring coupling partner for **24**. B. Synthesis of the A ring coupling partner for **27** and **28** was carried out by Dr. Snigdha Singh as shown. C. **24**, **27** and **28** are the products of cross-couplings with a phenol partner; for each compound the B ring is synthesised in 1 step, see appendix (Section 7.4) for full details. D. Synthesis of **29** and **30** from an acidic deprotection of **28** and substitution with varied benzyl chlorides.

2.2.2 SAR of dehydrodieugenol B analogues

To establish the SAR, the anti-parasitic activity of all compounds had to be compared. All analogues were tested in an intracellular amastigote assay against *L. infantum* to establish the EC_{50} – the concentration at which half of all amastigotes have been killed. In addition, the toxicity of the compounds against mammalian NCTC cells was tested to determine the CC_{50} – the concentration at which half of all mammalian cells have been killed. The relative selectivity index is then calculated as the ratio between EC_{50} (amastigotes) and CC_{50} (NCTC cells); an important consideration to ensure selectivity for the intracellular parasite over the mammalian host. In total, 39 synthetic compounds

based around the core scaffold were tested by our collaborator Prof. Tempone, the results of which are shown in Tables 3–6. I then proceeded to evaluate the anti-parasitic activity results, comparing these analogues to the activity of the parent compound dehydrodieugenol B (**DDB**, EC_{50} 35.9 µM, selectivity index 2.1), previously published by Tempone and co-workers.[319]

The first consideration was the addition of an ether at position S1 (Table 3). Although the *para*-methoxybenzyl ether **1** had shown high activity against *T. cruzi* amastigotes previously (4.0 ± 1.4 µM), it proved inactive in this assay.[318] Analogues **5**–**8** indicate that a polar nitrogen containing group is necessary for activity; all other modifications at the S1 position rendered the compounds inactive. The more basic amines **5** and **6** had lower EC_{50} values than the corresponding amides **7** and **8**, but this was accompanied by undesirable mammalian cytotoxicity.

Table 3. *L. infantum* amastigote activity and mammalian cytotoxicity of dehydrodieugenol B analogues with functionalisation of phenol S1 to various ethers while keeping the rest of the core unchanged.

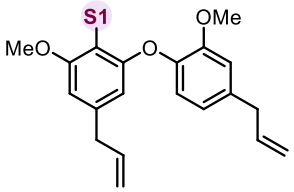

Compound	S1	EC_{50} (µM) ± SD	CC_{50} (µM) ± SD	SI
1	OPMB	NA	>200	ND
2	OMOM	NA	>200	ND
3	OAllyl	NA	>200	ND
4	H	NA	>200	ND
5	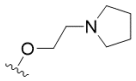	4.1 ± 1.1	24.9 ± 2.6	6.0
6	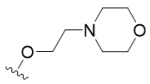	9.6 ± 3.6	63.7 ± 0.2	6.6
7	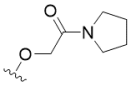	20.3 ± 5.9	52.9 ± 15.2	2.6
8	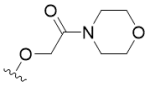	NA	111.5 ± 8.2	ND
Miltefosine	–	6.5 ± 3.0	119.7 ± 4.2	18.4
DDB[319]	OH	35.9 ± 6.6	75.0 ± 13.8	2.1

NA = Not Active (>50 µM), ND = Not determined, SD = Standard Deviation, SI = Selectivity Index, $n \geq 2$.

We evaluated the effect of deletion or saturation of the allyl chains at position S2 on either the A or B ring (analogues **9**–**22**, Table 4), often in combination with OPMB at S1 for synthetic ease. There was no anti-leishmanial activity over 50 µM in any of these analogues with the exception of **9** and **11**, which exhibited minimal improvement over the **DDB** selectivity index. In addition, **15**, **17** and **18** had undesirable mammalian cytotoxicity, but this is likely due to the presence of a free phenol at position S1 and not a direct result of the S2 saturation or deletion. Analogous mammalian cytotoxicity is observed for phenol **DDB**, and in the *T. cruzi* data with phenol compounds.[318] It has been proposed that phenol cytotoxicity is due to a mitochondrial interaction – perhaps through phenoxy radicals formed *in vivo* – enhancing caspase-mediated apopotosis, which could be at play here.[341]

Table 4. *L. infantum* amastigote activity and mammalian cytotoxicity of dehydrodieugenol B analogues with saturation or deletion at position S2 accompanying functionalisation of phenol S1.

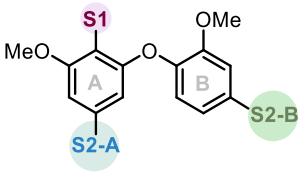

Comp.	S1	S2-A	S2-B	EC_{50} (µM) ± SD	CC_{50} (µM) ± SD	SI
9	OPMB	Allyl	H	24.2 ± 18.2	>200	>8.3
10	OPMB	H	Allyl	NA	>200	ND
11	OAcyl	Allyl	H	32.7 ± 5.0	>200	>6.1
12	OAcyl	H	Allyl	NA	>200	ND
13	OMe	Allyl	H	NA	>200	ND
14	OMe	H	Allyl	NA	>200	ND
15	OH	Allyl	H	NA	31.6 ± 11.3	ND
16	OH	H	Allyl	NA	>200	ND
17	OH	Allyl	*n*-Pr	NA	42.0 ± 3.8	ND
18	OH	*n*-Pr	Allyl	NA	14.2 ± 0.1	ND
19	OMe	Allyl	*n*-Pr	NA	>200	ND
20	OPMB	Allyl	*n*-Pr	NA	>200	ND
21	OPMB	*n*-Pr	Allyl	NA	>200	ND
22	OPMB	*n*-Pr	*n*-Pr	NA	>200	ND
Milt.		–		6.5 ± 3.0	119.7 ± 4.2	18.4
DDB[319]	OH	Allyl	Allyl	35.9 ± 6.6	75.0 ± 13.8	2.1

NA = Not Active (>50 µM), ND = Not determined, SD = Standard Deviation, SI = Selectivity Index, $n \geq 2$.

Position S2 was also substituted with polar morpholine, piperidine or pyrrolidine groups, paired with benzyl ethers or free phenols at position S1 (Table 5). The nitrogen-containing, 6-membered ring substitutions of morpholine or piperidine led to potent anti-leishmanial activity in almost all cases (**24**–**30**) while substitutions with the 5-membered pyrrolidine (**23** and **32**) led to inactivity. This preference for 6-membered rings could be due to a shape or size effect in a potential binding pocket. Analogues **24**–**26** show that substitution at position S2-B results in higher anti-leishmanial activity (EC_{50} from 3.7 to 9.7 µM) than S2-A (**28**–**30**, EC_{50} ranging from 13.2 to 26.3 µM).

Table 5. *L. infantum* amastigote activity and mammalian cytotoxicity of dehydrodieugenol B analogues with substitution of polar functionality at position S2 accompanying functionalisation of phenol S1.

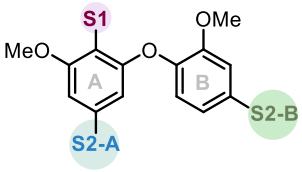

Comp.	S1	S2-A	S2-B	EC_{50} (µM) ± SD	CC_{50} (µM) ± SD	SI
23	OPMB	Allyl		NA	6.2 ± 1.2	ND
24	OPMB	Allyl	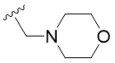	9.7 ± 2.0	>200	>20.6
25	OPMB	*n*-Pr	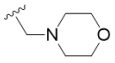	7.7 ± 0.8	74.4 ± 4.4	9.7
26	OPMB	*n*-Pr	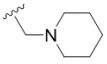	3.7 ± 0.5	14.5 ± 0.2	3.9
27	OPMB	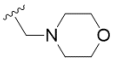	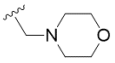	27.8 ± 7.4	74.4 ± 5.8	2.7
28	OPMB	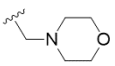	*n*-Pr	16.4 ± 4.3	>200	>12.2
29	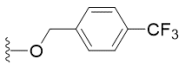	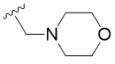	*n*-Pr	13.2 ± 2.1	>200	15.1
30	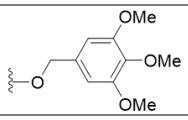	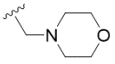	*n*-Pr	26.3 ± 3.2	>200	>7.6
31	OH	Allyl	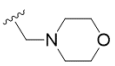	NA	51.4 ± 4.7	ND
32	OH	Allyl		NA	43.3 ± 5.3	ND
Milt.		–		6.5 ± 3.0	119.7 ± 4.2	18.4
DDB[319]	OH	Allyl	Allyl	35.9 ± 6.6	75.0 ± 13.8	2.1

NA = Not Active (>50 µM), ND = Not determined, SD = Standard Deviation, SI = Selectivity Index, $n \geq 2$.

Compound **27**, bearing a substitution at both S2-A and S2-B, did not amplify the anti-parasitic activity but instead had an EC_{50} value of magnitude close to the less potent S2-A substitutions. Unlike at position S1, there is no consistent EC_{50} trend corresponding to the basicity of S2 substitutions for morpholine (least basic), piperidine and pyrrolidine (most basic). However, these compounds broadly fit the trend of higher basicity corresponding to higher mammalian cytotoxicity, similar to the polar modifications at position S1. Once again, the free phenol compounds **31** and **32** exhibited mammalian cytotoxicity despite inactivity in the *L. infantum* assay.

Deletion of either *ortho*-methoxy group at position S3 from the parent **DDB** (**37**, **39**) or S1-OPMB analogue (**36**, **38**) led to no anti-leishmanial activity (Table 6). Analogues **33** and **34** have potent anti-parasitic activity despite deletion of the methoxy group on the B ring. **34** and its direct methoxy-

Table 6. *L. infantum* amastigote activity and mammalian cytotoxicity of dehydrodieugenol B analogues with deletion of *ortho*-methoxy groups at positions S3-A or S3-B in combination with modifications at S1 and S2.

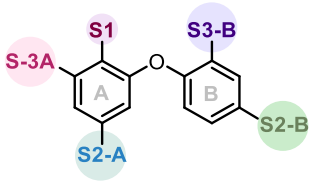

Comp.	S1	S2-A	S2-B	S3-A	S3-B	EC_{50} (μM) ± SD	CC_{50} (μM) ± SD	SI
33	OPMB	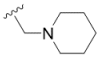	*n*-Pr	OMe	H	3.0 ± 1.1	22.7 ± 0.9	7.6
34	OPMB	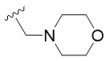	*n*-Pr	OMe	H	15.3 ± 1.9	>200	>13.1
28	OPMB	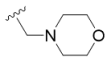	*n*-Pr	OMe	OMe	16.4 ± 4.3	>200	>12.2
35	OPMB	*n*-Pr	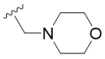	H	OMe	NA	33.8 ± 4.9	ND
25	OPMB	*n*-Pr	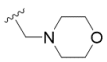	OMe	OMe	7.7 ± 0.8	74.4 ± 4.4	9.7
36	OPMB	Allyl	Allyl	OMe	H	NA	>200	ND
37	OH	Allyl	Allyl	OMe	H	NA	123.4 ± 9.4	ND
38	OPMB	Allyl	Allyl	H	OMe	NA	>200	ND
39	OH	Allyl	Allyl	H	OMe	NA	128.6 ± 5.2	ND
Milt.			–			6.5 ± 3.0	119.7 ± 4.2	18.4
DDB[319]	OH	Allyl	Allyl	OMe	OMe	35.9 ± 6.6	75.0 ± 13.8	2.1

NA = Not Active (>50 μM), ND = Not determined, SD = Standard Deviation, SI = Selectivity Index, $n \geq 2$. Data for the molecular matched pairs **25** and **28** have been repeated here.

containing variant **28** have the same anti-parasitic activity indicating that this methoxy group is expendable. Analogue **35** tells a different story, being inactive against *L. infantum* compared to the corresponding highly active methoxy-containing **25**, therefore the methoxy group – or similar polar and/or H-interaction functionality – at S3-A is crucial.

In general, it is clear that the presence of a polar functionality such as morpholine, pyrrolidine or piperidine is required for anti-leishmanial activity: 12 of the 14 active analogues contain one of these functional groups. The only exceptions are **9** and **11**, which have relatively low activity of 24.2 and 32.7 μM respectively. Piperidine group S2 substitution is more potent than morpholine substitution: **26** and **33** have a lower EC_{50} of approximately 3 μM compared with their corresponding morpholine analogues **25** and **34** (7.7 and 15.3 μM). However, this trend is mirrored in the mammalian cytotoxicity, which overall gives the morpholine analogues a better selectivity index. This preference for polarity could be linked to compound solubility and cell membrane permeability. Due to the nature of *L. infantum* amastigotes residing intracellularly, any compound must cross the macrophage, parasitophorous vacuole, and amastigote membranes to access the target directly. All analogues with a free phenol at position S1 are inactive against *L. infantum*, even when paired with a polar functionality at position S2 (**31** or **32**). In contrast, benzylic ethers are much more active; this could again be due to differences in cell membrane permeability compared to the free phenol. Compounds **28**–**30** showed the effect of decreasing electron density at the benzylic S1 position while keeping all other substituents the same. Electron-withdrawing *para*-trifluoromethylbenzyl (**29**) had a slightly lower EC_{50} value than strongly electron-donating trimethoxybenzyl (**30**), with *para*-methoxybenzyl (**28**) falling between the two (statistical significance derived from a two-tailed *t*-test has $P \leq 0.05$ for comparison between **29** and **30** only). These changes are of a small magnitude, and mostly non-significant, therefore we conclude that electronics at this position does not play a major role in compound activity.

Compound **24** emerged as the best: it has the highest selectivity index coming from a potent EC_{50} of 9.7 μM coupled with no mammalian cytotoxicity (>200 μM), and showed improvement over **DDB**. Compounds **28** and **34** were the next best performers (discounting **29** as it is identical to **28** with only

small electronic changes to the benzylic ether). These compounds all have in common a morpholine group at position S2-A or B and a *para*-methoxybenzyl ether at S1, which we conclude are optimal structures for compound activity in the series tested.

2.2.3 *In silico* prediction of pharmacokinetic properties

An *in silico* prediction of pharmacokinetic properties for the three best compounds **24**, **28** and **34** was conducted using ADMETlab 2.0, admetmesh.scbdd.com (Table 7).[342] This online tool has a larger range of predictable parameters than its competitors and performs with the best accuracy and precision.[343] The output includes a pharmacokinetic radar; if the compound falls within the orange region it has ideal "drug-likeness" – a term often used to describe compound properties that go beyond bioactivity and take into account features such as bioavailability.[344] For all three compound predictions the pharmacokinetic radar was very similar, as shown for **24** in Table 7 (pharmacokinetic radars for **28** and **34** can be found in the appendix, Section 7.1.1, Figure 65).

Compound **24** is predicted a close-to-optimum logD value of 3.82 and water solubility (logS) of −5.27, which falls into the moderate solubility class. LogS is an important characteristic that relates to oral bioavailability, shown here to be high (≥ 30%). The predicted logP value of 5.18 is higher than the recommended lipophilicity limit (ideal: 0 < logP < 3.0), although values up to 5.0 are still considered reasonable by Lipinski's rules which are a useful guide.[344] The polarity of **24** is predicted to be favourable (ideal TPSA: 0 < TPSA < 140 $Å^2$); these characteristics are better for **24** than **28** or **34**, further justifying **24** as the best compound from this series.

Compound **24** exceeds the suggested flexibility limit with 12 rotatable bonds (ideal: < 11), and lies close to the recommended boundary for size (100 < MW < 600). Compounds **24** and **28** fail Lipinski's rule due to the molecular weight limit (< 500 Da) which is lower than the ADMETlab 2.0 recommendation, although they are close to the boundary at 505 and 507 respectively. These compounds are predicted to have moderate (**28**, **34**) to optimum (**24**) Caco-2 permeability – a model of intestinal absorption, suitably high human intestinal absorption (HIA) ≥ 30%, and no permeability to the blood–brain barrier which can lead to side effects in the nervous system.[345]

Table 7. *In silico* predictions of physicochemical, structural and ADMET parameters. Compound structures and bioavailability radar for **24**.

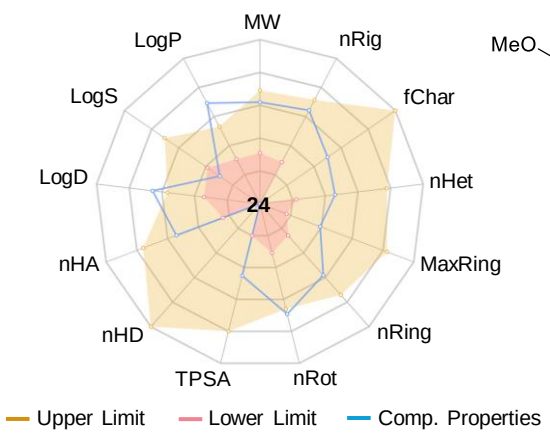

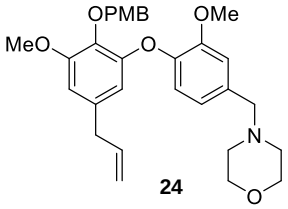

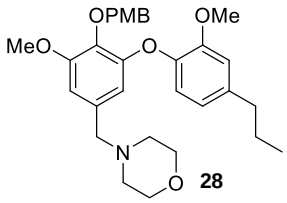

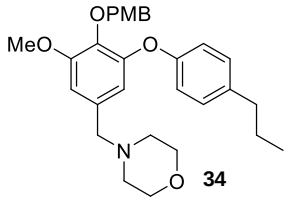

Properties	24	28	34
Molecular weight	505.25	507.26	477.25
LogP	5.18	5.65	5.69
LogD	3.82	4.12	4.17
LogS	-5.27	-6.03	-6.07
TPSA	58.62	58.62	49.39
Caco-2 permeability	−5.03, Optimal	−5.46, Moderate	−5.30, Moderate
P-gp inhibitor	Yes	Yes	Yes
P-gp substrate	No	No	No
HIA (≥ 30%)	Yes	Yes	Yes
Oral bioavailability	≥30% F	≥30% F	≥30% F
BBB penetration	No	No	No
Distribution (V_D) (L/Kg)	0.72, Optimal	0.72, Optimal	0.95, Optimal
CYP1A2 inhibitor	No	No	No
CYP2C19 inhibitor	Yes	Yes	Yes
CYP2C9 inhibitor	Yes	No	Yes
CYP2D6 inhibitor	No	No	No
CYP3A4 inhibitor	Yes	Yes	Yes
Clearance (mg/min/kg)	11.6, Moderate	11.6, Moderate	11.7, Moderate
hERG blockers	Yes	Yes	Yes
Human hepatotoxicity	No	No	No
AMES toxicity	No	No	No
DILI	Moderate	Moderate	Moderate
Lipinski rules	Fail	Fail	Pass
PAINs	0 alerts	0 alerts	0 alerts

TPSA = Topological Polar Surface Area, P-gp = P-glycoprotein, HIA = Human Intestinal Absorption, BBB = Blood Brain Barrier, V_D = Volume of Distribution, CYP = Cytochrome P450, DILI = Drug-Induced Liver Injury, PAINs = Pan-Assay Interference compounds, hERG = human ether-a-go-go related gene.

Cytochrome P450 enzymes (CYPs) are generally responsible for drug metabolism; inhibition of these enzymes can lead to accumulation of drug metabolites, and decreased metabolism of endogenous biomolecules.[346] Of the five main isoforms, only two or three of them are hits of the compounds, with CYP2C9 only a weak positive result. The series has favourable predictions for toxicity, with no indication of human hepatotoxicity or AMES mutagenicity, and only moderate drug-induced liver injury measurements. Importantly, there were no structural similarities to pan-assay interference compounds (PAINs). All three compounds have a moderate probability of inhibiting hERG channels which can cause heart arrhythmia. This is due to the compound structure: hERG inhibitors often contain a tertiary nitrogen with hydrophobic groups such as aromatic rings a given distance away.[347] Fitting this overall structure does not necessitate hERG inhibition but it will be a hit in the prediction tools.[348] As discussed in the introduction (Section 1.4.4), not all ADMET predictions are equal. In particular, the toxicity predictions for hERG blockers, hepatotoxicity and AMES toxicity are the least reliable and should be followed up with *in vitro* experiments before definitive conclusions about the compound behaviour can be drawn.

According to Drugs for Neglected Diseases *initiative* (DND*i*), a new hit compound for visceral leishmaniasis should: i) be synthesised in no more than 8 steps; ii) have an EC_{50} below 10 μM in amastigotes; iii) have a selectivity index higher than 10; iv) exhibit an appropriate *in silico* ADME profile and, v) show no structural alerts.[349, 350] Compound **24** emerged as the most potent compound from the EC_{50} studies against *L. infantum* amastigotes and fits all these criteria, making it a promising hit. This compound was used as the basis for all MoA experimental work on this family of natural product-inspired analogues, hereafter referred to as **DDB-1**.

2.3 Activity of Asci and BI compounds

Two other compound families: ascididemin and benzyltetrahydroisoquinolines (BIs) were studied alongside **DDB-1** in some assays to provide insight into their MoA in trypanosomatids, and allow comparison to **DDB-1**. The compounds were synthesised by colleagues in the Department of Chemistry, University of Oxford, and all cell biology work was carried out by myself or under my

supervision. Three compounds were tested in a cell counting assay to establish their effect on the 24 h growth of *L. mexicana* promastigotes (Figure 13). For ascididemin (**Asci**), EC_{50} falls between 100 and 250 nM, which is improved over *L. donovani*.[326] A solvent-only control of 0.1% v/v DMSO had no significant change in cell growth. With two BI compounds, **BI-1** and **BI-2**, concentrations of 50 µM are sufficient to inhibit growth, which reflects the published findings in *L. infantum*.[335] These compound families both display good anti-leishmanial activity against *L. mexicana*, which merits their inclusion in the following MoA studies.

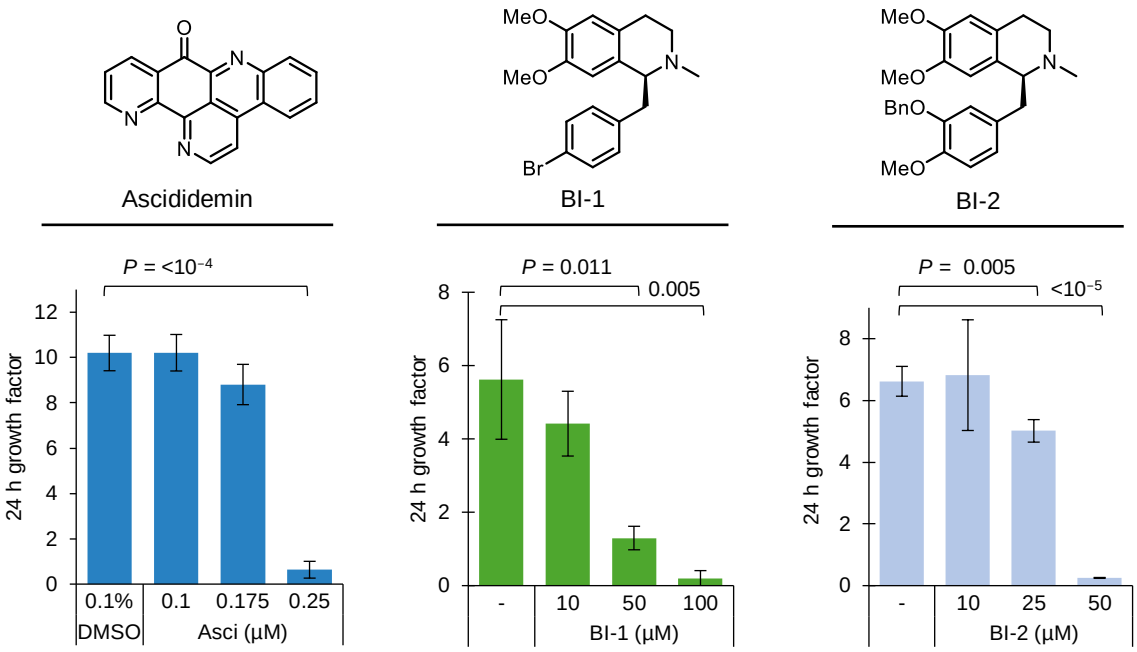

Figure 13. Asci and the **BI** compounds have potent activity against *L. mexicana* promastigotes. A–C. Chemical structure and 24 h growth factor for **Asci** (A), **BI-1** (B) and **BI-2** (C). Mean ± SD, $n = 3$, statistical significance was derived from a two-tailed *t*-test versus DMSO (A) or untreated (-) (B–C). Only $P < 0.05$ are shown. **BI-1** and **BI-2** share the same substituted tetrahydroisoquinoline core and a benzyl group with differing substituents.

2.4 Assay development to measure EC_{50} against *L. mexicana* and *T. brucei*

Using 24 h growth quantification of cell culture in flasks serves as a good indication for the EC_{50} of compounds. Each flask of cells is treated with a different drug concentration, and then manually counted with a haemocytometer at the start T = 0 h and end T = 24 h of the experiment. This time-intensive counting means that only a few concentrations are sampled and therefore some

information about the compound behaviour is lost. It is more beneficial to measure the EC_{50} on a 96-well plate to capture a large range of concentrations while simultaneously reducing the manual intensity required.

I used AlamarBlue™, a resazurin based dye to optimise in-house EC_{50} determination on 96-well plates in *Leishmania*. Resazurin is reduced in the presence of viable cells to highly fluorescent resorufin and is therefore an indirect measure of cytotoxicity.[351] Optimisation began with identifying an appropriate starting plating density that will be used for EC_{50} determination. To do this, 200 µL of *L. mexicana* promastigotes were serially diluted 2-fold across the plate, ranging from 1×10^7 cells/mL to 3.9×10^4 cells/mL, then incubated for 24 h in a 5% CO_2 atmosphere. AlamarBlue™ was added according to manufacturer's instructions and the plate incubated for a further 6 h or 24 h to determine optimum experiment length. Due to laboratory constraints, cells need to be killed before fluorescence output is read: either 1% SDS detergent or 2% formaldehyde fixative was trialled. An ideal plating density will remain within linearity of the assay during the duration of EC_{50} determination.

For the 6 h AlamarBlue™ incubation, plating cell densities above 6.25×10^5 cells/mL were out of linearity range of the assay, while at 24 h this was even lower at 1.5×10^5 cells/mL (Figure 14A–B). It was unnecessary to prolong the experiment to 24 h as this provided no increase in maximum fluorescence intensity. A 6 h incubation with a starting cell density of 5.5×10^5 cells/mL was used to ensure the assay did not extend beyond linearity while still having a good number of starting cells, bearing in mind that addition of active compounds to the assay will almost certainly decrease the cell number. Killing with either SDS or formaldehyde showed a consistent result: SDS was chosen as it is safer to handle than formaldehyde. These established assay conditions were used to determine EC_{50} values for **DDB-1** and **Asci** in *L. mexicana* promastigotes after a 24 h drug incubation, and published conditions used for **DDB-1** in *T. brucei* bloodstream forms after a 72 h drug incubation with an SDS killing as the final step (Figure 14C–D).[352, 353] The drugs amphotericin B (AmB) and pentamidine were included to confirm that the assay is behaving as expected. The AmB EC_{50} of 87.7 nM is in good agreement with the literature value of 62.4 nM in *L. mexicana*,[275] while the value

for pentamidine of 1.25 nM is comparable to 8.10 nM as reported.[353] Through the AlamarBlue™ assay method development, we confirm potent EC_{50} values for **DDB-1** in both *L. mexicana* promastigotes and *T. brucei* bloodstream forms; neither species had previously been tested.

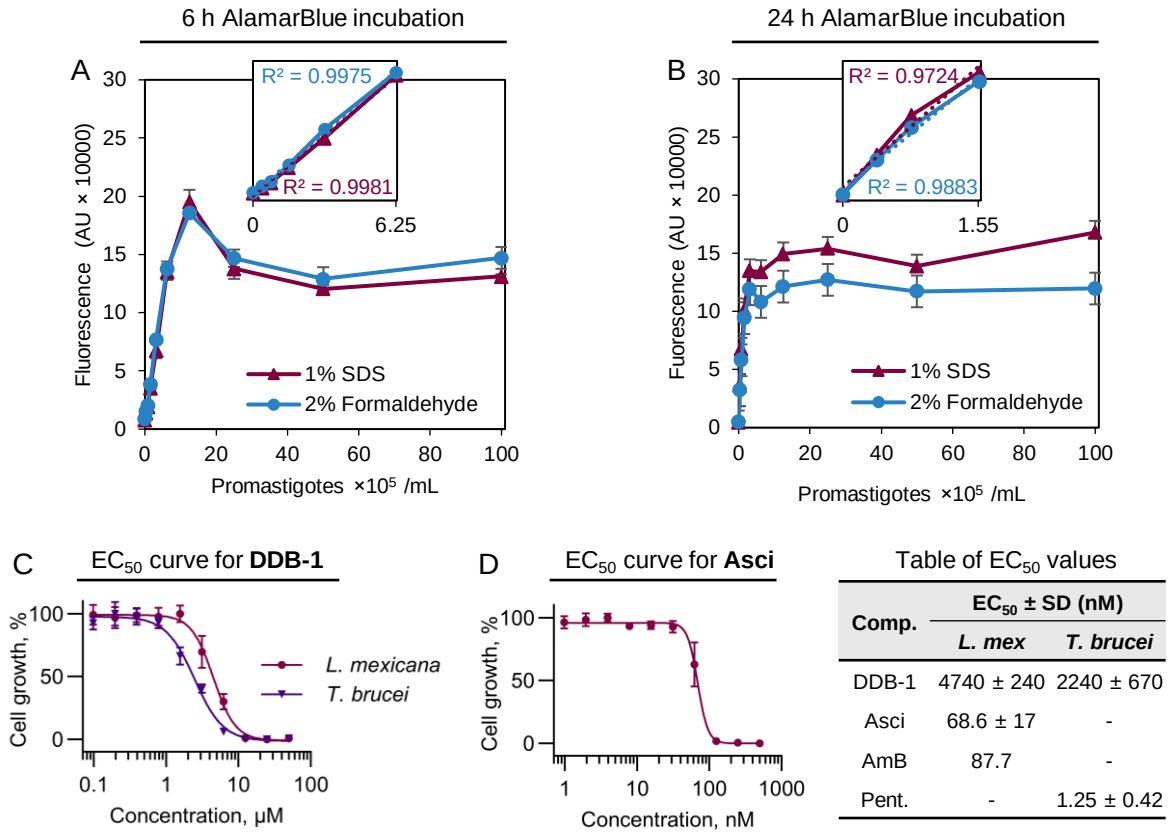

Table of EC_{50} values

Comp.	EC_{50} ± SD (nM)	
	L. mex	*T. brucei*
DDB-1	4740 ± 240	2240 ± 670
Asci	68.6 ± 17	-
AmB	87.7	-
Pent.	-	1.25 ± 0.42

Figure 14. AlamarBlue™ assay for EC_{50} determination in *L. mexicana* is optimum with a starting density of 5.5×10^5 cells/mL, 6 h incubation and 1% SDS killing. A–B. Fluorescence output for promastigotes serially diluted across a 96-well plate following 6 h (A) or 24 h (B) incubation with AlamarBlue. For each, the initial linear section is shown inset with a dotted line of linear regression. $n = 3$ wells, 1 replicate. C–D. Representative dose-response curves for **DDB-1** in *L. mexicana* and *T. brucei* bloodstream forms (C) and **Asci** in *L. mexicana* (D), the mean is plotted with error bars representing standard deviation for 6 technical replicates. EC_{50} values for curves C–D and drugs amphotericin B (AmB) and pentamidine (Pent.), are shown in the table, $n = 3$ biological replicates.

2.5 Compound treatment causes morphology changes in *L. mexicana*

All compounds tested performed well in the phenotypic potency assays; this could be accompanied by morphological changes. We aim to use light, fluorescence and transmission electron microscopy to identify changes in cell shape or organelle structure. Organelles with drastically changed morphology could be a direct or downstream response to compound.

2.5.1 Morphology changes caused by Asci, BI's and DDB-1 identified by light microscopy

Examination by light microscopy is an easy starting point for identifying changes in phenotype upon compound treatment; it enables visualisation of any irregular morphology within live cells on a micrometre scale. Live *L. mexicana* promastigote cell cultures were imaged using light microscopy following compound treatment. At 50 µM, **BI-1** and **BI-2** caused a phenotype with a spherical cell body and shortened flagellum (F) in 25% (n = 286) or 66% (n = 79) of the population respectively (Figure 15B–C). DNA staining was ambiguous with an abnormal number and positioning of the nucleus (N) and kinetoplast (K).

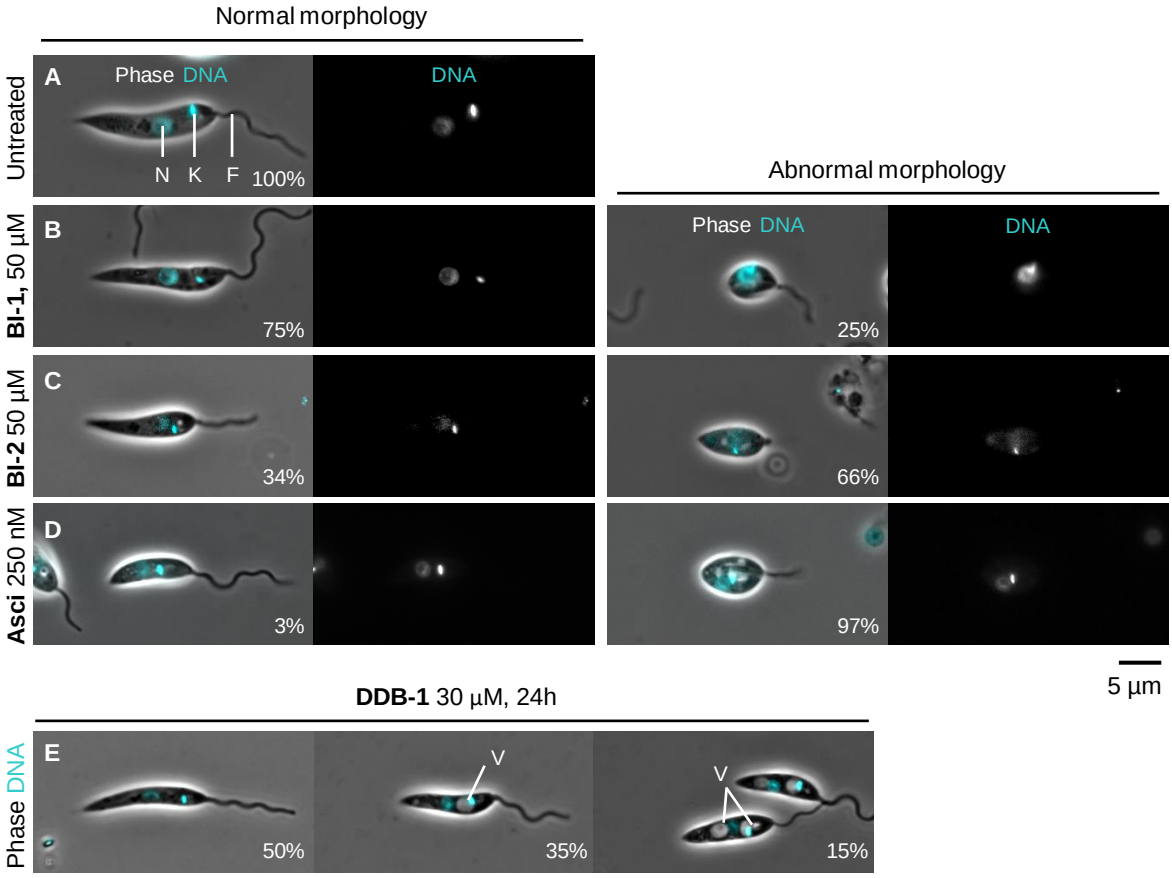

Figure 15. An abnormal rounded cell morphology is induced by **BI**s and **Asci**, intracellular vacuoles are induced by **DDB-1**. Representative fluorescence microscopy images showing untreated cells (A) in comparison to treated cells (B–E). 24 h treatment with **BI-1** (B), **BI-2** (C) and 6 h treatment with **Asci** (D) causes a rounded cell morphology in 25% (n = 286), 66% (n = 79) and 97% (n = 200) of the population respectively. E. 24 h treatment with **DDB-1** causes vacuoles (V) to appear in the cell body (n = 115). DNA was labelled with Hoechst 33342 (cyan), nucleus (N), kinetoplast (K), and flagellum (F) are indicated in the untreated example (A). Images are representative of n > 70 cells for each condition, from n > 2 biological replicates.

Asci treated cells had the same rounded phenotype in 97% of the population after only 6 h treatment (n = 200) (Figure 15D). Cells treated with **DDB-1** appeared different to the other compounds: overall cell shape and flagellum length was retained in all cells, but large vacuole-like structures (V) appeared in the cell body in approximately 50% of cells, often positioned between the nucleus and kinetoplast, while 15% of cells had two vacuoles (n = 115) (Figure 15E).

2.5.2 Transmission electron microscopy for morphology changes in *L. mexicana*

Light microscopy gives a general overview of cell shape, but no detailed information about internal cell features. Transmission electron microscopy (TEM) images of **DDB-1** treated samples were analysed to identify changes within internal organelles and the nature of the vacuole-like structure identified by light microscopy. **DDB-1** causes multivesicular bodies (MVBs) in 47% of cells (n = 64) (Figure 16C–D), which appear in only 8% of the untreated control cells (n = 45). The shape and fine-structure of the mitochondrion is affected by **DDB-1**: the mitochondrion is normally close to the kinetoplast it surrounds (83% of n = 17 kinetoplasts in the untreated control, Figure 16A).

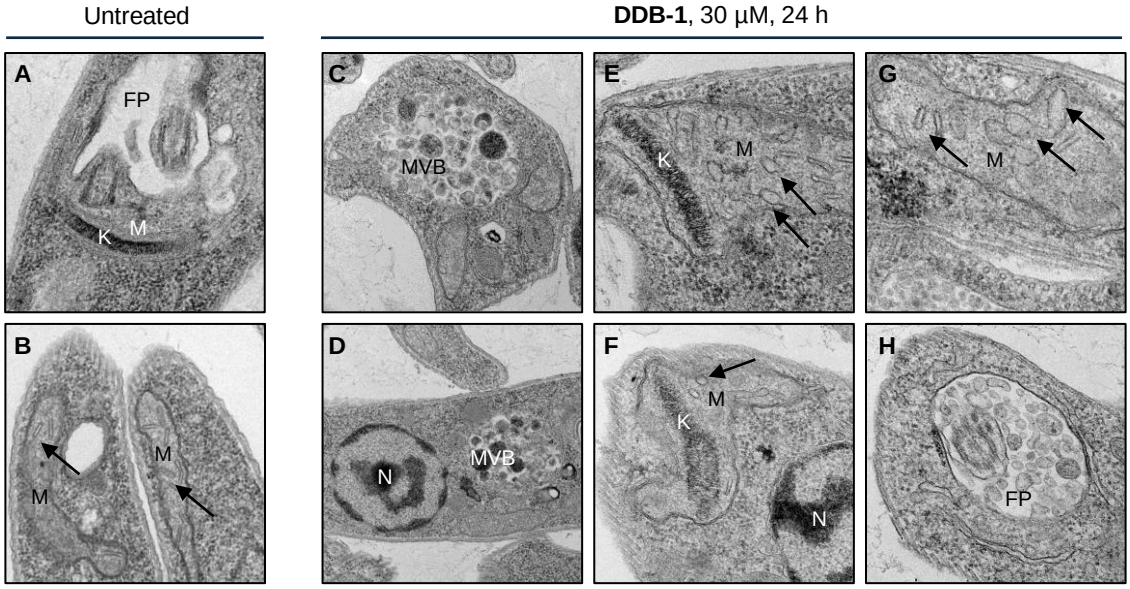

Figure 16. DDB-1 causes multivesicular bodies and enlarged mitochondrial cristae apparent by transmission electron microscopy. Representative TEM images showing untreated (A–B) and **DDB-1** treated cells (C–H). Nucleus (N), multivesicular body (MVB), kinetoplast (K), flagellar pocket (FP) and mitochondrion (M) are labelled, cristae are indicated with arrows: enlarged in the **DDB-1** treatment and normal shape in the untreated control. $n \geq 45$ cells for each condition, 2 biological repeats.

In treated cells this area is greatly expanded for 70% of kinetoplasts visualised (n = 20) (Figure 16E–F). The mitochondrial cristae (black arrows) are oblong/tubular in shape in untreated samples (Figure 16B), although in 29% of untreated mitochondria (n = 50) the cristae were larger and more rounded. This is increased to 68% of mitochondria (n = 50) in **DDB-1** treatment (Figure 16E–G). There is also an accumulation of extracellular material in the flagellar pocket (FP) upon treatment (Figure 16H).

Using TEM, the vacuole-like structures visible by light microscopy were identified as multivesicular bodies contained within the promastigote cell. No cells were identified with more than one MVB by TEM, although this is dependent on cell orientation within the sample. This is likely to be a stress response, similar to the increased vesicular material in the flagellar pocket.[354, 355]

2.6 Cell cycle progression and differentiation

2.6.1 Alterations to *L. mexicana* cell cycle caused by Asci and BI-1

To investigate whether the morphological changes are a consequence of cell cycle interference, we analysed the cell cycle over a 24 h period. *L. mexicana* promastigotes have a typical doubling time of 7.1 h, during which the DNA-containing organelles replicate in the order nucleus (N) then kinetoplast (K), followed by cytokinesis into two daughter cells.[51, 356] This happens within the final 10% of the cell cycle, therefore at all times there is a heterogeneous population of cells with the majority in the organelle configuration 1K1N, and a small percentage in 1K2N or 2K2N. If there is an arrest during the promastigote cell cycle, we would expect to have an accumulation of cells stuck in a specific cell cycle phase, a common feature of most drugs.

After 6 h and 24 h, promastigotes treated with **DDB-1** remained in the same proportions as the untreated control (Figure 17A). **Asci** and **BI-1** deviated from the typical cell cycle, giving rise to abnormal categories of cells with incorrectly replicated organelles, or unexpected positioning of organelles within the cell (Figure 17A–B). **BI-1** caused the presence of an eXtra DNA-stained region (1K1N1X) that could not be confidently assigned as K or N, generally toward the posterior end of the cell body. After 6 h, 10% of cells had a 0K1N configuration, while 3% were in each of the 1K0N

or 2K1N categories (n = 716). The two timepoints are similar, suggesting that the abnormalities do not accumulate over time. **Asci** treatment led to a distinctive organelle arrangement in which the kinetoplast was oriented adjacent to the nucleus (1K1N-side), or slightly to the posterior side of the nucleus in 42% of cells (n = 540). Quantification of the kinetoplast to anterior cell tip distance was the same for **Asci** treated and untreated samples (an average of 3.59 and 3.38 µm respectively), therefore kinetoplast positioning is as expected despite the round cell shape. The kinetoplast and nucleus positioning is microtubule mediated. A follow-up experiment investigating the effect of these compounds (**Asci** in particular) with a microtubule fluorescent stain – such as labelled tubulin, could be informative to observe any time-dependent changes to microtubule formation and positioning during the course of the cell cycle.

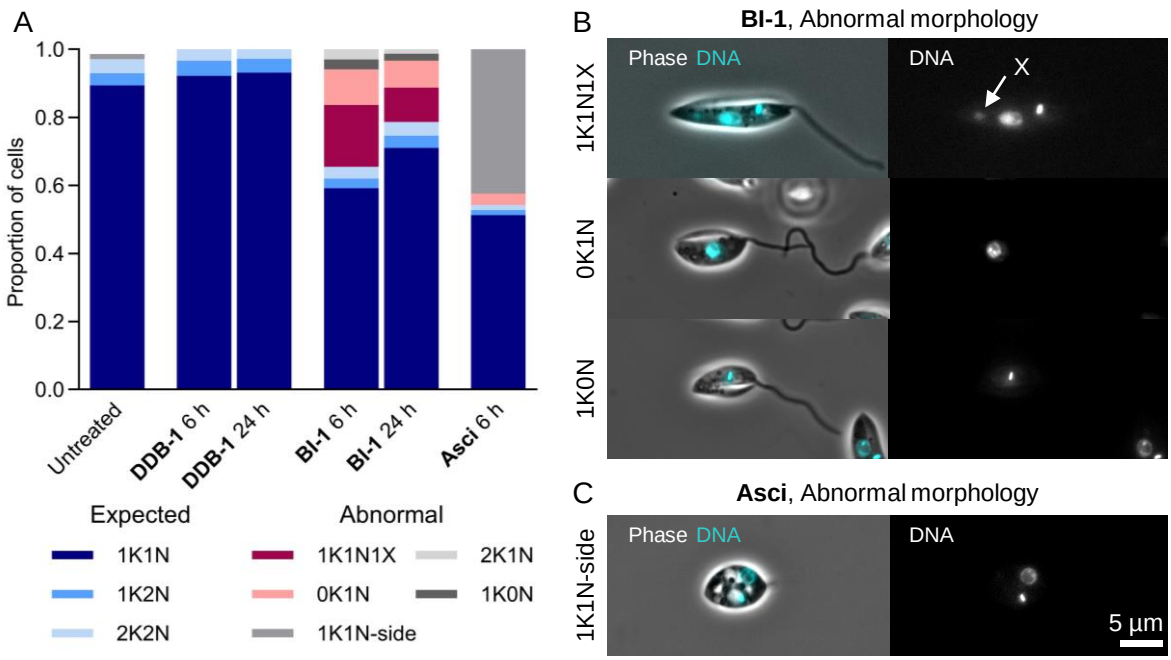

Figure 17. DDB-1 does not affect progression through the *L. mexicana* promastigote cell cycle unlike **BI-1** and **Asci**. A. Proportion of cells with different kinetoplast (K) and nucleus (N) numbers, n > 500 cells per condition, representative example from n = 2 repeats. B–C. Representative fluorescence microscopy images of abnormal DNA categories 1K1N1X, 0K1N, and 1K0N from cells treated with **BI-1**, 50 µM, 6 h (B) and 1K1N-side from cells treated with **Asci**, 250 nM, 6 h (C).

2.6.2 DDB-1 does not change the rate of promastigote differentiation to amastigotes

We wanted to investigate if **DDB-1** has an effect on the differentiation process by triggering promastigote to amastigote differentiation of treated cells using acidic media and temperature

change. In these conditions, 98% of the promastigote population visually appear as amastigotes within 24 h, and no elongated flagellated cells are seen after two days. 30 µM **DDB-1** added to promastigotes in these culture conditions did not change the rate of growth or differentiation for the first 24 h compared to a 0.1% v/v DMSO control (Figure 18, bold lines). After the initial 24 h differentiation window, **DDB-1** caused a slowing of growth and then growth arrest beyond two days. This is in contrast to promastigotes that are under normal growth conditions without triggering differentiation (Figure 18, dotted lines): the 24 h growth factor for treatment with DMSO is approximately 10, but is only approximately 2 when treated with **DDB-1**. The differentiation process itself led to a slowed 24 h growth factor in the DMSO treated cells, and the resulting amastigotes maintained slower growth than promastigotes.

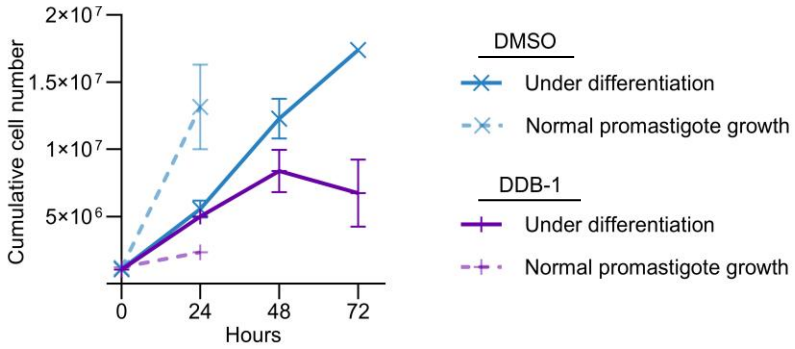

Figure 18. DDB-1 does not change the rate of *L. mexicana* promastigote differentiation to amastigotes. Growth of promastigotes from 10^6 cells/mL in M199 at 28 °C (dotted) or SM5.5 at 34 °C in 5% CO_2 (bold) to trigger differentiation, $n = 3$.

2.7 Compounds do not interact with DNA in the tested assays

Chemicals can interact with cellular DNA, interfering with replication and causing general toxicity.[357] This can be through direct interaction, for example DNA helix intercalation, or through indirect processes such as generation of ROS which cause DNA damage. **Asci** and the **BI** compounds have flat, planar structures that are amenable to DNA intercalation. Additionally, both these families have anti-cancer properties *via* inducing double-stranded DNA breaks (DSBs).[358, 359] DSBs can cause cytotoxicity, which could explain the observed compound activity in *Leishmania*.[360-362]

2.7.1 Intercalation of double-stranded DNA

I ran a DNA intercalation assay in collaboration with the Wyllie lab at the University of Dundee. The assay uses double-stranded DNA pre-incubated with fluorescent reporter acridine orange (AO) which intercalates between DNA bases.[363] The compound of interest is then added and fluorescence polarisation is read to quantify the displacement of AO by competing intercalators. The output can be considered as an EC_{50} value for 100% AO competition and compared to the known DNA intercalator daunorubicin.[364] **Asci** reaches 50% intercalation at the highest concentrations tested (50 µM), while **DDB-1** does not intercalate – unsurprising given the compound structure (Figure 19). **Asci** intercalation occurs at 700× the *L. mexicana* EC_{50}, so if this is the cause of compound toxicity there must be a local accumulation taking place. DNA intercalation could drive compound accumulation in the nucleus such that sufficiently high concentrations are reached to cause toxicity.

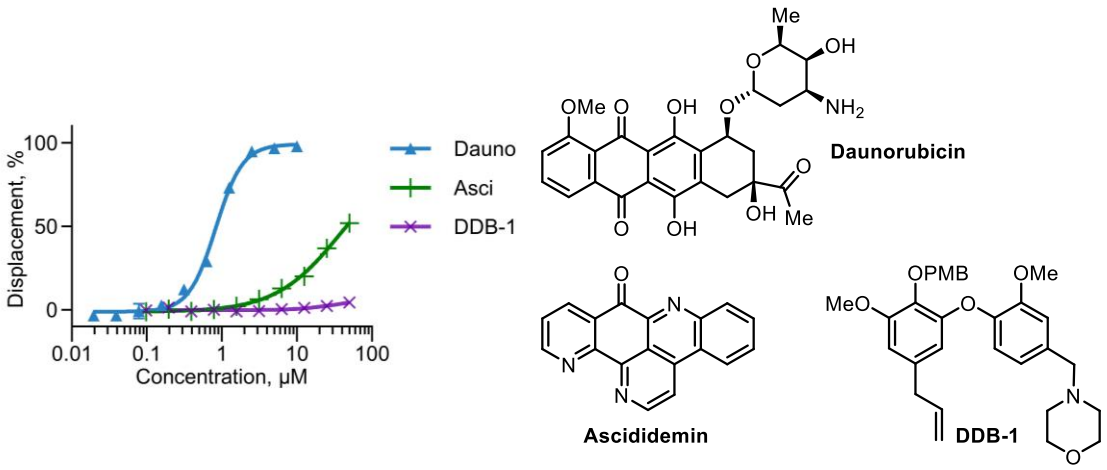

Figure 19. Acridine orange displacement from DNA by competing intercalators. Representative dose-response curves for the displacement of acridine orange, $n = 3$. The mean is plotted with error bars representing standard deviation.

2.7.2 Compounds do not induce double-stranded nuclear DNA breaks in *L. mexicana*

In order to monitor double-stranded DNA breaks (DSBs) in the nucleus of *L. mexicana* promastigotes, we generated a cell line with N-terminally tagged mNeonGreen (mNG) RAD51 (Section 6.2).[269] *Leishmania* employ the RAD51 DNA recombinase protein as part of their DNA repair machinery to fix naturally occurring nuclear DSBs *via* homologous recombination.[365-368] The

mNeonGreen cell line will allow observation of RAD51 recruitment to foci in the nucleus in response to DSBs, as has been shown in *T. brucei*.[369, 370] Phleomycin induces nuclear DSBs and was used to validate the mNG::RAD51 cell line, causing an accumulation of fluorescent foci in the nucleus in > 80% of cells from 2 hours of treatment (Figure 20).[371] In contrast, none of the other compound treatments led to analogous foci for up to 24 h, and therefore did not cause DSBs. However, this methodology is only sensitive to DSBs in nuclear DNA, and any effects on kinetoplast DNA (kDNA) remain to be investigated. Compound accumulation can be mediated either by active transport systems or passive diffusion driven by concentration gradients. Since kDNA resides within the mitochondrion, compounds would need to first penetrate the mitochondrial membrane and then access the kinetoplast within – a dual barrier to entry. On the other hand, nuclear pores provide relatively straightforward access for small molecules to the nucleus, making nuclear accumulation more feasible, and therefore kDNA DSBs are a less likely MoA.

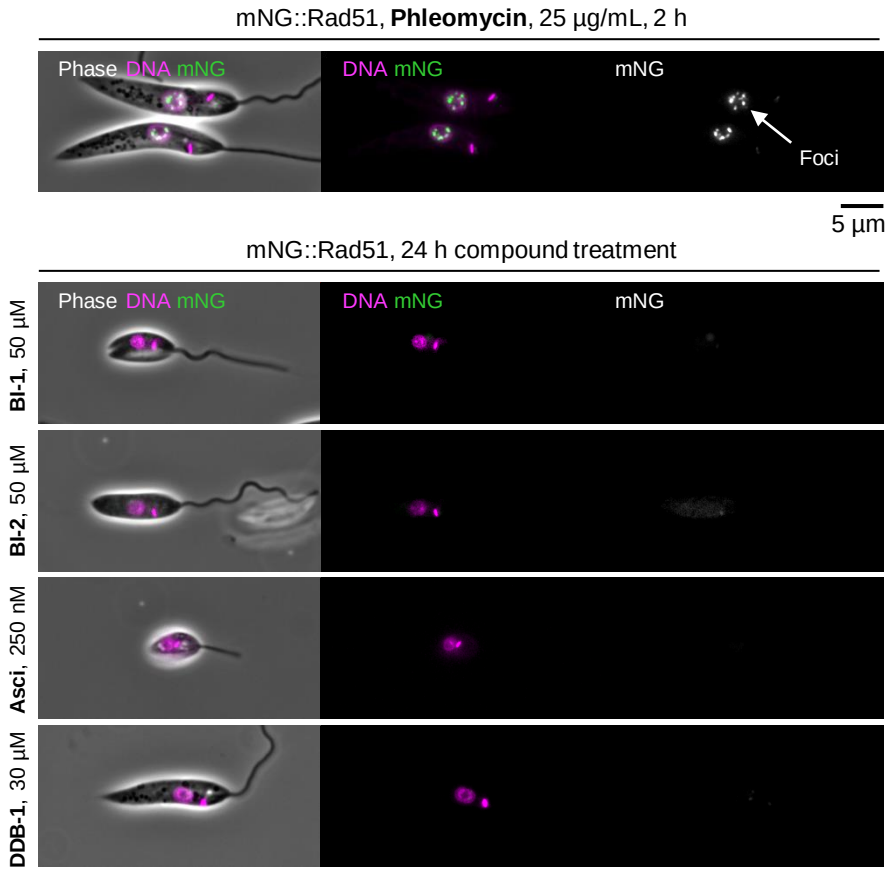

Figure 20. Compounds do not induce double stranded nuclear DNA breaks in *L. mexicana* promastigotes. DNA was stained with Hoechst 33342 (magenta), foci are labelled in the phleomycin control treatment, all mNeonGreen images are shown with equivalent contrast. $n > 100$ cells for each condition.

2.8 Mitochondrial fitness assays

Initial investigations by our collaborators suggest that **DDB-1** causes mitochondrial dysfunction and Ca^{2+} release in *L. infantum* promastigotes.[320] A selection of assays that measure biochemical changes in mitochondrial function were used to confirm these results in *L. mexicana*, and expand on the nature of mitochondrial disruption.

2.8.1 DDB-1 decreases ATP production

Measurement of cellular ATP production can test for the correct functioning of the mitochondrial oxidative phosphorylation pathway (reliant on mitochondrial membrane potential), as this is the main ATP source in *Leishmania*.[70, 372] A luminescence assay was used to measure the total ATP in treated cells, as well as the ADP to ATP ratio which gives information on cell viability. The two-step assay works by lysing cells to immediately detect ATP by the production of light from an ATP-dependent reaction between recombinant firefly luciferase and its D-luciferin substrate. Any ADP is then enzymatically converted to ATP and a second light measurement is taken. Total promastigote ATP was significantly decreased by **DDB-1** after 6 h of treatment compared to a 0.1% v/v DMSO negative control (Figure 21A). The ADP/ATP ratio for the DMSO treatment was 0.6 at 6 h (i.e., more ATP than ADP) and 1.1 at 24 h (i.e., a similar quantity of ATP and ADP) which indicates slowed proliferation as cells enter stationary phase. In comparison, **DDB-1** treatment had a ratio of 0.5 at 6 h and only 0.7 at 24 h. The ADP/ATP ratios are plotted for a 6 h or 24 h incubation with compound, normalised to the DMSO sample which is assumed to be in proliferation (Figure 21B). The quantity of ATP and ADP in the **Asci** treated sample was the same as DMSO treatment for both time points. The observed decrease in total ATP with **DDB-1** agrees with the previous *L. infantum* result;[320] we can conclude that oxidative phosphorylation could be similarly impaired in *L. mexicana*. After 24 h, the total cell number differs between the **DDB-1** and DMSO treated samples so a comparison of total ATP values is no longer valid, instead the ADP/ATP ratios should be considered. The lower ratio for **DDB-1** treatment versus DMSO treatment indicates that while the quantity of total ATP was

decreased, the quantity of ADP had decreased even more, and after 24 h the **DDB-1** treated cells did not behave as if entering stationary phase.

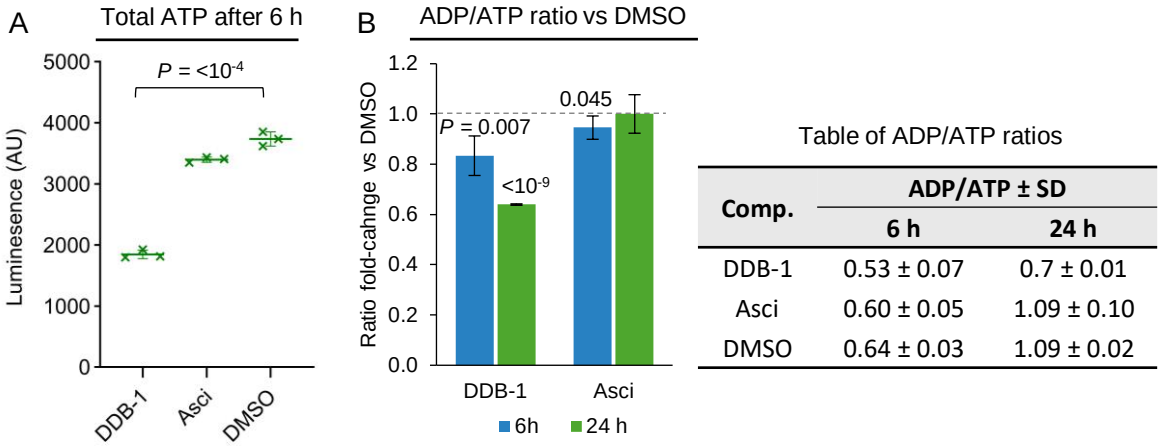

Table of ADP/ATP ratios

Comp.	ADP/ATP ± SD	
	6 h	24 h
DDB-1	0.53 ± 0.07	0.7 ± 0.01
Asci	0.60 ± 0.05	1.09 ± 0.10
DMSO	0.64 ± 0.03	1.09 ± 0.02

Figure 21. The quantity of ATP and ADP in *L. mexicana* is decreased by **DDB-1**. A. Representative luminescence readout corresponding to the total promastigote ATP following 6 h compound incubation, $n = 3$ replicates. B. ADP/ATP ratios are normalised to DMSO and the fold-change plotted. The dotted line at fold-change = 1 corresponds to DMSO, other treatments show decreased ratios following 6 h or 24 h compound incubation, $n = 2$ replicates. Statistical significance was derived from a two-tailed *t*-test versus DMSO, only $P < 0.05$ are shown. The table contains calculated values for the ADP/ATP ratio before normalisation, $n = 2$.

2.8.2 DDB-1 increases mitochondrial calcium ions

A dramatic increase in total cellular Ca^{2+} caused by **DDB-1** was reported by our collaborators in *L. infantum*.[320] In mammalian cells, cytosolic Ca^{2+} increase leads to mitochondrial Ca^{2+} loading,[373] which has also been demonstrated by *Leishmania* mitochondrial isolates.[374] I aimed to measure mitochondrial Ca^{2+} to investigate whether a similar loading is taking place in **DDB-1** treated *L. mexicana*. Rhod-2 is a fluorescent Ca^{2+} indicator that is targeted to the mitochondrion, which upon Ca^{2+} binding increases fluorescence > 100-fold. H_2O_2 induces Ca^{2+} release from intracellular compartments so was used as a positive control,[373, 375] and exogenous Ca^{2+} was added as an assay control. Following a 1 h incubation of compound with *L. mexicana* promastigotes, there is a small increase in fluorescence for H_2O_2 treatment, a significant increase for **DDB-1** treated cells, while **Asci** treated cells remain unchanged (Figure 22A). The experiment was repeated in *T. brucei* for comparison: H_2O_2 did not induce Ca^{2+} release, and **DDB-1** is the only treatment to increase Ca^{2+} levels (Figure 22B).

Increased intracellular Ca^{2+} by **DDB-1** in *L. infantum* had been previously shown by our collaborators Amaral *et al.* using fluorescent probe Fluo-4 which is not mitochondrion specific.[320] This is somewhat corroborated in *L. mexicana* and *T. brucei* in which we demonstrate a mitochondrial specific Ca^{2+} increase. Although the comparison here is cross-species, this result still implies that there is a mechanism at play causing cytosolic Ca^{2+} influx with the knock-on effect of low-level mitochondrial loading. This could plausibly be due to the release of Ca^{2+} from the acidocalcisomes, which has not been directly tested.

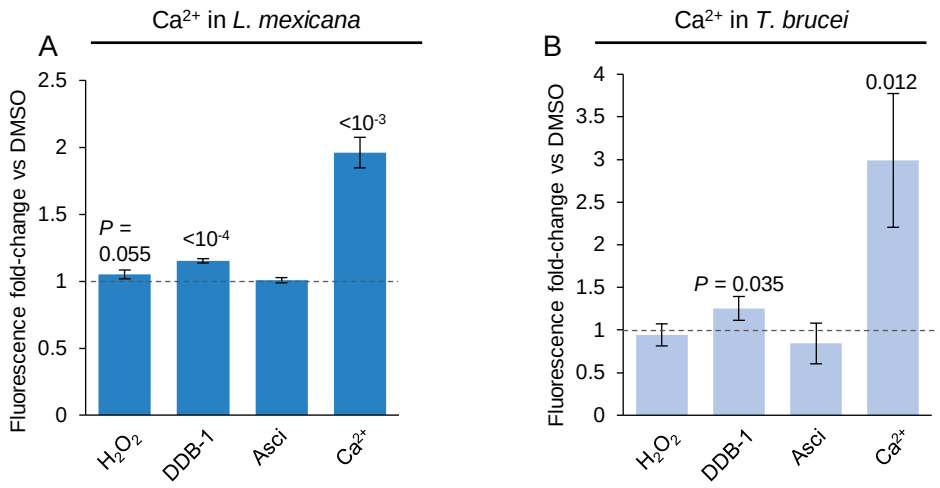

Figure 22. Mitochondrial Ca^{2+} levels in *L. mexicana* and *T. brucei* are increased by **DDB-1**. Rhod-2 fluorescence readout is normalised to DMSO and the fold-change plotted. The dotted line at fold-change = 1 corresponds to DMSO, other treatments show increased (above) or decreased (below) Ca^{2+} levels following 1 h incubation in *L. mexicana* (A) or *T. brucei* (B). $n = 3$ replicates, statistical significance was derived from a two-tailed *t*-test versus DMSO; only $P < 0.06$ are shown.

2.8.3 Glutathione has no impact on DDB-1 toxicity to *L. mexicana*

Glutathione (GSH) is a thiol with important cellular roles including damage protection by acting as a promiscuous scavenger to quench reactive species like covalent inhibitors and ROS.[376] **DDB-1** could be acting as a covalent inhibitor – which is thought unlikely given its chemical structure – or could generate ROS. I aimed to test this by the addition of exogenous GSH to **DDB-1** treated cells: if either MoA is involved in compound action, there should be a shift in EC_{50}. This has been demonstrated by Susan Wyllie (unpublished) whereby glutathione sensitivity was a feature of a Michael acceptor covalent inhibitor compound. Levels of GSH in *Leishmania* range from 0.04 to

0.12 nmol/10^7 parasites,[377] and the M199 medium used here has a GSH concentration of 163 nM.[378] **DDB-1** EC_{50} was insensitive to exogenous glutathione added to the media at a comparatively high concentration of 30 µM (Figure 23). Therefore as expected, **DDB-1** does not act as a covalent inhibitor, and furthermore is unlikely to induce ROS. However, it is important to note that a glutathione-sensitive positive control was not included in this assay due to difficulties accessing the necessary compound; this result should be validated by a repeat inclusive of the appropriate control.

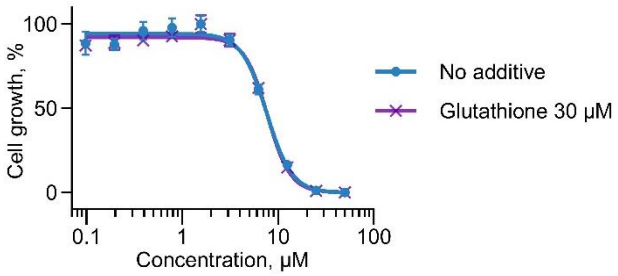

Figure 23. Dose-response curve for **DDB-1** is unchanged in the presence of exogenous glutathione. Representative EC_{50} curves for **DDB-1** treated promastigotes grown in M199 with or without the addition of 30 µM glutathione. The mean is plotted with error bars representing standard deviation for n = 6 technical replicates.

2.9 Discussion

We set out to establish the SAR of dehydrodieugenol B (DDB) analogues in *Leishmania*, and identify accompanying cellular changes with compound treatment both visually and biochemically. I carried out extensive SAR analysis on 39 compound analogues which revealed sites on the biaryl ether scaffold that are tolerant to modification, summarised in Figure 24. Interestingly, the SAR conclusions differed somewhat from the *T. cruzi* results, although as none of the polar-containing analogues were tested in *T. cruzi*, it is possible that differences arise from membrane permeability or lack thereof. Membrane transport can occur *via* an active, transporter-mediated process or a passive diffusion process; both scenarios could be affected by subtle differences between the constituent membrane transporters and/or channels in the two species even though the membrane composition is relatively well conserved, and they possess similar vacuolar structures.

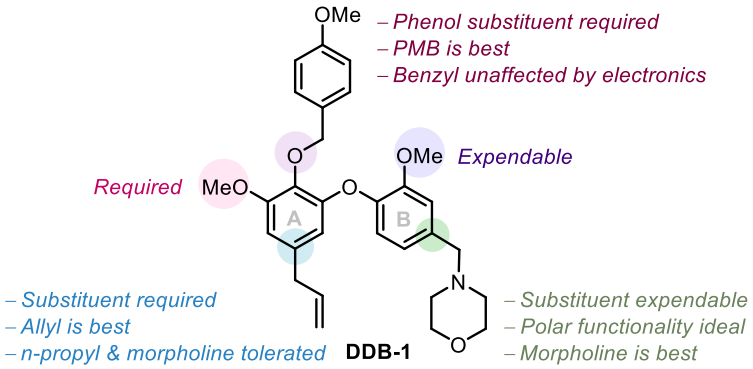

Figure 24. Structure of the best dehydrodieugenol B analogue **DDB-1**. Sites tolerant to modification are indicated.

Compound **DDB-1** was identified as the best hit against *L. infantum* amastigotes according to the DND*i* criteria, and activity against related trypanosomatids *L. mexicana* and *T. brucei* has been established. Using this compound alongside **Asci**, **BI-1** and **BI-2** as representatives of their respective compound families, we have investigated morphological, biochemical and cell cycle changes. These were designed to answer questions about the changes to organelles, the compound effect on cell cycle, and confirm the hypothesis that **DDB-1** is a mitochondrial poison. We confirm mitochondrial interruption with **DDB-1**, and present the first steps towards elucidating the mode of action for all three families in *Leishmania*.

2.9.1 DDB-1 does not behave as an expected drug compound

We anticipated that **DDB-1** would behave as a standard anti-leishmanial compound and induce the classic stress responses of drug treatment. Contrary to this, we observed no effect on the cell cycle progression, and the overall cell shape and size was conserved throughout the duration of drug treatment until cultures were dead. The inclusion of **Asci** and **BI-1** in these experiments highlights how unusual the lack of disrupted cell morphology and cell cycle is for an anti-leishmanial compound: these both display typical changes to morphology leading to “unhappy” looking cells. This lack of phenotypic changes with **DDB-1** could in itself be informative, particularly around the modes of cell death.

2.9.1.1 DDB-1 causes a phenotype characteristic of necrosis

Both fluorescence microscopy and transmission electron microscopy investigations of **DDB-1** treatment showed large vacuole-like multivesicular bodies (MVBs), with no other major morphological defects apart from enlarged mitochondrial cristae in the TEM imaging (Figure 15, Figure 16). In *Leishmania*, small MVBs are located between the lysosome and the flagellar pocket that play a role in transportation of material.[54] The MVBs in **DDB-1** treated cells are much larger than is expected for normal transportation MVBs or the cross-section through a lysosome. They appear of comparable size to the nucleus, and are located indiscriminately throughout the cell body, not confined to the anterior end.

Modes of cell death due to compound interference in trypanosomatids are generally restricted to apoptosis or necrosis. In eukaryotes, apoptosis can be differentiated from necrosis by a set of defined morphological changes. Key among these are cytoplasmic condensation, chromatin cleavage and aggregation of condensed chromatin to the nuclear envelope in apoptosis, while necrosis is characterised by the formation of cytoplasmic vacuoles and swollen or ruptured mitochondria.[379] There is some debate as to the ability of trypanosomatids to undergo apoptosis, i.e., programmed cell death in a similar manner to higher-level eukaryotes. Zangger *et al*. reported stress triggers in *Leishmania* that could lead to an "apoptosis-like" cell death mechanism that differs from "traditional" apoptosis.[354] They observed this response in nitric oxide treated *Leishmania*, which demonstrated MVBs, swollen mitochondria, and nucleus fragmentation. Moreira *et al.* report the result of heat shock in *L. amazonesis* promastigotes with TEM imaging showing chromatin condensation at the nuclear periphery for an apoptosis-like death, and conversely a swollen mitochondrion–kinetoplast complex for cell necrosis.[355] The morphological changes due to **DDB-1** are reminiscent of necrosis as there is crucially no nuclear disruption accompanying the MVBs and enlarged mitochondrial cristae. We can conclude from the morphology that **DDB-1** does not trigger an apoptosis-like cell death mechanism, although further work would be necessary to precisely dissect the cell death pathway.

Depending on the compound MoA, morphological changes can be highly informative, such as the disappearance of kinetoplasts in pentamidine treatment directly speaking to its kDNA damage MoA. For **DDB-1**, this only answered questions around the modes of cell death and therefore was not as informative as hoped – although the swelling of the mitochondrion and its cristae could be a direct compound effect and not only a feature accompanying necrosis.

2.9.1.2 Cell cycle perturbation is unusually not observed in DDB-1 treatment

In trypanosomatids, replication and division cycles of the kinetoplast, nucleus, and cytokinesis occur independently of one other with minimal to no cross-talk between the sub-cycles, which can lead to cells failing in one stage but continuing replication of the others.[75, 380] Most drugs cause an arrest or perturbation to promastigote cell cycle, so we expected the same for the compounds tested. It is very interesting that **DDB-1** does not present any cell cycle interference in *L. mexicana* promastigotes; this has not been reported to date with any anti-leishmanial compounds to the best of our knowledge. In comparison, both **BI-1** and **Asci** caused observable changed morphologies and disrupted cell cycles. Despite **DDB-1** having the most "drug-like" structure, it does not behave as a traditional compound causing cell cycle disruption (often a stress response), while the proposed intercalators **Asci** and **BI** do.

Treatment with **BI-1** led to > 10% of cells lacking a kinetoplast, suggesting a failure of kinetoplast duplication. Although the abnormal category of highest proportion was 1K1N1X (with extra DNA staining along with the identified nucleus and kinetoplast), this could be an artefact of stain accumulation not necessarily a third organelle. **Asci** has been reported to disrupt DNA and RNA synthesis, and cause an increase in sub-G_1 and decrease in G_1 phase leukaemia cells, with chromatin not well stained.[322, 381] It is plausible that the incorrect axially adjacent positioning of the 1K1N nucleus in **Asci** treated *Leishmania* – presumably microtubule mediated,[75] prevents correct DNA segregation, eventually leading to cell death. These observations cannot be attributed to the main MoA for either compound without evidence of direct interaction with cell cycle control proteins, and we would not necessarily expect that to be the case.

It is difficult for a compound to affect a cell without triggering observable effects on the cell cycle: either cell cycle arrest and accumulation of cells in one of the cell cycle phases, or the appearance of abnormal organelles. One explanation could be that the **DDB-1** mechanism acts in a way that does not interfere with the ability to replicate, divide or grow before being killed. The fact that complete culture death is not immediate, and there is a (albeit dramatically decreased) growth factor of 2 in the first 24 h following compound treatment, indicates that cell division is still occurring in the presence of **DDB-1**. Cells that are able to progress through the cell cycle do so uninterrupted, with additionally no observable effect on nuclear dsDNA. This could be due to an all-or-nothing effect of the compound: cells are either affected rapidly and dramatically such that they die before getting the chance to attempt division, or remain unaffected and are able to proceed with division normally. This would also account for the generally unchanged cell morphology apart from morphological changes linked with necrosis. Scenarios where the cell cycle remains unaffected could be envisaged if the mechanism triggers *rapid* necrosis, without time for the accompanying stress markers to affect the cell cycle. This raises questions about the compound uptake: could there be a critical threshold of intracellular compound required before triggering a response? Cells are always ultimately killed, which would fit with a threshold requirement. An alternative and more likely explanation is that the **DDB-1** action is stochastic and time-dependent, acting uniformly across the different stages of the cell cycle causing a general cell cycle arrest. This would also lead to the observed absence of accumulation in a specific phase, and could be expected from a MoA that deprives the cells of ATP as it is required by all cell cycle phases.

During promastigote to amastigote differentiation, **DDB-1** has no effect on the culture growth rate (Figure 18). The differentiation process to axenic amastigotes is not fully understood, it involves slowed metabolism and protein synthesis, alongside various amino acids and fatty acids being preferentially taken up or excreted.[382, 383] Consideration of these growth rates indicates that the MoA for **DDB-1** is not active during the differentiation window. This could be due to decreased uptake of **DDB-1** – particularly if a threshold concentration is required for cell death, or a temporary shutdown of the affected pathway while the cell is focussing its energy on differentiation. It is not generally

desirable to have a drug that is inactive during the differentiation process; this is considered a "vulnerable point" in the life cycle which could be targeted to prevent the transition to mammalian infection. There could additionally be resistance concerns: drug-resistant amastigotes could emerge from susceptible promastigotes if there is an opportunity to develop resistance during differentiation. However, provided the activity against amastigotes is retained, there are still opportunities for treating established amastigote infections, or combination therapy.

2.9.2 DDB-1 affects mitochondrial function but the exact impact is unknown

I hypothesised that **DDB-1** would cause mitochondrial disruption in *L. mexicana*, as reported in *L. infantum* promastigotes.[320] Treatment with **DDB-1** led to a decrease in total cellular ATP (Figure 21), therefore oxidative phosphorylation is disrupted which could be through a variety of mechanisms. Disruption to complexes I to V though mutations, improper protein folding or inhibition would block ATP production. Flow of electrons through the electron transport chain (ETC) could be impeded, or uncoupling could occur, leading to a loss of the proton gradient which would reduce ATP production. The substrates that feed into oxidative phosphorylation from other energy metabolism pathways could also be diminished. I attempted to measure mitochondrial membrane potential to determine if the ETC is maintained on **DDB-1** treatment, but the assay was met with technical failure, therefore we cannot determine which of these is the likely cause of the observed decrease in ATP.

The activity of **DDB-1** against bloodstream form *T. brucei* is an important result: the compound MoA cannot *only* be disrupting ETC/oxidative phosphorylation as bloodstream forms do not make use of this pathway for ATP production. Bloodstream forms still possess ATP synthase which works in reverse to "normal" to maintain the mitochondrial membrane potential in the absence of an ETC.[384, 385] All species tested have an ATP synthase so it is a plausible target of **DDB-1**. Its inhibition during oxidative phosphorylation is predicted to i) decrease production of ATP and ii) increase ROS.[386] In *L. mexicana*, **DDB-1** indeed decreased ATP production, but ROS levels were not directly

quantified: an assay measurement of mitochondrial superoxide failed, while the addition of glutathione (a ROS scavenger), did not change the compound EC_{50}. In *L. infantum*, overall ROS levels decreased with **DDB-1** treatment.[320] These data combined indicate that ROS is *not* increased by **DDB-1** and therefore ATP synthase is not targeted despite decreased ATP levels.

Under non-phosphorylating conditions i.e., low concentrations of ADP, there is reduced activity of ATP synthase and therefore H^+ leak across the partially permeable inner mitochondrial membrane.[387, 388] This is in conjunction with a feedback loop between ROS and H^+ leak: increased levels of mitochondrial superoxide trigger H^+ leakage, which results in reduced overall levels of ROS (in mitochondria without additional respiratory inhibition).[388, 389] The observed decreased ADP concentration relative to the DMSO control and likely decrease in ROS point towards H^+ leakage taking place due to **DDB-1** treatment. It remains to be investigated how, if at all, this contributes to compound MoA, or if it is just a biochemical consequence of an unidentified inhibition.

Mitochondrial membrane potential is closely linked to intracellular calcium ion levels: an increase in Ca^{2+} causes mitochondrial membrane depolarisation.[375] Ca^{2+} uptake was somewhat inconclusive in these experiments: the positive control of H_2O_2 led to only 1.05-fold increase in mitochondrial Ca^{2+} in *L. mexicana* (compared to the 1.3-fold increase reported for *L. donovani*),[375] and no increase in *T. brucei* bloodstream forms. **DDB-1** increased levels of mitochondrial Ca^{2+} in both species to a greater magnitude than the H_2O_2 control. Because the H_2O_2 control was not working as expected, we are hesitant to draw any concrete conclusions from this, although increased mitochondrial Ca^{2+} is likely to cause membrane depolarisation.

While we sought to clarify the exact nature of mitochondrial dysfunction caused by **DDB-1**, we were unable to answer this question due to the technical failure of key assays to measure mitochondrial membrane potential and mitochondrial superoxide, and an inconclusive positive control for Ca^{2+} quantification. When contrasted to the result that **Asci** did not change ATP levels or induce mitochondrial Ca^{2+}, it becomes more likely that the mitochondrion is involved in the action of **DDB-1**, and not **Asci**. We propose that **DDB-1** disrupts oxidative phosphorylation in *L. mexicana*,

but note that this cannot be the only MoA due to the key result of activity against *T. brucei* bloodstream forms; these conclusions are not definitive at this stage due to the lack of enough direct, positive evidence.

2.9.3 **Asci** could act *via* a ROS generation mechanism in *Leishmania*

We set out to elucidate **Asci** MoA in *Leishmania* which has not been investigated to date. Reported MoA of **Asci** and related analogues in mammalian cell lines are somewhat conflicting, involving i) DNA intercalation, ii) topoisomerase II (topo II) inhibition, and iii) ROS generation. **Asci** is a known DNA intercalator, in common with structurally related planar polyaromatics.[381, 390] Matsumoto *et al.* note that: "Although all these compounds have the ability to intercalate DNA, this capacity did not correlate with DNA cleavage activity".[359] Meanwhile, Bonnard *et al.* report that DNA intercalation is the likely cause of **Asci** cytotoxicity.[390] Intercalating ability is closely linked to topo II activity: topo II transiently generates double-stranded DNA breaks (DSBs) which can be induced by intercalators.[391-393] **Asci** weakly inhibits topo II,[322] although in many reports it does not generate topo II-dependent DSBs or form a DNA–topo II cleavable complex, and predominantly causes single-stranded DNA nicks.[359, 381] We demonstrate **Asci** intercalation of DNA at 50 µM (Figure 19) in agreement with the literature, although this was not carried out intracellularly. In the follow-up experiment, nuclear DSBs were not induced in live *L. mexicana* for up to 24 h post treatment. This is a significant result confirming that nuclear DSBs are *not* the MoA for **Asci** in *Leishmania.* The third MoA proposed for **Asci** in mammalian cells, namely ROS generation, has been widely investigated. The consensus is that **Asci** undergoes a redox cycling mechanism, converting oxygen to ROS in the process. This is not *via* a Fenton-type metal-mediated oxidation, but is proposed to be thiol dependent.[359, 394] In related natural product sampangine (possessing one less aromatic ring), Mahdi *et al.* demonstrated an oxygen-dependent ROS MoA with no mitochondrial involvement.[395]

We now propose a non-mitochondrial MoA in *L. mexicana* due to negative results in the mitochondrial fitness assays, although these are by no means a conclusive representation. Although we were unable to directly measure superoxide levels in *Leishmania,* a ROS mediated mechanism

remains the most likely MoA of **Asci**. As discussed above (Section 2.6.1), the incorrect positioning of the nucleus and kinetoplast during cell division could also play into the MoA *via* microtubule disruption and/or incorrect DNA segregation, and remains to be further explored.

The combination of morphology and biochemical assays are informative as a first step towards MoA determination. MoAs that involve clear defects in organelles are best suited for phenotypic analysis to elucidate mechanisms; however, this can only be determined after the experiment is carried out – for our compounds it was not particularly informative. We would still expect to see cell cycle defects for all compounds as a more general stress response – **DDB-1** is unusual in this regard.

3 Whole-cell compound localisation

3.1 Introduction

Small molecule drugs are vital to treat disease, and account for over 90% of marketed drugs.[396] Unlike larger biologic drugs that often target extracellular proteins, small molecule drugs can penetrate cells and interact directly with intracellular targets. We sought to visualise compound localisation and by extension, protein target localisation in whole cells as a method for target identification, and for monitoring compound uptake for the dehydrodieugenol B (DDB) family. This has been successfully applied and is well established in mammalian cells,[397] but there are only a few examples in trypanosomes. Orlistat-based probes are taken up quickly in bloodstream form *T. brucei* and localise to the cytoplasm,[398] and both an azadipeptide nitrile derivative and a cysteine protease inhibitor probe localise to the lysosomal compartments of bloodstream form *T. brucei*, in agreement with their expected targets.[399, 400]

3.2 Click chemistry for bioorthogonal attachment

Fluorescence microscopy is a straightforward way to visualise compound subcellular localisation in whole cells. This is due to the plethora of chemical fluorophores available to label the compound, cells can be co-labelled with fluorescent proteins and/or organelle stains to aid in pinpointing compound localisation, and imaging experiments are relatively easy to carry out. Using click chemistry, we aim to synthetically attach a fluorophore to the **DDB-1** scaffold. We can then use fluorescence and phase contrast microscopy to simultaneously image the whole cell, key organelles, and the fluorescently attached compound, giving an overall cellular localisation.

The three main click methods each have their merits and drawbacks as discussed in the introduction (Section 1.6.1.1). Consideration had to be taken when deciding the best for our desired application of fluorophore attachment to a synthetic small molecule. Copper-catalysed azide–alkyne

cycloaddition (CuAAC) was chosen as this would allow us to benefit from the relatively small perturbation expected to **DDB-1** by adding only a terminal alkyne or azide handle. The compound should therefore maintain its ability to cross cell membranes, unlike the cyclooctyne modification required for the strain-promoted azide–alkyne cycloaddition. Additionally, the substrate for CuAAC is more synthetically accessible than the phosphine substrates for Staudinger ligation.

Live cell cultures will be exposed to the handle-containing compound, thus ensuring that it maintains its "real" localisation. Once the compound has permeated live cells, they will be fixed with aldehyde, and the fluorophore clicked on – this negates the copper toxicity to cells as they are biologically fixed before CuAAC. Fixation is necessary to ensure that the compound localisation is not perturbed during CuAAC, and to allow subsequent cell permeabilisation to enable the click reagents to access the intracellular compound. Previous research in similar CuAAC applications has recommended using a fluorophore–azide and having the alkyne already installed in the cell; this minimises background reactivity of a fluorophore–alkyne in the reverse set-up.[401]

3.2.1 Click optimisation

The click chemistry protocol required optimisation for our desired application in *Leishmania*. To achieve this, we selected alkyne EdU (5-ethynyl-2'-deoxyuridine) as the intracellular component. EdU is a thymidine base mimic that efficiently incorporates into DNA during synthesis, providing a highly abundant clickable handle localised specifically within the nucleus and kinetoplast with proven utility in CuAAC.[402]

The *L. mexicana* promastigote cell cycle is approximately seven hours long, therefore culture was treated with 1 mM EdU for 24 h (> three cycles) to ensure that the entire culture had incorporated EdU. Cells were paraformaldehyde-fixed, NP-40 permeabilised and stuck to glass microscope slides to which were added the click reagents (described in detail in Section 6.7). The copper content of the CuAAC reaction will have an effect on the click efficiency, which can be modulated by varying the ratio of copper(II) sulfate reagent to a copper chelator (Invitrogen, "copper protectant"). Copper(II) sulfate is then reduced to the active copper(I) catalyst *in situ* by sodium ascorbate, another component

of the click reagents. DNA was stained using Hoechst 33342 to identify the nucleus and kinetoplast. Cells showed intense nuclear staining after CuAAC reaction with red fluorescent AlexaFluor555 (AF555) azide (Figure 25). As predicted, a copper concentration-dependent labelling of EdU was observed, reaching high signal intensity with a 9:1 ratio of copper(II) sulfate to protectant. A moderate ratio of 3:2 was chosen for optimum signal intensity without using unnecessary excess copper in the click reagents.

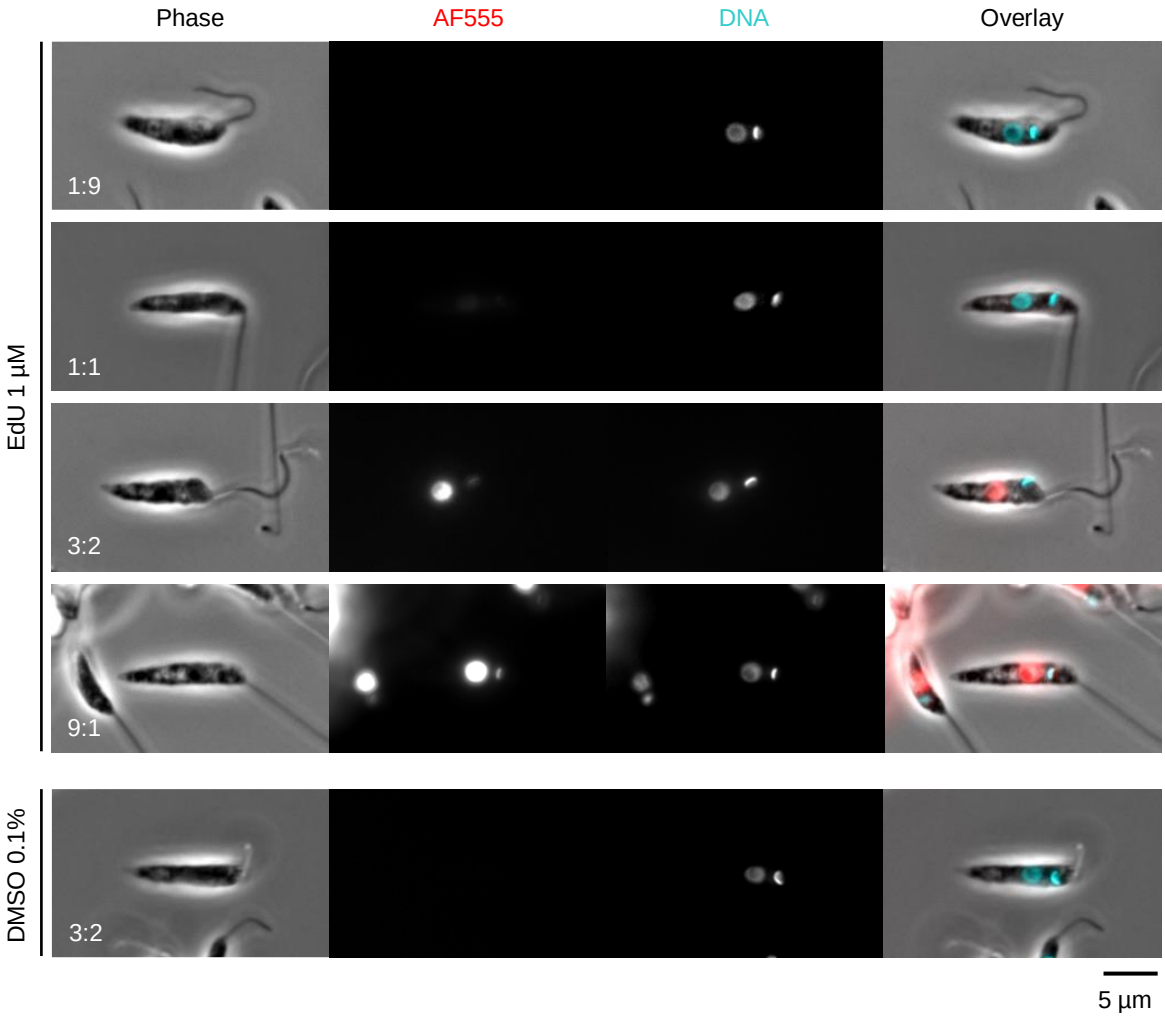

Figure 25. Optimal fluorescence microscopy imaging of EdU-labelled DNA uses a 3:2 ratio of $CuSO_4$ to copper protectant in the click reaction. Representative fluorescence microscopy images from > 3 fields of view, n > 50 cells. Images show EdU localisation following CuAAC of fluorescent AF555 for different $CuSO_4$ to protectant ratios, all AF555 images are shown with equivalent contrast. There is increasing AF555 signal observed as the copper(II) sulfate content of the click catalyst increases. DMSO treatment at 0.1% represents the negative control i.e., no alkyne present for the click reaction; no AF555 labelling is seen in this case.

3.2.2 Synthesis and evaluation of a clickable analogue

I synthesised a **DDB-1** analogue with a clickable handle at the phenol position, as this site is tolerant to modification (Section 2.9). A terminal alkyne handle was introduced at the end of a 6-carbon linker *via* an ether bond, giving compound **DDB-yne** (Scheme 2).

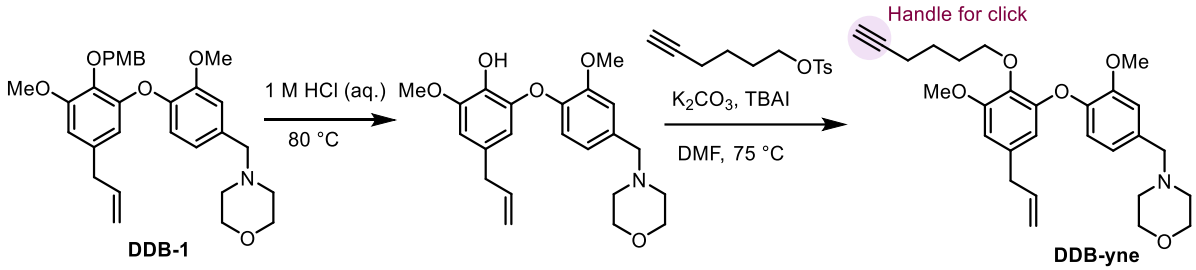

Scheme 2. Synthesis of alkyne analogue **DDB-yne** for click chemistry

DDB-yne had a similar effect to **DDB-1** on the growth of *L. mexicana* promastigotes over 24 h (Figure 26A). The relatively modest structural perturbation of **DDB-yne** compared to **DDB-1**, coupled with the similar activity leads us to believe that both compounds still interact with the same target, although this has not been definitively proven. We nevertheless proceeded with the optimised click conditions using compound **DDB-yne** as an alkyne-containing equivalent of **DDB-1**.

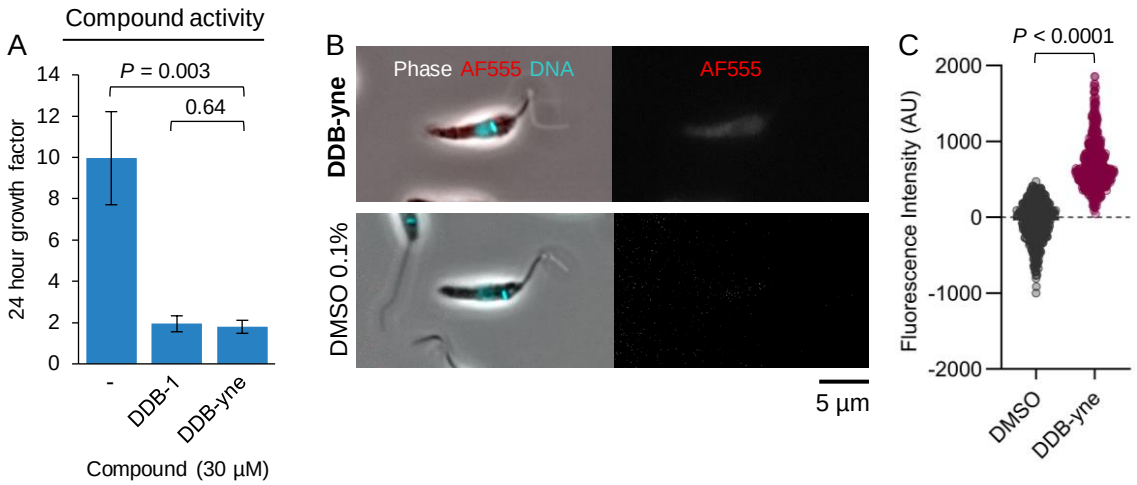

Figure 26. DDB-yne as a clickable derivative of **DDB-1** does not label cells with high signal intensity. A. 24 h growth factor for **DDB-yne** is unchanged from the parent **DDB-1**, and lower than an untreated control (-). Mean ± SD, $n = 3$. Statistical significance was derived from a two-tailed *t*-test. B. Representative fluorescence microscopy images from > 3 fields of view, $n > 50$ cells. Images show lack of fluorescent signal for AF555 clicked to **DDB-yne**; localisation cannot be determined. C. AF555 labelled **DDB-yne** has a higher signal intensity than the DMSO control, but a low overall magnitude, $n = 2$ biological replicates, $n > 100$ cells, $n = 2$ fields of view. Statistical significance was derived from a Mann-Whitney U test vs 0.1% DMSO treatment.

DDB-yne treated and clicked cells did not show a high intensity signal in all attempts (Figure 26B). While signal quantification within **DDB-yne** treated cells is statistically significant over the DMSO control (Figure 26C), the intensity was 200-fold lower than observed in the EdU experiment, making localisation hard to define. This result could be due to three likely scenarios: 1. Compound binding is weak such that during the multiple washes of the click protocol the compound is washed out, and therefore no fluorescence is visualised once the slides are imaged, 2. Compound is internalised too slowly or the compound target is of too low abundance, or 3. Compound MoA is not *via* direct interaction with a target that can be localised, but instead works by altering the cell environment in a more complex manner such as affecting cell signalling pathways. With this in mind, we turned to photoaffinity labelling techniques that would allow fluorescent attachment and prevent compound washout.

3.3 Photoaffinity labelling (PAL) for small molecule attachment to proteins *in situ*

3.3.1 Design and synthesis of a PAL analogue

Probes for photoaffinity labelling (PAL) are made up of the active molecule – in our case the DDB core, and a PAL linker. The linker will comprise a photoactivatable group and an alkyne for the click chemistry previously optimised (Section 3.2.1). Given the merits of different examples of linkers in the literature (introduced in Section 1.6.1.2) we chose to use the minimalist linker designed by Li *et al*. This is due to the favourable characteristics of alkyl diazirines over other PAL moieties, such as the small size of the functionality – which should cause minimal perturbation to **DDB-1** activity and cell permeability – and their proven utility in similar applications. Additionally, these linkers are relatively synthetically accessible, and as we envisaged using an amide bond for attachment, we required a carboxylic acid linker which made the minimalist tag best suited.

The linker was synthesised in four steps following the protocol by the Cravatt lab,[256] then attached to the active core of **DDB-1** *via* an amide bond to give a photoactivatable analogue **DDB-PAL**

(Scheme 3). This relatively cell-stable amide linker should allow steric accessibility of the alkyne once *in situ*, increasing the likelihood that it will be exposed to fluorophore–azide during CuAAC.

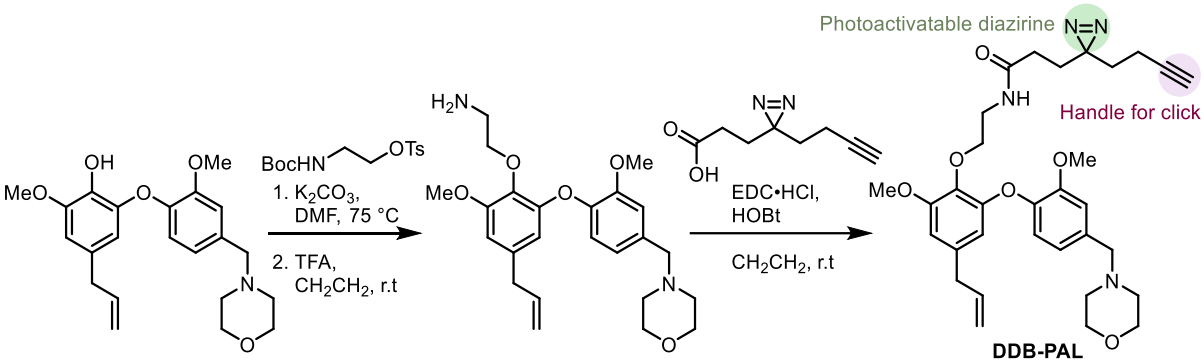

Scheme 3. Synthesis of analogue **DDB-PAL** with PAL and click capabilities.

3.3.2 DDB-PAL fluorescence localisation

As hoped from the minimalist linker design, **DDB-PAL** had no significant shift in EC_{50} compared to the parent **DDB-1** (Figure 27). We therefore proceeded with the fluorescence localisation experiment. *L. mexicana* in culture was incubated with **DDB-PAL** and then exposed to 10 Watt 365 nm UV light for 10 min to trigger diazirine cross-linking. Cells were aldehyde-fixed, attached to microscope slides and then treated with the optimised CuAAC conditions previously used for **DDB-yne**. All cells showed a fluorescence signal of comparable intensity to the optimised EdU experiment (Figure 28). The fluorescence appeared to label a specific reticulated structure, indicating successful PAL and click. To aid the identification of labelled organelles within cells, the images required deconvolution. Image deconvolution is a processing step that restores out-of-focus signal to its focus position, thereby making images sharper.[403]

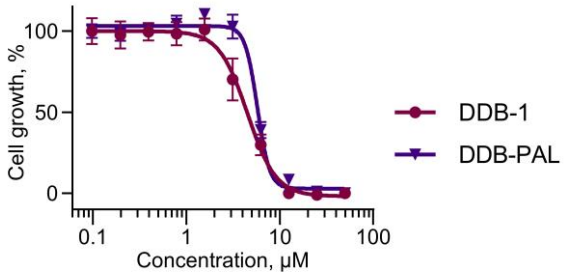

Compound	EC_{50} ± SD (µM)
DDB-1	4.74 ± 0.24
DDB-PAL	5.33 ± 1.07

Fold-change = 1.1, *P* = 0.40

Figure 27. Activity of analogue **DDB-PAL** in *L. mexicana* is unchanged from the parent compound **DDB-1**. Graph shows representative dose-response curves for compound treatment, *n* = 6 wells. The table shows EC_{50} values for *n* = 3 replicates; statistical significance was derived from a two-tailed *t*-test.

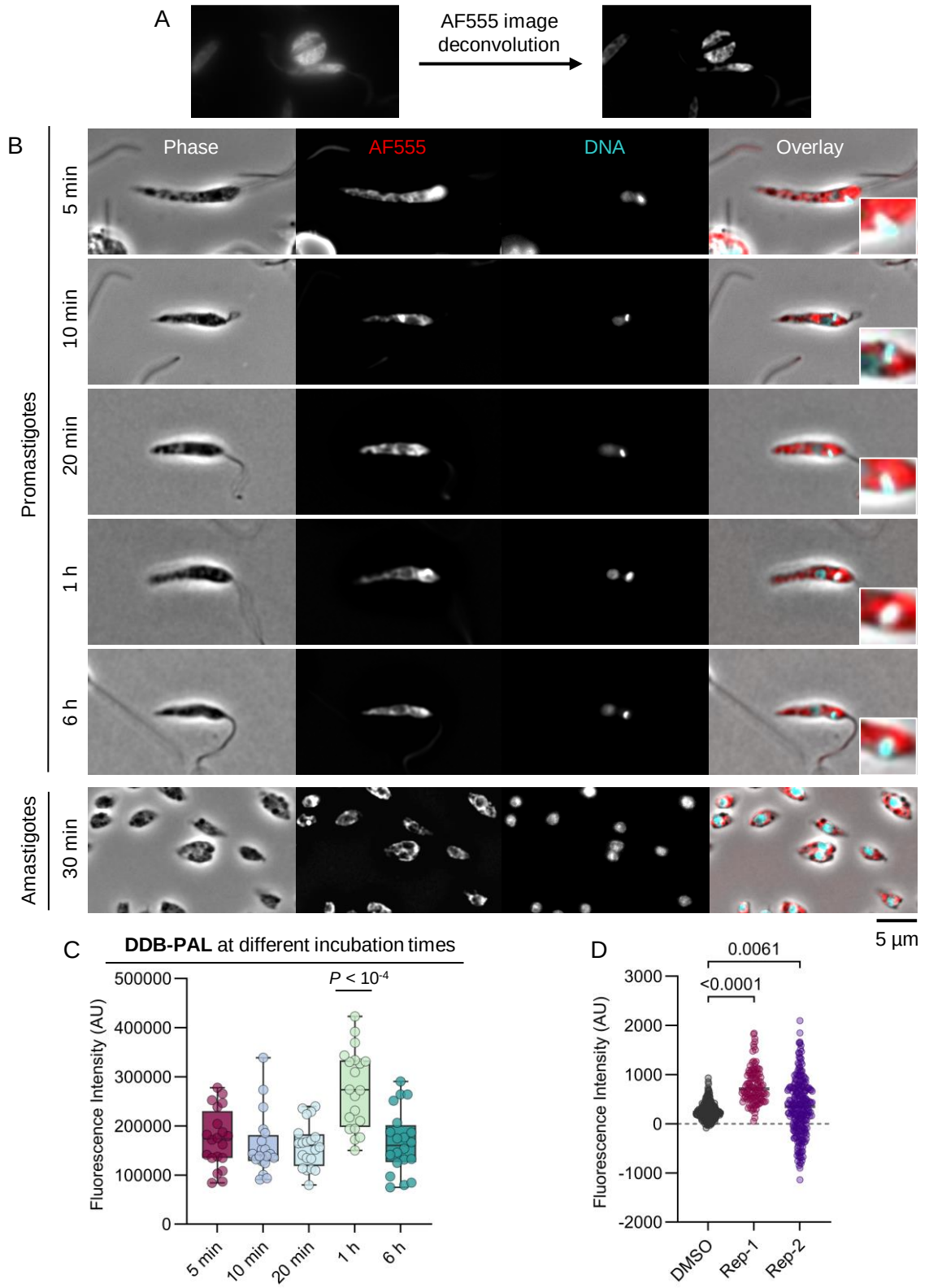

Figure 28. DDB-PAL localises to a reticulated structure, likely to be the mitochondrion. A. Image deconvolution results in sharpened fluorescence signal. B. Representative fluorescence microscopy images from > 3 fields of view, n > 50 cells. Images show **DDB-PAL** localisation following CuAAC with AF555 for different **DDB-PAL** incubation times. DNA was labelled with Hoechst 33342 (cyan), the AF555 channel has undergone image deconvolution, 2.7× zoomed inset in the overlay shows overlap of kinetoplast and AF555 signal. C. AF555 signal intensity within the promastigote cell body for different incubation times, n = 20 cells. Statistical significance was derived from an ordinary one-way ANOVA, P < 0.05 shown compared to all other samples. D. AF555 signal intensity is low following a 5 h "chase"; two biological replicates (Rep-1, Rep-2), n > 100 cells, n = 2 fields of view. Statistical significance derived from a Mann-Whitney U test vs 0.1% DMSO.

We applied deconvolution to the **DDB-PAL** fluorescence localisation, which allowed a clearer subcellular localisation to be identified (Figure 28A). The CuAAC experiment was conducted for various incubation times with **DDB-PAL** (5 min to 6 h incubation) in *L. mexicana* promastigotes, and a 30 min treatment of axenic amastigotes (Figure 28B). In all cases, we observed a distinctive reticulated pattern which overlaps with kinetoplast signal (Figure 28B, kinetoplast overlap shown in the overlay). By comparing the images with known organelles, we conclude that the localisation is likely to be the mitochondrion.[44, 404, 405] This is reinforced as the kinetoplast is included within the AF555 fluorescence. Fluorescence signal intensity within the cell body was not time-dependent apart from an anomalously high intensity at 1 h (Figure 28C). This peak in fluorescence at 1 h could indicate an accumulation event followed by compound removal such as drug breaking down. Maximal signal intensity could be reached while the rate of accumulation is faster than rate of break down, after which the free drug concentration drops and accumulation rate decreases, with a subsequent reduction in signal intensity.

We wanted to verify whether the compound is washed out during the click protocol, as was suspected for the non-PAL analogue **DDB-yne**. To investigate this, a pulse-chase experiment with **DDB-PAL** was carried out and compared to a 0.1% DMSO negative control. Promastigotes were incubated with 30 µM **DDB-PAL** for 30 min – a "pulse", then washed twice with fresh media and incubated in compound-free media for 5 h. Following this 5 h "chase", the compound was cross-linked with UV light and clicked to AF555 azide. Signal intensity within the promastigote from **DDB-PAL** treated cells is significantly increased over DMSO treatment (Figure 28D); however, the fluorescence intensity is low: approximately 10-fold less than expected for labelled cells. The signal is sufficiently weak that its localisation cannot be determined, therefore localisation studies need to be conducted without the 5 h chase. We can conclude that the compound is not strongly bound to a target, as PAL is necessary to allow the visualisation of localisation and prevent compound wash out.

3.3.3 mNeonGreen labelling to validate localisation

In order to validate the compound localisation, we sought to carry out co-localisation studies with a fluorescent protein of known organelle localisation. Co-localisation is a measure of both co-occurrence i.e., in the same place, and correlation i.e., of the same magnitude.[406] mNeonGreen (mNG) (Ex-Max 506 nm/Em-Max 517 nm) was the fluorescent protein of choice as its excitation and emission wavelengths are different to both AF555 used in the click chemistry (Ex-Max 553 nm/Em-Max 568 nm) and Hoechst 33342 DNA stain (Ex-Max 350 nm/Em-Max 461 nm).[407] Distinct fluorescence wavelengths are essential to minimise bleed-through or bleaching, and avoid cross-talk, which would affect co-localisation measurements.[408]

We generated mNeonGreen tagged cell lines mNG::LmxM.09.1130 and mNG::LmxM.29.29080, TIM17 mitochondrial and GAPDH glycosome proteins respectively (as described in Section 6.2). These well-known proteins have previously been tagged and shown to localise to these organelles.[44] The glycosome tag was included in this experiment as it has a localisation in granular dots within the cell body, which could be similar to the reticulated pattern of **DDB-PAL**. The generated cell lines were confirmed to have integrated the mNeonGreen tagging construct by microscopy: the observed localisation in > 99% of cells in every imaging field of view (overall > 500 cells) was as expected. Cell lines also maintain drug resistance to drug markers included in the tagging construct.

We applied the optimised **DDB-PAL** cross-linking and CuAAC conditions to these mNeonGreen tagged cell lines. AF555 fluorescence localisation corresponding to **DDB-PAL** was as expected, however there was no or poorly defined fluorescence of the mNeonGreen tag after click (Figure 29A). Copper ions from the click catalyst are known to quench mNeonGreen fluorescence which requires restoration by washing with a complexing agent.[409] A 2 h incubation with 40 mM EDTA post-CuAAC visually restored mNeonGreen signal fully for mNG::GAPDH, and to some extent for mNG::TIM17, allowing an overlay with AF555 signal to be created (Figure 29B).

Images were subjected to an automated co-localisation analysis. A cytofluorogram – where every dot represents a pixel and its position along the axes shows the pixel intensity – displayed a positive correlation between mNeonGreen and AF555 fluorescence for both cell lines, as shown for an example cell of each cell line (Figure 30A–B). Pearson's coefficient (R) measures the spread of the data: averaged over 10 cells, R = 0.77 for the mitochondrial TIM17 tag and R = 0.42 for the glycosomal GAPDH tag. This means there is better co-localisation with **DDB-PAL** and the mitochondrion than the glycosome. In this analysis, co-occurrence is particularly interesting for assessing signal co-localisation as there is no expectation that AF555 and mNeonGreen signal intensity will correlate. It is therefore appropriate to also consider thresholded Manders' coefficients

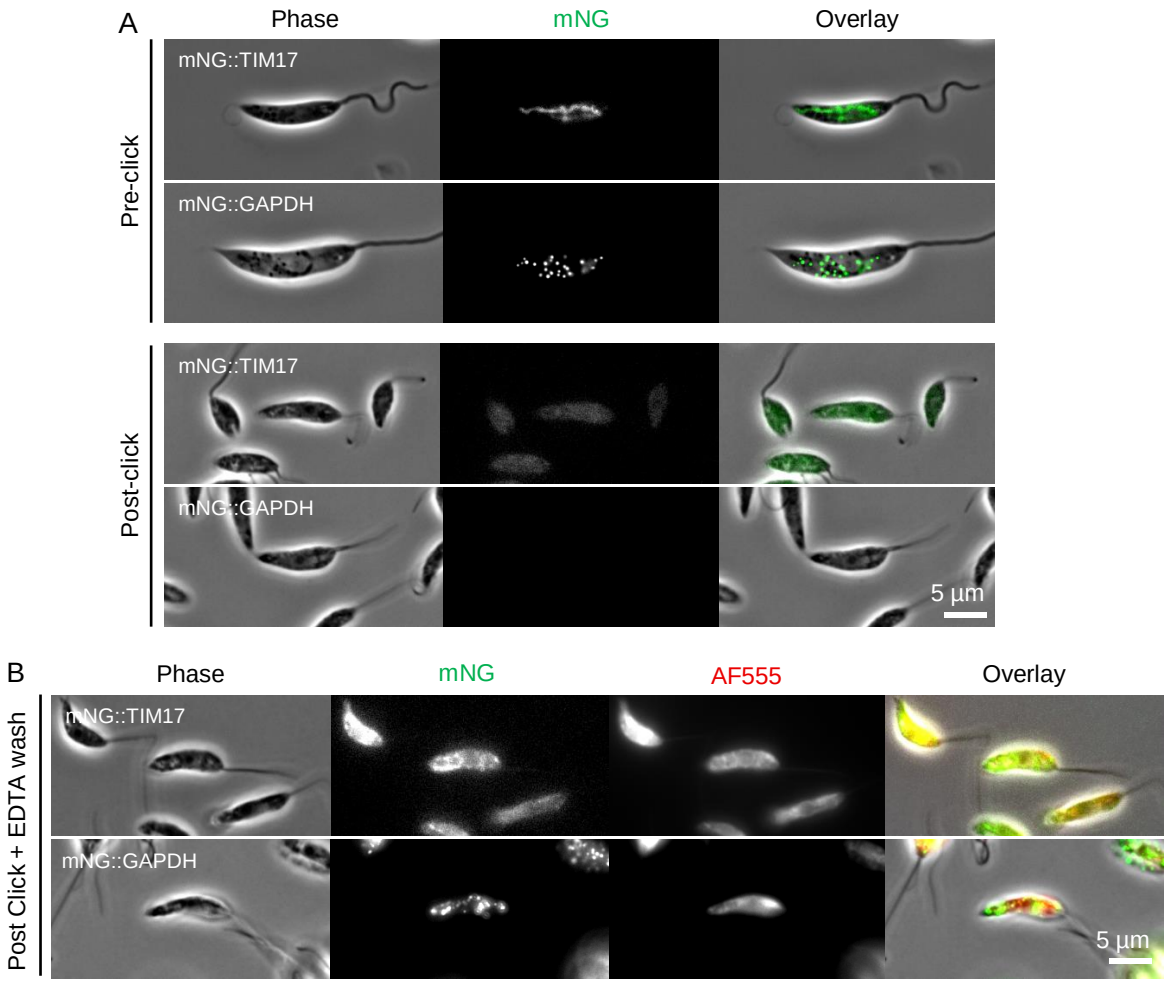

Figure 29. mNeonGreen fluorescence is quenched by the CuAAC conditions unless an EDTA restoration wash is included. Representative fluorescence microscopy images from > 3 fields of view, n > 50 cells. A. Images show loss of mNeonGreen fluorescence after CuAAC. B. Images show AF555 and mNeonGreen fluorescence after CuAAC and EDTA wash for mNeonGreen fluorescence restoration; all images are shown without deconvolution.

(tM_1 and tM_2) for each channel, which gives the fraction of signal from channel 1 that overlaps with channel 2 and vice versa, with no dependency on signal intensities.[410] For mNG::TIM17, tM_1 = 0.79 and tM_2 = 0.90 meaning overlap is high in both cases. For mNG::GAPDH, tM_1 = 0.68 which indicates that more than half the glycosome signal is co-localised, while a lower tM_2 of 0.46 means the majority of AF555 signal is not localised within the glycosomes (Figure 30C).

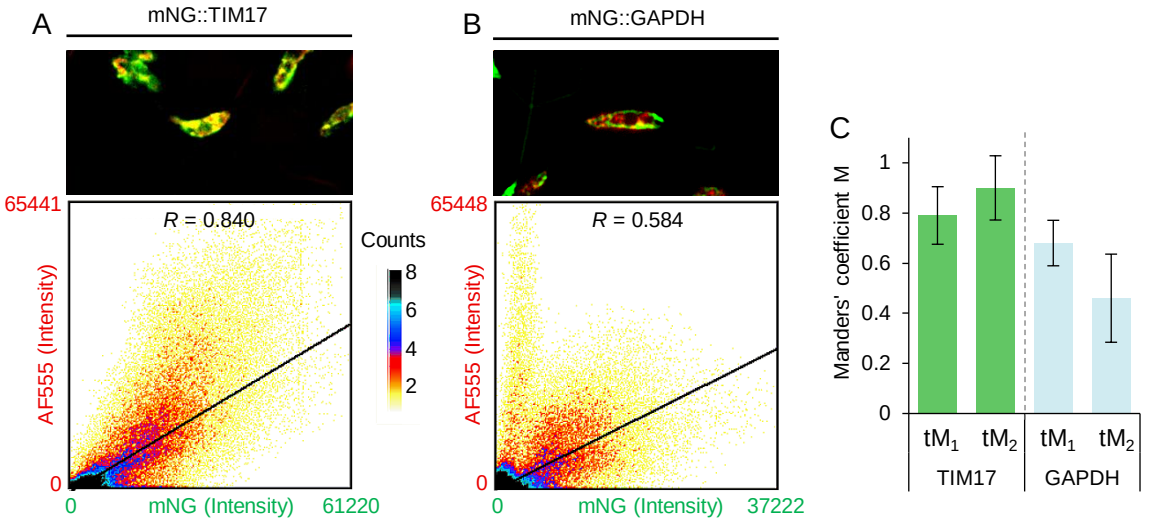

Figure 30. DDB-PAL shows good co-localisation with mNeonGreen tagged mitochondria, and moderate co-localisation with mNeonGreen tagged glycosomes. A–B. AF555 (corresponding to **DDB-PAL**) and mNeonGreen image overlay and cytofluorogram for an example cell of each cell line. In the image, overlap between the AF555 (red) and mNeonGreen (green) channels is yellow. The *R* value for each cytofluorogram is shown, *R* ranges from −1 to 1, where 1 is full co-localisation, −1 is complete exclusion, and 0 is no correlation C. Thresholded Manders' coefficient for each cell line, n = 10 cells. tM_1 represents overlap of mNeonGreen signal with AF555, tM_2 represents overlap of AF555 signal with mNeonGreen.

3.3.4 HaloTag labelling to validate localisation

Due to the incomplete restoration of mNeonGreen fluorescence even with an EDTA wash, a HaloTag alternative labelling strategy was used for co-localisation studies. HaloTag protein is genetically encoded fused to the protein of interest (POI) using CRISPR-Cas9, which results in a construct that can be chemically labelled using a haloalkane ligand (such as a small molecule fluorophore), with high specificity (Figure 31A).[269, 411] The resultant fluorescent signal should survive the CuAAC conditions as it is a chemical fluorophore, unlike the mNeonGreen fluorescent protein which is quenched by copper ions. I generated a range of HaloTag cell lines for proteins of known localisation (where localisation has been previously shown by mNeonGreen tagging), listed in Table 8.

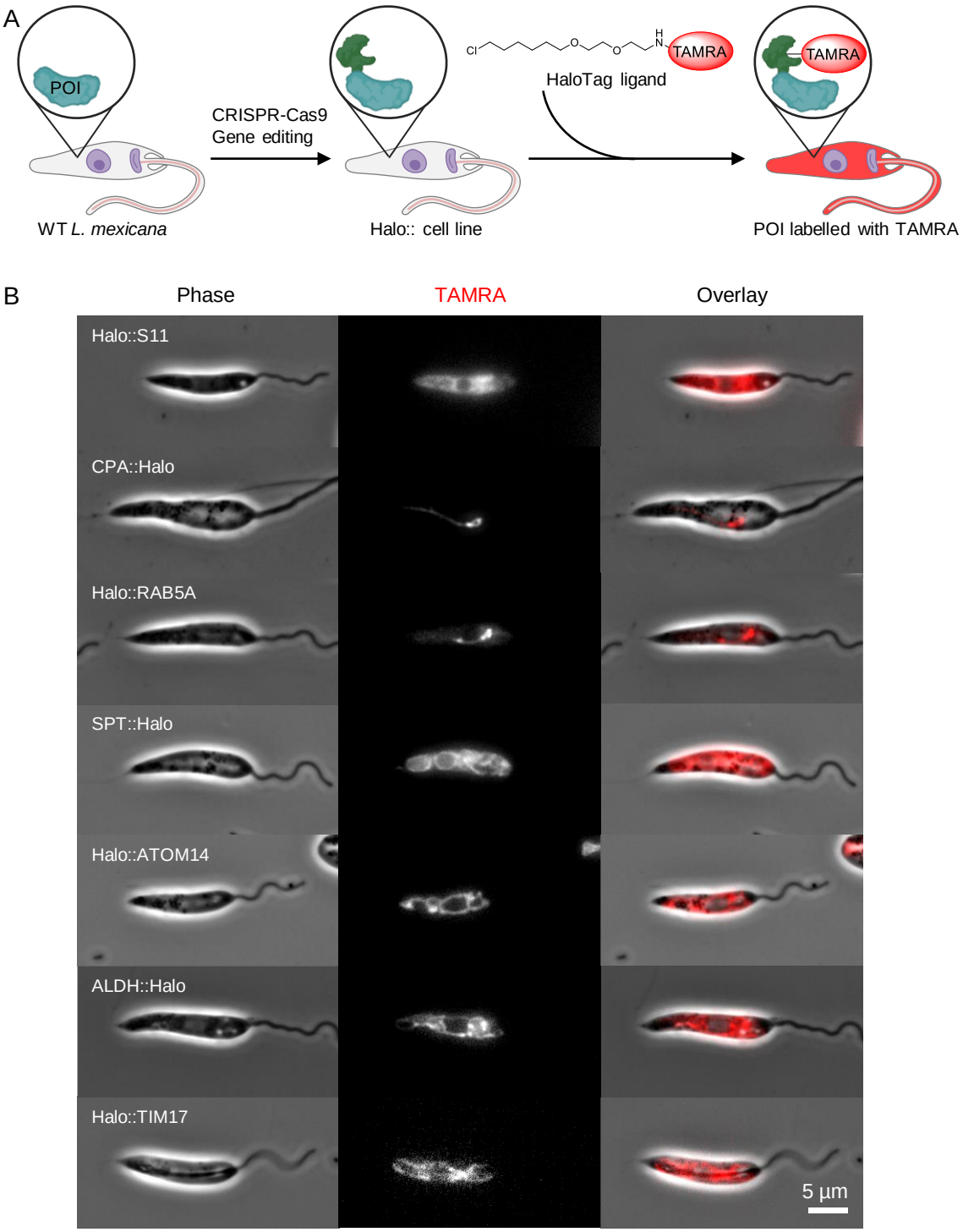

Figure 31. Fluorescence microscopy images of TAMRA label representing localisation of HaloTag protein. A. Workflow for sample processing to generate TAMRA labelled cell lines for different cellular localisations. *L. mexicana* promastigotes are genetically modified using CRISPR-Cas9 to add a HaloTag construct (dark green) to a protein of interest (POI) with known localisation. A chloroalkane ligand containing TAMRA (red) is fed to the cells to enable HaloTag labelling of the POI, which is imaged with fluorescence microscopy to visualise the protein localisation in live cells. B. Representative images from > 3 fields of view, n > 50 cells; cellular localisation is as expected for the different HaloTag generated cell lines. Contrast for TAMRA is adjusted to optimise visualisation and does not represent relative fluorescence intensities for each cell line.

Table 8. Identity of genes used in HaloTag validation experiments

Gene ID	Shorthand	Expected localisation	Tagged terminus
LmxM.20.1650	S11	cytoplasm[44]	N
LmxM.19.1420	CPA	lysosome[44]	C
LmxM.18.1130	RAB5A	endocytic system/lysosome[44]	N
LmxM.33.3740	SPT	endoplasmic reticulum[44]	C
LmxM.24.0940	ATOM14	mitochondrion[412]	N
LmxM.36.1760	ALDH	mitochondrion[412]	C
LmxM.09.1130	TIM17	mitochondrion[44]	N

Tagged cell lines were labelled with a red 5-carboxytetramethylrhodamine (TAMRA) ligand. TAMRA is a relatively small, cell permeable, pH insensitive dye (between pH 3 to 13), so is suitable for this application. The majority of cell lines displayed the expected localisation in > 95% of cells in every field of view (Figure 31B). CPA::Halo had only approximately 50% of cells labelled, and could represent a failure of the genetic modification since the TAMRA labelling worked well for the other cell lines. Halo::TIM17 showed > 95% of cells with the expected mitochondrial localisation, but less than half the signal intensity of the other mitochondrion-localised HaloTag proteins, indicating low expression levels and/or poor localisation behaviour which could be due to the tag.

Ligands with red fluorescence such as TAMRA are thought to perform better as HaloTag labels than green ligands (Richard Wheeler, unpublished). However, TAMRA (Ex-Max 557 nm/Em-Max 576 nm) and the AF555 previously optimised to label **DDB-PAL** in the CuAAC reaction have overlapping excitation and emission wavelengths; an unsuitable combination for simultaneous orthogonal labelling of both the HaloTag localisation and **DDB-PAL**. The azide partner for the click reaction was therefore switched to a green AF488 fluorophore (Ex-Max 494 nm/Em-Max 517 nm) (Figure 32A). This proved to work with the same efficiency as AF555 to visualise **DDB-PAL** following the standard CuAAC conditions.

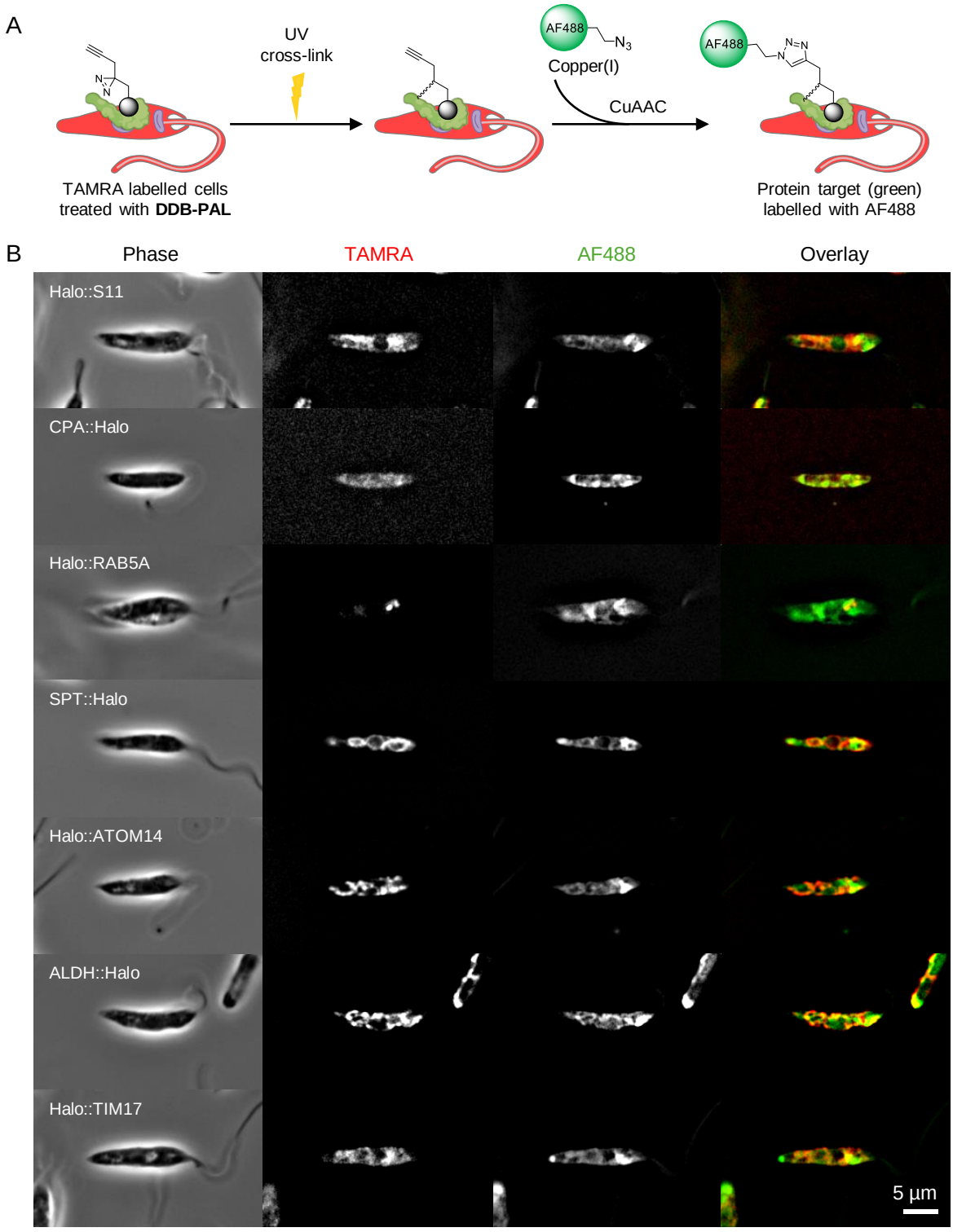

Figure 32. DDB-PAL shows varying co-localisation with HaloTag TAMRA labelled cell lines. A. Workflow for sample processing to carry out click reaction on TAMRA labelled cell lines. Live *L. mexicana* promastigotes with TAMRA labelling already in place are treated with **DDB-PAL** represented as a cartoon chemical structure. This is UV cross-linked to the interacting protein (green) before the CuAAC reaction to attach a fluorophore (AF488, green circle). Fluorescence microscopy imaging enables the overlay to be assessed between TAMRA (known localisation given in Table 8) and AF488 (unknown localisation corresponding to protein target). B. Representative fluorescence microscopy images of 1 slice from a z-stack, from > 3 fields of view, $n > 50$ cells, all images shown with deconvolution of both TAMRA and AF488 channels. Contrast for TAMRA and AF488 is adjusted to optimise visualisation and does not represent relative fluorescence intensities.

Some cell lines suffered a decrease in TAMRA HaloTag labelling efficiency following CuAAC processing (Figure 32B). CPA::Halo lost the expected lysosome localisation giving instead a weak cytoplasmic signal, and similarly Halo::RAB5A retained only dots at the endocytic system with no characteristic lysosome fluorescence. Loss of TAMRA signal corresponding to HaloTag in the lysosome was not unexpected; the CuAAC conditions contain a detergent permeabilisation step which could interfere with the lysosome lipid membrane. However, this means that if **DDB-PAL** localises to the lysosome, no signal would be detected.

The HaloTag cell lines retaining strong TAMRA signal were used for quantification of co-localisation analysis for 10 representative cells of each cell line (as described in Section 6.8.3, results shown in Table 9). Mitochondrial tagged ATOM14 and ALDH, and endoplasmic reticulum (ER) tagged SPT show moderate co-localisation *R* values, with high Manders' coefficients ≥ 0.75 for all. This indicates that while the signal intensities may not correlate well, there is high co-occurrence, but the signal cannot be explained as only mitochondrial or only ER. Cytoplasmic S11 has a high tM_2 of 0.84 therefore majority of the cytoplasm is labelled. This lack of specificity is expected as the compound is likely to enter the cytoplasm, and even if it is not the final target, some low-level, potentially non-specific labelling can occur. Finally, for RAB5A, the high tM_2 of 0.94 but low tM_1 of 0.13 indicates that the majority of the endocytic system contains compound, but the compound is mainly localised elsewhere.

Table 9. HaloTag TAMRA localisation, Pearson's *R* and thresholded Manders' coefficient for cell lines versus AF488 signal

Cell line	Localisation post-CuAAC	Pearson's *R*	tM_1	tM_2
Halo::ATOM14	mitochondrion	0.57 ± 0.14	0.77 ± 0.13	0.80 ± 0.08
ALDH::Halo	mitochondrion	0.46 ± 0.10	0.79 ± 0.08	0.77 ± 0.07
SPT::Halo	endoplasmic reticulum	0.61 ± 0.09	0.90 ± 0.06	0.76 ± 0.06
Halo::S11	cytoplasm	0.59 ± 0.11	0.69 ± 0.09	0.84 ± 0.06
Halo::RAB5A	endocytic system	0.64 ± 0.10	0.13 ± 0.08	0.94 ± 0.10

tM_1 represents overlap of AF488 signal with TAMRA, tM_2 represents overlap of TAMRA signal with AF488.

Four of the HaloTag promastigote cell lines were differentiated to axenic amastigotes for 96 h, after which the retention of HaloTag was assessed with TAMRA ligand. In SPT::Halo, only 12% of cells

were strongly labelled by the TAMRA ligand which suggests a loss of HaloTag following differentiation, while Halo::S11 signal intensity was 3-fold weaker than in promastigotes. AF488 used for CuAAC attachment to these amastigote cell lines treated with **DDB-PAL** generated successful overlay images, with the labelled structure most closely resembling the mitochondrion and endoplasmic reticulum. i.e., ATOM14, ALDH and SPT (Figure 33).

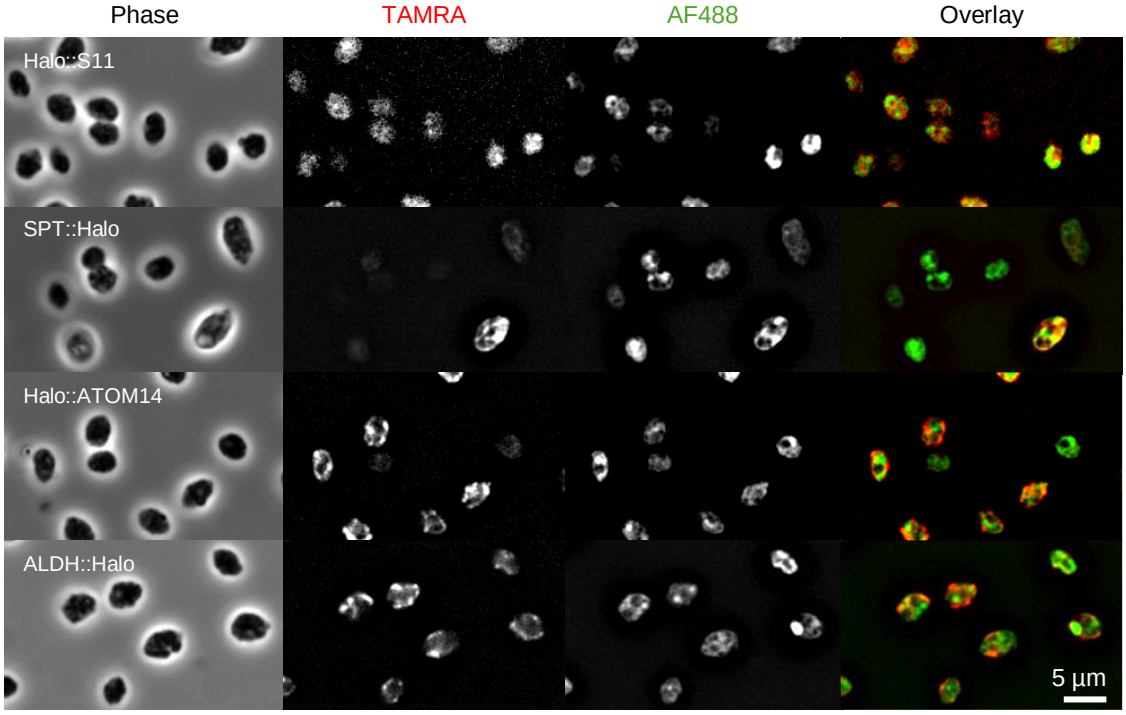

Figure 33. DDB-PAL shows good co-localisation with TAMRA labelled HaloTag mitochondria and endoplasmic reticulum in amastigotes. Representative fluorescence microscopy images of 1 slice from a z-stack, from > 3 fields of view, $n > 50$ cells; all images shown with deconvolution of both TAMRA and AF488 channels. SPT::Halo has only 12% of cells with TAMRA labelling (corresponds to HaloTag retention).

Quantification with labelled cell lines enables assessment of the co-localisation which goes beyond the visual co-occurrence that is readily seen in the deconvolved images. Based on the pattern of fluorescence and the co-localisation quantification, there is compound in the mitochondrion and endoplasmic reticulum for both life cycle stages (Figure 32, Figure 33, Table 9). It is likely that the compound also localises to the endocytic system, as shown by the Manders' coefficient for Halo::RAB5A.

3.3.5 *T. brucei* localisation of DDB-PAL

We sought to identify compound localisation in the related species *T. brucei*, which has comparable **DDB-1** activity. Both bloodstream forms and procyclics were used for this experiment as they have similar organelle structures with a distinctive mitochondrion, which can confirm the localisation seen in *Leishmania*. EdU was a positive control for fluorophore entry to cells and showed good labelling in both life cycle stages (Figure 34). A higher EdU concentration of 100 µM is required, which agrees with the literature.[413]

Click with **DDB-PAL** and image deconvolution as described for *Leishmania* in Section 3.3.2 led to the now familiar reticulated pattern being observed (Figure 35A–B). To save creation of new HaloTag or mNeonGreen tagged cell lines for co-localisation studies, a comparison to published mNeonGreen fluorescent images was made instead. This allows a visual comparison of the localisation pattern, but will not allow for co-localisation quantification as the click reaction will not be carried out on a labelled cell line. TrypTag.org is an extensive database containing the subcellular localisation of mNeonGreen tagged proteins in procyclic *T. brucei*.[405] The **DDB-PAL** pattern in procyclic forms can be attributed to the mitochondrion when compared with images of known mitochondrial protein MCP13 from TrypTag.org (Figure 35C). The AF555 fluorescence labels a linear structure down the anterior cell body but not into the flagellum (white arrow), as is also the case in mNeonGreen tagged MCP13.

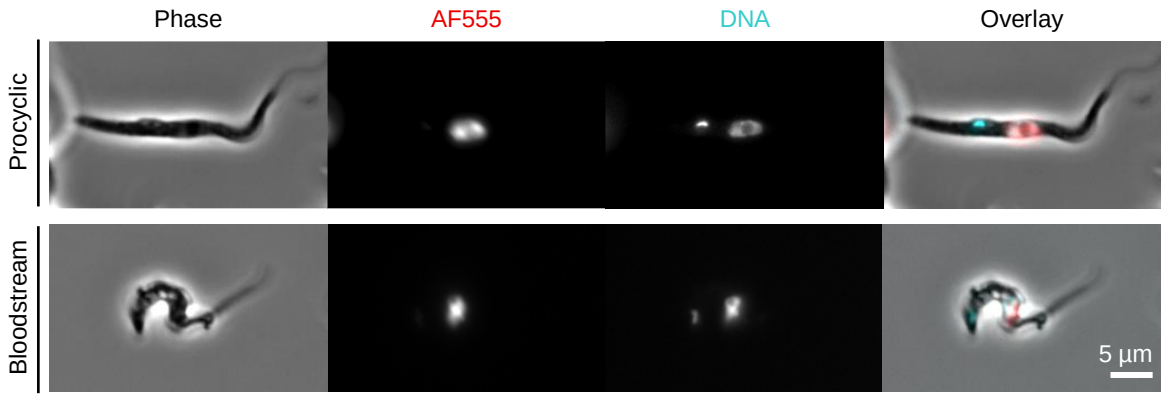

Figure 34. Optimal fluorescence microscopy imaging of CuAAC labelled EdU in *T. brucei* shows localisation to the nucleus with the same reaction conditions as *L. mexicana.* Representative fluorescence microscopy images from > 3 fields of view, $n > 50$ cells. Images show EdU localisation following CuAAC of fluorescent AF555 in procyclic and bloodstream forms, DNA is labelled with Hoechst 33342 (cyan).

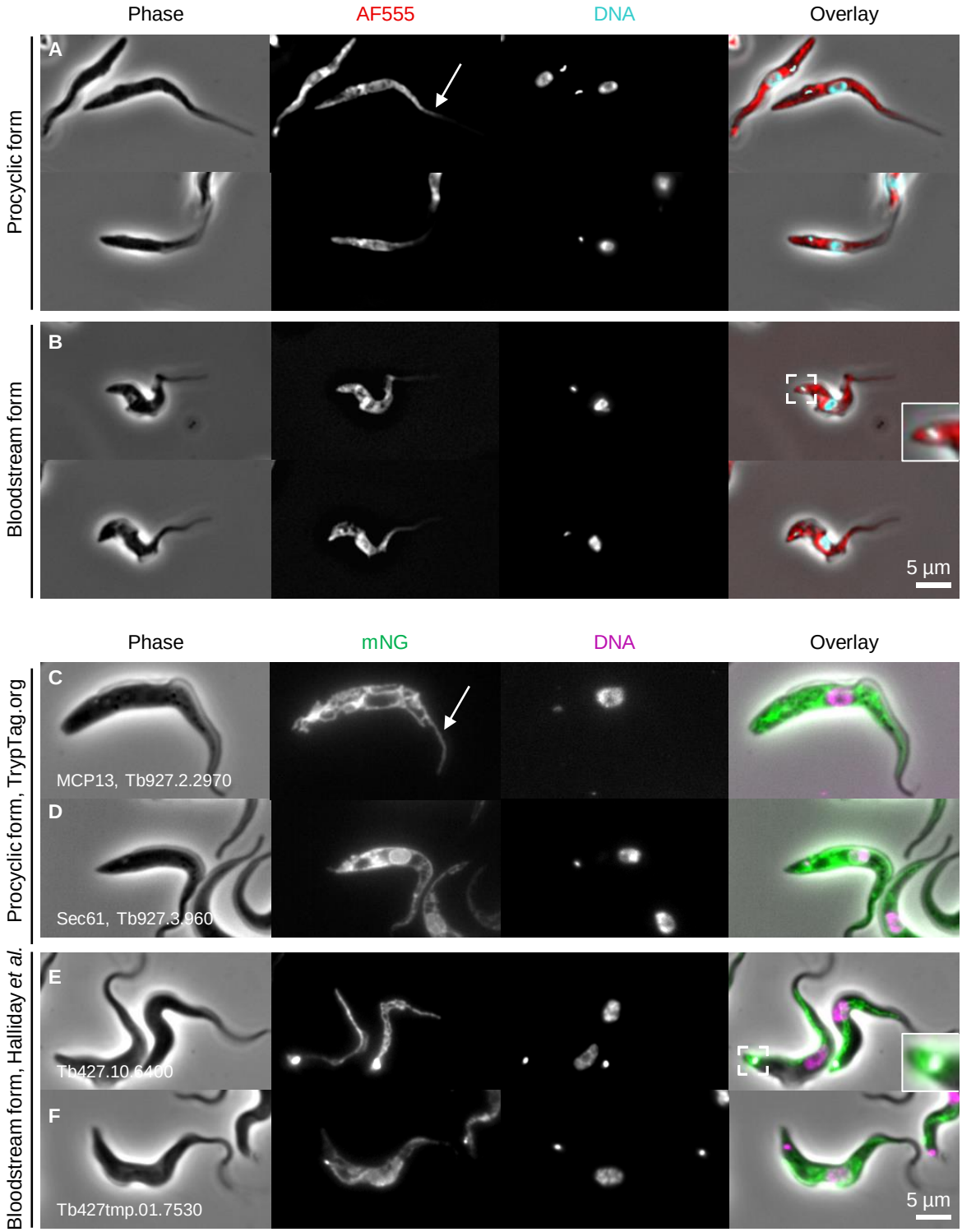

Figure 35. DDB-PAL localises to a reticulated structure in *T. brucei*, likely to be the mitochondrion and the endoplasmic reticulum. A–B. Representative fluorescence microscopy images of AF555 clicked **DDB-PAL** labelled *T. brucei* from > 3 fields of view, $n > 50$ cells, with deconvolution of the AF555 channel. DNA was labelled with Hoechst 33342 (cyan). C–D. Images taken from TrypTag.org.[405] Example of mNeonGreen tagged mitochondrion MCP13 (C) and endoplasmic reticulum Sec61 (D) proteins. E–F. Images taken from the literature.[64] Example of mNeonGreen tagged mitochondrial Tb427.10.6400 (E) and endoplasmic reticulum Tb427tmp.01.7430 (F) proteins. Extension of mitochondrion towards the anterior cell tip is indicated with white arrow in procyclic forms (A, C). 3× zoomed inset in the overlay shows overlap of AF555 signal and kinetoplast (B), or overlap of mNeonGreen and kinetoplast (E).

There is likely to also be ER labelling as was the case with *L. mexicana*. Various ER subdomains exist in *T. brucei*, with appearances ranging from more nuclear envelope/cisternal, to more reticulated.[405] The AF555 signal lacks the characteristic peri-nuclear nuclear envelope labelling illustrated by mNeonGreen tagged ER protein Sec61 from TrypTag.org (Figure 35D), but contributions could be coming from a more reticulated-type ER compartment.

In bloodstream forms, a selection of mNeonGreen tagged proteins analogous to the TrypTag.org database have been published.[64] The simplified bloodstream form mitochondrion appears as a line along the cell body with very few branches or reticulation when mNeonGreen tagged (Tb427.10.6400, Figure 35E). The AF555 labelling goes beyond this (Figure 35B), encompassing the majority of the cell body with reticulation. There is still mitochondrial labelling based on the overlap of kinetoplast and AF555 signal (inset in overlay, Figure 35B), and the extended reticulation is likely to be the bloodstream form ER when visually compared to the published mNeonGreen tagged ER protein Tb427tmp.01.7430 (Figure 35F).

3.4 Transmission Electron Microscopy

To improve the resolution of compound localisation beyond the capabilities of fluorescence microscopy, we turned to transmission electron microscopy (TEM). We chose to use the immunogold route from the two approaches previously introduced (Section 1.6.1.3) as this was expected to be more straightforward than the DAB method, whose optimisation would go beyond the scope of this compound localisation project.

3.4.1 Resin embedding for CuAAC gold labelling

For TEM, samples must first undergo processing which typically involves cell fixation, embedding into a resin, sectioning with an ultramicrotome, capturing on a grid and finally heavy metal staining to add contrast. In traditional immunogold labelling, the embedding resin is acrylic-based which is permeable to the antibody gold conjugates, whereas epoxy resins are preferred where permeability is not a requirement as they are better at preserving cell ultrastructure.[414, 415] We have already

established a reliable protocol for cross-linking and CuAAC of **DDB-PAL** to a fluorescent azide (Section 3.3.2). To combine this with TEM, we replaced the fluorescent azide with gold azide which will allow TEM detection of electron-dense gold. The gold azide reagent is comprised of gold nanoparticles covalently functionalised *via* sulfide or amide bonds to polyethylene glycol-based linkers containing an azide. We carried out CuAAC of cells treated with **DDB-PAL** or positive control EdU, with gold azide at two different points in the sample preparation: 1. Pre-embedding CuAAC which then undergoes epoxy resin embedding with the gold already in place, or 2. Post-embedding CuAAC, in which a relatively permeable acrylic resin is used, followed by CuAAC once the sample is mounted to TEM grids. This follows the sample processing workflow shown for **DDB-PAL** (Figure 36A), and the same for EdU without the UV cross-link step. We expect to see the gold nanoparticles appearing as electron-dense circular spots in the nucleus and kinetoplast for EdU, and in the mitochondrion and ER for **DDB-PAL** treated samples. There were varying levels of gold in each of the embedding approaches, but none was successful even following some optimisation (Figure 36B–I).

In the pre-embedding click experiment, we sought to optimise two parameters during the CuAAC step: sample permeabilisation, and choice of gold azide. Permeabilisation of samples is vital to allow access of the CuAAC reagents to the intracellular alkyne of **DDB-PAL**, particularly as the 10 nm gold azide used is approximately 10 times larger than AF555 azide. However, harsh detergents can damage the ultrastructure visible by TEM. To optimise the permeabilisation step, 1% NP-40 or 0.1% saponin incubation was used (described in detail in Section 6.9.2). The 0.1% saponin treatment was milder and cells retained intact outer membranes, while 1% NP-40 caused destruction of cell membranes and some loss of cytoplasmic material (Figure 36J–K, position of outer membrane indicated with an arrow). No gold was present in the TEM images for samples prepared with either permeabilisation agent. Due to concerns about the poor permeability of the CuAAC reagents, 1% NP-40 detergent was chosen despite the cost to sample quality. Three different gold azide suppliers were used: two 10 nm nanoparticles and one 5 nm nanoparticles, to investigate the quality of gold azide and the effect of nanoparticle size.

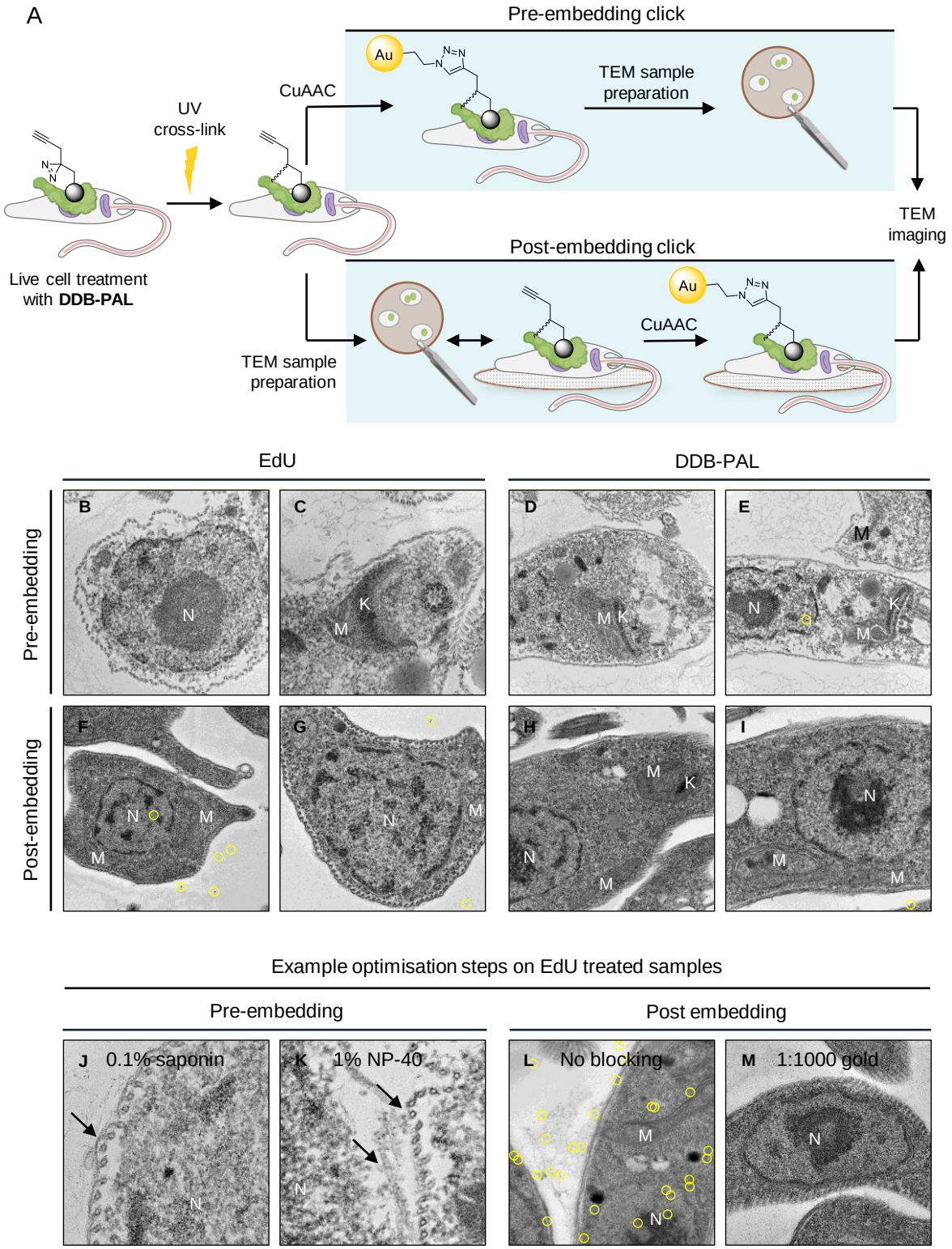

Figure 36. Pre-embedding and post-embedding click with gold azide for TEM was unsuccessful at generating specific gold labelling. A. Workflow for sample processing for pre-embedding and post-embedding click. *L. mexicana* promastigotes are treated with **DDB-PAL** represented as a cartoon chemical structure. This is UV cross-linked to the interacting protein (green) before the CuAAC reaction to attach gold nanoparticles (Au, yellow). B–M. Representative TEM images of *L. mexicana* showing gold (yellow circles). Nucleus (N), kinetoplast (K) and mitochondrion (M) are labelled. B–I. Samples prepared with optimised conditions 1% v/v NP-40 permeabilisation, 1% BSA blocking buffer, 1:30 dilution of 10 nm gold azide (Cytodiagnostics). J–M illustrate discoveries during optimisation. None of the images are labelled as expected.

Gold azide was used at a 1:30 dilution, which is the approximate molar equivalent of the fluorophore previously used in Section 3.3.2. TEM images showed a low level of non-specific gold labelling independent of supplier; 10 nm azide from Cytodiagnostics was used going forward for consistency with other ongoing experiments. A blocking buffer of 1% bovine serum albumin (BSA) was used in all cases to prevent off-target binding of the gold azide. Use of these "optimised" conditions showed no gold labelling in the expected organelles in any of these attempts for EdU or **DDB-PAL**. (Figure 36B–E). It is plausible that even if the click reaction does proceed, the gold nanoparticles could be lost during downstream processing. This could be due to a breaking of the bonds that link the gold to the azide, or a displacement of the gold during the multiple resin exchanges of sample embedding.

Having no success with the pre-embedding click, we attempted optimisation of the post-embedding click on prepared copper grids (described in detail in Section 6.9.3). This is easier and quicker than optimising the pre-embedding click as the more complex sample preparation is done on a uniform **DDB-PAL** treated sample. Optimisation of the CuAAC step then only requires 1 grid per condition, as opposed to pre-embedding in which each condition requires independent sample preparation. Three key parameters: permeabilisation, blocking buffer, and concentration of gold azide were varied combinatorially. To test permeabilisation, 1% NP-40 or 0.1% Triton-X were used. Both are quite aggressive conditions due to concerns about the permeability of the gold nanoparticles into the resin and then into the sample. There was no apparent difference between the two reagents: 1% NP-40 was chosen as this is consistent with the already established CuAAC of fluorescent azide. The blocking buffer was varied as this will play a key role in ensuring no off-target attachment of gold nanoparticles to the sample or the resin. Three different blocking buffers: 1% BSA, 0.1% BSA, and 0.5% fish gelatin, alongside no blocking buffer i.e., just phosphate buffered saline (PBS) were used. A blocking buffer is necessary; with no blocking there was non-specific gold in the TEM images indiscriminately across the cells and resin (Figure 36L). 1% BSA worked best as fewer gold particles appeared in the resin background (outside the cell) than with the other blocking buffers. The concentration of gold azide in the CuAAC mixture was used at 1:30 or 1:1000 dilution. TEM images from the 1:1000 dilution had no gold, so this is too dilute (Figure 36M). 1:30 dilution with

1% BSA blocking buffer and 1% NP-40 permeabilisation gave the best amount of gold in the TEM images. However, in all cases there was no specific gold labelling of the expected organelles for either alkyne substrate (Figure 36F–I). As an extra control, the various fixatives, blocking buffers and permeabilisation reagents were confirmed not to interfere with the **DDB-PAL** alkyne by using some samples for a parallel CuAAC with fluorescent azide. Subsequent fluorescence microscopy confirmed the expected localisation for all optimisation conditions.

3.4.2 Tokuyasu for CuAAC gold labelling

The milder but more technically complex Tokuyasu sample preparation technique was used instead of resin embedding as the resins could be a barrier to CuAAC reagent permeabilisation. Tokuyasu is a cryopreservation-based technique that maintains cell structural integrity by freezing the sample in a sucrose cryo-protectant, producing grids that are thawed and used for immunolabelling.[416, 417] Three different CuAAC approaches were attempted, which will maximise the chances of success by using different types of gold reagent, each with a different stability and permeability (Figure 37). In the first instance, we carried out CuAAC of 10 nm gold particles to only EdU-treated samples immobilised on grids as this should have a known localisation to the nucleus and kinetoplast.

First, direct gold attachment *via* CuAAC of gold azide was attempted as was previously done with resin-embedded samples. This resulted in a high level of gold labelling, particularly outside cells which could be due to poor blocking or promiscuity of the gold azide (Figure 38A). Dilution of the gold azide from 1:30 (as optimised for resin-embedded samples, Section 3.4.1) to 1:1000 did not improve labelling sensitivity.

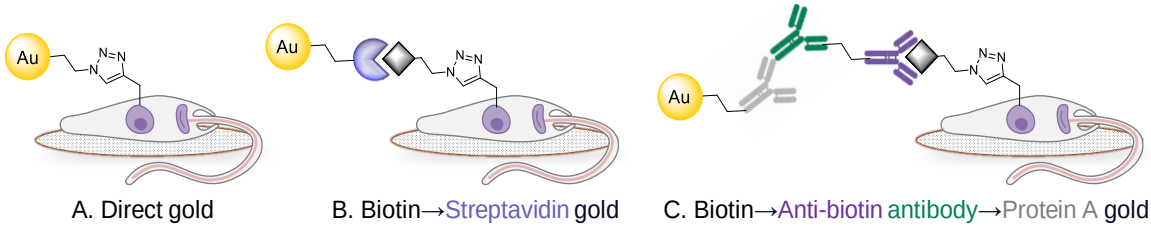

Figure 37. Photoaffinity labelling and gold CuAAC approaches to detect intracellular alkyne. *L. mexicana* promastigotes containing alkyne are linked to gold nanoparticles (Au, yellow) *via* direct CuAAC of gold azide (A), CuAAC of biotin and detection with gold–streptavidin (B), or CuAAC of biotin, primary detection with anti-biotin antibody and secondary detection with Protein A gold antibody (C).

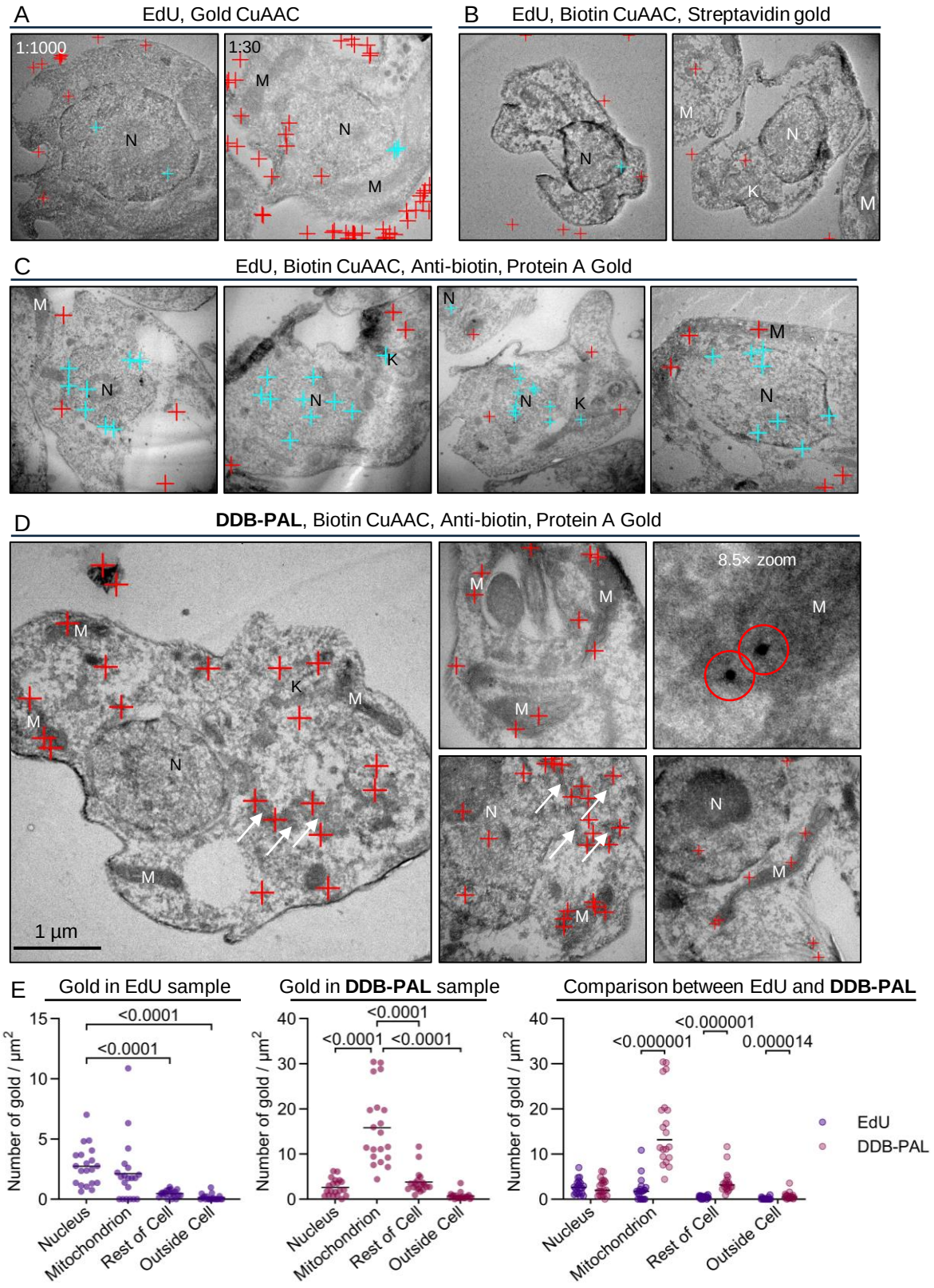

Figure 38. TEM observed gold is as expected for Tokuyasu sample preparation with antibody detection. A–D. Representative TEM images from $n = 2$ independent replicates; kinetoplast (K), mitochondrion (M) and nucleus (N) are labelled, white arrows indicate endoplasmic reticulum. Direct gold click (A) or biotin click and streptavidin–gold detection (B) did not work; two-step antibody detection was successful (C–D). A–C. Gold is indicated with a cross in cyan for expected localisation (nucleus and kinetoplast), red for incorrect localisation D. Gold labelling of **DDB-PAL** is indicated by a red cross or circled (8.5× zoom). E. Number of gold per region for treated samples from $n = 20$ images; statistical significance derived from multiple Mann-Whitney U tests, $P < 0.05$ shown. Comparisons are: EdU only, **DDB-PAL** only, and between the two.

Second, CuAAC of biotin azide was detected with streptavidin–gold conjugates. The resultant TEM images had less gold than the direct gold azide click, however there was no specificity: gold particles were randomly distributed, equally prevalent within the cells as outside (Figure 38B). Third, CuAAC of biotin azide but this time followed by a two-step detection using rabbit anti-biotin antibody followed by Protein A gold antibody. Only in this method were gold particles detected specific to the nucleus, as expected for EdU treated samples (Figure 38C). This result is likely due to the amplification effect achieved by using antibodies, and the possibility that the detectable marker is more accessible as it is now a further distance from the initial alkyne.

Having established the antibody system for EdU treated cells, CuAAC and detection of samples treated with **DDB-PAL** was then carried out with the same conditions (Figure 38D). Biotin azide for the CuAAC was used at 5 μM (the same as for the fluorescent azides), an increase to 2× or 4× did not improve labelling. The primary anti-biotin antibody dilution was optimised to be 1:2500, and the secondary Protein A gold diluted 1:20. Visually there is high labelling of the endoplasmic reticulum which appears as a membrane structure often close to the nuclear envelope (white arrows in images) as well as mitochondrial labelling with **DDB-PAL**. The gold was quantified in a semi-automated manner and counted within the cellular compartments of interest (Figure 38E). As the endoplasmic reticulum cannot be easily and consistently outlined, this organelle was not included and fell under the "rest of cell" category. Any label in the kinetoplast was classed under mitochondrion as this was difficult to unambiguously assign. In the EdU treated sample, there was significant labelling of the nucleus compared to the rest of the cell and the surrounding grid. The **DDB-PAL** sample had significant mitochondrial labelling when compared with the other compartments within the cell, and also compared to the mitochondrial labelling of EdU which serves as a negative control.

3.5 Discussion

These data provide an investigation of **DDB-1** localisation using microscopy in *L. mexicana* and *T. brucei*. We hypothesised that the compound would localise to the mitochondrion due to the biochemical assays in *L. infantum*[320] and *L. mexicana* showing mitochondrial disruption (Section

2.9.2) and the fact that small molecules with direct target binding will localise to the target. We show here that the compound indeed localises to the mitochondrion, as well as the endoplasmic reticulum and endocytic system. These results come from extensive fluorescence microscopy experiments including co-localisation analyses with known organelles, and are further supported by TEM imaging.

3.5.1 DDB-PAL mainly localises to the mitochondrion

DDB-PAL localises to the mitochondrion of *L. mexicana* promastigotes and axenic amastigotes, evidenced by overlap with the kinetoplast signal and co-localisation imaging (Figure 28, Figure 30, Figure 32, Figure 33). The labelling in *T. brucei* is almost identical to *L. mexicana* which is expected as organelles in the two species are relatively well conserved.[418] Additionally, the **DDB-PAL** fluorescence is structurally similar to the 3D mitochondrion of *L. mexicana* reconstructed from volume electron microscopy imaging by Hair *et al.*[419] Analogous labelling experiments with an alkyne small molecule clicked intracellularly to a fluorophore in *T. brucei* have been carried out by the Yao lab, their probes were efficiently taken up in both procyclics and bloodstream forms, and show lysosomal and/or cytoplasmic localisation.[398-400] **DDB-PAL** represents the first mitochondrial localisation of a PAL and click approach in these species.

The labelling is highly specific, reproducible and the corresponding organelles are validated with co-localisation. The pattern can all be considered "real" signal and not due to off-target labelling caused by the minimalist linkers; Li *et al.* describe negligible background labelling with these systems.[244] Fluorophores in close proximity can undergo Förster Resonance Energy Transfer (FRET) if the emission wavelength of one overlaps with the excitation of the other,[420] but this is not the case for the co-localisation experiments here as care was taken not to have overlapping fluorophore wavelengths. We can therefore consider the observed localisation as a reliable representation of the intracellular location of **DDB-1**, and infer MoA accordingly.

3.5.1.1 Implications of mitochondrial localisation

Numerous drugs are known to target the mitochondrion of eukaryotes, particularly in a mitochondrial protective context. These are often intended to exert an anti-oxidant effect by neutralising ROS, such as MitoQ[421] and SkQ1[422] which prevent mitochondrial oxidative damage by scavenging ROS. Szeto-Schiller (SS) small cell-permeable peptides such as SS-31 selectively target the inner mitochondrial membrane and reduce ROS, prevent mitochondrial depolarisation, and improve mitochondrial respiration.[423] Conversely, there are a limited number of examples where the drug is designed to cause mitochondrial damage and lead to cell death, as would be the case for **DDB-1**. Bisphosphonium salts are known to accumulate in the mitochondrion, and are proposed to inhibit complex II in *Leishmania*,[181] and ATP synthase in *T. brucei*.[182] MitoTam, a mitochondrial targeted derivative of tamoxifen has been applied to drug repurposing against *L. mexicana* and *T. brucei*, demonstrating lowered ATP levels, disrupted inner mitochondrial membrane and cell death.[424] The authors who investigated MitoTam MoA propose either an inhibition of ATP synthase or a disruption of mitochondrial membrane integrity. **DDB-1** could be acting in a comparable way to MitoTam, as it similarly accumulates in the mitochondrion, is active against both *Leishmania* and *T. brucei* bloodstream forms, and shares many of the biochemical changes reported in *T. brucei*.

Mitochondrion targeting compounds are often lipophilic and positively charged, which drives accumulation in the negatively charged mitochondrial matrix by taking advantage of the mitochondrial membrane potential. For example, MitoQ and SkQ1 are linked to a triphenyl phosphonium cation, rhodamine 123 mitochondrial dye is positively charged, and F16 is a lipophilic small molecule with delocalised positive charge.[425] The structure of **DDB-1** does not contain any delocalised positive charge. At physiological pH, the morpholine ring tertiary amine could be protonated to some extent, however we would not expect this to be sufficient to drive the mitochondrial localisation. Therefore, the observed localisation is not an artefact of positive charge causing accumulation, but indicates that an uptake mechanism must be in place to allow transport across the mitochondrial membrane, which could allow interaction with a mitochondrial target, supporting the hypothesised mitochondrial MoA.

3.5.1.2 Other cellular localisations

Aside from the mitochondrion, the compound also localises to the ER, given the high overlap coefficient for known ER signal with labelled **DDB-PAL** (Table 9), and the *T. brucei* bloodstream form reticulated labelling (Figure 35). The ER is a continuous structure comprised of different domains including the nuclear envelope, from which it radiates out into the intracellular space, and is also closely associated with the sub-pellicular microtubules at the cell surface.[419, 426, 427] It is a heterogenous organelle with the smooth and rough ER having varied components, but being particularly indistinguishable in *Leishmania*.[55, 426] It is unclear whether the **DDB-PAL** labelling corresponds to the complete mitochondrion and ER, or just parts of both as is suggested by the overlap coefficients, and what implications this has on MoA. Both these organelles are Ca^{2+} stores, therefore proteins involved in calcium signalling could be potential interaction partners, especially as **DDB-1** induces a release of Ca^{2+} (Section 2.8.2) and a slight alkalinisation of the acidocalcisomes in *L. infantum*.[320] This is an indirect effect however, as **DDB-1** itself does not localise to the acidocalcisomes.

3.5.1.3 DDB-1 uptake and accumulation

Fluorescence labelling can be used to monitor compound uptake as well as overall localisation. **DDB-PAL** co-occurs with Halo::RAB5A which is localised to the early endocytic system, where cargo from the cell surface is initially transported to for sorting.[428, 429] **DDB-PAL** is likely to enter cells *via* the canonical eukaryote endocytic pathway, and then be transported to the early endocytic system. It is unclear what fate the compound then faces.

Lysosome labelling of CPA::Halo, and the lysosomal region of Halo::RAB5A cell lines completely disappeared after CuAAC (Figure 31), so there is a differential effect on the lysosomes and early endosomes from the fixation, permeabilisation or CuAAC protocol. It is also plausible that **DDB-PAL** itself causes the loss of lysosomal signal by a disrupting the lysosome. In order to test this hypothesis, the fluorescence microscopy imaging could be carried out on the lysosome tagged cell lines treated with **DDB-PAL** but without proceeding with the CuAAC reaction, to check if the

TAMRA-labelled lysosome remains intact. However, due to the presence of intact lysosomes visible in the **DDB-PAL** treated TEM images, it is more likely that the lack of fluorescence is due to sample processing for fluorescence microscopy and not a direct result of compound action, therefore the described follow-up experiment was not done. **DDB-PAL** could proceed to a lysosomal degradation pathway after endocytosis, but due to the sample preparation for fluorescence microscopy, this cannot be visualised. There did not appear to be a particular concentration of gold labelled **DDB-PAL** in the lysosome by TEM which could indicate that the lysosome does not feature as an organelle of compound concentration.

Inherently fluorescent pentamidine analogues accumulate *via* two distinct rises in drug concentration up to approximately 12-fold the initial internalised concentration.[430] "Off-target" accumulation is visualised in acidocalcisomes and other perinuclear organelles after 2 hours of treatment, and comparable results are obtained with pentamidine analogues in *L. donovani*.[176] These examples are superior for uptake monitoring: inherent fluorescence allows consistent imaging of live cultures without the need to biologically fix at discrete time points as is required for **DDB-PAL** click-mediated visualisation. Attempts to attach a fluorophore directly to the active scaffold of **DDB-1** for live cell imaging were synthetically challenging and caused a loss of compound activity, therefore this route was abandoned. Information about **DDB-1** uptake instead has to be extrapolated from the imaged timepoints. **DDB-PAL** labelling is unchanged from 5 minutes up to 6 hours in both fluorescence pattern and intensity. This quick uptake is consistent with published fluorescence imaging of other compounds in *Leishmania* visualised 5 – 10 minutes after treatment,[55, 431, 432] and suggests that **DDB-1** quickly establishes an equilibrium between import and clearance from cells, but does not give insight into the nature of this equilibrium. The imaging does not show accumulation over time apart from the increase at 1 h discussed previously (Section 3.3.2), contrary to the suggestion of a minimum compound threshold proposed in Section 2.9.1.2. The spread of the data is consistent across the timepoints (Figure 28) with an approximately 3-fold range in fluorescence intensity – if there is a threshold at play then it must be within this 3-fold range to allow some minimal cell division while killing the majority of the culture.

3.5.2 PAL is necessary for visualisation of the DDB compounds

Microscopy can provide a helpful tool to aid in drug discovery projects, as compound localisation can inform on compound mode of action, an approach that is often underexplored. In special cases where the active chemical compound is inherently fluorescent, it would be trivial to carry out imaging experiments as there is valuable information to be gained. This is exemplified by fluorescent analogues of the drug pentamidine that localise to the mitochondrion and kinetoplast in *T. brucei* and *L. donovani*, in keeping with the pentamidine MoA blocking replication of kDNA.[176, 430]

However, for many compound families, inherent fluorescence is unlikely to be the case as it depends on a particular chemical structure. The main drawback to visualising localisation is then the requirement for comprehensive SAR knowledge of the compound family, to inform on locations tolerant to handle attachment. This approach is therefore only suitable for compound families that can be easily synthesised and/or modified to rapidly generate analogues for SAR studies. Once this information is known, synthetically easiest is the addition of an alkyne handle to the small molecule for click modifications without requiring PAL. Most examples of direct attachment of small molecules to target proteins without PAL rely on the intrinsic chemical reactivity of the compound acting as covalent modifiers. Compounds would therefore require an electrophilic trap such as a Michael acceptor or β-lactam, or a way to generate an electrophile *in vivo*.[433] **DDB-1** has no obvious electrophilic motifs, and it is hard to propose a sensible biotransformation to yield one, so it was likely that PAL would be necessary for compound visualisation. Indeed **DDB-yne** showed no significant labelling (Figure 26), and **DDB-PAL** is washed out if PAL is not carried out (Figure 28). The requirement for an analogue containing a photoaffinity cross-linkable and clickable handle to allow compound attachment and visualisation as with **DDB-PAL** is likely to be the case for most compound families. This strategy requires the challenging synthesis of a linker containing a photo cross-linkable warhead such as a diazirine to attach to the active compound. Whilst there is a benefit to the localisation information, this does not necessarily outweigh the significant technical challenges of preparing a PAL-compatible analogue. We recommend only undertaking this approach where

there is a need for extra MoA information such as where other MoA determination methods have failed, or if the analogue is to be used in conjunction with chemo-proteomics experiments.

The **DDB-PAL** TEM results are consistent with the labelling pattern observed by fluorescence microscopy. This followed a thorough investigation of TEM sample preparation compatibility with CuAAC. Although successful, the technically complex Tokuyasu sample preparation technique must be used in this application, rendering it unfit as a standard MoA determination method. Disappointingly, we could not visualise with confidence a higher resolution localisation within the mitochondrion as had been the intention of this experiment. Further optimisation would be required to achieve higher-density labelling that could allow this resolution. It could be that the **DDB-PAL** mitochondrial labelling is a limitation, and a different localisation could provide better answers. Nevertheless, we achieved the first example of TEM applied to clickable small-molecule drugs.

The biological result that **DDB-1** lacks covalent activity necessitated PAL for visualisation, but is beneficial to its potential use as a drug candidate. Covalent binding drug hits are often considered undesirable as they can exhibit poor specificity, leading to false positives.[434] Although there has been a resurgence in interest in covalent modifiers in recent years, they are still treated somewhat with caution.[435] The result agrees with the previously discussed glutathione experiment (Section 2.8.3) that **DDB-1** is not a covalent binder. We confirmed that **DDB-1** localises to the mitochondrion and could additionally be localising to the ER and the endocytic system. On this basis, **DDB-1** is likely to have a mitochondrial MoA, an ER target remains a possibility, while the endocytic system localisation is probably associated with compound uptake, and does not represent the final site of action. With the photoaffinity labelling compound **DDB-PAL** in hand, we turned to chemo-proteomics pull-down experiments, and anticipate that mitochondrial proteins will be identified.

4 Advanced cell biology: Omics approaches

This chapter details studies of genomics, transcriptomics and proteomics approaches that were applied to **DDB-1** and **Asci** in order to elucidate MoA. Experiments with genome-wide trypanosomatid libraries (Section 4.2.2 and Section 4.2.3) and the *L. donovani* resistance library (Section 4.2.4) were carried out by myself under the supervision of Dr Sandra Carvalho, while hosted for a short research placement in the Wyllie (Mode of Action) group, University of Dundee. Resulting DNA from these experiments was sequenced by Beijing Genomics Institute (BGI), Hong Kong, and bioinformatics analysis carried out by Dr Sandra Carvalho and Dr Michele Tinti at the University of Dundee. Subsequent evaluation of the results is my own work. Biological activity data against mammalian HepG2 cells (Table 10), and metal chelation data against *L. donovani* (Section 4.3.3.2) was provided Dr Sandra Carvalho. The on-beads protein pull-down experiment described in Section 4.4.1 was carried out by PhD student Ludwig Bauer in the Huber group, Target Discovery Institute, University of Oxford. All other experimental and analysis work in this chapter is my own.

4.1 Introduction

Omics approaches have a strong track record of success in MoA deconvolution, therefore we anticipated these to be successful for **DDB-1** and **Asci** MoA investigations. Genomics experiments make use of the readily available published genomes of *L. mexicana* and *L. donovani*,[82, 436] such that comparisons can be made between the genomes of *in vitro*-generated resistant cell lines and the susceptible wildtype cell line, to identify genetic mutations that are beneficial to survival. Similarly, changes to the transcriptome in response to compound can identify key genes implicated in compound activity. These two approaches should inform on genes involved in both MoA and mechanisms of resistance. Chemo-proteomics experiments will make use of the PAL compound **DDB-PAL**, which provides an opportunity to search for directly interacting proteins. By combining evidence from each unbiased approach, we aim to build a comprehensive picture of MoA.

4.2 Genomics approaches to MoA discovery

Traditionally, MoA genomics experiments involve generating resistance to a compound and then whole genome sequencing (WGS) of the resulting cell line. We intend to use this alongside Mut-Seq (introduced in Section 1.6.2.1) which will accelerate the resistance cell line generation. Results from this experiment should identify genetic mutations that result in a fitness gain, which informs on mechanisms of resistance – often informative to MoA. In addition, a collaboration with the Wyllie (Mode of Action) group at the University of Dundee enabled me to access specialist overexpression, knockdown, and resistance trypanosomatid libraries. These libraries are specifically designed for MoA studies so should fast-track identification of genes implicated in the activity of the compounds. Hits from the libraries presented here were not independently validated due to time constraints.

4.2.1 Generation of resistant lines and WGS

The aim is to apply compound selection pressure to *L. mexicana* cultures to generate **DDB-1** resistance, so that genes involved in compound resistance can be identified. Cultures are considered resistant to a compound if they can sustain growth at prolonged exposure to > 10× EC_{50}.[261] Mut-Seq was run in parallel with traditional resistance generation from a wildtype cell line in order to accelerate resistance generation. Two mutagens: ethyl methanesulfonate (EMS) and *N*-ethyl-*N*-nitrosourea (ENU) were chosen for the Mut-Seq experiment as these have high reported levels of mutagenicity and performed well in *L. infantum* experiments.[280] A *L. mexicana* promastigote clonal cell line was grown under standard conditions (described in Section 6.1.1) with additional 40 mM EMS or 4 mM ENU for 6 h. Following the mutagenesis period, cells were washed twice in fresh media and then grown for a further 24 h under standard conditions which constitutes a recovery period. This recovery period ensures cell cultures have reached stable growth following mutagenesis, before a further pressure of compound selection is applied. I observed that ENU was a harsher mutagen; cultures were consistently at a lower cell density after the 24 h recovery than EMS mutagenised cultures. I used three different methods of **DDB-1** selection on each mutagenised culture alongside the un-mutagenised wildtype cells.

First, selection from a low, sub-lethal concentration of compound which is then increased step-wise until resistance is achieved. This is a routinely applied method and has been the most successful in trypanosomatids.[437] Cultures were grown under standard conditions for a minimum of two passages in 3 µM (0.6× EC_{50}) **DDB-1**, before this was increased approximately 2-fold once cells displayed exponential growth. At 20 µM (4× EC_{50}), cell growth slowed and then stopped after the first few passages, therefore the concentration was decreased back to 10 µM (2× EC_{50}), and a slower concentration increment attempted (Figure 39A). However, no cells survived in prolonged exposure to 20 µM **DDB-1** (4× EC_{50}).

Second, a harsher "shock" selection at high **DDB-1** concentration was attempted. This has proven successful in *T. brucei* [438] and *L. donovani*,[439] and is relatively quick so was deemed worth trying. Cultures were maintained with **DDB-1** at 20, 50, or 100 µM (i.e., 4×, 10×, or 20× EC_{50}); in all cases there was no cell growth. Cultures were incubated for up to one month to await cell emergence but no cells survived the treatment. Alternatively, cells were replenished with fresh media every two to three days maintaining a high **DDB-1** concentration, with or without 10% extra foetal calf serum to encourage growth, however no cells remained alive beyond three media replacements.

Third, inspired by Bhattacharya *et al.*, cells were grown in 96-well plates at 30 µM **DDB-1** (6× EC_{50}), mimicking their successful 5× or 10× EC_{50} growth on agar plates.[280] After two to three weeks, wells

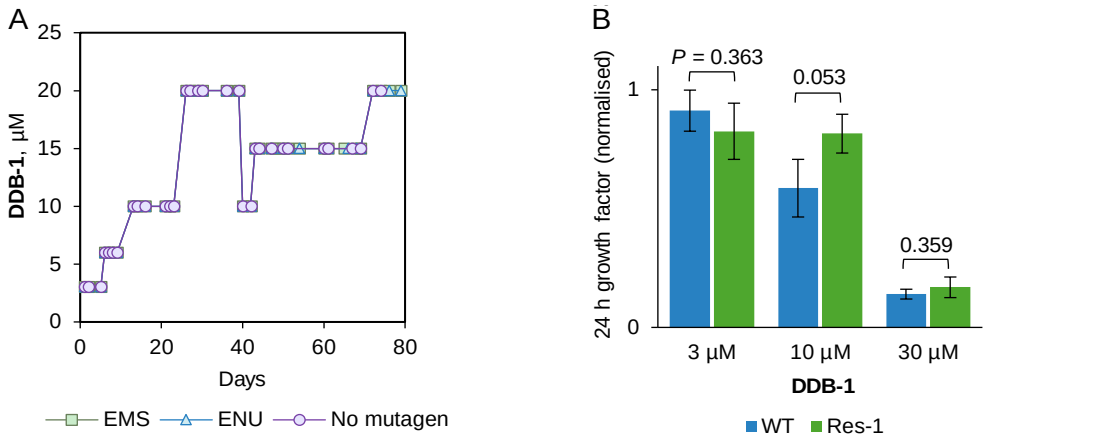

Figure 39. It is not possible to achieve *L. mexicana* promastigote resistance to **DDB-1**. A. Culture over time under the continuous pressure of **DDB-1** starting with pre-mutagenised cultures (EMS, ENU) or un-mutagenised wildtype cells (No mutagen). B. 24 h growth factor for **DDB-1** is unchanged in the "desensitised" cell line Res1. Mean ± SD, $n = 3$. Statistical significance was derived from a two-tailed *t*-test.

that emerged last were transferred to flask culture, with the rationale that these are most likely to be resistant (in our experience cells resistant *via* transfection often emerge last). The 12 "desensitised" cell lines – six each from EMS and ENU – emerged in individual wells so could plausibly be clonal. Clonal cell lines are more desirable, as the downstream genomic data will be easier to interpret. Activity for one of the ENU "desensitised" cell lines (Res-1) was compared with the wildtype, showing only a non-significant desensitisation to **DDB-1** at 10 µM and no change at 30 µM (6× EC_{50}) (Figure 39B).

WGS of the 12 "desensitised" mutant cell lines and the parental clone was carried out by BGI genomics. From the resulting data, we identified mutations in the protein coding sequence which correspond to synonymous SNPs, non-synonymous SNPs and new stop codons. Genes were prioritised if they were mutated in at least 3 of the 12 mutants, with either no synonymous SNPs or a ratio of > 2 non-synonymous:synonymous SNPs. This ratio is commonly used in evolutionary biology, based on the principle that the accumulation of non-synonymous SNPs indicates a beneficial change, while the accumulation of synonymous SNPs indicates a benefit for the protein sequence to remain unchanged. The resulting genes were filtered using TriTrypDB for: 1. Orthologs in both *L. infantum* and *L. donovani* since the compound family is active in these species, and 2. > 5 transcripts per million in the sequencing data to only consider proteins expressed at an appreciable level. We identified 27 protein coding genes from this screen, including two with orthologs linked to parasite-drug interactions in the literature: LmxM.08.1040 peptidase has a *T. brucei* ortholog that is linked to suramin susceptibility,[291] and LmxM.20.1185 cysteine peptidase orthologs are downregulated in antimony resistant *L. amazonesis*.[295] The pattern and identity of SNPs was almost entirely identical across the 12 different clones even though they arose from two different mutagens. This information coupled with the lack of a significant activity shift in the Res-1 cell line implies a weak compound selection, and therefore the WGS results are detecting non-lethal SNPs caused by the mutagens, instead of those conferring a fitness advantage to **DDB-1**. Due to the lack of truly resistant clones and the SNPs being non-specific, these genes were not analysed further.

I was unable to generate resistance to **DDB-1** despite employing both traditional resistance generation and Mut-Seq with three different compound selection protocols. This could indicate multiple targets i.e., polypharmacology, therefore it is hard to select resistance for all in combination. Failed resistance generation is often observed in a metal chelation MoA,[207, 208] presumably due to the essential and varied function of metal cations in cells. Alternatively, this result implies an essential target that cannot tolerate mutations or be mutated in a way to circumvent **DDB-1** activity.

4.2.2 Genome-wide overexpression libraries

In collaboration with the Wyllie lab at the University of Dundee, I carried out screening of **DDB-1** and **Asci** against their trypanosomatid overexpression libraries. This will identify any genes that, when overexpressed, lead to a fitness gain: these are likely to encode proteins carrying out drug efflux and degradation, or protein targets that the drug inhibits. This first required an in-house EC_{50} determination for these compounds against *L. donovani* promastigotes, amastigotes, *T. brucei* bloodstream forms and toxicity against mammalian HepG2 cells using their standard resazurin-based assay.[276] **DDB-1** is active against both parasites as expected (Table 10) although against *T. brucei* it is 6-fold more toxic than I had previously determined (Section 2.4). **Asci** was highly potent against both parasites with activity in the low nanomolar range.

Table 10. EC_{50} values for **DDB-1** and **Asci** against *L. donovani*, *T. brucei* and HepG2 cells.

Compound	EC_{50} (nM) ± SD			
	***L. donovani* (Pro)**	***L. donovani* (Ama)**	***T. brucei* (BSF)**	**HepG2**
DDB-1	7352 ± 833	40244 ± 2096	340 ± 24	22223 ± 4572
Asci	20 ± 1	11 ± 0	1.6 ± 0.1	64 ± 3

SD = standard deviation, Pro = promastigotes, Ama = axenic amastigotes, BSF = Bloodstream forms. EC_{50} represents weighted means from $n \geq 2$ replicates.

With the *L. donovani* overexpression library, **DDB-1** selection commenced at 55 µM ($EC_{98.2}$) but showed no increase in cell number until day 18 at which point concentration was halved to encourage growth (Figure 40). **Asci** selection at 65 nM (EC_{96}) grew comparably to the control and concentration was therefore increased every two to three days until 120 nM ($EC_{99.2}$) by day 9 which was maintained for two days; in a parallel attempt starting at 110 nM **Asci** all cells died.

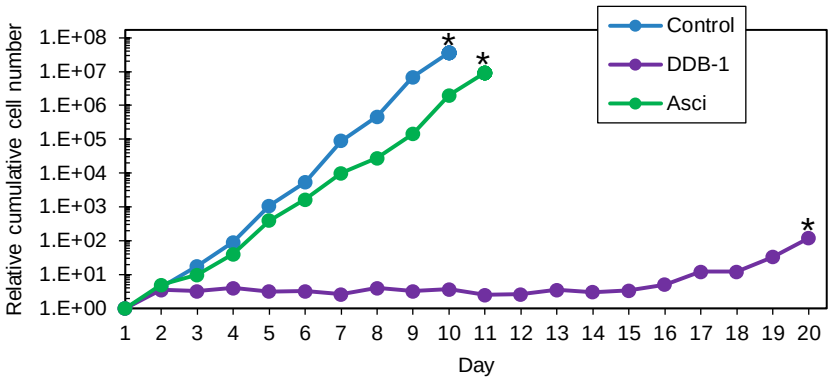

Figure 40. Cumulative growth of the *L. donovani* cosmid overexpression library selected with **DDB-1** and **Asci**. Asterisks represent points of DNA harvesting.

Cosmids in the "resistant" parasites were harvested at day 20 (**DDB-1**) or day 11 (**Asci**) and submitted for next generation sequencing (NGS) alongside the untreated control harvested at day 10. Sequencing results were analysed by collaborators Dr Michele Tinti and Dr Sandra Carvalho at the University of Dundee. Briefly, sequences were mapped to the *L. donovani* BPK282A1 genome, DNA fragments ranked according to RPKM (Reads per kilobase per million mapped reads), and individual fragments inspected for flanking barcodes. DNA fragments are often composed of multiple genes, therefore the flanking barcodes are used to identify which genes were detected. The ideal outcome from this library screening is to have a specific genomic location being highly enriched corresponding to > 50% of the total reads, which was not the case for either compound. For both drug selections, reads mapped to a range of genes within the genome (Figure 41A–B). For **DDB-1**, the highest confidence DNA fragment contributed to only 5.7% of total reads, which can be attributed to five genes within the fragment (Table 11). For **Asci**, the highest confidence fragments accounted for 12.3, 1.0 and 0.7% of total reads, the responsible genes of which are in Table 12.

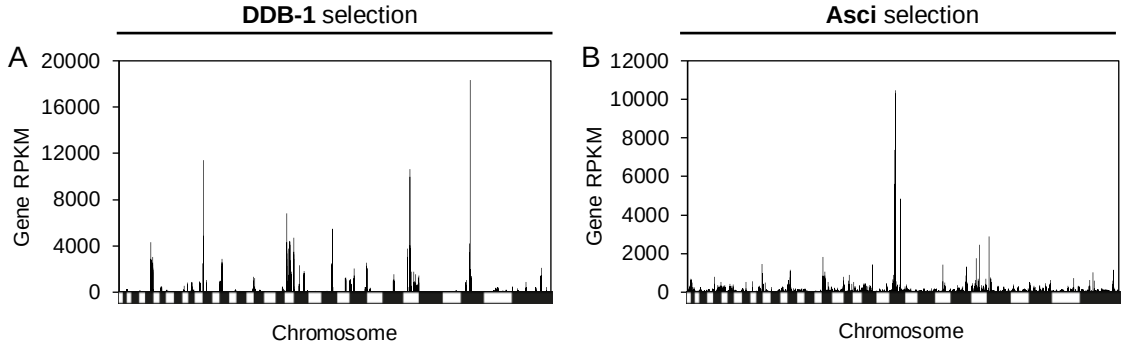

Figure 41. No specific genomic location has the majority of reads for **DDB-1** or **Asci** selection. RPKM for each gene and the corresponding chromosome location in *L. donovani* selected by **DDB-1** (A) or **Asci** (B).

Table 11. Identities of the genes responsible for the highest RPKM DNA fragments in *L. donovani* overexpression library selected by **DDB-1**. These represent the most promising hits.

Gene ID	Gene name	RPKM	Total reads
230670	galactose oxidase, central domain containing protein, putative	3223	54609
230680	tRNA binding domain containing protein, putative	4452	3565
230690	metallo-beta-lactamase family protein-like protein	4100	7916
230700	PAP2 superfamily, putative	4363	5240
230710	ubiquitin-activating enzyme E1, putative	2773	14686

LdBPK gene IDs from the top DNA fragment. Only genes where correct flanking barcodes were found are shown. RPKM = Reads per kilobase per million mapped reads

Table 12. Identities of the genes responsible for the highest RPKM DNA fragments in *L. donovani* overexpression library selected by **Asci**. These represent the most promising hits.

Gene ID	Gene name	RPKM	Total reads	Fragment%
260790	asparagine synthetase a, putative	9492	18402	12.3
191550	hypothetical protein, conserved	779	3352	1.0
191560	peptidylprolyl isomerase-like protein	873	2070	
221550	hypothetical protein, conserved	1834	713	
191570	choline/carnitine o-acyltransferase-like protein	705	3344	
302860	succinate dehydrogenase subunit 3	1296	745	0.7
302870	hypothetical protein, conserved	1311	833	

LdBPK gene IDs from the top 3 DNA fragments. Only genes where correct flanking barcodes were found are shown. RPKM = Reads per kilobase per million mapped reads. Fragment% is the percentage of total reads for each DNA fragment.

Selection with **DDB-1** of the *T. brucei* overexpression library was poor: compound was maintained at 15 µM ($EC_{98.1}$) for 8 days and then re-drugged at the same concentration, however cell growth never reached comparable levels to the control suggesting no selection had taken place (Figure 42A). **Asci** selection started at two different concentrations: **Asci**-1 at 2.3 nM ($EC_{97.6}$) and **Asci**-2 at 2.5 nM (EC_{99}). Both grew at comparable rates to the control necessitating a sequential concentration increase to 7.5 nM and 8 nM respectively (>EC_{99}). Growth was maintained at these concentrations until day 9 (**Asci**-1) or 10 (**Asci**-2) at which point DNA was harvested (Figure 42A). The cultures were re-drugged at the same concentration to confirm resistance, but this caused cell death therefore resistance is unlikely.

Analysis was carried out by collaborators in Dundee in a similar manner to the *L. donovani* overexpression library described above. As expected from the growth curves, both **Asci** concentrations returned no meaningful reads indicating that compound selection had failed. **DDB-1** selection showed 19.1% of reads mapped to a 9.6 Kb fragment of DNA on chromosome 3 (Figure 42B). Three genes in this fragment are responsible for the hit, and seven other fragments had high RPKM with the genes responsible shown in Table 13. The *T. brucei* overexpression library makes use of tetracycline to induce RNA polymerase I to drive the expression of transfected vectors containing fragments of the genomic DNA (gDNA). Depending on the orientation of the gDNA fragment in the construct, i.e., sense or anti-sense, the RNA pol I will produce sense-RNA or anti-sense-RNA, which leads to either overexpression, as intended in the overexpression library, or RNA knockdown. The top hits selected by DDB-1 were a combination of knockdown and overexpression.

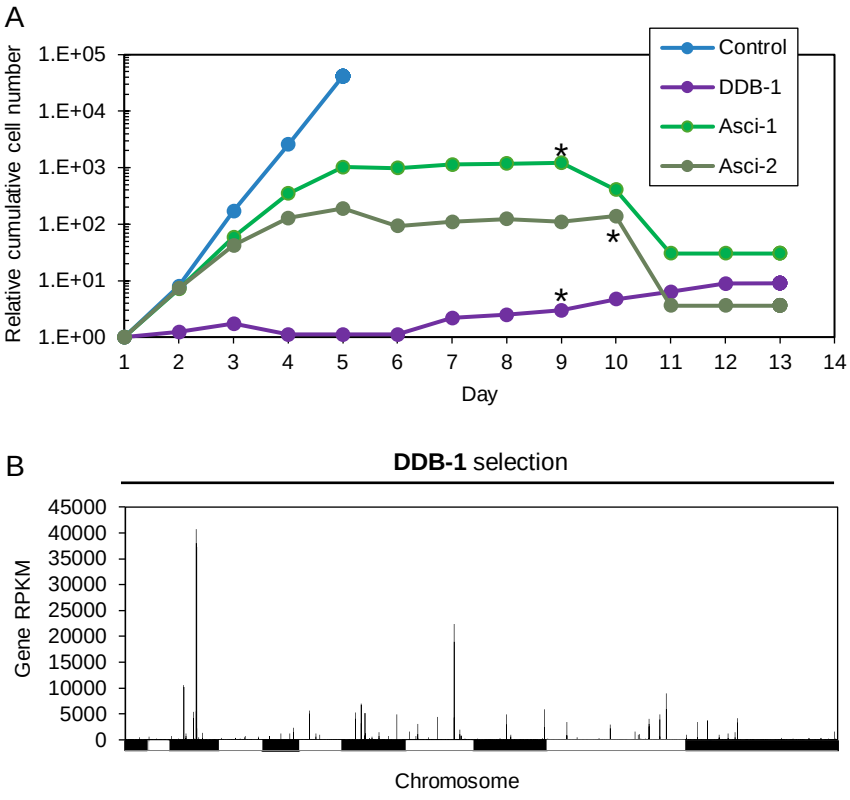

Figure 42. The *T. brucei* overexpression library was poorly selected by **DDB-1** and **Asci**. A. Cumulative growth of the *T. brucei* overexpression library selected with **DDB-1** and **Asci** at two different concentrations. Asterisks represent points of DNA harvesting. B. RPKM for each gene and the corresponding chromosome location in *T. brucei* selected by **DDB-1**. No specific genomic location has majority of reads.

Table 13. Identities of the genes responsible for the highest RPKM DNA fragments in *T. brucei* overexpression library selected by **DDB-1**. These represent the most promising hits.

	Gene ID	Gene name	RPKM	Total reads	Frag.%
Knockdown	3.3600	hypothetical protein	37984	111873	19.1
	3.3610	peroxisomal targeting signal 2 receptor, putative	40748	90080	
	3.3620	hypothetical protein, conserved	37255	95049	
	11.8460	amastin-like protein	25701	75963	6.9
	11.8470	zinc finger protein family member, putative	2781	29954	
	6.4040	mitochondrial ribosomal protein L28	6934	9114	1.8
	6.4050	zinc finger ccch domain-containing protein 14	6773	16080	
	6.4060	eukaryotic protein of unknown function (DUF872), put.	3171	5516	
	11.15050	cation efflux family, putative	1361	4335	2.1
	11.15060	hypothetical protein, conserved	945	2103	
Overexpression	2.3390	hypothetical protein, conserved	10546	65802	4.9
	2.3400	hypothetical protein, conserved	10251	18500	
	9.4310	tricarboxylate carrier, putative	8919	60717	4.7
	11.9370	hypothetical protein, conserved	8076	27522	2.8
	11.15020	iron superoxide dismutase	5761	11615	2.1

Tb927 gene IDs from the top 8 DNA fragments. Only genes where correct flanking barcodes were found are shown. RPKM = Reads per kilobase per million mapped reads. Put. = putative. Frag.% is the percentage of total reads for each DNA fragment. These are a mixture of knockdown (magenta) and overexpression (cyan).

There were no genes in common between the overexpression in *T. brucei* and the overexpression *L. donovani* library for **DDB-1** selection. This indicates that the selection may have been poor in both libraries, as was seen with the growth curves, and none of these proteins is likely to constitute a "real" result as there is no agreement between the libraries. As the *T. brucei* selection failed for **Asci**, no comparison can be made with the *L. donovani* library.

4.2.3 Genome-wide knockdown library

In collaboration with the Wyllie group at the University of Dundee, I carried out screening against an RNAi *T. brucei* knockdown library. Selection with **DDB-1** at 15 µM ($EC_{98.1}$) caused cell growth to crash such that no parasites were detectable until day 12 (Figure 43A). Following cell emergence, the culture was split and maintained at the same concentration (**DDB-1**-1) or at a lower concentration corresponding to 5× EC_{50} (**DDB-1**-2). **Asci** selection at two different starting concentrations of 2.3 nM ($EC_{97.6}$) for **Asci**-1 or 2.5 nM (EC_{99}) for **Asci**-2 had no immediate growth defect so

concentration was increased daily to 8.5 nM and 8 nM (>EC_{99}) on day 4 and day 3 respectively. This caused a slower growth rate than the control while selection takes place, followed by an increase in growth rate; a characteristic pattern indicating good selection (Figure 43A).

As previously, reads from the NGS were analysed by collaborators for each compound following mapping to the *T. brucei* TREU927 reference genome. **DDB-1** genes with the most promising reads were identical for both **DDB-1**-1 and **DDB-1**-2 with the exception of two additional genes detected at the lower concentration. However, all detected genes had very low total number of reads and therefore were not considered further, this is likely due to the poor selection. Additionally, none of the detected genes were in common with the knockdown results from the *T. brucei* overexpression library. **Asci** strongly selected for two members of the nitroreductase family located on chromosome 7 at 11.5% and 9.4% of total barcoded reads for **Asci**-1 (Figure 43B), and 7.7% and 6.7% for **Asci**-2.

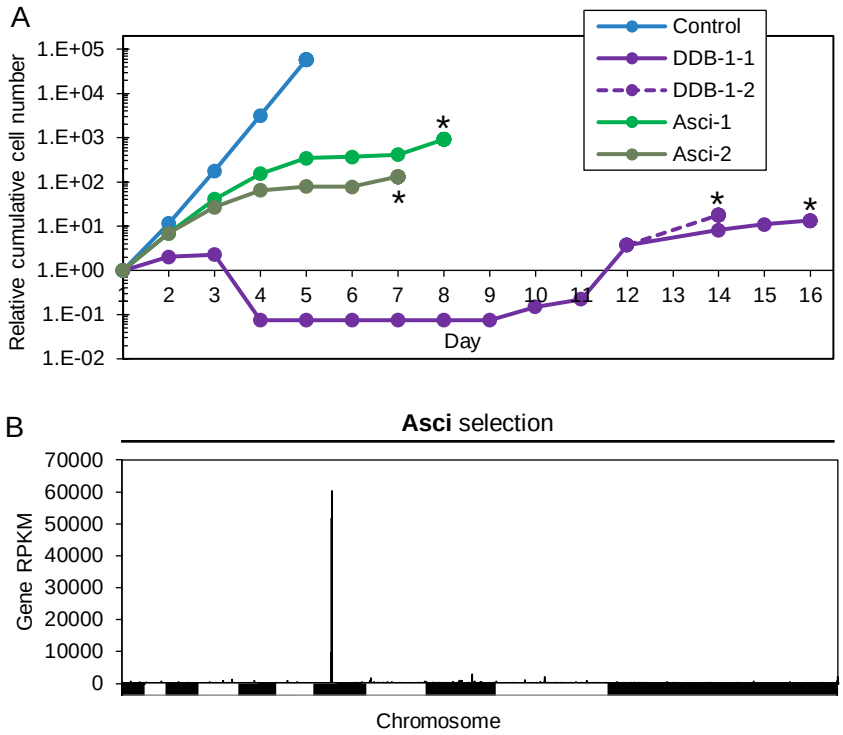

Figure 43. The *T. brucei* RNAi library was poorly selected by **DDB-1**, and well selected with **Asci**. A. Cumulative growth of the *T. brucei* knockdown library selected with **DDB-1** which was split to two compound concentrations at day 12, or **Asci** at two different starting concentrations. Asterisks represent points of DNA harvesting. B. RPKM for each gene and the corresponding chromosome location in *T. brucei* selected by **Asci**-1. A specific locus on chromosome 7 corresponds to majority of the reads. The plot for **Asci**-2 selection is almost identical, not shown here.

An additional RNA helicase with RPKM above the threshold was identified in only **Asci**-2 (Table 14). The total read number here was also low but due to the strong selection for the nitroreductase genes and good selection growth curve, it is likely that this represents a real hit.

Table 14. Identities of the genes responsible for the highest RPKM DNA fragment in the *T. brucei* RNAi library selected by **Asci**. These represent the most promising hits.

Gene ID	Gene name	RPKM	Total Reads
7.3020	nitroreductase family, putative	60253	8644
7.2980	nitroreductase family, putative	51824	7452
7.2970	ATP-dependent DEAD/H RNA helicase, putative	9726	4046

Tb927 gene IDs from the top DNA fragment. Only genes where correct flanking barcodes were found are shown. RPKM = Reads per kilobase per million mapped reads.

4.2.4 *L. donovani* resistance library

A resistance library has been recently developed in *L. donovani* which consists of cell lines with resistance to compounds with defined modes of action and molecular targets.[440] Screening against this library (RES-Seq) will identify cross-resistance or shared MoA to ensure that diversity is maintained across compounds in development. The library consists of 31 different barcoded cell lines, with resistance derived either experimentally or genetically engineered (consequently there is some redundancy), and an additional barcoded wildtype cell line.

Compound selection with **DDB-1** and **Asci** was with 3× or 10× EC_{50} as is the standard protocol for this library. **DDB-1** growth was much slower than the control at both concentrations (Figure 44A). Selection with **Asci** at 10× EC_{50} caused cell death which never recovered. At the lower concentration of 3× EC_{50}, following an initial slowed growth at days 1–2, **Asci** selected culture grew similarly to the control. We extracted DNA from the three cultures with surviving cells and this was sequenced by BGI genomics. Analysis by Dr. Sandra Carvalho involved quantifying relative fitness of each cell line in the selected cultures versus the unselected control. If there was a cross-resistance MoA we would expect to see a cell line with a relative fitness of > 50% and also enriched over the wildtype (WT). For both compounds there was no significant fitness increase of any particular cell line relative to the wildtype or the control, therefore no cross-resistance (Figure 44B–D).

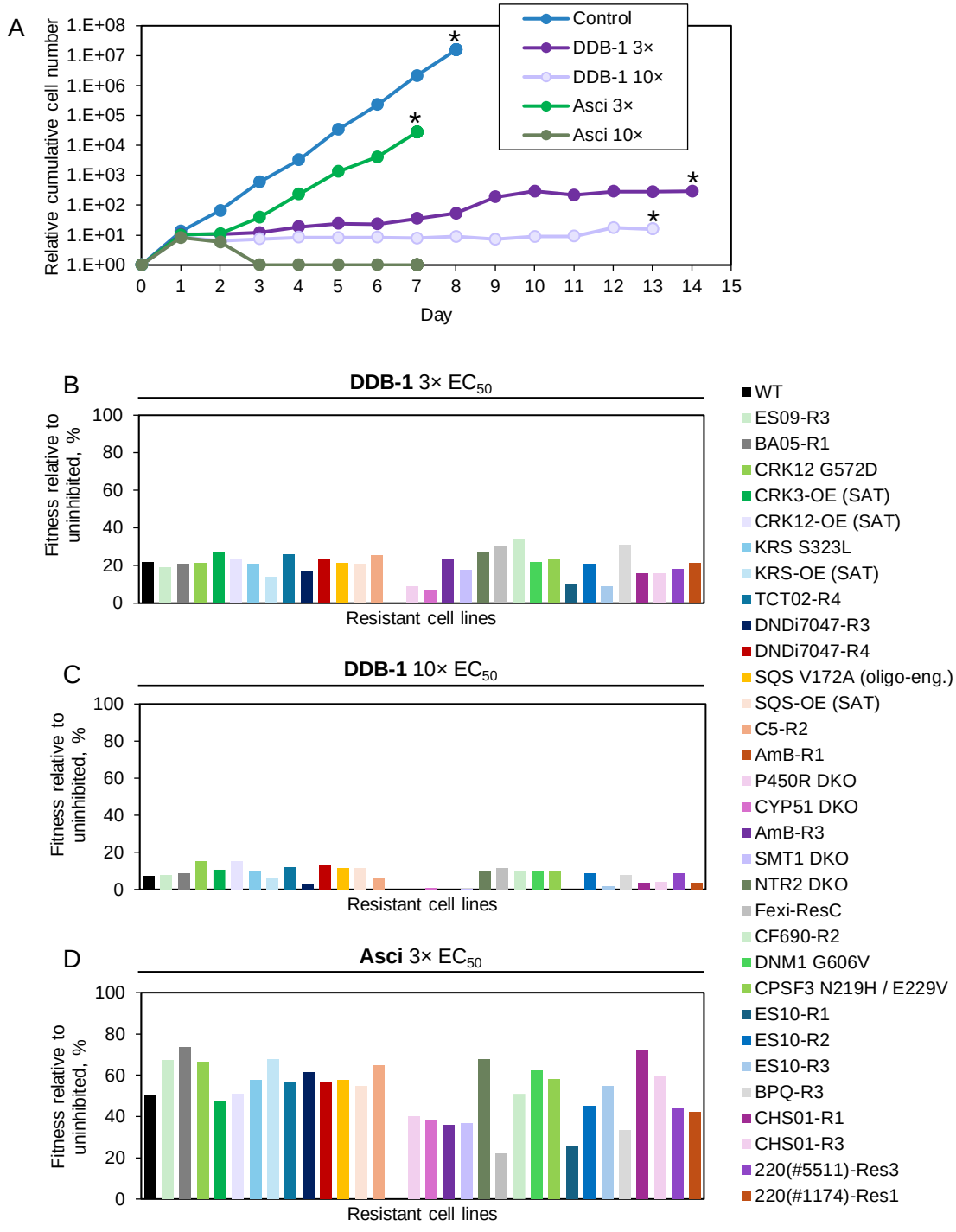

Figure 44. There is no cross-resistance of either **DDB-1** or **Asci** with known MoA in the RES-Seq library. A. Cumulative growth of the *L. donovani* RES-Seq library selected with **DDB-1** or **Asci**. Asterisks represent points of DNA harvesting. B–D. Fitness of selected cell lines relative to the uninhibited control cell line. There was no enrichment of any resistance cell lines with either compound in comparison to the uninhibited control or the wildtype barcoded cell line (black).

4.3 Transcriptomics approaches to MoA discovery

4.3.1 Transcriptome changes due to compound treatment

High-throughput profiling of the transcriptome (RNA-Seq) can be used to detect changes in mRNA expression levels due to compound treatment, which represent attempts by the parasite to overcome effects of the compound. We aimed to use RNA-Seq to probe the transcriptome of **DDB-1** treated cells; this may yield successful results where genomics approaches failed as it doesn't require resistant cultures to emerge. *L. mexicana* promastigotes were grown under standard conditions (described in Section 6.1.1) in the presence of 30 µM **DDB-1**, 30 µM **DDB-PAL** or a 0.1% DMSO negative control for 24 h, after which mRNA was extracted. Quantification of the mRNA transcripts after only 24 h will allow identification of changes following growth by a factor of approximately two, while maintaining a high enough number of cells. Two different active compounds were used in this experiment to identify any overlapping hits. Extracted mRNA was sent to BGI genomics for sequencing.

Each transcript corresponds to a gene; we filtered the genes to have > 2-fold change in expression compared to the control (ensures biological relevance), a *P*-value for three replicates > 0.05 (ensures statistical significance), and transcripts per million (TPM) > 10 (ensures genes are expressed at an appreciable level). In **DDB-1**, there were 44 genes above these thresholds: 17 upregulated and 27 downregulated (Figure 45A). In **DDB-PAL**, there were only three genes above the fold change and

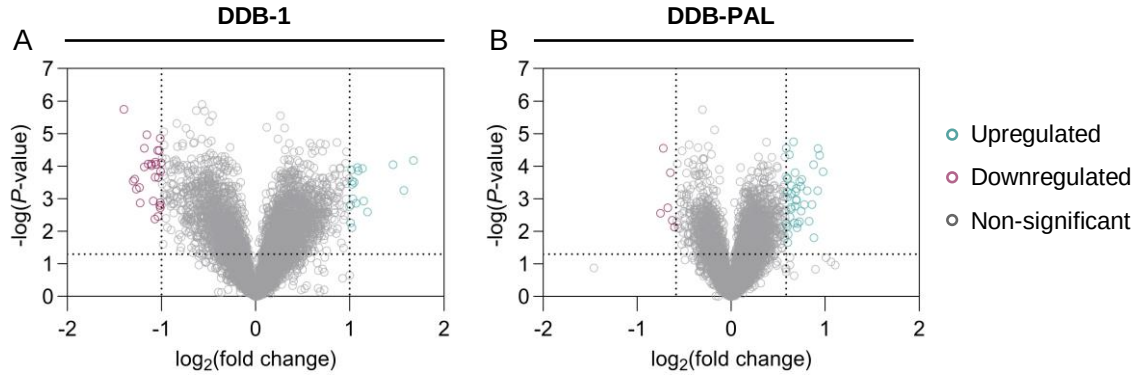

Figure 45. A number of genes were upregulated and downregulated above thresholds due to **DDB-1** and **DDB-PAL**. Volcano plot of genes with > 10 TPM. *P*-value derived from a two-tailed *t*-test from $n = 3$ replicates. Genes with *P*-value > 0.05 and fold change of drug/DMSO > 2 (A, **DDB-1**) or > 1.5 (B, **DDB-PAL**) are highlighted in magenta (downregulated) and cyan (upregulated).

P-value threshold, none of which met the TPM requirement, therefore the fold change cut-off was lowered to > 1.5 which resulted in 48 genes of interest: 40 upregulated and 6 downregulated (Figure 45B). There were no highly (> 5-fold) upregulated or downregulated genes for either compound i.e., no obvious genes to investigate further. To narrow down potential hits, the 12 genes changed by both compounds (Table 15) as well as the top five upregulated or downregulated for each compound (excluding the overlapping genes) (Table 16) were considered further: a total of 20 genes of interest.

Table 15. Identities of genes above threshold upregulated (cyan) or downregulated (magenta) by both **DDB-1** and **DDB-PAL**.

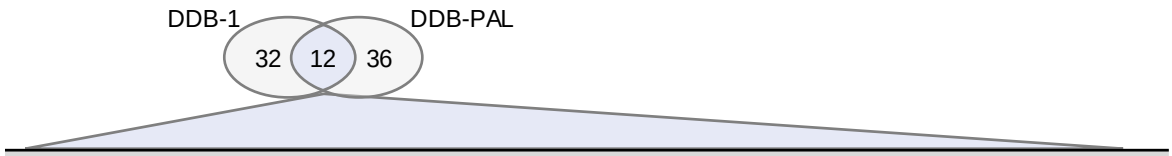

Gene ID	Gene name	DDB-1 FC	DDB-PAL FC	mRNA (TPM)
04.0130	hypothetical protein	3.19	1.89	80.57
19.1420	cysteine peptidase A (CPA)	2.28	1.63	191.24
33.0140	malate dehydrogenase	2.19	1.66	561.46
27.0090	cytochrome p450-like protein	2.13	1.97	125.86
18.0440	phosphatidic acid phosphatase, putative	2.10	1.56	73.37
17.0890	META domain containing protein, putative	2.06	1.71	419.74
30.0453	hypothetical protein	2.04	1.92	147.97
03.0600	arginine N-methyltransferase, putative	0.38	0.61	72.95
34.4380	hypothetical protein, conserved	0.41	0.65	152.61
27.1710	eukaryotic translation release factor, put.	0.45	0.64	74.54
24.1210	eukaryotic translation initiation factor 1, put.	0.47	0.63	140.48
30.1800	amino acid permease	0.50	0.59	132.66

LmxM gene IDs, FC = fold change (drug/DMSO), put. = putative, mRNA in TPM is the average of 3 replicates.

Table 16. Identities of the top five upregulated (cyan) and downregulated (magenta) genes by **DDB-1** or **DDB-PAL**, not including those already listed in Table 15 above.

Gene ID	Gene name	DDB-1 FC	DDB-PAL FC	mRNA (TPM)
29.2090	alcohol dehydrogenase, putative	2.98	1.81	12.43
33.0070	ascorbate peroxidase, putative	2.75	1.48	143.23
18.0640	serine/threonine kinase-like protein, putative	2.22	1.35	70.82
30.0450c	hypothetical protein	1.95	1.90	460.98
23.1062	hydrophilic surface protein 2	1.88	1.84	149.89
30.3070	ferrous iron transport protein	0.41	0.80	153.26
30.3060	ferrous iron transport protein	0.42	0.79	100.88
15.1470	ribosomal protein S6, putative	0.43	0.67	489.43

LmxM gene IDs, FC = fold change (drug/DMSO), mRNA in TPM is the average of 3 replicates.

Each of the 20 genes was individually assessed for the likelihood of it being a true hit. Priority was given to genes with orthologs in the other trypanosomes that **DDB-1** is active against (*T. cruzi, T. brucei, L. infantum* and *L. donovani*). The protein coding sequence was manually checked for abnormal amino acid composition, and protein identity (or ortholog identity for hypothetical proteins if known) was used to prioritise any mitochondrial related proteins (based on discussions from Section 2.9.2 and Section 3.5.1).

In parallel, an analysis of the whole transcriptome was conducted using the LeishCyc database, which provides a comprehensive overview of all *Leishmania* biochemical processes based on data from *L. major*.[441] Proteins were mapped to their orthologs in the cellular metabolic overview to identify effects on specific pathways, shown for **DDB-1** (Figure 46). The results from **DDB-PAL** created a near identical overview, shown in the appendix (Section 7.2.1, Figure 66).

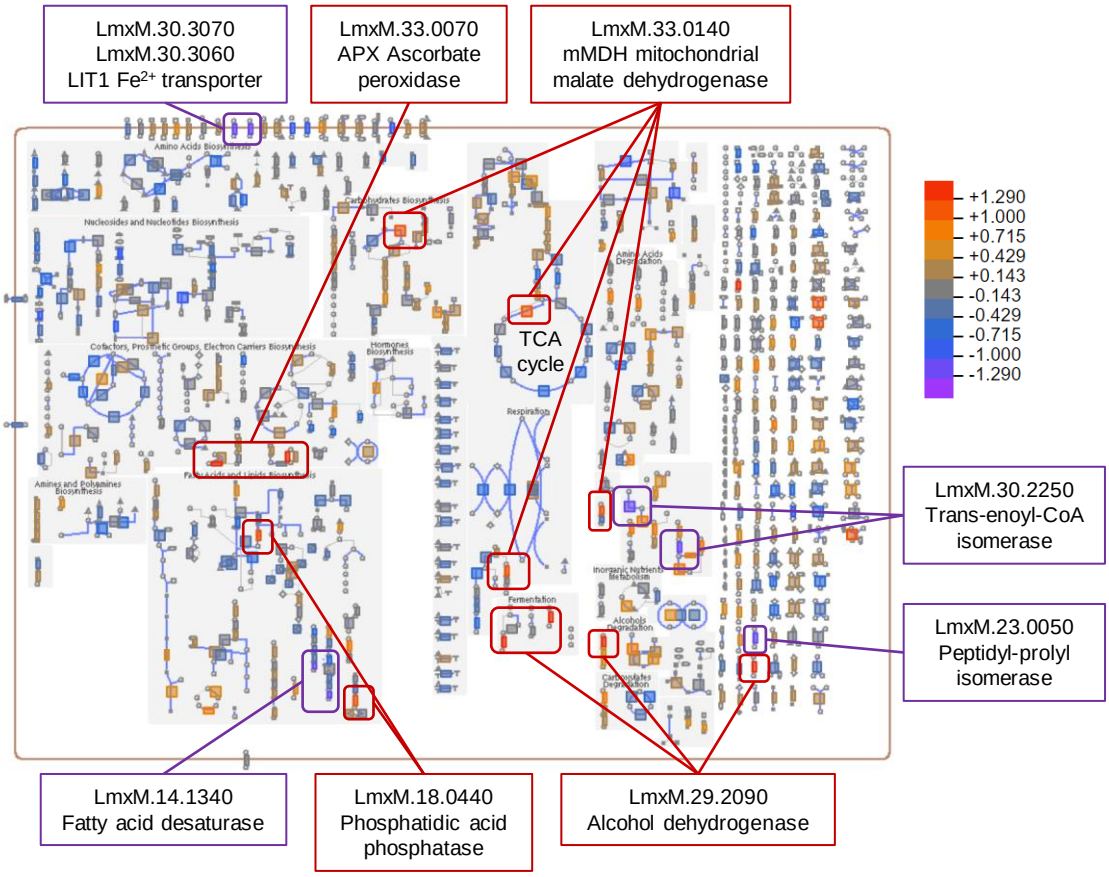

Figure 46. None of the top upregulated or downregulated proteins by **DDB-1** are involved in any one specific metabolic pathway. Overlay of the transcriptome changes in **DDB-1** treated *L. mexicana* promastigotes onto LeishCyc cellular overview. Upregulated proteins are shown in red, downregulated proteins are shown in purple, the highest of which are labelled.

The highest upregulated and downregulated metabolic proteins are discussed here in more detail – this will by definition include any metabolic proteins from Table 16 and could include some from Table 15. Upregulated LmxM.33.0140 mitochondrial malate dehydrogenase (mMDH) is the most promising hit: it was detected with a TPM of > 500, and has a mitochondrial localisation for its mNeonGreen tagged ortholog Tb927.10.2560 (TrypTag.org).[405] There are two other malate dehydrogenases in *L. mexicana*: cytosolic and glycosomal; neither are expressed to a high level in promastigotes,[442] and there was no change in expression level of these upon either treatment. There is a slight downregulation of enzymes before mMDH in the tricarboxylic acid (TCA) cycle (Figure 46) which is itself upregulated, this could indicate that the compound is affecting the TCA cycle.

LmxM.33.0070 ascorbate peroxidase (APX) is among the top five genes upregulated by **DDB-1** treatment, and there is only a single copy of APX in *Leishmania*, which makes it a more appealing hit, although it has no ortholog in *T. brucei*. LmxM.18.0440 phosphatidic acid phosphatase is part of the fatty acid and lipid biosynthesis pathway, and is upregulated above the threshold in both compound treatments. Its paralogs LmxM.19.1350 and LmxM.19.1351 (predicted to act on the same pathway) show no change in TPM upon compound treatment, indicating **DDB-1** is unlikely to be targeting this pathway. LmxM.29.2090 is a putative alcohol dehydrogenase upregulated by both compounds although detected with very low reads (< 10 TPM for **DDB-PAL**). The related NADP-dependent alcohol dehydrogenase LmxM.23.0360, predicted to play the same cellular role, did not have altered expression levels which again indicates this pathway is not being targeted.

The highest downregulated metabolic proteins were metal transporters LmxM.30.3070 and LmxM.30.3060 in **DDB-1** treatment (also downregulated by **DDB-PAL** although not more than 1.5-fold). Downregulated putative fatty acid desaturase LmxM.14.1340 was close to the fold change cut-off for **DDB-1** and below the cut-off for **DDB-PAL**. It is involved in the biosynthesis of fatty acids in *Leishmania* but is unlikely to be of further interest due to only moderate fold change.[443] LmxM.30.2250 putative 3,2-trans-enoyl-CoA isomerase mitochondrial precursor was downregulated barely beyond 2-fold by **DDB-1** and not beyond 1.5-fold by **DDB-PAL**. It is not detected in promastigotes,[444] and the other two genes in this pathway were unchanged, all of which

points to it not being a key result. Finally, LmxM.23.0050 codes for a putative peptidyl-prolyl cis-trans isomerase, a part of a wider group of 18 other enzymes/isoenzymes that carry out the same role, none of which had changed expression by compound and are therefore uninteresting.

There were no pathways in common among the highest upregulated and downregulated metabolic proteins for either compound. Based on the analyses from LeishCyc and inspections of the 20 genes listed in Table 15 and Table 16, nine proteins were classified as the best hits. For a complete rationale of the decision for each protein see appendix Section 7.2.2, Table 20.

4.3.2 Validation of selected genes

In order to further investigate the transcriptomics hits, I aimed to generate deletion cell lines for each gene and compare the **DDB-1** EC_{50}. Gene downregulation upon treatment with **DDB-1** implies that this is advantageous to cell survival in the presence of compound. I therefore hypothesised that the deletion of these downregulated genes would also be advantageous to survival, and expected that in deletion cell lines the **DDB-1** EC_{50} should increase. Conversely, genes that were upregulated due to the **DDB-1** compound are likely to provide a protective benefit against **DDB-1**, and therefore their deletion could lead to greater compound sensitivity, i.e, decreased EC_{50}. Deletions of the detected upregulated genes are more likely to be lethal to *Leishmania* as there is no indication that the cells can survive without their expression, while the downregulated genes have shown a tolerance to low expression levels – although this is still different to complete deletion. Attempted deletion cell lines were generated for the nine best hits. Each of these was also tagged with mNeonGreen (mNG) to confirm localisation (Table 17, Figure 47A). Successful deletion (Δ) cell lines were generated for four of the eight cell lines (LmxM.30.3060 and LmxM.30.3070 LIT1 transporters were deleted in tandem). Attempted deletion of Cyp450, eRF and eIF1 resulted in no cells emerging despite multiple attempts, indicating that the deletions are probably lethal. This is expected for eRF and eIF1 as both have key roles in translation. Attempted deletion of NMT could not be validated. However, none of the successful deletions resulted in a statistically significant change to **DDB-1** EC_{50} (Figure 47B).

Table 17. Identity of the nine best hits from transcriptomics experiments and their localisation from mNeonGreen tagging. Upregulated genes are shown in cyan and downregulated genes are shown in magenta.

Gene ID	Shorthand	Gene name	Localisation
04.0130	Hyp0130	hypothetical protein	endoplasmic reticulum
33.0140	mMDH	mitochondrial malate dehydrogenase	mitochondrion
27.0090	Cyp450	cytochrome p450-like protein	cytoplasm – patchy
33.0070	APX	ascorbate peroxidase	mitochondrion
03.0600	NMT	arginine *N*-methyltransferase, put.	cytoplasm
27.1710	eRF	eukaryotic translation release factor, put.	endoplasmic reticulum
24.1210	eIF1	eukaryotic translation initiation factor 1, put.	endoplasmic reticulum
30.3060	LIT1	ferrous iron transport protein	cytoplasm, flagellum, fp
30.3070	LIT1	ferrous iron transport protein	cytoplasm, flagellum, fp

LmxM gene IDs, put. = putative, fp = flagellar pocket. Gene name is taken from TritrypDB,[305] localisation is defined from mNeonGreen imaging in comparison to mNeonGreen tagged proteins with known localisation.[44]

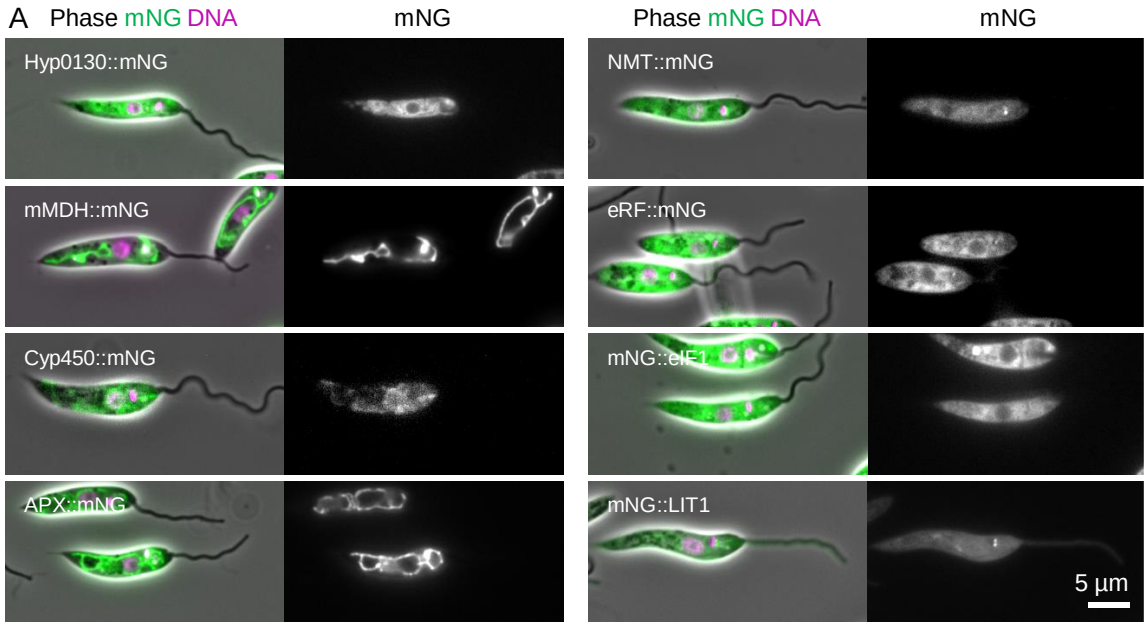

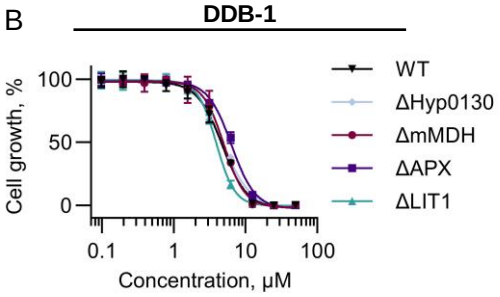

Cell line	EC_{50} ± SD (µM)	Fold-change
WT	4.74 ± 2.35	-
ΔHyp0140	4.48 ± 1.22	0.9
ΔmMDH	5.38 ± 1.54	1.1
ΔAPX	6.43 ± 1.92	1.4
ΔLIT1	4.34 ± 1.07	0.9

Figure 47. None of the deletion cell lines led to a **DDB-1** EC_{50} change. A. Representative fluorescence microscopy images from > 3 fields of view, n > 50 cells. Images from one non-clonal cell line (apart from mNG::LIT1) with > 95% of the population having signal as shown. LIT1 mNG::LmxM.30.3070 and mNG::LmxM.30.3060 had the same localisation, shown here is mNG::LmxM.30.3070. B. Representative dose-response curves for **DDB-1** treatment in deletion (Δ) cell lines, the mean is plotted with error bars representing standard deviation for 6 technical replicates. The table shows EC_{50} values of n = 3 biological replicates. Statistical significance derived from a two-tailed t-test had P-value > 0.05 for all deletions (Δ) verses wildtype (WT).

4.3.3 Metal ion chelation assays

Based on the transcriptomics data, there could be an association between **DDB-1** activity and metal ions: Fe^{2+} transporter LIT1 was downregulated, upregulated Hyp0130 and Cyp450 have predicted "metal ion binding", and upregulated APX requires heme and iron.[445, 446] Additionally, the fact that resistant cell lines could not be generated for **DDB-1** is in line with a metal chelation MoA.[207, 208] Compounds with a chemical structure amenable to metal ion chelation can act *via* this MoA, as is the case for the anti-trypanosomal 8-hydroxy-naphthyridines (introduced in Section 1.5.6, Figure 6).[208] **Asci** has a plausible metal binding site, and UV-Vis titration experiments by DPhil student Yasmine Biddick have shown that it indeed binds Zn^{2+} in a 1:2 ratio, and Fe^{2+} in a more complex manner (Figure 48). We hypothesised that if either compound exhibits its toxicity *via* sequestering metal ions, then addition of exogenous metal ions to the cell growth medium would create a surplus and thereby decrease toxicity. In order to test this, the EC_{50} of **Asci** and **DDB-1** was measured in the presence of different metal cations.

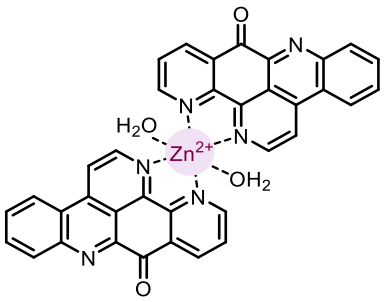

Figure 48. Proposed 1:2 binding of Zn^{2+} to **Asci**.

4.3.3.1 Maximal metal ion concentration tolerated in *Leishmania*

To quantify the effect of exogenous metal ions on the EC_{50} of active compounds, the maximal tolerated concentration of various metal ions by *L. mexicana* first needed to be established. Inspired by the work of Wall *et al.* on divalent metal chelators, EC_{50} curves were plotted for the metal M^{2+} chlorides: Zn^{2+}, Fe^{2+}, Ca^{2+}, Mg^{2+}, Mn^{2+} and Cu^{2+} in promastigotes. Fe^{2+}, Zn^{2+} and Cu^{2+} had clear growth–concentration relationships, allowing a maximal dose to be calculated from the EC_{50} curves (Figure 49). The effect of Mn^{2+} was less clear cut, although it was still detrimental at higher

concentrations. Interestingly, Mg^{2+} and Ca^{2+} were actually beneficial to promastigote growth. Maximal tolerated concentration was established as 800 µM for Zn^{2+}, 1.5 µM for Fe^{2+} and 30 µM for Cu^{2+}; toleration for the other metal ions could not be established from this experiment.

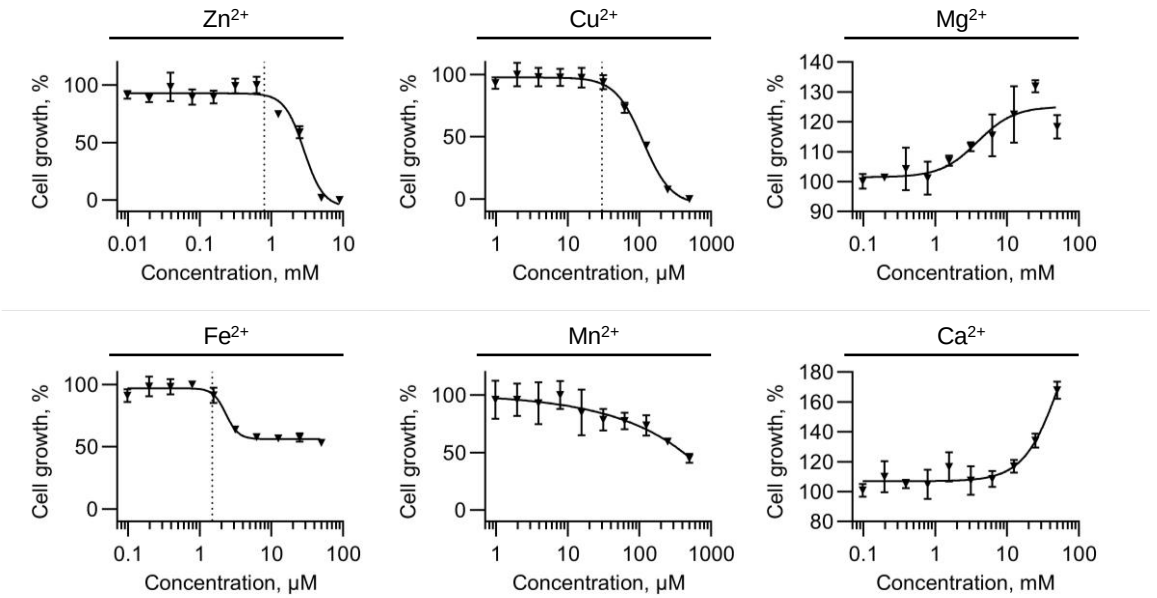

Figure 49. Maximal tolerated exogenous M^{2+} in *L. mexicana* promastigotes. Representative dose-response curves for M^{2+} treatment, $n = 3$ biological replicates, each with 6 technical replicates. The mean is plotted with error bars representing standard deviation. Dotted lines represent the maximal tolerated concentration for Zn^{2+}, Fe^{2+} and Cu^{2+}.

4.3.3.2 Exogenous M^{2+} effect on DDB-1 and Asci

In *L. mexicana* promastigotes, there was no significant effect on the EC_{50} of **DDB-1** by the addition of exogenous Zn^{2+}, and with Fe^{2+} only a small 1.3-fold shift (Figure 50A). Cu^{2+} was able to modulate **DDB-1** toxicity significantly with cells maintaining 50% growth even at the highest concentration of **DDB-1** tested. Exogenous Zn^{2+} decreases **Asci** toxicity, causing a 4.8-fold EC_{50} shift from 68.6 ± 16.8 nM to 330.8 ± 60.9 nM (Figure 50B), while exogenous Fe^{2+} does not affect **Asci** toxicity despite its potential ability to chelate Fe^{2+}. In collaboration with the MoA group in Dundee, the same experiments were carried out on *L. donovani* promastigotes with exogenous Fe^{2+} and Zn^{2+}, again there was no effect on **DDB-1**, and a moderate 1.8-fold shift for **Asci** in Zn^{2+}. This result could be explained as a chelation of free **Asci** with exogenous M^{2+} leading to either an inactive complex, or a complex that cannot be taken up into the cells: chelation with 800 µM Zn^{2+} is sufficient to give a pronounced effect, but is undetectable with 1.5 µM Fe^{2+}.

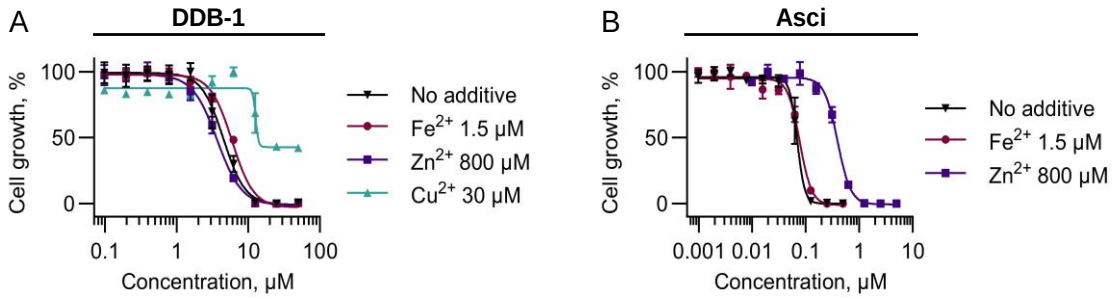

Figure 50. EC_{50} of **DDB-1** is shifted in the presence of exogenous Cu^{2+}, and EC_{50} of **Asci** is shifted in the presence of exogenous Zn^{2+}. Representative dose-response curves for **DDB-1** (A) or **Asci** (B) in the presence of exogenous M^{2+}, n = 3 biological replicates, each with 6 technical replicates. The mean is plotted with error bars representing standard deviation. Statistical significance derived from a two-tailed *t*-test had *P*-value < 0.05 for Fe^{2+} and Cu^{2+} (A), and Zn^{2+} (B), when each was compared with no additive.

Alternatively, **Asci** EC_{50} shift in exogenous Zn^{2+} along with its proven chelation in spectrometry experiments fits the hypothesis of a MoA involving depletion of Zn^{2+}. To determine whether **Asci** is directly depleting intracellular Zn^{2+}, the fluorescent reporter FluorZin™-3 was employed: it increases fluorescence > 50-fold upon binding to Zn^{2+}, is highly metal selective, and localises intracellularly. Contradictory to expectation, **Asci** did not deplete *L. mexicana* intracellular Zn^{2+} but instead *increased* intracellular Zn^{2+} relative to a 0.1% DMSO control (Figure 51A). The known chelator TPEN acted as a positive control for Zn^{2+} chelation. As **Asci** is active in *T. brucei*, the experiment was also performed on bloodstream forms for comparison, but in this case there was no

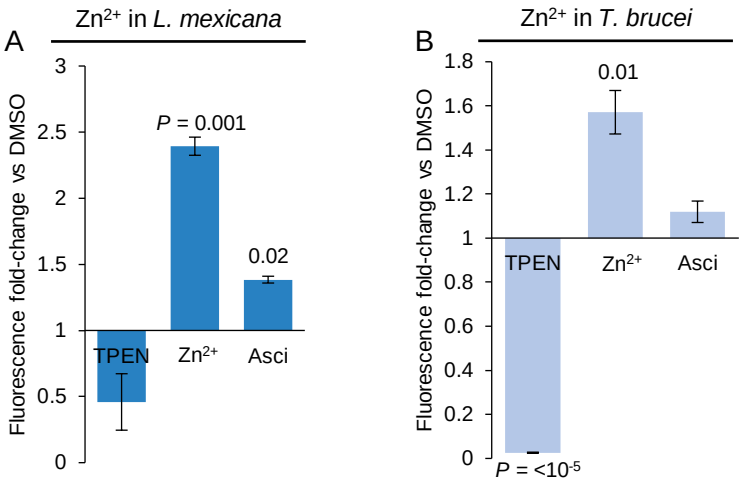

Figure 51. Intracellular Zn^{2+} is increased by **Asci** in *L. mexicana* promastigotes but unchanged in *T. brucei* bloodstream forms. FluorZin-3 fluorescence readout is normalised to 0.1% DMSO treatment and the fold change plotted relative to 0.1% DMSO fold change of 1. Treatments show increased (above) or decreased (below) Zn^{2+} levels following 5 min compound incubation in *L. mexicana* promastigotes (A) or *T. brucei* bloodstream forms (B). n = 3 replicates, the mean is plotted with error bars representing standard deviation, statistical significance was derived from a two-tailed *t*-test versus DMSO; only $P < 0.05$ are shown.

significant change by **Asci** on intracellular Zn^{2+} (Figure 51B). The dissociation constant (Kd) for these compounds with Zn^{2+} was not taken into account: a fluorescence change requires competition for Zn^{2+} which may not be detected if **Asci** is a much weaker Zn^{2+} binder than the fluorescent reporter – this however does not account for the unexpected fluorescence increase.

Based on the increase in intracellular Zn^{2+} by **Asci**, we anticipated that deletion of Zn^{2+} importers should decrease intracellular Zn^{2+} counteracting the effect of **Asci**, and the converse for deletion of Zn^{2+} exporters. To test this, deletion (Δ) cell lines of Zn^{2+} importer LmxM.28.1930 (ZIP3) and M^{2+} exporter cation efflux protein LmxM.31.1870 (CatEff) were created. CatEff::mNG localised to the Golgi as expected (Figure 52A): its *T. brucei* ortholog is predicted to facilitate uptake of Zn^{2+} into the Golgi from the cytosol.[208] ZIP3::mNG localised to the cell surface and a reticulated internal structure, although only at low Zn^{2+} conditions (growth in M199 medium with additional 1 mM EDTA for 24 h) consistent with its *L. infantum* ortholog (Figure 52A).[447] There was no significant change in the EC_{50} of **Asci** in the ΔCatEff cell line indicating that increased intracellular Zn^{2+} does not affect **Asci** toxicity (Figure 52B). **Asci** was significantly less cytotoxic to both importer deletion cell lines tested: ΔLIT1 M^{2+} (Fe^{2+} preferential) importer introduced previously (Section 4.3.2) and ΔZIP3, with EC_{50} shifting 3.2 and 2.6-fold respectively. However, the magnitude of EC_{50} shift in the deletion cell lines is low, and therefore care should be taken not to overinterpret the results as any shifts could be due to subtle changes in the cell line fitness and not a direct link to **Asci** activity.

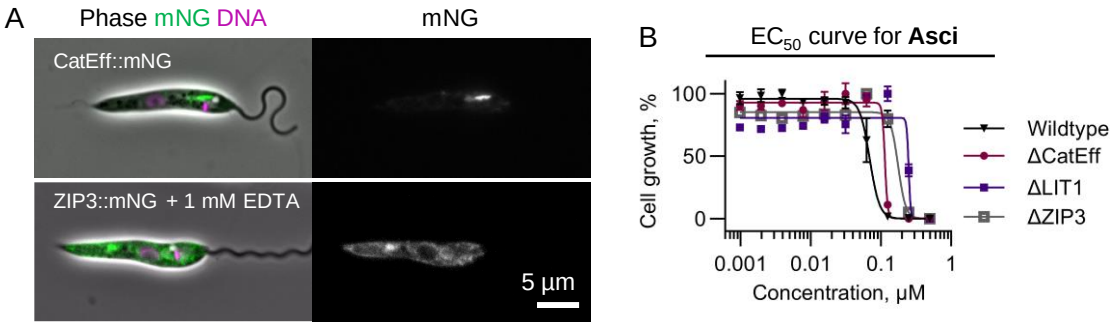

Figure 52. Deletion of M^{2+} importer proteins decreases toxicity of **Asci**. A. Representative fluorescence microscopy images from > 3 fields of view, $n > 50$ cells. Images from one non-clonal cell line with > 95% of the population having signal as shown. B. Representative dose-response curves for **Asci** deletion cell lines, $n = 3$ biological replicates, each with 6 technical replicates. The mean is plotted with error bars representing standard deviation. Statistical significance was derived from a two-tailed *t*-test versus wildtype, $P = 0.017$ for both ΔLIT1 and ΔZIP3, $P > 0.05$ for ΔCatEff.

Despite hints from the transcriptomics analysis, **DDB-1** does not have a MoA directly related to Zn^{2+} or Fe^{2+} concentration in *L. mexicana* or *L. donovani* promastigotes, although excess Cu^{2+} was able to modulate **DDB-1** toxicity. **Asci** causes an increase in intracellular Zn^{2+} and its activity is modestly diminished by exogenous Zn^{2+} or deletion of Zn^{2+} importers.

4.4 Chemo-proteomics for DDB-1 target identification

We wanted to use chemo-proteomics to identify any binding proteins of **DDB-1** by mass spectrometry. Knowledge of the binding target will provide direct information on the compound MoA. Pull-down of proteins interacting with a compound can be applied *via* two main approaches: 1. Immobilisation of the compound to beads and enriching proteins from cell lysate, or 2. *In situ* probing of cells with modified compound that includes an attachment handle used to pull out the compound–target complex. Both of these approaches were employed here to maximise chances of success.

4.4.1 Compound immobilisation on beads for protein pull-down

In order to immobilise compound to beads, we required a **DDB-1** derivative that allows attachment *via* an amide linkage as this is compatible with the beads used by our collaborators. Having established that the **DDB-1** scaffold tolerates modification at the phenol position (Section 2.9, Figure 24), I synthesised amine **DDB-NH₂** in 47% yield over two steps from the intermediate phenol (Scheme 4). The amine handle will be used for amide attachment to carboxylic acid containing beads.

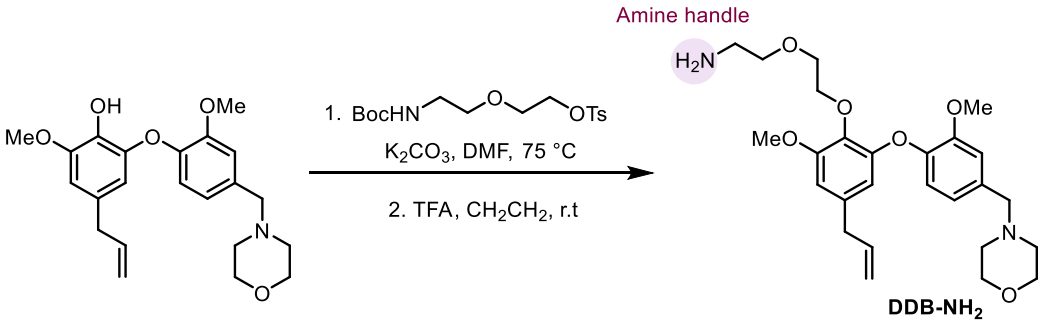

Scheme 4. Synthesis of amine analogue **DDB-NH₂** for attachment to beads *via* an amide linkage.

Following synthesis, **DDB-NH$_2$** and *L. mexicana* promastigote lysate were given to collaborator Ludwig Bauer (Target Discovery Institute, University of Oxford) who carried out the pull-down experiment. Briefly, **DDB-NH$_2$** was amide-linked to beads to create a compound–bead matrix. This was used for protein pull-down from lysate in competition with **DDB-1** as well as in comparison to null beads to look for protein enrichment, and then any proteins eluted from the beads were detected by mass spectrometry. The mass spectrometry data showed no highly enriched and competed proteins pulled-down from the cell lysate i.e., this approach was unsuccessful. This is not a surprising result given that PAL was necessary for compound visualisation in whole-cell labelling (Section 3.5.2), and we do not expect a strong target engagement from the DDB scaffold itself.

4.4.2 Photoaffinity labelling (PAL) for protein pull-down

The real advantage of using PAL for protein pull-down is the ability to bind proteins *in situ* which we hoped would be successful where bead immobilisation failed. A recent review by Wyllie *et al.* notes that "The use of photoactivatable linkers (PAL) to facilitate chemical pulldowns … has yet to be applied to drug target identification studies in kinetoplastids".[261] PAL compatible **DDB-PAL** showed excellent results for cellular compound localisation (Section 3.5.1) and should therefore be transferrable to protein pull-down experiments. The diazirine for PAL will enable strong binding between the compound and its target, after which the compound–target complex can be "fished out" using CuAAC to biotin azide *via* the alkyne handle, and streptavidin affinity purification (Figure 53).

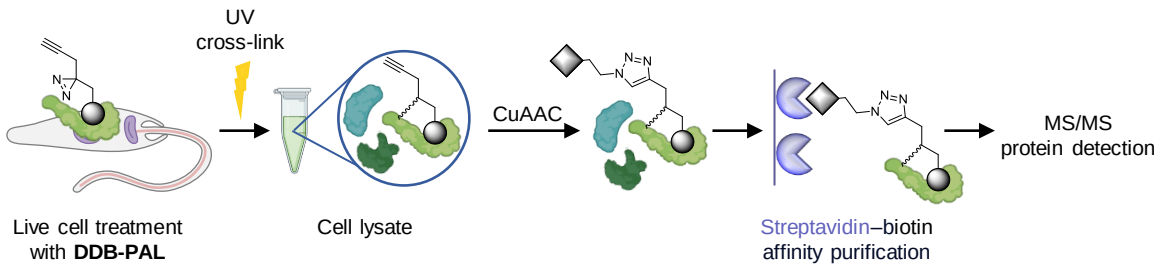

Figure 53. Schematic for photoaffinity labelling and affinity purification to pull-down interacting proteins of **DDB-PAL**. *L. mexicana* promastigotes are treated with **DDB-PAL** represented as a cartoon chemical structure. This is UV cross-linked to the interacting protein (green) before cells are lysed. Cell lysate undergoes the CuAAC reaction to attach biotin (grey diamond) which is used to pull-down the cross-linked protein using streptavidin beads (purple).

4.4.2.1 In-gel visualisation of interacting proteins using TAMRA dye

Before proceeding with costly mass spectrometry experiments, we first validated that **DDB-PAL** could label proteins by using CuAAC to a fluorophore–azide. *L. mexicana* promastigotes treated with **DDB-PAL** (at 6× EC_{50} to ensure a high level of labelling) under the standard PAL conditions were lysed, and the protein pellet submitted to CuAAC with red fluorescent TAMRA azide as the coupling partner. Controls with no **DDB-PAL** (0.1% DMSO), no UV and no click $CuSO_4$ catalyst were included to validate the method. In collaboration with Ludwig Bauer, protein precipitates were run on an SDS-PAGE gel to identify fluorescent bands corresponding to interacting proteins. Fluorescent bands were present in the samples treated with **DDB-PAL** under the full PAL and CuAAC conditions (Figure 54). Lack of TAMRA fluorescence in lanes C–E proves that **DDB-PAL**, UV light and $CuSO_4$ catalyst are all necessary, although the catalyst causes slight smearing of the protein bands (Coomassie, lanes A–D verses E). There was no obvious competition of bands by **DDB-1** (TAMRA lane A verses B).

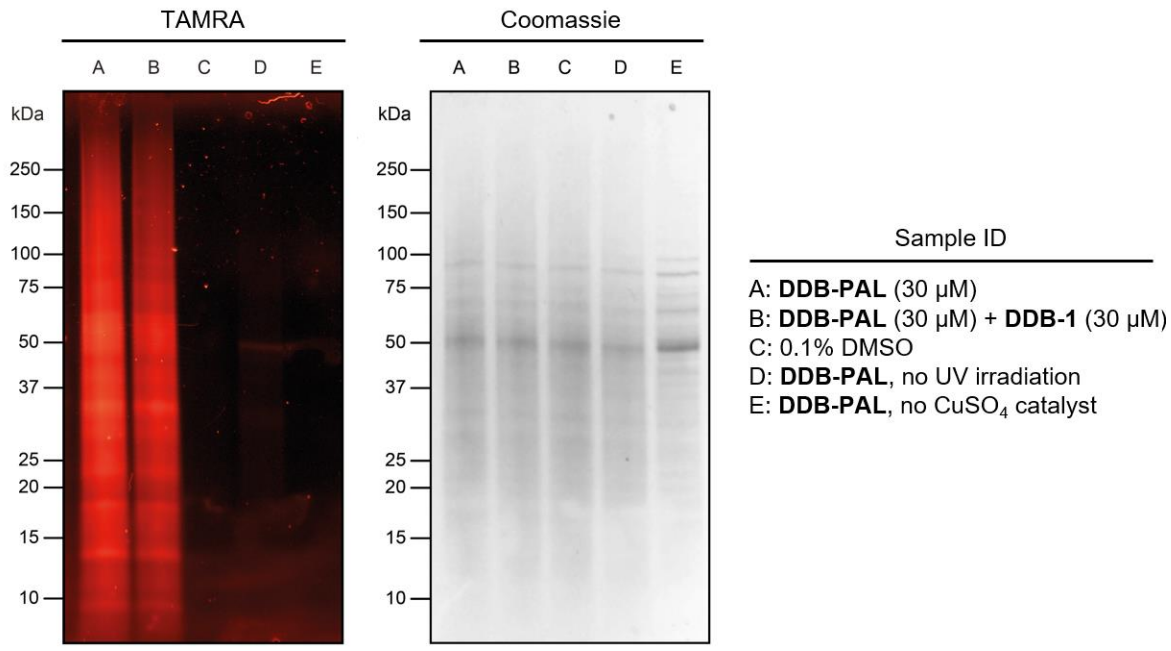

Figure 54. DDB-PAL labelled protein is detectable as bands on a gel. No protein bands were competed by **DDB-1** in the TAMRA fluorescence, protein loading is shown with a Coomassie stain.

4.4.2.2 Affinity purification of bound proteins for mass spectrometry

DDB-PAL was used for the pull-down experiment to generate proteins for mass spectrometry identification, alongside a competition experiment with **DDB-1**. The same conditions were used as for the in-gel visualisation with the CuAAC coupling partner changed to biotin azide. The sample was then enriched by streptavidin magnetic beads in solution and any unbound protein (flow through) removed (described in detail in Section 6.10.4). Proteins eluted from the beads were run on an SDS-PAGE gel and biotin-containing proteins detected by western blot to ensure there is detectable protein before mass spectrometry (schematic shown in Figure 55A).

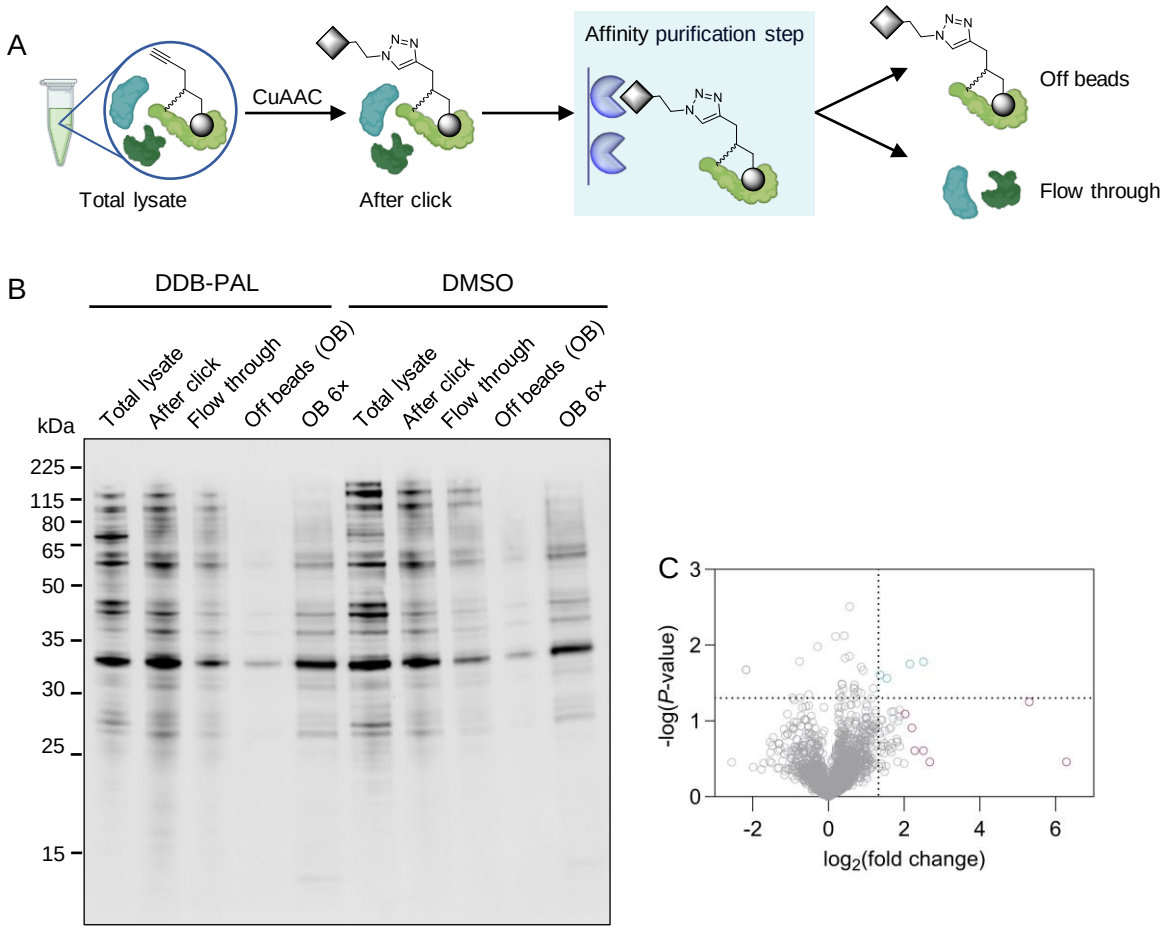

Figure 55. Pull-down with a **DDB-PAL**–biotin–streptavidin system did not identify any highly enriched proteins. A. Schematic to show the identity of protein samples on the western blot, detection of biotin (grey diamond). B. No extra protein bands appear in the western blot for samples cross-linked with 30 µM **DDB-PAL** and biotin CuAAC (off beads) compared to the input total lysate or the 0.1% DMSO treated control. Western blot detection with avidin HRP antibody. C. Volcano plot shows enriched proteins from **DDB-PAL** pull-down versus 0.1% DMSO. Proteins above the threshold *P*-value > 0.05 and fold change > 2.5 are highlighted in cyan, additional proteins with > 4-fold change are highlighted in magenta, $n = 4$.

The total cell lysate before CuAAC displays a characteristic pattern due to endogenous biotin (Figure 55B, Total lysate). Streptavidin bead capture of biotin was not very efficient: there is a relatively high detection of biotin in the flow through samples (Figure 55B, Flow through). Optimisation of the bead pull-down step included changing the incubation time for bead enrichment from 2 hours to 24 hours, and changing the exact bead composition, however none of these improved the efficiency based on the western blot. As the total protein eluted from beads was much lower than the protein samples at the other experimental steps it was run on the gel at 6× cell equivalents to enable bands to be seen (Figure 55B, OB 6×). There are no bands obviously appearing after biotin click in comparison to the initial total lysate therefore no protein being highly labelled. Nevertheless, the sensitivity of mass spectrometry could allow the detection of subtle changes. Samples were submitted for on-bead digest and mass spectrometry analysis by the mass spectrometry facility (Department of Chemistry, University of Oxford). With the resultant identified list of proteins we generated a volcano plot of the fold change between proteins enriched by the **DDB-PAL** pull-down verses control DMSO pull-down. Proteins were filtered to those detected with > 2.5-fold increase compared to the control (ensures a biologically interesting change), and a *P*-value for four replicates > 0.05 (ensures a statistically significant change). Only four proteins are above this threshold, labelled in cyan in the top right-hand quadrant of the plot (Figure 55C) and listed in Table 18.

Table 18. Gene identities for proteins above the thresholds: *P*-value > 0.05 and fold change > 2.5 (cyan), or fold change > 4 only (magenta).

LmxM Gene ID	Gene name	FC vs DMSO
19.0220	polyprenyl synthase, putative	5.68
14.0220	PX domain containing protein, putative	4.44
24.0300	hypothetical protein, conserved	2.91
28.0140	pantothenate kinase subunit, putative	2.57
27.0840	hypothetical protein, conserved	78.05
24.1350	hypothetical protein, conserved	39.56
05.1100	methyltransferase domain containing protein, putative	6.40
03.0520	hypothetical protein, conserved	5.68
08.0200	Inositol phosphosphingolipids phospholipase C	4.85
33.2270	Dynamin family, putative	4.62
21.0470	vacuolar sorting-associated-like protein	4.07

FC = fold change

Additionally, the seven proteins with > 4-fold change were included regardless of *P*-value (Table 18, magenta). A separate analysis of proteins that were undetected in the DMSO control sample but were detected at high proportions in **DDB-PAL** pull-down yielded another 29 proteins. Of the total list of 40 proteins, approximately 20 were competed by **DDB-1** at an appreciable level. This can be difficult to interpret as competition may not be a linear relationship. Each protein was evaluated for the likelihood of being a target protein involved in the MoA, however there was not time within the scope of this PhD for in-depth validation of these potential hits. Notably, none of the proteins detected overlapped with the results from the transcriptomics experiment or the genomic sequencing. In addition, due to time constraints the experiment was only performed once with four technical replicates so should be repeated to build on this pilot experiment.

4.4.2.3 Pantothenate kinase as a protein hit from pull-down

One of the identified proteins – LmxM.28.0140, encodes a putative pantothenate kinase according to TritrypDB, and there is only predicted to be one copy of pantothenate kinase in *L. mexicana*.[305, 448] This enzyme catalyses the conversion of pantothenate into 4'-phosphopantothenate which generates ADP from ATP in the process, as part of CoA biosynthesis.[449] Pantothenate is not synthesised *de novo* in trypanosomes but relies on uptake through pantothenate transporters.[448] I hypothesised that if **DDB-1** is disrupting the activity of pantothenate kinase *via* competitive inhibition, then additional pantothenate in the media could decrease **DDB-1** toxicity as more substrate is available. Normal growth media for *L. mexicana* promastigotes contains 21 nM of calcium pantothenate;[378] dosing of additional calcium pantothenate at 100 nM (5×) or 100 µM (5000×) did not shift the EC_{50} for **DDB-1** (Figure 56).

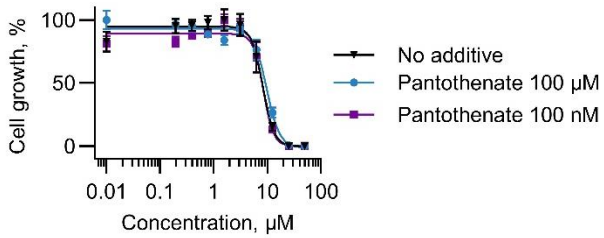

Figure 56. EC_{50} of **DDB-1** is unchanged in the presence of exogenous pantothenate. Representative dose-response curves for **DDB-1** in the presence of exogenous pantothenate, $n = 2$ biological replicates, each with 4 technical replicates. The mean is plotted with error bars representing standard deviation.

Therefore, despite being pulled down by the proteomics experiment, **DDB-1** is unlikely to be inhibiting pantothenate kinase.

4.5 Discussion

Three different parallel omics methods were applied to **DDB-1** to identify genes involved in MoA, mode of resistance, and direct interacting proteins. These experiments had mixed success, however piecing together information from the results including biological failure still allows for conclusions to be drawn. **Asci** was included in the genomics experiments that I ran in collaboration with the Wyllie group, and fared better than **DDB-1**, leading to genes of interest being identified with more certainty.

4.5.1 A wider perspective of the DDB treated transcriptomes

Cells have in-built feedback mechanisms to cope with normal cellular imbalances by upregulating or downregulating pathways as necessary, dependent on cell signalling to trigger a response. The action of drugs can lead to big regulatory changes in cells, either by causing cellular imbalance that triggers the relevant signalling pathway, or affecting the signalling pathway directly. These regulatory changes can be detected by transcriptomics, which was the intention with the **DDB-1** RNA-Seq experiment. If a drug disrupts a pathway normally regulated by cells, we would expect a characteristic transcriptome; for example, disrupted ER homeostasis triggers the unfolded protein response (UPR), and metal ion imbalance would regulate expression of metal ion transporters. However, if a drug inhibits/disrupts a part of the cell that has no feedback mechanism already in place, it could be difficult to detect affected targets or pathways.

The transcriptomes of drug resistant *Leishmania* have been published for all the major drugs.[297] These give characteristic transcriptome fingerprints for each drug mode of resistance: Amphotericin B causes 7-fold downregulation of 24-sterol methyltransferase (SMT) in keeping with a membrane disruption MoA. Pentavalent antimonials cause huge alterations in the transcriptome owing to their broad spectrum of resistance mechanisms including upregulation of metal transporters and multiple

transcripts on the trypanothione biosynthesis pathway, supporting a general antioxidant resistance response. Paromomycin causes 56-fold and 32-fold upregulation of D-lactate dehydrogenase-like protein and branched-chain amino acid aminotransferase respectively, which could allow for compensation of mitochondrial dysfunction alongside its ribosome interference MoA. Miltefosine mainly downregulates transcripts with the highest changes being only 3.6-fold. In comparison, **DDB-1** and **DDB-PAL** had no transcriptome changes greater than 3.5-fold and only 44 genes significantly changed, while the published drug transcriptomes had differentially expressed transcripts (> 1.5-fold change) ranging from 1006 (pentavalent antimonials) to 129 (paromomycin). Interestingly, hypothetical proteins LmxM.30.0453 and LmxM.30.0450c were among the most upregulated by **DDB-1** and **DDB-PAL** treatment, both of which have orthologs in other trypanosomatids annotated as amastins. The global overview of transcriptomes for the four anti-leishmanial drugs discussed above had an anomalously high number of amastins leading the authors to conclude "overexpression of amastin genes in *Leishmania* might lead to an increased parasite fitness against the cellular stresses elicited by drugs".[297] These however are changes in established resistance cell lines compared to susceptible lines, whereas our experiment was an investigation of 24 h treatment on susceptible parasites, necessitated due to the inability to select for resistance (Section 4.2.1). Quick-response transcriptome experiments in *Leishmania* include investigating heat shock in promastigotes at 37 °C after 2 h to look for immediate regulatory changes in *L. major*: this induces upregulation of mainly heat shock proteins (HSPs), with 52 upregulated and 76 downregulated transcripts (> 2-fold) overall.[450] The modest number of transcripts changed in the **DDB-1** and **DDB-PAL** treatment therefore is not attributed to the short nature of the experiment.

Comparison with transcriptomes in cells undergoing mitochondrial distress would be beneficial as this is involved in the MoA of **DDB-1**. Hughes *et al.* showed the power of comparative transcriptome analysis in yeast by demonstrating that the expression profiles for 300 diverse treatments cluster according to affected cellular pathway, which included a cluster for direct effects on mitochondrial function.[451] In mammalian systems with oxidative phosphorylation dysfunction, one report indicates that ubiquinone biosynthesis enzymes are downregulated, while enzymes of the mitochondrial single

carbon metabolism pathway are upregulated.[452] In another review, metallothioneins and HSPs are transcriptionally upregulated in mammalian complex I deficit, while oxidative phosphorylation deficiency causes differential expression of cyclin-dependent kinases, apoptosis indicators, and upregulation of UPR.[453] None of these responses, nor those for the *Leishmania* drugs (including the paromomycin upregulated compensation for mitochondrial dysfunction), overlap with the significantly upregulated and downregulated transcripts by **DDB-1** or **DDB-PAL**. The transcriptome fingerprint due to the DDB compounds has most similarities with the heat shock response, including downregulated transcripts for eukaryotic translation initiation factors, a fatty acid desaturase and the same LIT1 Fe^{2+}/Zn^{2+} transporter LmxM.30.3070. Our RNA-Seq results are of comparable quality to those published, but have such a small magnitude of transcriptome change that it will be a challenge to gain a conclusive mode of resistance result from them. This may be due to experimental design of generating the transcriptome for treated, susceptible cells. Nevertheless, a short further discussion on the transcripts is merited.

4.5.1.1 APX upregulation is in common with heat shock response

Interestingly, ascorbate peroxidase (APX) LmxM.33.0070 which was highly upregulated in our experiments also represented the highest upregulated protein following heat shock.[450] This protein catalyses the oxidation of ascorbate with H_2O_2 which has a protective effect against oxidative damage,[445, 454, 455] hence is upregulated in amastigotes to protect from macrophage oxidative burst,[456] and in amphotericin B resistance.[457] APX has an N-terminal signal peptide driving localisation to the mitochondrion[458] – the location of the **DDB-1** target protein (Section 3.5.1), and *in silico* models have shown it is capable of binding a quinazoline drug at a second binding site.[459] While this could plausibly be an interacting partner of **DDB-1**, APX was not detected in the PAL proteomics experiment and is more likely appearing in the RNA-Seq data as a general stress response.

4.5.1.2 DDB-1 has a weak effect on the TCA cycle

LmxM.33.0140 mitochondrial malate dehydrogenase (mMDH) is a part of the tricarboxylic acid (TCA) cycle, and was upregulated 2-fold by **DDB-1**. The TCA cycle is a series of biochemical

processes taking place within the mitochondrial matrix generating metabolites for biosynthesis and cell signalling.[460] *L. mexicana* promastigotes utilise the complete TCA cycle, its activity is required for growth, and it causes metabolite fluxes closely linked to the glycosome.[461] mMDH catalyses the conversion between malate and oxaloacetate, reducing NAD+ in the process and also functioning as a shuttle of reducing equivalents between the mitochondrion and cytosol.[462-464] Upregulation could decrease the amount of malate available while increasing the amount of oxaloacetate. Without in-depth analysis of the processes in the TCA cycle, a conclusion on the biological effect within the wider context of the cell cannot be drawn. It is likely that this upregulation corresponds to the respiration deficiency expected from mitochondrial dysfunction, requiring a greater reliance on glycolysis for energy production. A similar upregulation of transcripts for mMDH was observed in the yeast *Saccharomyces cerevisiae* that lack functional mitochondria and are absolutely dependent on glycolysis.[465]

4.5.1.3 Transcriptome overview indicates quiescence

Quiescence, a reversible non-proliferative state induced by external stresses is reported for *L. mexicana, L. braziliensis and L. major*.[466-468] Drug-induced quiescence in *L. lainsoni* promastigotes causes a global downregulation of transcripts and diminished translation.[469] Quiescence also causes a decrease in malate, accompanied by an overall downregulation of the TCA cycle.[469] **DDB-1** induces downregulation of eukaryotic translation initiation factor 1 and eukaryotic translation release factor, therefore a likely global reduction in translation, as well as inferred decrease in malate due to mMDH upregulation. Taken together this suggests a drug-induced quiescence by **DDB-1**. In the resistance generation experiments, any cells that emerged following compound incubation on plates had no sustained resistance to compound (Figure 39) which is further evidence of a quiescent state. Without quantification of total mRNA and a metabolomic fingerprint, this cannot be definitely confirmed.

4.5.2 DDB-1 inability to generate resistance

Resistance to all major anti-leishmanial drugs can be selected for in a laboratory with relative ease.[275, 280, 470, 471] On the one hand this is undesirable as it could indicate a high chance of drug resistance emerging in the field, although *in vitro* selection differs significantly and is not representative of real-use conditions. On the other hand, drug resistance generation *in vitro* can be exploited for MoA studies. **DDB-1** possesses an unusual inability to select for resistance, despite repeated attempts for over a year with all standard laboratory resistance generation techniques. Indeed the Wyllie group notes that "In our experience over several years, generation of resistance in *L. donovani* promastigotes *in vitro* is eminently achievable …", and have reported just one instance of failure.[208] This made it difficult to probe the MoA using standard resistance generation and whole genome sequencing, and could have contributed to the failure of **DDB-1** selection in the specialist overexpression and knockdown libraries. Of the genes that were identified in the libraries, all had a low number of reads (likely to be background), and there were no common gene identities between the three libraries. It is highly unusual that **DDB-1** did not perform well – this is a compound specific phenomenon as even in the case where the Wyllie group were unable to select for resistance in normal cell lines, the *T. brucei* overexpression library gave them meaningful hits.[208]

Failure to generate resistance to **DDB-1** indicates that if there is a direct binding target it cannot accumulate and sustain mutations i.e., any mutations which would confer resistance are themselves lethal. Poor selection even with the genome-wide libraries alternatively suggests a polypharmacology MoA in which multiple pathways are affected simultaneously, hence the libraries cannot be selected as they are unlikely to have the correct combination of overexpression and knockdown targets. The compound curcumin similarly cannot select for *in vitro* resistance against *T. brucei*, which is attributed to polypharmacology and a mechanism involving membrane fluidity.[472] While this lack of resistance is a limitation for MoA determination, it is a promising trait for **DDB-1** as a compound hit. Kinetoplastid phenotypic hits are often found to interact with the same few targets: CYP51, cytochrome bc_1 and the proteasome.[440] The RES-Seq *L. donovani* cross-resistance library has a good coverage of these targets including mutations in different binding pockets and

overexpression, as well as a breadth of other MoA although this is limited to only the 31 lines in the library. The important result that **DDB-1** has no hits in the RES-Seq library confirms a unique MoA. This is key for new hits given the increasing levels of resistance to established drugs and represents opportunities for use in drug combination strategies.

4.5.3 DDB-1 does not act *via* a metal chelation MoA

Metals play a vital role in eukaryotes, and the trypanosomatids are no exception. Metal ion chelation is a known MoA in trypanosomatids which works *via* decreasing the intracellular concentration of metal ions.[208] This MoA has been implicated in cases where resistance generation is not possible.[207] Despite the inability to generate resistance with **DDB-1**, metal chelation MoA is unlikely given other evidence.

First, metal ion importers LmxM.30.3060 and LmxM.30.3070 (LIT1) were downregulated in the transcriptome of **DDB-1** treated cells. These LIT1 ion transporters are responsible for transport of Fe^{2+} (preferentially) and Zn^{2+} from the extracellular space into the cytosol.[473, 474] LIT1 downregulation would decrease intracellular M^{2+} i.e., compounding the effect of a chelation MoA instead of counteracting it. Second, the activity of **DDB-1** was not modulated by exogenous Fe^{2+} or Zn^{2+} which would be expected in a chelation MoA as the exogenous M^{2+} provides a surplus of the required ions. Of note was the fact that Cu^{2+} did significantly decrease the toxicity of **DDB-1**, although it is unclear what effect the copper ions could be having on the compound. Third, the chemical structure of **DDB-1** does not have any obvious metal ion chelation sites. All proposed bidentate M^{2+} binding sites for **DDB-1** are *via* weakly binding aryl ether oxygen atoms, and are therefore unlikely (Figure 57). Finally, chelation MoA tends to be non-specific to cell type, however **DDB-1** maintains a high selectivity index for *Leishmania* and low mammalian cytotoxicity (Section 2.2.2, Table 5). This evidence is conclusive enough to rule out chelation as the MoA for **DDB-1**. This is a good result as the non-specificity of metal chelation MoA raises toxicity concerns and has previously led to the termination of an anti-trypanosomatid compound in development.[208]

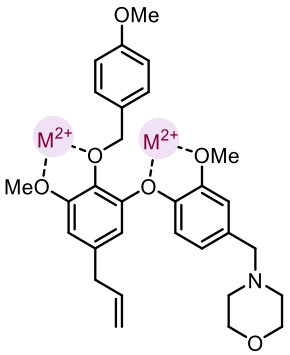

Figure 57. DDB-1 proposed M^{2+} chelation sites *via* ether oxygen are unlikely due to weak binding.

4.5.4 **Asci** partial success in the specialist libraries indicates ROS generation MoA

In the *T. brucei* library, knockdown of two putative nitroreductases (NTRs) Tb927.7.3020 and Tb927.7.2980 provide a selective advantage to parasite survival in **Asci** (Table 14). NTRs catalyse the reduction of aromatic nitro compounds such as the drugs benznidazole, nifurtimox and fexinidazole. Loss of NTR leads to resistance of these and other nitro aromatic compounds, which has been confirmed through resistance generation, gene knockout/knockdown and gene overexpression.[192, 291, 475, 476] The identification of putative NTRs in the knockdown screen of **Asci** is unexpected as there are no nitro groups in its structure. Oxygen insensitive NTRs of bacteria are known to reduce quinones as well as nitro aromatics *via* a two-electron "ping-pong" mechanism with low substrate specificity, which has also been shown for type I NTRs in *T. brucei*.[477-479] **Asci** could be behaving in a similar way to the quinone substrate in this mechanism (Figure 58).

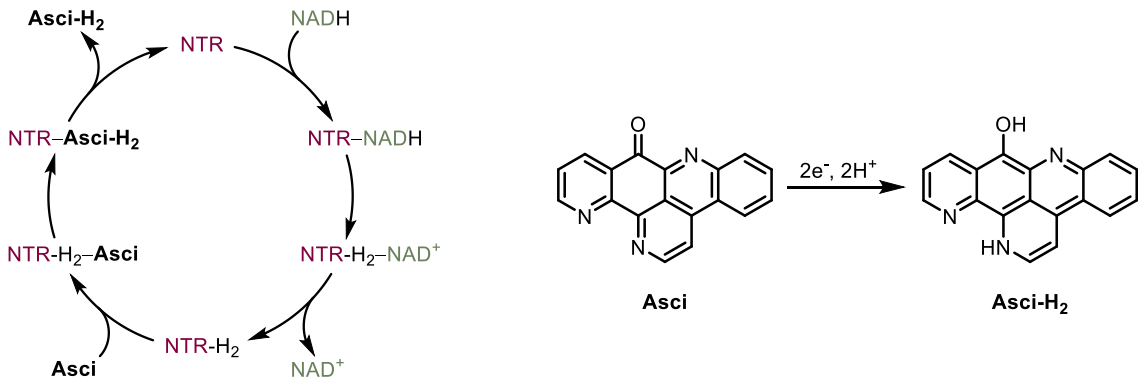

Figure 58. Proposed reduction of **Asci** *via* a two electron quinone-like mechanism with type I NTR.

Reduced **Asci-H_2** could have enhanced toxicity, and the mechanism could be the source of ROS predicted to play a role in the **Asci** MoA (previously discussed in Section 2.9.3). It is unexpected that **Asci** did not show cross-resistance with the NTR2 DKO or Fexi-ResC lines in the RES-Seq library: these are cell lines to which the nitroimidazole compounds are resistant, and have a deletion of NTR2 and functional deletion of NTR1 respectively.[440] The RES-Seq result could benefit from repeating at a concentration closer to 10× EC_{50}; even though this caused growth to crash irrecoverably, higher concentrations are recommended for efficient identification of high-level resistant cell lines.

Neither of the overexpression genomic libraries performed as expected with this compound: The *T. brucei* overexpression library did not have a good selection and no reads were detected. The *L. donovani* overexpression library produced a list of seven "highest confidence" proteins, but these did not encompass a large enough proportion of total reads to give confidence in the overall experiment (Figure 41). The identities of these genes additionally did not have any links to ROS which is the suspected MoA for **Asci**. It is unclear why **Asci** did not have good reads in the *L. donovani* overexpression library, as the treated cells grew slower than the control from day 0 to day 1 indicating a selection window. Although small, the window should have been sufficient to select for specific genes. It would be beneficial to repeat these experiments as there is scope to generate resistance by adjusting compound concentration during selection which could yield results that corroborate the nitroreductase hit. Alternatively, depending on the exact MoA for **Asci**, there may be no selective survival advantage in the case of overexpression, which is a fundamental requirement for the success of the libraries.[283]

4.5.5 Asci chelation of Zn^{2+} is a secondary effect to ROS generation

Asci is a chelator of divalent metal ions Zn^{2+} and Fe^{2+}, and has the ability to transport Zn^{2+} across a synthetic lipid bilayer (Yasmine Biddick, unpublished). This led us to investigate a chelation MoA for this compound. In both compounds with confirmed metal chelation MoA against *L. donovani*, [207, 208] a > 20-fold shift in EC_{50} is observed with the addition of exogenous Zn^{2+}. In our case,

exogenous Zn^{2+} only modestly reduced **Asci** potency < 5-fold, Fe^{2+} did not affect **Asci** EC_{50}, and counter to expectation intracellular Zn^{2+} was increased by **Asci** treatment in *L. mexicana*. Of note, no Zn^{2+} transporters were identified in the RNAi knockdown screen or indeed the *L. donovani* overexpression library. The published *L. donovani* chelation MoA examples have produced a fingerprint for expected genes overexpressed in *Leishmania* under chelation stress. Characteristic proteins include glutathione peroxidase, vacuolar-type proton ATPase, and putative vacuolar-type Ca^{2+} ATPase.[207] Of these, only glutathione peroxidase (LdBPK_260780) was present on one of the overexpression fragments in our screen, however the correct flanking barcodes could not be identified. Glutathione peroxidase has an antioxidant role,[480] although it has been suggested that in *Leishmania* the enzyme is not active unless under oxidative stress.[481, 482] This points towards a generation of ROS by **Asci** as discussed in Section 2.9.3.

Zinc has a diverse role within the antioxidant system: i) It binds to thiol groups preventing oxidation by sterically blocking thiol containing enzymatic sites and/or inducing a conformational change that prevents disulphide bridges from forming,[206, 483] ii) It competes with redox active metals for binding sites on enzymes that would otherwise generate oxygen free radicals,[206, 484] and iii) It indirectly interacts with the synthesis pathway for antioxidant glutathione (GSH).[205, 485] In *Leishmania*, zinc depletion corresponds to increased cytosolic ROS, presumably due to its role as an antioxidant.[486, 487] The addition of exogenous zinc could therefore provide an antioxidant benefit, or additionally sequester **Asci**, thus decreasing its ROS generating capabilities and explaining the decreased **Asci** toxicity. This is also consistent with Fe^{2+} having no effect on **Asci** toxicity as it is not involved in the antioxidant pathway. Zn^{2+} chelation is therefore likely to be a secondary result, while ROS production is the main MoA.

Overall, the omics experiments were reasonably productive. While they did not completely elucidate the MoA for **DDB-1** as initially hoped, they revealed an unusual compound inability to generate resistance, and they do not contradict the hypothesised mitochondrial MoA. The **Asci** experiments were significantly more successful, with the genomics data enabling the proposal of a mechanism for ROS generation. This should be followed up with experiments to confirm the interaction between

Asci and NTRs, such as incubation with cellular extracts or even purified NTRs followed by metabolomics analysis.

5 Perspectives and Conclusion

Leishmaniasis remains a huge threat to global health, and the contributions of increasing drug resistance to treatment failure should not be underestimated.[488] There are currently only five drugs licenced for use, and five new compounds in clinical development for visceral leishmaniasis (as of June 2024) (Figure 59).[163] Within this drug development pipeline there are already toxicity concerns for both DNDI-6148 and DNDI-0690,[166, 167] while GSK245/DDD01305143, LXE408 and pre-clinical candidate DNDI-8526 (not shown) target the proteasome, i.e., limited to a common MoA.[198-200] There clearly remains a need for novel compounds to combat this disease, which should have a distinct MoA from those already in use or under development, both to enable combination therapy and decrease the chances of cross-resistance. One might expect that validated *Leishmania*-specific targets would be best suited to explore for new MoA as these should have fewer off-target mammalian toxicity concerns. In reality, no compounds against these targets have progressed far in the drug pipeline, and all the small molecule compounds in late-stage development

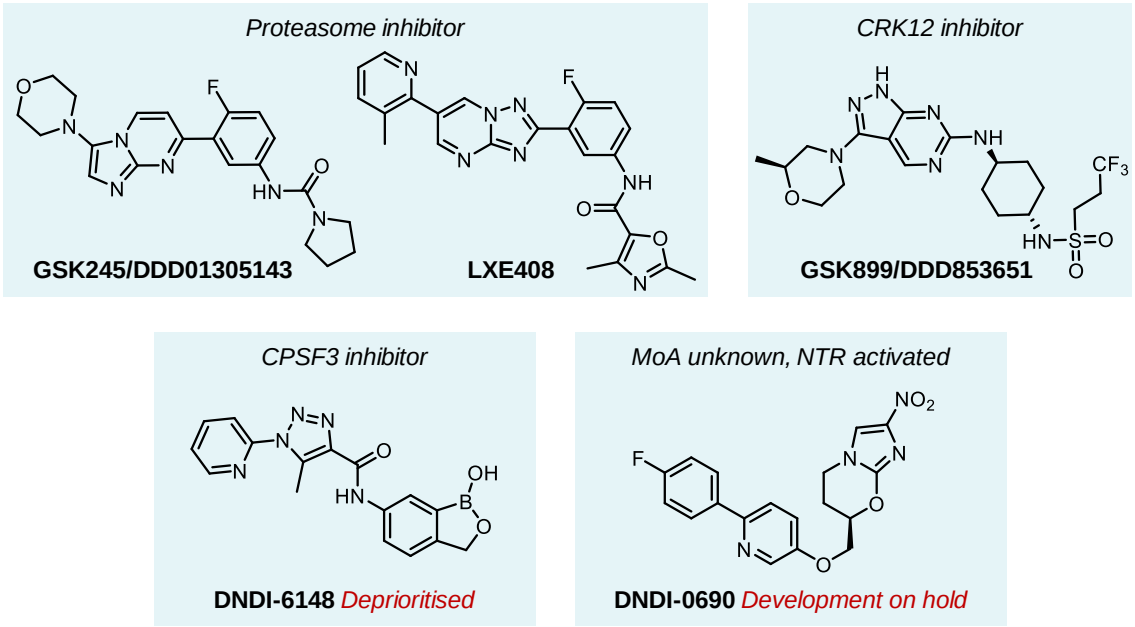

Figure 59. New chemical compounds in clinical development for visceral leishmaniasis (as of June 2024). Modes of action are indicated, both DNDI-6148 and DNDI-0690 have reported toxicity concerns.

were discovered through phenotypic screening.[152, 198, 201, 489-491] Amphotericin B relies on a stronger binding to ergosterol than cholesterol, which is not found in mammalian cell membranes,[492] antimonials cause a loss of trypanothione and inhibit trypanothione reductase – a parasite-specific thiol,[195] and pentamidine acts on kinetoplast DNA.[176] Not all MoA rely on parasite-specific pathways; some compounds can instead capitalise on subtle differences between the host and *Leishmania* biology. The clinical candidate inhibitors of the proteasome bind to a specific chymotrypsin-like binding pocket between the β4 and β5 subunits that is absent in the human orthologue.[198, 199, 493] The *T. brucei* target CRK12 has a 35% sequence homology with the human CDK13, which could account for the selectivity of GSK899/DDD853651.[201, 304] There is a steric clash with a tyrosine in the human CPSF3 binding pocket with the oxaborole compounds, which is absent in *T. brucei* and *Leishmania*.[285, 491] This shift towards more sophisticated MoA coincides with modern medicinal chemistry programmes, in which rational compound design is guided by *in silico* docking studies to capitalise on human and parasite differences, making use of AlphaFold and RoseTTa fold modelling in the absence of a protein crystal structure.[494, 495] Some MoA are considered undesirable, particularly biochemical responses likely to affect all cells. We would expect that a metal chelation MoA is unfavourable, with no way to control selectivity for parasites over the host, and an indiscriminate ROS generation is also likely to be host toxic. CYP51 and cytochrome bc_1 inhibitors have been identified as undesirable MoA, due to a non-cytocidal effect and a high potential for resistance generation respectively.[496, 497] Other mitochondrial poisons could be of concern due to the essentiality of the mitochondrion for host survival, but crucially, these present opportunities for selectivity given the evolutionary divergence between a *Leishmania* mitochondrion and a mammalian one.[62, 498]

In this context, **Asci** is immediately highlighted as a bad drug candidate. Its MoA is likely to involve ROS generation with contributions of metal ion chelation – both of which could cause severe mammalian toxicity. This is observed in the low nanomolar activity against HepG2 cells which is of concern (Section 4.2.2, Table 10). The **BI** compounds were not investigated to a great degree, but their similarities to **Asci** (planar aromatics with DNA intercalating abilities) mean we anticipate these

to be poor candidates as well. **DDB-1** on the other hand poses an interesting question, is this a good hit? The chemical structure of **DDB-1** does not raise any immediate concerns: it fits within the DND*i* criteria for a hit against leishmaniasis – requiring a tractable chemotype amenable to structural variation,[349] and is considered drug-like by our ADMET analysis (Section 2.2.3, Table 7). In comparison, the approved drugs have highly "un-druglike" chemical structures that violate many ADMET guidelines (Figure 60). Miltefosine and pentamidine fit within these guidelines, but have unusual chemical structures that have been linked to poor solubility, being detergent-like and symmetrical, respectively.[499] In a modern drug discovery programme, these drugs would probably not have made it to the clinic. Compounds in the development pipeline show a shift towards drug-likeness – this could also be due to more stringent safety profiles required for new drugs, increasing the priority of ADMET behaviour.[349]

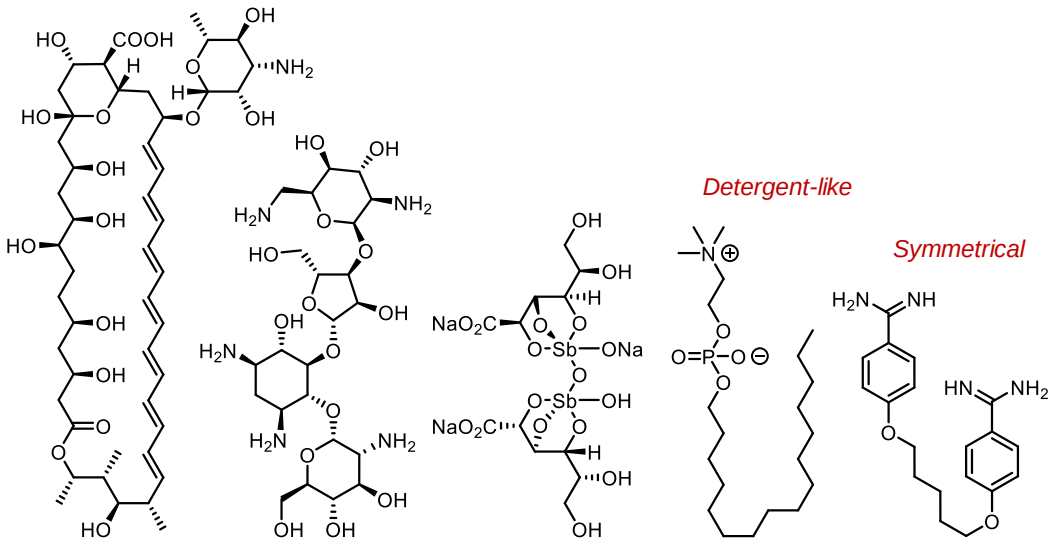

Guideline	AmB	Paromomycin	Na stibogluconate	Miltefosine	Pentamidine
Lipinski	×	×	×	✓	✓
GSK	×	×	×	×	✓
Golden Triangle	×	×	×	✓	✓

Figure 60. Approved drugs for leishmaniasis have "un-druglike" chemical structures with corresponding poor ADMET predictions. General guidelines for ADMET rules based on structure are Lipinski (Mw ≤ 500, logP ≤ 5, H-bond acceptors ≤ 10, H-bond donor ≤ 5), GlaxoSmithKline (Mw ≤ 400, logP ≤ 4) and Golden Triangle (200 ≤ Mw ≤ 50, −2 ≤ logD ≤ 5), predicted using ADMETlab 2.0, admetmesh.scbdd.com.[342]

It is not necessary to determine the MoA of a compound for it to proceed in the drug discovery pipeline, and yet it is becoming increasingly expected. Given the fact that many drugs have no clear MoA, and no new anti-leishmanials have emerged *via* target-based drug discovery, we could question how useful MoA information is. Both miltefosine and the pentavalent antimonials work through multiple different MoA that would probably frustrate an elucidation programme if MoA determination had been required in advance of drug approval. On the other hand, MoA studies can be an important risk-mitigation step in drug discovery pipelines, both from a safety and monetary investment point of view, and as a predictor of eventual long-term success in the field. Early drug discovery guidelines (in an anti-cancer context) estimate a $0.5 million cost of target identification, but potential losses of over $1.9 million for failure as early as during pre-clinical investigations, a failure which is more likely in the absence of a known target.[500] Perhaps it is not a coincidence that the only compound in the leishmaniasis drug discovery pipeline to be completely put on hold has an unknown MoA (Figure 59).

5.1 A critical evaluation of MoA determination methods

In this thesis we used a five-pronged approach to MoA deconvolution for three different compound families, highlighting that different techniques are best suited to different MoA, depending on the exact compound family. In our experience, the easiest approach is a phenotypic evaluation and carrying out biochemistry assays. While interesting, these were least informative to a specific MoA such as interacting target(s) or pathways, and were most likely to detect downstream responses or general cell-stress effects. These experiments were an initial indication that **DDB-1** does not cause drug-related stress changes to the cell cycle, unlike **Asci** and the **BI**s. They did confirm mitochondrial involvement for **DDB-1** and ROS generation for **Asci**, but cannot determine a target.

Whole genome sequencing of resistant cell lines is a well-established method for informing both on MoA and on modes of resistance, with successful applications in retrospectively elucidating the MoA for approved trypanosomatid drugs,[297, 501] summarised in a 2020 review.[502] This was initially an appealing approach for us since no specialist cell libraries are required, and with the availability

of the complete, annotated *L. mexicana* genome, it is a very accessible technique.[82] Despite its proven track record, we met with complete failure at selecting for **DDB-1** resistance in both wildtype and mutagenised *L. mexicana* (Section 4.5.2). Selection efforts are ongoing for **Asci** and **DDB-1** in *L. donovani* by collaborators, it remains to be seen if these will be successful – we suspect not in the case of **DDB-1**. We turned to transcriptomics experiments as an alternative that should show immediate gene expression changes in response to compound, without the need for resistant cell lines.[450] Here, the lack of highly changed transcripts was another confirmation that *Leishmania* cannot easily overcome **DDB-1** by regulating its genome expression, although this could have been due to the experimental design.

There are excellent examples using genome-wide libraries for MoA determination by the Wyllie group: Target overexpression in *L. donovani* identified oxidosqualene cyclase as a drug target,[276] and both *L. donovani* and *T. brucei* overexpression were used to validate *N*-myristoyltransferase as a drug target.[284, 285] Knockdown with the *T. brucei* RNAi library identified cyclin-dependent kinase CRK12 and the proteasome as targets,[198, 304] and identified a chelation MoA for the 8-hydroxy-naphthyridines.[208] A placement at the University of Dundee allowed me to access these specialist libraries for screening with **DDB-1** and **Asci**, which we anticipated would succeed where traditional resistance selection had failed. Once again, **DDB-1** was not suited to this methodology, which we suspect is related to the inability to select for resistance in the wildtype cell lines. For **Asci**, although the overexpression libraries did not yield any results, the knockdown library identified nitroreductases as hits, which was directly informative to its proposed ROS generation MoA. These libraries rely on overexpression or knockdown leading to a selective advantage which may not always be the case, and could account for the failure of **Asci** in the overexpression libraries.[283] The libraries are at the cutting edge of MoA deconvolution, but care should be taken not to end up with an overreliance on these methods, as that will introduce an implicit bias towards compounds benefiting from overexpression or knockdown, and, as we demonstrate with **DDB-1**, not all drug-like compounds are suitable.

Chemo-proteomics should be the gold standard as this is the only way to conclusively show drug–target engagement. We did not attempt thermal proteome profiling (TPP) due to the expensive nature of this experiment, the requirement for saturating concentrations which would use large quantities of compound, and the lack of other target identification – it could have provided a good target validation method had the project reached that stage, and justified the investment. Protein pull-down using photoaffinity labelling did not generate a conclusive result for **DDB-PAL** (Section 4.4.2). This method is complex and would require further optimisation to ensure that adequate sensitivity is achieved, and is worth repeating – this was not done due to time constraints. Although protein pull-down has the potential to be highly informative, the need for an immobilised compound or PAL probe is a limitation not to be underestimated, and prevented its use on **Asci** or the **BI** compounds.

For the DDB compounds, whole-cell fluorescence localisation proved to be the most informative to MoA. We had initially anticipated this as a supporting result to a complete picture involving a determined pull-down target and genomic evidence. The time and effort invested in synthesising **DDB-PAL** and optimising this application was able to yield a localisation consistent with the hints of mitochondrial function that were known before the start of this project.[320] The localisation imaging

Increasing difficulty of technique ↑

	DDB-1	Asci	BI-1/BI-2	Information potential
Protein pull-down	*To repeat*			++
Whole cell localisation	✓			+
Genome-wide libraries	×	✓		++
Resistance generation and WGS	×			++
Transcriptomics	*Inconclusive*			+
Mitochondrial biochemistry assays	✓	✓		–
Phenotype and cell cycle changes	✓	✓	✓	–

Figure 61. Success and failure of each MoA determining technique applied to **DDB-1**, **Asci** and the **BI** compounds. An overview of the different methods used in this thesis, ordered from hardest to easiest to implement, in our opinion. A tick represents that successful information was gained from the experiment; a cross represents experimental failure. Transcriptomics was marked as inconclusive for **DDB-1**: it did not result in a changed transcriptome, but it is unclear if that is the correct biological result or a failure due to the method design. Information potential is ranked from – (least) to ++ (most) for the likelihood of each technique to lead to a conclusive MoA, in our opinion.

success also gives us the confidence to recommend repeating the protein pull-down as there are target(s) being bound. Applying this photoaffinity labelling to TEM detection was a challenge, and was not as informative as hoped – this is likely to be the case regardless of compound family and so should not be included as a routine MoA investigation. We are pleased however to report successful TEM imaging of gold nanoparticles clicked to a synthetic small molecule probe, and anticipate that this could find other applications in answering fundamental cell biology questions.

A good MoA determination project should be a combination of both target engagement investigation such as photoaffinity probing, and genomics and/or transcriptomics experiments. Another key approach is metabolomics, although this was not carried out for **DDB-1** and **Asci**. The use of multiple orthologous unbiased approaches then gives confidence in the determined MoA. Any compounds with activity can and should be investigated for morphology and biochemical changes to get an initial MoA picture. We would recommend that resistance generation should also be attempted – with specialist cell libraries if these are available – as this could lead directly to a target that can then be validated. In the event that genomics approaches fail, it becomes worth the synthesis of specific probes, but this should only be employed where SAR is known and/or synthetically accessible compound families are under investigation. Synthetic expertise is additionally required to enable access to the probe compounds which may not always be possible. We would comment that there should not be an overreliance on generating drug-resistant lines: if these are the main determinant of MoA (and if MoA knowledge is recommended for a drug candidate progression), then only candidates that can easily select for *in vitro* drug resistance will be progressed. With hindsight, MoA determination for the DDB family should have focussed more on the photoaffinity cross-linking for protein pull-downs, and placed less emphasis on resistance generation which we hoped would elucidate modes of resistance informative to MoA. As far as we are aware, there is no way to predict the success of a drug compound in the resistance selection approaches, so we could not have known this in advance. The approach of focussing on genomics methods worked well for **Asci**, and highlights that there is no "best way" to design such a project.

5.2 Biological interpretations and future work

Prior to this thesis, the DDB family was known to be active in *L. donovani*, *L. infantum*, and *T. cruzi*, and to cause some mitochondrial disruption in *L. infantum* promastigotes.[313-320] We have shown that it is additionally active in the species *L. mexicana* and *T. brucei* (Section 2.4, Figure 14). Particularly notable is the result in bloodstream forms and the implications this has on the nature of mitochondrial dysfunction, i.e., that oxidative phosphorylation cannot be the directly targeted pathway or the only pathway affected. Biochemistry assays showed an increase in mitochondrial Ca^{2+} and a decrease in ATP upon treatment, which is supporting evidence for a mitochondrial MoA. We have carried out SAR analysis which enabled us to develop a probe to confirm mitochondrial localisation, although we have not yet discovered a definitive target or MoA. **DDB-1** does not behave expected for a typical drug-like molecule: it does not disrupt the cell cycle, the treated transcriptome remains unaltered, and we cannot select for resistant cell lines. Metabolomics was not carried out – it could be interesting to monitor any changes in the metabolome upon treatment, although being sceptical this may remain largely unchanged, as with the transcriptome. The **DDB-1** compound could form interesting metabolites *in situ* as it is an electron-rich aromatic, prone to oxidation by cytochrome P450s.[503] Metabolites of **DDB-1** were not investigated, but could additionally explain the potentially

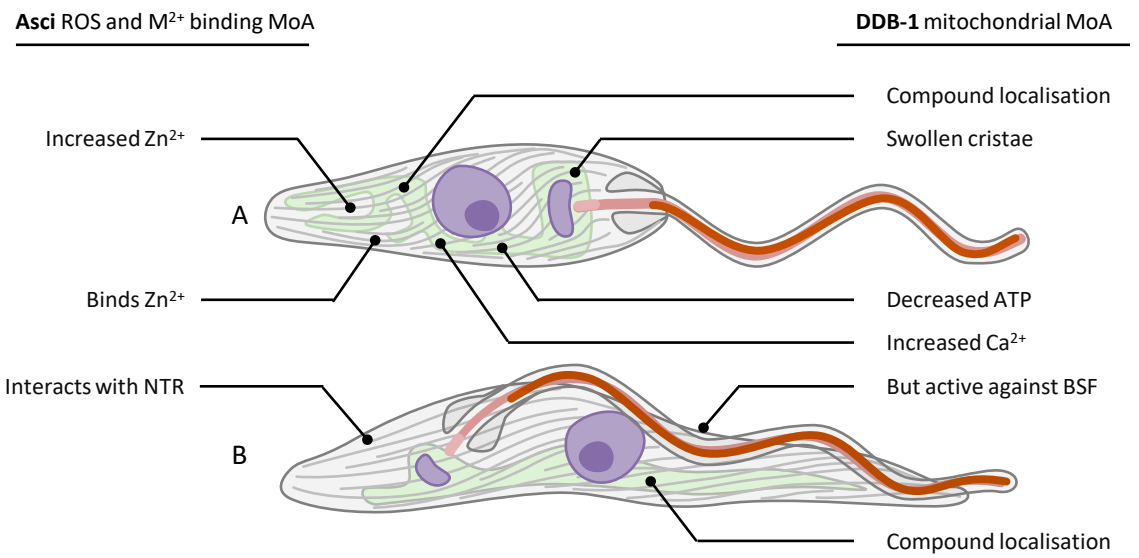

Figure 62. Evidence for a ROS and M^{2+} binding MoA for **Asci** and a mitochondrial MoA for **DDB-1**. Summary of key results in *L. mexicana* and *T. brucei* for each compound are shown represented on a *L. mexicana* promastigote (A) or *T. brucei* bloodstream form (B), for experiments in the respective species. Image adapted from Richard Wheeler.

complex, multi-target mechanism suspected. For **Asci**, we propose a ROS generation MoA (in keeping with its anti-cancer activity), which could be tied to its metal ion binding capabilities, particularly Zn^{2+}. Initial investigations into the **BI** family indicate it disrupts the cell cycle, typical of a stress-causing drug. Based on the ROS generation and metal chelation information gained from experiments in **Asci**, we would recommend that it is not investigated further. Although MoA determination was not exhaustive, early indications show a likelihood of toxicity issues, and a similar result is expected for the **BI**s. **DDB-1** remains an interesting hit – and one possibly acting *via* multiple targets. The inability to generate resistance can be viewed as an advantage, and with repeated protein pull-down experiments a target may yet be determined – likely a mitochondrial protein. A known target would allow investigation of binding affinities, rational analogue design, and contribute a (hopefully) novel target to the existing knowledge.

Although **DDB-1** has favourable ADMET predictions, improvement is still required and therefore the scaffold should undergo further hit to lead optimisation, ideally aided by knowledge of the target. During the timeframe of this MoA project, **DDB-1** has undergone preliminary *in vivo* pharmacokinetic studies in rats by our collaborators.[320] It has a reasonable half-life of 31.4 h (males) and 10.7 h (females), the maximal concentration is reached sufficiently rapidly, and is sustained for long enough to ensure therapeutic action.[320] A mitochondrial MoA is promising (pentamidine is also a mitochondrial accumulator)[176] and this could be confirmed with further experiments: Attaching a lipophilic cation – such as a triphenyl phosphonium or quinolinium – to **DDB-1**, or modifying the structure to include a charged quaternary amine on the morpholine ring should lead to mitochondrial targeting and accumulation; if the targeted analogue has an increased activity this could prove a mitochondrial target, as has been shown with inhibitors of the trypanosome alternative oxidase.[504] **DDB-1** maintains a high selectivity index of > 20.6 in *L. infantum* amastigotes over mammalian cells, which is superior to miltefosine (Section 2.2.2, Table 5). It remains to be seen if this translates to *in vivo* efficacy, which should be addressed in future experiments. An inability to determine MoA should certainly not preclude this compound from continued investigation – it remains a promising hit.

6 Methods

6.1 Trypanosomatid culture

6.1.1 Cell lines and *in vitro* culture

Promastigote Cas9T7 *L. (L.) m. mexicana*, referred to as *L. mexicana* (derived from the World Health Organisation strain MNYC/BZ/62/M379, expressing Cas9 nuclease and T7 RNA polymerase)[269] were grown at 28 °C in M199 medium: M199 containing Earle's salts and L-glutamine (Gibco, 31100019) supplemented with 10% v/v heat inactivated South American origin foetal calf serum (FCS) (Gibco, 10500064), 5 mM 4-(2-hydroxyethyl)-1-piperazineethanesulfonic acid HEPES·NaOH (pH 7.4), 26 mM $NaHCO_3$ and 5 μg/mL hemin (Sigma-Aldrich H9039).

Axenic amastigote *L. mexicana* were grown at 34 °C with 5% CO_2 in SM5.5 medium: Schneider's *Drosophila* medium (Gibco 21720024) supplemented with 20% v/v heat inactivated South American origin FCS and 25 mM 2-(N-morpholino)ethanesulfonic acid (MES)·HCl (pH 5.5).

Procyclic *T. brucei brucei*, referred to as *T. brucei* (strain 927 1339 Cas9 TetR t7RNAP, derived from the reference strain TREU 927/4, expressing Cas9 nuclease, T7 RNA polymerase and tetracycline repressor TetR) were grown at 28 °C in SDM79 medium: Life Technologies special order (reference 07490916), supplemented with 10% v/v heat inactivated South American origin FCS, 24 mM $NaHCO_3$ and 7.5 μg/mL hemin (pH 7.3).[505]

Bloodstream form *T. brucei brucei*, referred to as *T. brucei* (reference strain Lister 427) were grown at 37 °C with 5% CO_2 in HMI9 medium: HMI9 supplemented with 15% v/v heat inactivated South American origin FCS, 36 mM $NaHCO_3$ and 5 μM β-mercaptoethanol.[506]

L. donovani 1S2D (World Health Organisation strain MHOM/SD/62/1S-CL2D) also known as LdBOB were used for experiments in collaboration with the Wyllie group, University of Dundee. Promastigotes were grown at 28 °C in LdBOB promastigote medium and axenic amastigotes were grown at 37 °C with 5% CO_2 in LdBOB amastigote medium.[507]

For all trypanosomatids, sub-culturing maintained a continuous log-phase culture with a density between 1×10^5 and 1×10^7 cells/mL (*Leishmania* and *T. brucei* procyclics), or below 2×10^6 cells/mL (*T. brucei* bloodstream forms). Culture density was measured using an Improved Neubauer haemocytometer. Media used for culturing cells was filter-sterilised using units with a 0.22 µM membrane (Corning, Millipore). Lack of mycoplasma contamination was confirmed by regular fluorescence microscopy with Hoechst 33342 DNA stain.

6.1.2 *In vitro Leishmania* promastigote differentiation to amastigotes

Promastigote *L. mexicana* was subcultured to 1×10^6 cells/mL followed by 3 days incubation to achieve stationary phase promastigote cells. *In vitro* differentiation to axenic amastigotes was induced by subculture to 1×10^6 cells/mL, direct dilution into SM5.5 medium.

6.1.3 Generation of clonal cell lines

Clonal *L. mexicana* promastigote cell lines were obtained by limiting dilution. A mid-log population of cells was diluted to 0.5 cells/mL in 20 mL modified M199 (M199 medium as described previously with an additional 10% FCS, 0.1 mM adenine hemisulfate (Sigma-Aldrich) and 1.2 µg/mL biopterin (Sigma-Aldrich)). 200 µL/well was dispensed into a 96-well plate and incubated at 28 °C in 5% CO_2 until turbidity indicated that a dense culture had been achieved (expected positive wells ≈ 5/96, 7–10 days). Cells harvested from selected wells were used for further analysis.

6.2 CRISPR-Cas9 mediated genome editing

L. mexicana promastigotes were genetically modified using CRISPR-based genome editing.[269, 508] The parental *L. mexicana* cell line was regularly drugged with 32 µg/mL hygromycin B and 50 µg/mL nourseothricin sulfate (Cambridge Bioscience Ltd) to ensure maintained expression of Cas9 nuclease and T7 RNA polymerase. Prior to transfection, cells were grown without any selection drugs for at least 24 h. Constructs and single guide DNA (sgDNA) for genome editing were generated using the long primer polymerase chain reaction (PCR) method.[269, 509]

In brief, protospacer adjacent motif (PAM) sites for single guide RNAs (sgRNAs) were taken from the database generated for *L. mexicana* MNYC/BZ/62/M379.[269] These were designed by searching a 105 base pair window upstream of the start codon and downstream of the stop codon using the eukaryotic pathogen CRISPR guide RNA/DNA design tool,[510] (Parameters: SpCas9; gRNA length 20; PAM NGG; off-target PAM NAG, NGA). Homology arms for repair constructs were the 30 base pair sequences immediately adjacent to the sgRNA target sequence. sgDNA encoding the CRISPR sgRNA and a T7 polymerase promoter was generated by templateless PCR, with one primer encoding the gene-specific PAM site and T7 promoter, and the other encoding the remainder of the sgRNA.

Endogenous tagging used repair constructs generated with the pLPOT plasmid series as template DNA, where the long primers introduce 30 base flanking homology arms to a fluorophore and drug-selectable marker encoded in the template plasmid.[509, 511] For endogenous tagging with mNeonGreen (mNG), the plasmids: pLPOT mNG/Puromycin or pLPOT mNG/Neomycin were used as the template. For endogenous tagging with HaloTag (Halo), the plasmid pLPOT Halo/Puromycin was used as the template. For N-terminal tagging, the sgRNA targets CRISPR cutting just upstream of the target ORF, for C-terminal tagging the CRISPR cutting target is just downstream of the target ORF. The flanking arms are homologous to the 5' UTR and start of the ORF for N-terminal tagging, and the end of the ORF and 3' UTR for C-terminal tagging. Deletion of each allele to generate a knockout mutant used the pT plasmid series as template DNA,[269] where the long primers introduce 30 base flanking homology arms to a drug selectable marker. A different drug was always used per allele to generate a deletion mutant cell line. For deletion of each allele of a gene, the plasmids: pT Puromycin, pT Neomycin, or pT Blasticidin were used as the template.

Primer sequences for constructs and sgRNA were designed as described and accessed from LeishGEdit (http://www.leishGEdit.net).[508] All cell lines created are listed (Table 19); full primer sequences can be found in the appendix (Section 7.3.1, Table 21).

Table 19. *L. mexicana* promastigote endogenous tagging and deletion mutant cell lines created by CRISPR-Cas9 with their corresponding gene ID, gene name defined by TritrypDB, and drug selection marker used.

Cell line name	Gene ID	Gene name	Drug marker
mNG::RAD51	LmxM.28.0550	DNA repair protein RAD51, putative	Puro
mNG::TIM17	LmxM.09.1130	mitochondrial import inner membrane translocase subunit TIM17, putative	Puro
Halo::TIM17	LmxM.09.1130	mitochondrial import inner membrane translocase subunit TIM17, putative	Puro
mNG::GAPDH	LmxM.29.2980	glyceraldehyde 3-phosphate dehydrogenase, glycosomal	Neo
Halo::S11	LmxM.20.1650	ribosomal protein S11 homolog	Puro
Halo::RAB5A	LmxM.18.1130	Ras-related protein Rab5A, putative	Puro
Halo::ATOM14	LmxM.24.0940	archaic translocase of outer membrane 14 kDa subunit, putative	Puro
CPA::Halo	LmxM.19.1420	cysteine peptidase A (CPA)	Puro
SPT::Halo	LmxM.33.3740	serine palmitoyltransferase-like protein	Puro
ALDH::Halo	LmxM.36.1760	aldehyde dehydrogenase, putative	Puro
Hyp0130::mNG	LmxM.04.0130	hypothetical protein	Puro
mMDH::mNG	LmxM.33.0140	malate dehydrogenase	Puro
CYP450::mNG	LmxM.27.0090	cytochrome p450-like protein	Puro
APX::mNG	LmxM.33.0070	ascorbate peroxidase, putative	Puro
NMT::mNG	LmxM.03.0600	arginine N-methyltransferase, putative	Puro
eRF::mNG	LmxM.27.1710	eukaryotic translation release factor, putative	Puro
CatEff::mNG	LmxM.31.1870	cation efflux family, putative	Puro
ZIP3::mNG	LmxM.28.1930	zinc transporter 3, putative	Puro
mNG::eIF1	LmxM.24.1210	eukaryotic translation initiation factor 1, putative	Puro
mNG::LIT1	LmxM.30.3060-70	ferrous iron transport protein	Puro
ΔHyp0130	LmxM.04.0130	hypothetical protein	Puro + Blast
ΔmMDH	LmxM.33.0140	malate dehydrogenase	Puro + Neo
ΔAPX	LmxM.33.0070	ascorbate peroxidase, putative	Puro + Blast
ΔLIT1	LmxM.30.3060-70	ferrous iron transport protein	Puro + Neo + Blast
ΔCatEff	LmxM.31.1870	cation efflux family, putative	Puro + Neo
ΔZIP3	LmxM.28.1930	zinc transporter 3, putative	Puro + Neo

tag::name indicates N-terminal tagging, name::tag indicates C-terminal tagging. Endogenous tags used were mNeonGreen (mNG) or HaloTag (Halo). Δ indicates deletion of all alleles of the gene. Puromycin (Puro), Neomycin (Neo) or Blasticidin (Blast) were the drug markers used.

Reagents used for PCR are from the Expand High Fidelity PCR System dNTPack (Roche). To amplify pLPOT plasmid or pT plasmid: 1 µL of each gene-specific forward and reverse primer (100 µM stock), 25 ng pLPOT plasmid, 1 µL deoxyribonucleotide triphosphates (dNTP, 10 mM stock), 1 µL DMSO in 20 µL H_2O were combined with 5 µL $MgCl_2$ (10×), 19 µL H_2O and 1 µL HiFi polymerase. PCR was at 94 °C for 5 min, followed by 35 cycles at 94 °C (15 sec), 65 °C (30 sec), 72 °C (2 min) then finally 72 °C (1 min). To amplify sgRNA templates: 1 µL dNTP (10 mM stock), 5 µL $MgCl_2$ (10×), 1 µL G00 sgRNA scaffold (100 µM stock), 1 µL HiFi polymerase and 1 µL gene-specific 5′or 3' sgRNA primer in 41 µL H_2O were combined. PCR was at 94 °C for 30 sec, followed by 30 cycles at 94 °C (30 sec), 60 °C (30 sec), 72 °C (30 sec) then finally 72 °C (2 min). 1 µL of each PCR product was run on a 1% agarose gel to confirm the presence of expected amplified plasmid or template. Combined PCR products were precipitated with 10 µL 3M sodium acetate and 300 µL EtOH at −80 °C for 20 min, pelleted by centrifugation (21910 g, 30 min), washed once with 70% EtOH, re-pelleted and resuspended in 10 µL H_2O.

Mid-log phase promastigotes (1×10^7 cells) were combined with PCR products and transfected using the Amaxa Nucleofector II.[509] Electroporation was performed using 2 mm cuvettes on the X-100 programme with 250 µL electroporation buffer (1:6:3 1.5 mM $CaCl_2$/H_2O/Roditi buffer concentrate (200 mM Na_2HPO_4, 70 mM NaH_2PO_4, 15 mM KCl, 150 mM HEPES·NaOH pH 7.4)[512]), followed by immediate suspension in pre-warmed M199 medium. Successful transfectants were selected and maintained using the necessary combination of drugs: 20 µg/mL puromycin (Puro), 40 µg/mL neomycin (Neo), or 5 µg/mL blasticidin (Blast). Drug was added 6–15 h after transfection, taking between 4–14 days to reach stable growth in culture.

For deletion mutant cell lines, a diagnostic PCR was performed by amplifying a short PCR product (100–300 bp) within the ORF of the target gene to verify loss of the target ORF. Unique primers for deletion validation were Primer3 designed.[508] If necessary, a clonal cell line was generated (Section 6.1.3) before being validated. Following drug selection, genomic DNA was extracted from deletion mutant cell lines: > 1×10^7 cells were harvested by centrifugation (1000 g, 3 min), resuspended in 100 µL lysis buffer (100 mM Tris.HCL (pH 8), 5 mM EDTA (ethylenediaminetetraacetic acid),

0.5% v/v SDS (sodium dodecyl sulfate), 200 mM NaCl and 10 µg/mL proteinase K) at 56 °C for 30 min, then 300 µL EtOH added and centrifuged (21910 g, 20 min, 4 °C) to give a DNA pellet that was resuspended in 10 µL H_2O. PCR was at 95 °C for 3 min, followed by 25 cycles at 95 °C (15 sec), 58 °C (30 sec), 72 °C (30 sec) then finally 72 °C (1 min). In the same diagnostic PCR, three different PCR products were required to demonstrate deletion: 1. Genomic DNA from the parental cell line to detect the target ORF, 2. Genomic DNA from the deletion mutant cell line to confirm absence of the target ORF, and 3. Genomic DNA from the deletion mutant cell line with primers for a control ORF (paralysed flagella protein 16 (PF16), LmxM.20.1400) as a technical control for the genomic DNA. Presence or absence of the PCR product was confirmed by agarose gel electrophoresis: 1.2% agarose gel with ethidium bromide, run at 120 V for 50 min (gels shown in appendix Section 7.3.3, Figure 67).

6.3 Compound activity studies

6.3.1 24 h growth studies

Promastigotes (1×10^6 cells/mL) in 5 mL of M199 medium were treated with 5 µL of compound dissolved in DMSO at a given concentration (final carryover of DMSO 0.1%) and incubated at 28 °C for 24 h. A negative control was always included, of either 0.1% DMSO or no additive. Culture density was measured using an Improved Neubauer haemocytometer at the start of the experiment and after 24 h. Growth study experiments were performed at least three times.

6.3.2 AlamarBlue™ assay

An AlamarBlue (Invitrogen) resazurin-based assay was used to determine the concentration at which cell growth was inhibited by 50% (EC_{50}). 96-well plates were set up with fresh media and compound serially diluted over a range of concentrations (two-fold serial dilutions). To this was added mid-log phase *L. mexicana* promastigotes (final density of 5×10^5 cells/mL per well) or *T. brucei* bloodstream forms (final density of 1×10^3 cells/mL per well) to a total well volume of 100 µL, and incubated at 28 °C in 5% CO_2 for 24 h (promastigotes) or 37 °C in 5% CO_2 for 72 h (bloodstream forms). 20 µL

of 1:1 AlamarBlue (10×, Invitrogen)/fresh media was added to each well and incubated for a further 4–6 h. 40 µL of 4% SDS in H_2O (final concentration 1% SDS) was added to each well and left to sit for 5 min to ensure complete killing. Fluorescence due to the production of resorufin was measured using a FluorStar Omega microplate reader: Fluorescence top, excitation 544 nm, emission 590 nm. Three biological replicates were carried out per experiment, each with at least two technical replicates. Data was processed using GraphPad Prism version 10.3.0 for Windows, GraphPad Software, and fitted to a four-parameter dose-response curve to obtain the EC_{50}.

To determine the effect on compound EC_{50} for exogenous additives, the assay was carried out as described with the addition of glutathione (30 µM), $FeCl_2$ (1.5 µM), $ZnCl_2$ (800 µM) $CuCl_2$ (30 µM) or calcium pantothenate (100 µM or 100 nM) to the media, from aqueous stock solutions.

6.4 Light microscopy

Light microscopy was performed with a widefield fluorescence microscope (Axio Observer A1, Zeiss) using a 63× NA 1.4 Plan-Apochromat oil immersion objective lens and a 120 V metal halide fluorescence light source (Zeiss, HXP 120 V). Image capture was performed with a Hamamatsu ORCA-Flash 4.0 camera, using Zeiss Zen-2.6 (Blue Edition). Fluorescence microscopy was performed with a Zeiss 20HE (red, AF555, TAMRA), ThorLabs MDF-GFP2 (green, AF488, mNeonGreen) and/or Zeiss, 49 (blue, Hoechst 33342) filter cube. Where necessary, z-stacks were taken of 10 images with a spacing of 240 nm. Images were analysed using Fiji (ImageJ).[513]

6.4.1 Sample preparation for light microscopy

Cells were washed three times by resuspension in 1 mL PBS and centrifugation (1000 g, 3 min), to improve adhesion to the glass slide and increase cell density. DNA was optionally stained with Hoechst 33342 (1 µg/mL) in the first wash. Cells were resuspended in 20 to 50 µL PBS and 1 µL was placed on a glass microscope slide outlined using a hydrophobic PAP pen, a coverslip was applied and immediately imaged.

6.5 Compound behaviour monitored by fluorescence light microscopy

6.5.1 Cell morphology and cell cycle analysis

Promastigotes (1×10^6 cells/mL) in 5 mL of M199 medium were treated with 5 µL of compound dissolved in DMSO to give a final concentration of 50 µM (**BI-1**, **BI-2**), 250 nM (**Asci**), or 30 µM (**DDB-1**) and incubated at 28 °C. At 6 h and 24 h post-treatment, a 1 mL aliquot was harvested by centrifugation (1000 g, 3 min) and the sample prepared for light microscopy (Section 6.4.1). The imaging experiment was preformed twice independently.

Cell morphology was identified as abnormal in comparison to an untreated control included in the same experiment. A manual identification was carried out for each cell from > 4 unbiased fields of view, where only cells completely in focus were considered.

Cell cycle progression was evaluated by manual counting of the Hoechst 33342 stained DNA organelles, from > 5 unbiased fields of view. Only cells in focus were considered. 1K1N1X was defined where there was the clear presence of a separate staining to the identified nucleus and kinetoplast. 0K1N and 1K0N were defined where there was the unambiguous absence of one of the DNA containing organelles. 1K1N-side was defined where the kinetoplast was further posterior than the mid-point of the nucleus.

6.5.2 Double-stranded DNA breakage

mNG::RAD51 promastigotes (Section 6.2) (5×10^6 cells/mL) in 7 mL of M199 medium were treated with 7 µL of compound dissolved in DMSO giving a final concentration of 50 µM (**BI-1**, **BI-2**), 250 nM (**Asci**), or 30 µM (**DDB-1**). Phleomycin was used as a positive control at a final concentration of 25 µg/mL. At T = 0, 15, 30, 60 min, and 2, 6, 24 h post-treatment, a 0.8 mL aliquot was harvested by centrifugation (1000 g, 3 min), and the sample prepared for light microscopy (Section 6.4.1).

6.6 Biochemistry MoA assays

6.6.1 DNA intercalation assay

This was run in collaboration with the Wyllie lab at the University of Dundee. Briefly; a 2× DNA/acridine orange (AO) solution (6 µL salmon sperm DNA (10 mg/mL, Invitrogen) and 15.1 µL AO (33.1 mM) in 5 mL detection buffer) was equilibrated for 1 h at r.t. A 384-well plate was set up with 10 µL of compound serially diluted over a range of concentrations (two-fold serial dilutions) for 10 wells (highest concentration was 50 µM for **DDB-1** and **Asci**, 10 µM for intercalation control daunorubicin). 50 µM amitriptyline was used as a negative control for no intercalation, and 10 µM mitoxantrone was used as a positive control for complete intercalation. To this was added an equal volume of 2× DNA/AO equilibrated solution and the plate read for fluorescence polarisation. Three biological replicates were carried out, each with two technical replicates. Data was processed using GraphPad Prism version 10.3.0 for Windows, GraphPad Software, and fitted to a four-parameter dose-response curve to obtain the EC_{50}.

6.6.2 Measurement of ADP/ATP ratio

ADP/ATP ratio assay kit (MAK135, Sigma-Aldrich) was run according to the manufacturer's instructions. *L. mexicana* promastigotes (5×10^6 cells/mL) in 5 mL of M199 medium were treated with 5 µL of compound dissolved in DMSO giving a final concentration of 250 nM (**Asci**), or 30 µM (**DDB-1**) and incubated at 28 °C. At 6 h and 24 h post-treatment, a 1 mL aliquot was harvested by centrifugation (1000 g, 3 min). Cells were washed once by resuspension in 1 mL PBS and centrifugation (1000 g, 3 min), resuspended in 100 µL of PBS, and 10 µL of the suspension added to a 96-well plate. 90 µL of ATP reagent (1.71 mL assay buffer, 18 µL substrate, 18 µL co-substrate, 18 µL ATP enzyme) was added to each well, incubated for 1 min at r.t and the plate read using a FluorStar Omega microplate reader (luminescence bottom) to generate reading RLUA. The same plate was incubated for a further 10 min at r.t and a second reading taken; this is reading RLUB. Immediately, 5 µL of ADP reagent (90 µL H_2O, 18 µL ADP enzyme) was added to each well, incubated for 1 min at r.t and the plate read to generate reading RLUC.

RLUA corresponds directly to the quantity of ATP in the sample. RLUC is a measure of the total ATP + ADP in the sample. RLUB is a measure of the residual ATP that is measured within RLUC. The ratio between ADP and ATP is calculated by:

$$\frac{ADP}{ATP} = \frac{RLUC - RLUB}{RLUA}$$

All calculations were carried out in Excel. The experiment was performed twice independently, each with 3 technical replicates.

6.6.3 Ca^{2+} measurement

Rhod-2, AM assay kit (R1244, Invitrogen) was run according to the manufacturer's instructions. Late-log phase *L. mexicana* promastigotes (4×10^8 cells) were harvested by centrifugation (1000 g, 8 min), washed once by resuspension in 5 mL PBS and centrifugation (1000 g, 4 min) and resuspended in 5mL of PBS. 10 µL of Rhod-2 AM mixture (5 µL Rhod-2 AM pre-mixed with 5 µL 20% pluronic in DMSO) was added and incubated at 28 °C for 1 h. Cells were washed three times by resuspension in 5 mL PBS and centrifugation (1000 g, 4 min) to remove excess Rhod-2. Cells were resuspended in 20 mL PBS then split into five tubes of 4 mL each. Two tubes were treated with 4 µL of compound dissolved in DMSO giving a final concentration of 700 nM (**Asci**), or 30 µM (**DDB-1**). The remaining three tubes acted as controls: 4 mM H_2O_2 was used as a positive control to induce Ca^{2+}, 3.75 mM $CaCl_2$ was used as an assay control (both from a stock solution in H_2O), and 0.1% DMSO was used as a negative control. The samples were aliquoted onto a black, clear bottomed 96-well plate (150 µL per well), then each well fixed with 8 µL of 37% formaldehyde (final concentration 2%), incubated 5 min at r.t and the plate read using a FluorStar Omega microplate reader: Fluorescence top, excitation 544 nm, emission 590 nm. The experiment was performed three times independently, each with two technical replicates.

The experiment was carried out similarly to the described for 3×10^8 *T. brucei* bloodstream form cells; in this case, PBS-G (PBS with 14 mM glucose) was used instead of PBS.

6.6.4 Intracellular Zn^{2+} measurement

FluoZin™-3, AM assay kit (F24195, Invitrogen) was run according to the manufacturer's instructions. Late-log phase *L. mexicana* promastigotes (2.5×10^8 cells) were harvested by centrifugation (1000 g, 8 min), washed once by resuspension in 5 mL PBS and centrifugation (1000 g, 4 min) and resuspended in 5 mL of PBS. 10 µL of FluoZin-3 mixture (5 µL FluoZin-3 AM pre-mixed with 5 µL 20% pluronic in DMSO) was added and incubated at 28 °C for 1 h. Cells were washed three times by resuspension in 5 mL PBS and centrifugation (1000 g, 4 min) to remove excess FluoZin-3. Cells were resuspended in 16 mL PBS then split into four tubes of 4 mL each. One each was treated with i) 4 µL of **Asci** dissolved in DMSO giving a final concentration of 700 nM, ii) 32 µL of TPEN from a 1 mM stock in methanol giving a final concentration of 8 µM, iii) 4 µL of DMSO giving a final concentration of 0.1% as a negative control, and iv) 32 µL of $ZnCl_2$ from a 100 mM stock in H_2O giving a final concentration of 800 µM as an assay control. The samples were aliquoted onto a black, clear bottomed 96-well plate (150 µL per well), then each well fixed with 8 µL of 37% formaldehyde (final concentration 2%), incubated 5 min at r.t and the plate read using a FluorStar Omega microplate reader: Fluorescence top, excitation 485/12 nm, emission 520 nm. The experiment was performed three times independently, each with two technical replicates.

The experiment was carried out similarly to the described for 4×10^8 *T. brucei* bloodstream form cells. Variations were: PBS-G (PBS with 14 mM glucose) was used instead of PBS, treatment i) was 4 µL of **Asci** dissolved in DMSO giving a final concentration of 250 nM, and treatment ii) was 4 µL of TPEN from an 8 mM stock in DMSO giving a final concentration of 8 µM.

6.7 The click reaction

Reagents for the click reaction are from Click-it™ Plus AlexaFluor™ 555 picolyl azide toolkit (C10642, Invitrogen), prepared according to the manufacturer's instructions. Reagents were added in the order listed.

Click cocktail A : 870 µL 1× reaction buffer (contains a THPTA stabilising ligand), 10 µL of 500 µM azide stock giving a final concentration of 5 µM, 20 µL of pre-mixed copper(II) sulfate/copper protectant solution at a 3:2 ratio to moderate the amount of copper used, and 100 µL of 1× reaction buffer additive (contains sodium ascorbate reducing agent).

Click cocktail B : 1× reaction buffer (contains a THPTA stabilising ligand), copper(II) sulfate 1 mM in H_2O, freshly prepared sodium ascorbate 10 mM in H_2O, and azide 5 µM.

6.7.1 Slide preparation for the click reaction

0.01% poly-L-lysine was added to a glass microscope slide outlined using a hydrophobic PAP pen, and incubated for 5 mins at r.t. The poly-L-lysine was pipetted off and the slide washed three times with PBS, and then left with PBS until it is replaced with a solution of cells. All slide incubations are in a humid box to prevent the slide from drying out.

6.7.2 EdU click optimisation

Mid-log phase *L. mexicana* promastigotes (1×10^6 cells/mL) in 5 mL of M199 medium were treated with 5 µL of 5-ethynyl-2'-deoxyuridine (EdU, Invitrogen, 1 mM stock in DMSO), giving a final concentration of 1 µM in a carryover of 0.1% DMSO. Cells were incubated at 28 °C for 24 h to ensure full incorporation of EdU into synthesised DNA. Flasks were treated with 270 µL of 37% formaldehyde (final concentration 2%), incubated for 5 min at r.t, then harvested by centrifugation (1000 g, 8 min). Cells were washed three times by resuspension in 1 mL of 3% BSA (freshly prepared 3% w/v bovine serum albumin fraction V (03117332001, Roche) in PBS) and centrifugation (1000 g, 3 min), then resuspended in 1% NP-40 (1% v/v Nonidet P-40 substitute (ChemCruz, sc-29102) in PBS) and incubated for 20 min at r.t. Cells were washed three times by resuspension in 1 mL of 3% BSA and centrifugation (1000 g, 3 min), resuspended in 100 µL of 3% BSA and added to prepared slides (Section 6.7.1). Slides were incubated for 20 min at r.t to allow the cell suspension to adhere to the slide.

The CuAAC click reaction was carried out on the surface of the slides: The residual cell suspension was pipetted off the slides and replaced with 300 µL of Click cocktail A with AlexaFluor 555 (AF555) picolyl azide, ensuring complete coverage of the adhered cells. Different ratios of copper(II) sulfate/copper protectant were trialled to optimise the copper content; 1:9, 1:1, 3:2, 9:1 (Section 3.2.1, Figure 25). The slide was incubated for 30 min in the dark, then washed once with 3% BSA, and once with PBS containing Hoechst 33342 (1 µg/mL) to aid with nucleus and kinetoplast identification, before slide sealing (Section 6.7.3).

For *T. brucei* cells, the experiment was carried out similarly to the described, from a starting cell concentration of 1×10^6 cells/mL in 5 mL (procyclic forms) or 2×10^5 cells/mL in 50 mL (bloodstream forms). Cells were treated with a final concentration of 100 µM EdU. Bloodstream forms were concentrated by centrifugation (1000 g, 8 min) and resuspended in 5 mL of HMI9 prior to fixation.

6.7.3 Slide sealing

A drop of ProLong™ Gold Antifade Mountant (P36930, Invitrogen) was added to the slide as a protective sealant, a coverslip was applied and partially sealed to the slide with nail varnish. The slide was imaged a minimum of 2 h after preparation (routinely > 24 h after preparation), and dried at r.t for 24 h before being fully sealed with nail varnish and stored at −20 °C indefinitely.

6.7.4 Optimised sample processing and click conditions for fluorescence microscopy

Mid-log phase cells (> 5×10^7 cells) in medium were treated with compound dissolved in DMSO giving a final concentration of 30 µM (**DDB-yne** or **DDB-PAL**) in a carryover of 0.1% DMSO. Cells were incubated for 30 min unless otherwise indicated for a specific time-varied experiment. Where necessary for treatments with **DDB-PAL**, PAL UV light irradiation was then carried out (Section 6.7.5). Flasks were fixed with 2% formaldehyde, incubated for 5 min at r.t, then harvested by centrifugation (1000 g, 8 min). Cells were washed three times by resuspension in 1 mL 3% BSA and centrifugation (1000 g, 3 min), resuspended in 1% NP-40 and incubated for 20 min at r.t. Cells were

washed three times by resuspension in 1 mL 3% BSA and centrifugation (1000 g, 3 min), resuspended in 100 µL 3% BSA and added to prepared slides (Section 6.7.1). Slides were incubated for 20 min at r.t to allow the cell suspension to adhere to the slide. The residual cell suspension was pipetted off the slides and replaced with 250 µL of Click cocktail A or Click cocktail B. Slides were incubated for 30 min in the dark, then washed once with 3% BSA, and once with PBS optionally containing Hoechst 33342 (1 µg/mL) before slide sealing (Section 6.7.3).

6.7.5 PAL UV light irradiation

For samples treated with **DDB-PAL**, a UV torch was suspended 10 cm above a 25 cm^3 cell culture flask on its side, in the dark. The flask was irradiated with 10 Watt 365 nm UV light for 10 min to trigger diazirine cross-linking. Control imaging for samples treated with **DDB-PAL** without undergoing UV light irradiation did not show fluorescence, indicating the essentiality of this step.

6.7.6 EDTA wash to restore mNeonGreen fluorescence

For mNeonGreen tagged cell lines, an acidic EDTA wash was included to chelate excess copper from the click reaction thereby restoring the mNeonGreen fluorescence.[409] Following incubation with the click cocktail, slides were washed once with 3% BSA, twice with acidic EDTA solution (40 mM ethylenediaminetetraacetic acid disodium salt and 10 mM 2-(*N*-morpholino)ethanesulfonic acid (MES) pH 5.3, in 3% BSA), then 300 µL of acidic EDTA solution added and incubated in the dark for a further 2 h. Slides were washed five times with 3% BSA to restore the pH, then once with PBS optionally containing Hoechst 33342 (1 µg/mL) before slide sealing (Section 6.7.3).

6.7.7 HaloTag cell line labelling with ligand

Mid-log phase HaloTag tagged cells (5×10^7 cells) (Section 6.2) were concentrated by centrifugation (1000 g, 4 min) and resuspended in 800 µL of pre-warmed media. To this was added 200 µL of 5× ligand solution (800 µL pre-warmed media and 4 µL of HaloTag® TAMRA (G8252, Promega)) and incubated for 15 min. Cells were pelleted by centrifugation (1000 g, 4 min), washed three times by resuspension in 1 mL media and centrifugation (1000 g, 3 min) and incubated in 3 mL media for a

further 30 min to remove unbound ligand. 500 µL from each sample was harvested by centrifugation (1000 g, 4 min) and prepared for light microscopy (Section 6.4.1). The remaining 2.5 mL was harvested by centrifugation (1000 g, 4 min), resuspended in 2.5 mL media and used for click reaction with AlexaFluor 488 (AF488) azide (A10266, Invitrogen) (Section 6.7.4).

6.8 Click image processing

6.8.1 Image deconvolution

Image deconvolution is necessary because fluorescence images have inherent blur due to the diffraction of light passing through the sample. To correct for this out-of-focus light requires the point spread function (PSF), a mathematical formula that models the spread of light through the system from its source. A theoretical PSF image z-stack for our system was predicted using the Diffraction PSF 3D plugin with the parameters: Refractive index: 1.518, numerical aperture: 1.4, wavelength in nm: 568 (AF555) or 517 (mNG) or 578 (TAMRA) or 525 (AF488), pixel spacing: 103.2 nm, slice spacing (z): 240 nm, width: 2048, height: 2048, and depth: 10. This was used with the algorithm Iterative Deconvolve 3D on the fluorescence channel z-stack images in Fiji.[514]

6.8.2 Quantification of the DDB-PAL treated cells at different time points.

For each timepoint, fluorescence intensity was quantified for the non-deconvolved AF555 channel. Cells were selected from > 1 field of view with the requirement of having no overlapping cells but otherwise unbiased selection. The 3D z-stack is flattened using Fiji, z-project – sum slices, which creates a 2D image of the combined pixel intensity from each z-slice. The Fiji selection tools are used to draw a region of interest (ROI) around the promastigote cell body, and then the measurement tools used to measure the mean signal intensity with the ROI. A measurement of the mean background intensity is similarly taken and subtracted from the cell body intensity before the values are plotted in Excel.

6.8.3 Co-localisation quantification with JACoP and Coloc2 plugins

To quantify co-localisation between fluorescence from mNeonGreen in tagged cell lines (mNG::TIM17 or mNG::GAPDH) and clicked AF555, two different opensource Fiji co-localisation plugins were evaluated. Images underwent pre-processing: image deconvolution (Section 6.8.1) for both AF555 and mNeonGreen channels, background subtraction using a rolling ball algorithm (radius of 5-50 pixels), and finally conversion to 16-bit. The two Fiji plugins commonly used for this application: Coloc2 and JACoP,[408, 513, 515] were both applied to this analysis for 10 images of each cell line. For each plugin, the AF555 and mNeonGreen image channels of a single cell were uploaded, the algorithm run to give a visual plot of the data as a cytofluorogram (Section 3.3.3, Figure 30), and output various coefficients discussed below.

6.8.3.1 Pearson's coefficient

Pearson's coefficient (*R*) was calculated using each plugin. This measures the spread of the data which varies from −1 to 1, where 1 is full co-localisation, −1 is complete exclusion, and 0 indicates no correlation.[516] Coloc2 allows the user to manually define a region of interest (ROI), in this case the promastigote cell body, so that co-localisation of background pixels is not considered. JACoP does not have a feature allowing a ROI to be defined, therefore the whole field of view contributes to the co-localisation. This leads to more accurate values for *R* with Coloc2; JACoP overestimates *R* because low-value background pixels will have good correlation (Figure 63). Therefore, *R* calculated using Coloc2 was used.

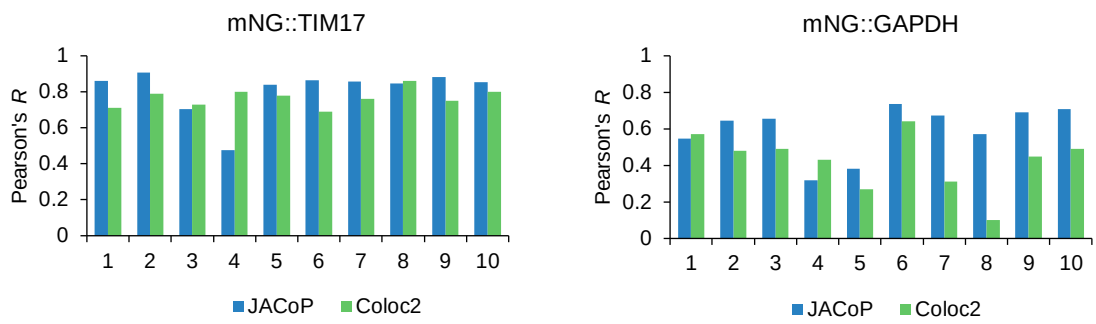

Figure 63. Co-localisation calculated by JACOP gives higher values of Pearson's *R* value than Coloc2. 10 cells of each cell line were used for the *R* calculation, JACoP tends to overestimate *R*. Values for mNG::TIM17 are higher than mNG::GAPDH as expected (Section 3.3.3).

Within each plugin, Pearson's coefficient is statistically evaluated using Costes' randomisation: channel 1 is randomly scrambled, a new Pearson's coefficient is calculated between this and channel 2, which is repeated 100 times. Comparing the generated "scrambled" *R*'s with the "real" *R* gives a *P*-value where $P = 1$ means none of the scrambled *R*'s had a better correlation, i.e., a high degree of confidence.[517] With both plugins, all images had a *P*-value of 1.

6.8.3.2 Manders' coefficient

Thresholded Manders' coefficients (tM_1 and tM_2) were calculated for each channel using both plugins. Costes' automatic thresholding was applied to set an intensity threshold below which $R \leq 0$, thus removing background noise.[517] The mNeonGreen channel has high levels of noise, particularly mNG::TIM17 even after all the necessary pre-processing, which makes the thresholding step crucial to the Manders' coefficient. Costes' automatic thresholding considers some of the noise to be "real" signal and sets the threshold below this, which leads to tM_1 and tM_2 values close to 1 as almost every pixel has intensity above the threshold (Figure 64).

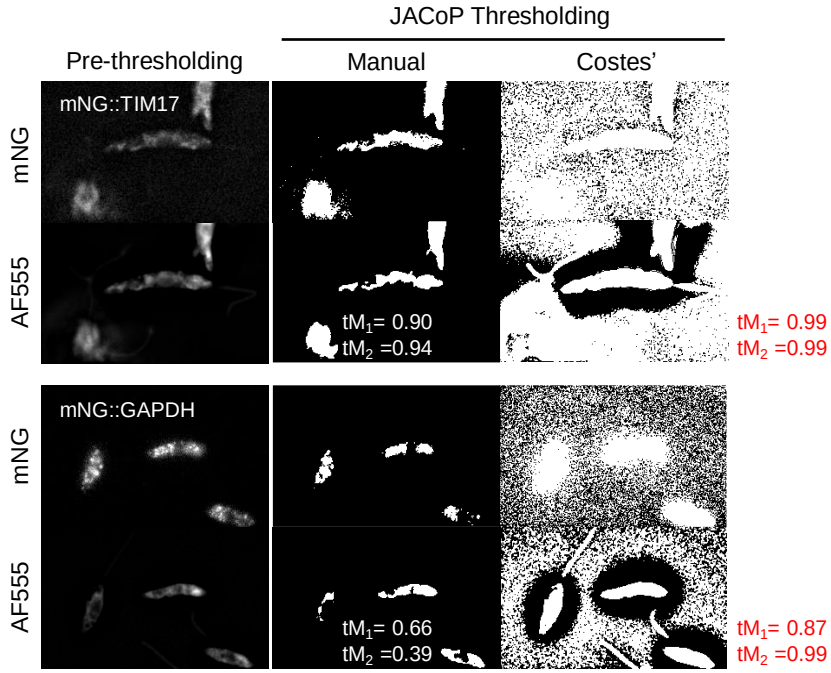

Figure 64. Failure of Costes' automatic thresholding in the calculation of tM_1 and tM_2. With the JACoP plugin, manual thresholding allows only real signal to be included giving meaningful values of tM_1 and tM_2 for each cell line. Costes' automatic thresholding overestimates the threshold such that background is included, giving tM_1 and tM_2 close to 1.00 every time. One example cell from each cell line shows in white the pixels included above threshold for both manual (correct) and Costes' (incorrect) thresholding.

With Coloc2, there is no option but to use Costes' automatic thresholding which gives incorrect results. With JACoP, a manual threshold can be set by the user, such that only true co-occurrence is measured – although manual thresholding can introduce bias to the system. Meaningful tM_1 and tM_2 were only obtained with manual thresholding using JACoP plugin.

6.9 Transmission Electron Microscopy (TEM)

All TEM experiments were carried out at the Electron Microscopy Facility, Sir William Dunn School of Pathology, University of Oxford. Observations and ultramicrotome sectioning was carried out by Dr. Cécile Fort. Observations were made on a Tecnai 12 transmission electron microscope (Thermo Fisher) or a JEOL 2100 Plus 200 kV transmission electron microscope, with a Gatan OneView camera. Images were analysed using Fiji (ImageJ).[513]

6.9.1 Standard TEM sample preparation

L. mexicana promastigotes (1×10^8 cells) were fixed in culture with 2.5% glutaraldehyde (25% stock solution, EM grade, Electron Microscopy Sciences) for 10 min at r.t. Cells were harvested by centrifugation (16000 g, 5 min), and the pellet was resuspended in fixative buffer (2.5% glutaraldehyde, 4% PFA (paraformaldehyde, 16% stock solution, EM grade, Electron Microscopy Sciences) in 0.1 M PIPES (1,4-piperazinediethanesulfonic acid, pH 7.2)) for a minimum of 2 h. Cells were washed three times by resuspension in 1 mL 0.1 M PIPES and centrifugation (1000 g, 5 min), then pelleted into agarose by resuspension in 1 mL 3% hot agarose solution and immediate centrifugation (16000 g, 5 min). The agarose cell pellet was trimmed, and contrasted with 1% OsO_4 (Osmium tetroxide 4% aqueous solution, Taab Laboratories Equipment) for 2 h at 4 °C. Samples were serially dehydrated with aqueous ethanol solutions (30% 2 h at r.t, 50% 2 h at r.t, 70% overnight at 4 °C, then 3× 100% 2 h at r.t) prior to embedding in low-viscosity Agar 100 (Agar Scientific, UK), and polymerised at 60 °C for 24 h. Ultrathin sections (90 nm thick) were collected on nickel grids using a Leica EM UC7 ultramicrotome, stained with 1% uranyl acetate (1% w/v uranyl acetate dehydrate in H_2O, Electron Microscopy Sciences) for 5 min, and lead citrate (80 mM lead nitrate (Thermo Fisher, L/1450), 120 mM sodium citrate (Sigma-Aldrich, 71405) and 1 M sodium

hydroxide (SLS, CHE3422))[518] for 5 min. Grids were dried for a minimum of 30 min before observation.

6.9.2 TEM with click: pre-embedding

L. mexicana promastigotes underwent the click reaction as previously described for EdU (Section 6.7.2) and compound **DDB-PAL** (Section 6.7.4), without addition to glass microscope slides. Instead, the reaction was carried out in 1.5 mL Eppendorf tubes with each wash involving 1 mL of buffer and centrifugation (1000 g, 3 min). For click optimisation, permeabilisation with either 1% NP-40 or 0.1% w/v saponin in PBS (SAE0073, Sigma-Aldrich), was used. Fluorescent azide was replaced with azide functionalised gold nanoparticles from three suppliers: i) 10 nm (Cytodiagnostics), ii) 10 nm, 10-PEG chain (Nanopartz), or iii) 5 nm (Sigma-Aldrich). Following the click protocol, samples were processed for TEM (Section 6.9.1) and observed.

6.9.3 TEM with click: post-embedding

Mid-log phase *L. mexicana* promastigotes (> 5×10^7 cells) were incubated with the desired click substrate at 28 °C for 30 min (**DDB-PAL**) or 24 h (EdU), then PAL UV light irradiation was carried out (Section 6.7.5). Samples underwent processing for TEM (Section 6.9.1) using an acrylic LR White resin (Sigma-Aldrich, 94188-59-7) for embedding, and without the final uranyl acetate and lead citrate staining until the end of this protocol.

Following grid preparation, the click reaction was carried out on grids, in all steps grids were placed sample-down on a droplet of incubation solution, all incubations were at room temperature. Grids were incubated in PBS for 5 min to hydrate, then 1% NP-40 or 0.1% v/v Triton-X (X100, Sigma-Aldrich) in PBS to permeabilise. Grids were washed three times by 5 min incubation in blocking buffer, then incubated a further 30 mins in blocking buffer. To optimise this step, four different blocking buffers were used: i) 1% w/v BSA in PBS, ii) 0.1% w/v BSA in PBS, iii) 0.5% w/v fish gelatin (G7041, Sigma-Aldrich) in PBS, or iv) PBS without additive. Grids were incubated in Click cocktail B with 10 nm gold-azide (Cytodiagnostics) 1/30 or 1/1000 dilution, for 1 h in the

dark, then washed three times by 2 min incubation in blocking buffer, washed three times by 5 min incubation in H_2O, and dried by blotting on filter paper. Grids were finally stained with uranyl acetate and lead citrate as previously described (Section 6.9.1), and observed.

6.9.4 Tokuyasu sample preparation

Mid-log phase *L. mexicana* promastigotes (5×10^8 cells) were incubated with the desired click substrate at 28 °C for 3 h (**DDB-PAL**) or 24 h (EdU), then PAL UV light irradiation was carried out (Section 6.7.5). Cells were fixed in culture with 2% PFA in 0.1 M phosphate buffer for 24 h, then a further 2.5% glutaraldehyde fixation for 1 h. Cells were harvested by centrifugation (1000 g, 5 min), washed three times by resuspension in 1 mL 0.1 M phosphate buffer and centrifugation (1000 g, 5 min), and incubated in PBS-glycine (0.15% w/v glycine in PBS) for 10 min at r.t. Cells were harvested by centrifugation (1000 g, 5 min), then pelleted into 12% gelatin by resuspension in 1 mL 12% hot gelatin solution at 40 °C for 10 min, centrifugation (16000 g, 5 min), and gelatin solidification on ice for 30 min. The gelatin cell pellet was trimmed, infiltrated with 2.3 M sucrose at 4 °C for 3 days, before blocks were mounted on pins and frozen at −80 °C for a minimum of 20 min. Ultrathin sections (90 nm thick) were created using a Leica EM UC7 ultramicrotome equipped with an EM FC7 cryochamber, collected on formvar-coated copper grids in looping solution (1.15 M sucrose, 1% methyl cellulose), and stored at 4 °C indefinitely.

Following grid preparation, the click reaction was carried out on grids, in all steps grids were placed sample-down on a droplet of incubation solution, all incubations were at room temperature unless otherwise indicated. Grids were incubated in PBS for 30 min at 37 °C to melt the infiltrated sucrose, then washed three times by 2 min incubation in PBS-glycine, and incubated a further 5 mins in 1% BSA blocking buffer. Grids were incubated in Click cocktail B for 1 h in the dark. Three conditions A–C were attempted, using two differed azides: A. 10 nm gold-azide (Cytodiagnostics) 1/10, 1/30, 1/500 or 1/1000 dilution, or B&C. 5 µM biotin-azide (PEG4 carboxamide-6-azidohexanyl biotin, B10184, Invitrogen). Grids from A proceeded to fixation. Grids from B&C were washed five times by 2 min incubation in 0.1% BSA-C (Aurion), incubated a further 5 min in 0.1% BSA-C, then

incubated with either B. 10 nm streptavidin gold (Aurion) 1/250 or 1/5000 dilution in 1% BSA or C. anti-biotin antibody, rabbit (ab53494, Abcam) 1/250 or 1/5000 dilution in 1% BSA. Grids from B proceeded to fixation. Grids from C were washed five times by 2 min incubation in 0.1% BSA-C, incubated 5 mins in 0.1% BSA-C, incubated a further 50 min with Protein A gold (Aurion) 1/20 dilution in 1% BSA, then proceeded to fixation.

Fixation: Grids were washed five times by 2 min incubation in PBS, incubated in 1% glutaraldehyde in PBS for 5 min, then washed five times by 1 min incubation in H_2O. On ice, grids were touched to a droplet of cold 0.4% uranyl acetate/1.8% methyl cellulose in H_2O, then incubated for 10 min on a second droplet of the same before blotting, air drying and observation.

6.9.5 TEM gold quantification for Tokuyasu prepared samples

The gold was quantified in a semi-automated manner. A Fiji (ImageJ) script was used to filter the images for gold labelling by considering circular dots of size 5–15 µm and adjusting the contrast allowing the gold to stand out. Gold was then manually identified and counted within the cellular compartments of interest, defined with the selection tools.

6.10 PAL for proteomics

6.10.1 PAL sample preparation and protein precipitation

L. mexicana promastigotes (5×10^6 cells/mL) in 5 mL of M199 medium were treated with 5 µL of **DDB-PAL** dissolved in DMSO giving a final concentration of 30 µM in a carryover of 0.1% DMSO, and incubated for 30 min. For competition experiments, cultures were pre-incubated with 30 µM **DDB-1** for 30 min before 30 µM **DDB-PAL** for 30 min. A 0.1% DMSO treated culture was run in parallel as a negative control. PAL UV light irradiation was then carried out (Section 6.7.5).

Cells were harvested by centrifugation (1000 g, 8 min), washed three times by resuspension in 1 mL PBS and centrifugation (1000 g, 3 min), resuspended in 210 µL ice-cold lysis buffer (Pierce™ RIPA buffer (Thermo Fisher), 1 µM E-64 protease inhibitor (324890, Merck), 2% v/v protease inhibitor

cocktail in DMSO (P8340, Sigma-Aldrich), 0.2% v/v benzonase nuclease (Standard 25 U/µL, 70664-3, Merck)), and incubated for 15 mins on ice. DNA was sheared by 10× needle pulls through a 0.8 mm needle, then incubated a further 15 mins on ice. 200 µL of Click cocktail B was added and the samples incubated for 1 h in the dark. Protein precipitation was carried out to remove the excess click reagents: addition of 2× sample volume of MeOH, 1× sample volume of H_2O and 0.5× sample volume of $CHCl_3$, vortex, then centrifugation (21910 g, 5 min). The protein appears as a precipitate between the two solvent layers, the top layer was removed and the precipitate washed three times by addition of 1 mL MeOH and centrifugation (1000 g, 3 min) before air drying (5 min).

6.10.2 In-gel fluorescence visualisation

PAL sample preparation and protein precipitation (Section 6.10.1) was carried out using TAMRA–azide as the click partner. Precipitate was resuspended in 500 µL of 2% SDS (2% v/v sodium dodecyl sulfate in PBS), vortexed thoroughly then sonicated three times (5 sec, 5 mA, SoniPrep150 needle sonicator, sample on ice) to ensure the pellet is dissolved. Samples were resolved using SDS-PAGE (Section 6.10.3) and the gel imaged with a fluorescent reader (ChemiDoc MP Cy5.5 module). Following fluorescence imaging, the gel was stained with SimplyBlue™ SafeStain (Coomassie G-250 based, LC6060, Invitrogen) following the manufacturer's instructions (microwave protocol) to visualise proteins.

6.10.3 SDS-PAGE for resolving protein samples

SDS-PAGE was carried out using the NuPAGE™ system (10673853, Invitrogen). Samples of 2×10^7 cell equivalents were diluted to 30 µL in 1× loading buffer (LDS sample buffer and sample reducing agent in H_2O), and denatured by boiling at 80 °C for 10 mins. 12% Bis-Tris 1.0 mm mini protein gels were loaded with 12 µL of sample, and the gel was run in MOPS running buffer (with 0.25% v/v antioxidant in the upper chamber running buffer) at 180 V for 60 min until the dye front was at the bottom of the gel. 5 µL of a spectra multicolour broad range protein ladder (26634, Thermo Fisher) 10 to 260 kDa was run alongside the samples.

6.10.4 Affinity purification

PAL sample preparation and protein precipitation (Section 6.10.1) was carried out from a 10× culture volume (50 mL), initially concentrated by centrifugation (1000 g, 10 min) and resuspension in 5 mL of M199 media. Biotin-azide (PEG4 carboxamide-6-azidohexanyl biotin, B10184, Invitrogen) was used in the click cocktail.

Precipitate was resuspended in 100 µL of 1% v/v SDS in PBS, vortexed thoroughly, then sonicated three times (5 sec, 5 mA) to ensure the pellet is dissolved. Samples were then diluted in 1 mL of affinity purification buffer (50 mM HEPES·NaOH (pH 7.4), 100 mM NaCl, 1% v/v NP-40 in PBS) to ≤ 0.1% SDS for efficient purification. Samples were incubated with 300 µL prepared streptavidin magnetic beads slurry (Section 6.10.4.1) for 18 h at −4 °C with rotation. Beads were held with a magnet (5 mins), supernatant flow through was removed, beads were washed once with 1 mL affinity purification buffer, twice with 1 mL wash buffer (50 mM HEPES·NaOH (pH 7.4), 500 mM NaCl, 1% v/v NP-40 in PBS) and resuspended in 500 µL wash buffer.

6.10.4.1 Streptavidin magnetic bead preparation

Streptavidin magnetic beads (Dynabeads™ MyOne™ Streptavidin T1, 65601, lot number: 2792769, Invitrogen) were used for affinity purification in combination with a DynaMag-2 magnet (Invitrogen). The bead container was vortexed thoroughly to mix (> 30 sec), then 300 µL per sample of beads added to 500 µL of PBS and vortexed. Beads were held with a magnet, the supernatant flow through was discarded, beads were washed twice with 1 mL PBS, and resuspended in 300 µL of PBS to form a slurry.

6.10.4.2 Western blot detection

50 µL of bead suspension (Section 6.10.4) was eluted by boiling in 100 µL of 1× sample buffer (NuPAGE™ LDS sample buffer (Invitrogen) in H_2O) at 90 °C for 10 mins. Beads were removed with a magnet and flow through sample used for resolution by SDS-PAGE (Section 6.10.3). The flow through sample was additionally loaded at 6× equivalents to enable visualisation.

Protein was transferred from the gel to a nitrocellulose membrane (10600012, Amersham Protran 0.45 µm pore size) by wet transfer western blotting (XCell SureLock™ Mini-Cell with XCell II blot module, Invitrogen) in transfer buffer (1× NuPAGE™ transfer buffer (NP0006, Invitrogen), 0.1% v/v NuPAGE™ antioxidant (NP0005, Invitrogen), and 10% MeOH in H_2O) for 1 h at 30 V. Following successful transfer, the membrane was washed five times with H_2O (5 min), then blocked with 5% w/v BSA in PBS-T (0.05% v/v Tween 20 in PBS) for 20 min. The membrane was washed with PBS-T (5 min), and incubated with agitation in HRP conjugate antibody (Avidin, NeutrAvidin™ horseradish peroxidase conjugate, A2664, Invitrogen) 1:5000 dilution in PBS-T, for 1.5 h. The membrane was then washed five times with PBS-T (5 min), detected with chemiluminescent substrate (SuperSignal™ west pico PLUS, 34578, Thermo Scientific) for 2 min and imaged with a CCD sensor (ImageQuant LAS 4000).

6.10.4.3 MS/MS submission and analysis

450 µL of bead suspension (Section 6.10.4) was submitted to the University of Oxford Department of Chemistry mass spectrometry facility for on-bead digest and MS/MS analysis. Four samples were submitted together, corresponding to four technical replicates i.e., the affinity purification experiment was carried out four times independently. Protein identification and quantification was carried out by Dr. Elisabete Pires.

Volcano plots were generated in Excel for proteins with non-0 reads, and the statistical significance (*P*-value) was derived from a two-tailed *t*-test. The coefficient of variation (CV) is a measure of the percentage variation, and was calculated as the standard deviation divided by the mean for each protein of the $n = 4$ replicates.[519] The cut-off for fold change was set as:

$$cut = \frac{1 + \widetilde{CV}}{1}$$

Where $\widetilde{CV}$ represents the 95th percentile of the measured coefficients from all proteins. This gave a value of 2.5 and indicates the technical variance.

A separate analysis was conducted for proteins where there were no reads detected in the DMSO negative control sample. Only proteins where reads were detected in 3 or 4 of the **DDB-PAL** labelled replicates *and* in 0 or 1 of the DMSO replicates were considered. The area detected for each protein was normalised to the whole sample before the fold change was calculated.

6.11 Resistant cell line generation, DNA sequencing and analysis

6.11.1 Mutagenesis

Clonal cells of *L. mexicana* promastigotes (1×10^6 cells/mL) in 10 mL of M199 were treated with 41.2 µL EMS (ethyl methanesulfonate, M0880, Sigma-Aldrich) to a final concentration of 40 mM, or 100 µL ENU solution (*N*-ethyl-*N*-nitrosourea, 400 mM stock in 1:1 H_2O/EtOH) to a final concentration of 4 mM. All waste contaminated with mutagen was neutralised with 0.3 M NaOH solution before disposal. Flasks were incubated for 6 h at 28 °C, then cells were washed twice by centrifugation (1000 g, 3 min) and resuspension in 1 mL M199 media. The pellet was then resuspended in 10 mL pre-warmed M199 media and incubated for 24 h at 28 °C to allow cell recovery before proceeding with further experiments.

6.11.2 Resistance generation

6.11.2.1 Sequential increase from sub-lethal concentration

Two independent cultures per mutagen (Section 6.11.1) and a non-mutagenised control culture were grown in the presence of **DDB-1** starting with a sub-lethal concentration of 3 µM. Concentration of compound was increased each time the cells displayed a healthy growth and motility comparable to an untreated control. Beyond 20 µM, cells did not survive, therefore the experiment was terminated.

6.11.2.2 High "shock" concentration

Two independent cultures per mutagen (Section 6.11.1) and a non-mutagenised control culture were grown in M199 medium in the presence of **DDB-1** at a high concentration (20, 50 or 100 µM). Every

2 to 3 days, cells were pelleted by centrifugation (1000 g, 3 mins), resuspended in M199 medium and re-treated with compound maintaining the same concentration. To some flasks an additional 10% FCS was added to the media. Cultures were monitored by microscopy; no live cell were visible after three media replacements therefore the experiment was terminated.

6.11.2.3 Selection on 96-well plates

Two independent cultures per mutagen (Section 6.11.1) were diluted to 1.5×10^5 cells/mL (ENU) or 3×10^4 cells/mL (EMS) with modified M199, plated onto a 96-well plate and treated with 30 µM of **DDB-1**. Plates were incubated at 28 °C, 5% CO_2 atmosphere for 2–4 weeks until cells emerged. Wells were ranked according to approximate cell density, and those with the highest cell density that were last to emerge were transferred to flasks and grown in M199 medium. Six cell lines resulted from each mutagen. The relative resistance of one "desensitised" cell line to **DDB-1** was assessed *via* a 24 h growth curve (Section 6.3.1) in comparison to the wildtype cell line.

Genomic DNA was extracted from cell lines using a DNeasy (Qiagen) kit as per the manufacturer's instructions with a final elution in 20 µL H_2O, and sent for sequencing at Beijing Genomics Institute (BGI), Hong Kong. Library preparation and sequencing was carried out by BGI genomics: DNBseq, 100 base pairs paired end reads, 2–40 Gbase, read filtering and clean-up. BGI genomics delivered clean reads, which then underwent bioinformatic analysis.

Sequence reads were aligned to the *L. mexicana* MHOMGT2001U1103 reference genome[305] using the software BWA (Version 0.7.17-r1188),[520] indexed using SAMtools (Version 1.7)[521] and a changes file generated using Pilon (Version 1.24).[522] The changes file identified mutations in the protein coding sequence corresponding to synonymous SNPs, non-synonymous SNPs and new stop codons compared to the starter clone.

6.11.3 *L. donovani* genome-wide overexpression library

This experiment was carried out in collaboration with the Wyllie group at the University of Dundee, using their standard protocol.[284] Briefly; the library was grown in the presence of **DDB-1**, **Asci**, or

untreated (as a control), with regular sub-culturing upon reaching densities of 1×10^7 cells/mL. After a period of selection, cells were harvested (2000 g, 5 min), washed once with cold PBS, and subjected to cosmid extraction: SDS/alkali lysis, phenol/$CHCl_3$ extraction and ethanol precipitation. Cosmids were amplified by transformation to electrocompetent *E. coli*, and extracted using the QIAprep kit (Midiprep, Qiagen) according to the manufacturer's instructions. Cosmid DNA was sent for sequencing at BGI genomics, and resultant reads were analysed by Dr. Michele Tinti and Dr. Sandra Carvalho.

6.11.4 *T. brucei* genome-wide overexpression library and RNAi library

The experiments were carried out in collaboration with the Wyllie group at the University of Dundee, using their standard protocols.[285, 523] Briefly; each library was grown in the presence of **DDB-1**, **Asci**, or untreated (as a control), with regular sub-culturing upon reaching densities of 5×10^5 cells/mL. After a period of selection, cells were harvested (2000 g, 10 min), and resuspended in DNA lysis buffer. Genomic DNA was extracted (phenol/$CHCl_3$) and amplified by PCR. DNA was sent for sequencing at BGI genomics, and resultant reads were analysed by Dr. Michele Tinti and Dr. Sandra Carvalho.

6.11.5 *L. donovani* barcoded resistance library

This experiment was carried out in collaboration with the Wyllie group at the University of Dundee, using their standard protocol.[440] Briefly; the library was grown in the presence of $3\times$ EC_{50} and $10\times$ EC_{50} **DDB-1** or **Asci** with regular sub-culturing upon reaching densities of 5×10^6 cells/mL, with an untreated control culture in parallel. After a two-week selection, cells were harvested (2000 g, 5 min), and resuspended in DNA lysis buffer. Genomic DNA was extracted (phenol/$CHCl_3$) and amplified by PCR. DNA was sent for sequencing at BGI genomics, and resultant reads were analysed by Dr. Michele Tinti and Dr. Sandra Carvalho.

6.12 Transcriptome changes and sequencing

L. mexicana promastigotes (2.5×10^7 cells) were incubated with 30 µM **DDB-PAL** or **DDB-1** at 28 °C for 24 h; a 0.1% DMSO treated culture was run in parallel. The experiment was performed three times independently. Total RNA was extracted using a RNeasy (Qiagen) kit according to the manufacturer's instructions with a final elution in 30 µL RNAse-free H_2O, and sent to BGI genomics for sequencing. Library preparation and transcriptome sequencing was carried out by BGI genomics: strand specific mRNA sequencing, DNBseq, 100 base pairs paired end reads, 10 Gbase, read filtering and clean-up. BGI genomics delivered clean reads, which then underwent bioinformatic analysis.

Bioinformatic analysis was carried out on the resultant reads by aligning transcripts to the *L. mexicana* MHOM/GT/2001/U1103 reference transcriptome[305] using BWA-MEM (Version 0.7.17-r1188),[520] and converting the output number of mapped reads to transcripts per million (TPM) – the best measure for quantification between samples.[524] Volcano plots were generated in Excel, and the statistical significance (*P*-value) was derived from a two-tailed *t*-test. TPM were uploaded to LeishCyc (leishcyc.org, based on the genomic data of *L. major* v5.2 obtained from the *L. major* Friedlin project by the Sanger Institute)[441] and overlaid onto the cellular overview.

6.13 Chemistry experimental

Full experimental and characterisation data for all compounds synthesised can be found in the Appendix Section 7.4.

7 Appendix

7.1 Supplemental data for Chapter 2

7.1.1 Pharmacokinetic radar for compound **28** and compound **34**

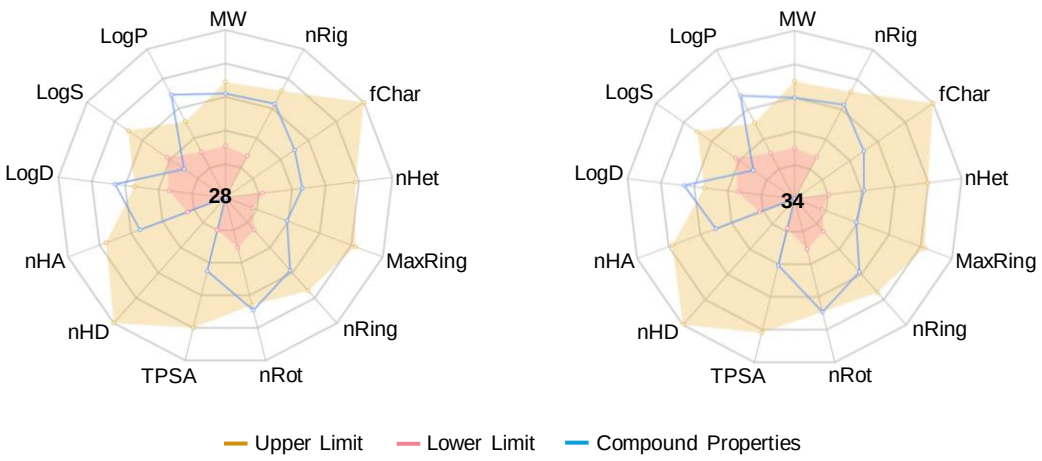

Properties

MW = Molecular weight, 100 – 600
nRig = Number of rigid bonds, 0 – 30
fChar = Formal charge, −4 – 4
nHet = Number of heteroatoms, 0 – 15
MaxRing = Number of atoms in the biggest ring, 0 – 18
nRing = Number of rings, 0 – 6
nRot = Number of rotatable bonds, 0 – 11
TPSA = Topological polar surface area, 0 – 140
nHD = Number of H-bond donors, 0 – 7
nHA = Number of H-bond acceptors, 0 – 12
LogD = LogP at pH 7.4, 1 – 3
LogS = Log of the aqueous solubility, −4 – 0.5
LogP = Log of the octanol/water partition coefficient, 0 – 3

Figure 65. *In silico* predictions of physicochemical, structural and ADMET parameters, bioavailability radar for analogues **28** and **34**.

7.2 Supplemental data for Chapter 4

7.2.1 LeishCyc cellular overview for DDB-PAL

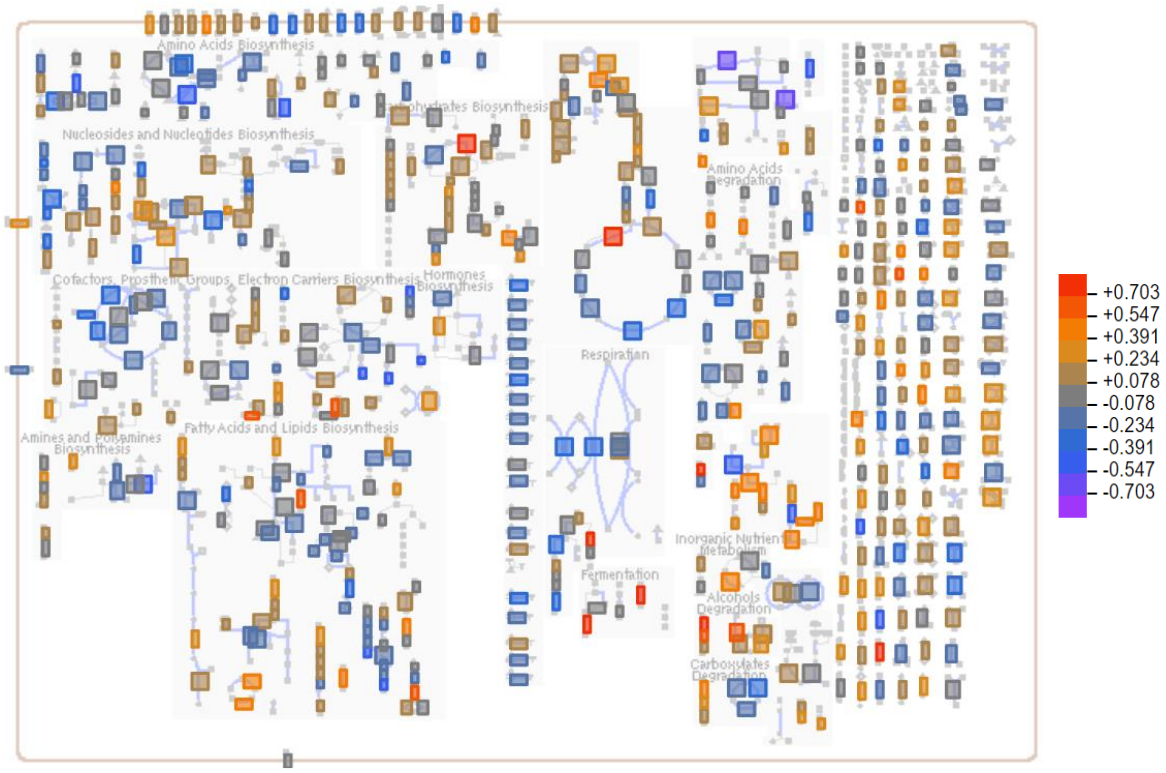

Figure 66. Overlay of the transcriptome changes in **DDB-PAL** treated *L. mexicana* promastigotes onto LeishCyc cellular overview. Upregulated proteins are shown in red, downregulated proteins are shown in purple.

7.2.2 Rationale for protein prioritisation

Table 20. Rationale for the prioritisation of the nine genes further investigated from all the genes identified in Table 15, Table 16 and Figure 46

Gene ID	DDB-1			DDB-PAL			Priority	Reason?
	FC	mRNA	*P*-value	FC	mRNA	*P*-value		
LmxM.04.0130	3.19	101.20	6.68E-05	1.89	59.93	5.66E-04	Y	Highly upregulated, is significant in both
LmxM.29.2090	2.98	15.45	5.58E-04	1.81	9.41	6.95E-03	N	Very low mRNA, other protein in same role unchanged
LmxM.33.0070	2.75	186.35	8.93E-05	1.48	100.11	1.90E-02	Y	Mitochondrial, high upregulation, only one copy of gene
LmxM.19.1420	2.28	222.82	2.57E-03	1.63	159.65	5.77E-03	N	Not that significant, unlikely to be interesting
LmxM.33.0140	2.19	639.54	1.18E-04	1.66	483.38	3.01E-04	Y	Mitochondrial, high abundance. Significant in both
LmxM.27.0090	2.13	130.68	1.38E-04	1.97	121.04	1.48E-04	Y	CYP often upregulated in drugs, is above threshold in both, is highest for **DDB-PAL**
LmxM.18.0440	2.10	84.16	1.36E-03	1.56	62.59	3.95E-04	N	Barely above threshold, 2 other genes on pathway unchanged
LmxM.17.0890	2.06	458.60	3.11E-04	1.71	380.88	1.50E-03	N	Barely above threshold for **DDB-1**, although is significant in both
LmxM.30.0453	2.04	152.41	3.60E-04	1.92	143.53	4.66E-05	N	Orthologs are amastins
LmxM.28.2690	2.01	10.80	5.47E-03	1.66	8.89	3.10E-02	N	Barely above threshold for **DDB-1**, also low abundance
LmxM.30.0450	1.95	467.50	3.63E-05	1.90	454.46	2.84E-05	N	Orthologs are amastins

LmxM.23.1062	1.88	151.48	2.24E-02	1.84	148.30	1.55E-02	N	No orthologs, abnormal amino acid sequence
LmxM.18.0640	1.35	53.59	1.17E-03	2.22	88.04	2.24E-02	N	Low significance
LmxM.30.3070	0.80	202.14	2.47E-04	0.41	104.39	8.26E-03	Y	Reasonably downregulated, both transporters affected
LmxM.30.3060	0.79	132.18	4.99E-04	0.42	69.58	8.75E-03	Y	Reasonably downregulated, both transporters affected
LmxM.30.2250	0.72	235.91	3.27E-05	0.49	161.18	1.60E-04	N	Barely above threshold, 2 other genes on the pathway unchanged, expected not to be expressed in promastigotes.
LmxM.23.0050	0.69	136.40	1.35E-03	0.43	83.95	2.54E-02	N	Barely above threshold, 18 other enzymes do the same role, no change in those.
LmxM.14.1340	0.69	112.09	8.50E-05	0.46	75.17	4.78E-04	N	Not over **DDB-PAL** threshold, barely above **DDB-1** threshold
LmxM.15.1470	0.67	598.81	4.51E-04	0.43	380.05	4.94E-03	N	Low significance
LmxM.30.1800	0.50	120.74	1.30E-03	0.59	144.58	2.78E-03	N	Barely above threshold for **DDB-1**
LmxM.24.1210	0.47	120.62	1.17E-03	0.63	160.35	1.88E-03	Y	Very downregulated, related to 27.1710?
LmxM.27.1710	0.45	61.52	1.08E-05	0.64	87.56	1.60E-04	Y	Very downregulated, related to 24.1210?
LmxM.34.4380	0.41	117.75	2.87E-04	0.65	187.47	4.62E-03	N	Abnormal amino acid sequence
LmxM.03.0600	0.38	56.07	1.80E-06	0.61	89.82	2.78E-05	Y	Extreme downregulated, is significant in both

FC = fold change, mRNA is average of TPM for $n = 3$ repeats, P-value was derived from a two-tailed t-test.

7.3 Supplemental data for Chapter 6

7.3.1 Primer sequences used for CRISPR-Cas9 mediated genome editing

Table 21. Primer sequences used for constructs and sgRNA designed as described (Section 6.2) from LeishGEdit.[508]

Gene ID	Shorthand	Primer	Primer Sequence	Drug marker
LmxM.28.0550	mNG::RAD51	UF	TCGCGCAGGGTCCTACCACTCACCCTACCAgtataatgcagacctgctgc	Puro
		UR	GCGAGCCTTGGCCTTGGAACGAGTCTGCATactacccgatcctgatccag	
		5sg	gaaattaatacgactcactataggAGGAACGGAAAAACAAAAGGgttttagagctagaaatagc	
LmxM.09.1130	mNG::TIM17,	UF	CTCCCTCCCCGCATCGTCTGCCTTGTACCAgtataatgcagacctgctgc	Puro
	Halo::TIM17	UR	GGGCTGCCTAGGGTCCAGGATGGATGTCATactacccgatcctgatccag	Puro
		5sg	gaaattaatacgactcactataggTACAGGCTTGCTTTCTGATTgttttagagctagaaatagc	
LmxM.29.2980	mNG::GAPDH	UF	ACAAGCTCTTTCTCTCTCTCAAGACAACCGgtataatgcagacctgctgc	Neo
		UR	GCCGTTGATACCGACCTTGATAGGCGCCATactacccgatcctgatccag	
		5sg	gaaattaatacgactcactataggGGGGGTGAGGGATGTTAGTTgttttagagctagaaatagc	
LmxM.20.1650	Halo::S11	UF	TCTATAATACGTATGTGTATGTATGCTCCAgtataatgcagacctgctgc	Puro
		UR	CGCGTGGTAGTACTGGGGCGCAACGGACATactacccgatcctgatccag	
		5sg	gaaattaatacgactcactataggTTGACGGAGTAAAACCTCTGgttttagagctagaaatagc	
LmxM.18.1130	Halo::RAB5A	UF	TCTGCTCACTGGGAAAGAACATATACACCGgtataatgcagacctgctgc	Puro
		UR	CTCCATCAGCTGAGGTGGGTGGATGTTCATactacccgatcctgatccag	
		5sg	gaaattaatacgactcactataggTGTGGGTGATGTTGCTTTGTgttttagagctagaaatagc	
LmxM.24.0940	Halo::ATOM14	UF	CACTCACATACACTAAGCTGAGCAGCACCTgtataatgcagacctgctgc	Puro
		UR	GATGTGGTACTTCTCCATGAATGCGGACATactacccgatcctgatccag	
		5sg	gaaattaatacgactcactataggGAGGAAGAGGTGCGCTCAGTgttttagagctagaaatagc	
LmxM.19.1420	CPA::Halo	DF	CACACCCCGCACGTGCCGACGACAACGGCCggttctggtagtggttccgg	Puro
		DR	CCACTCGAAAAAAAAGCAGCTCATTCGCCCccaatttgagagacctgtgc	
		3sg	gaaattaatacgactcactataggAGCCCAGGCCCACGGTGCCTgttttagagctagaaatagc	

LmxM.33.3740	SPT::Halo	DF	ATCGAGACAGCCGTCAAGGCCGAGTTTGCGggttctggtagtggttccgg	Puro
		DR	TCACATAAGCGAAGCTATGGGCGCACGCCAccaatttgagagacctgtgc	
		3sg	gaaattaatacgactcactataggTACAGCTGCGATGCCGGGTGgttttagagctagaaatagc	
LmxM.36.1760	ALDH::Halo	DF	GACATCAAGTATGTCCTCTTCTCGACTGTCggttctggtagtggttccgg	Puro
		DR	TGAGCTGAACCAAACCCCTCGCCCCTGCCCccaatttgagagacctgtgc	
		3sg	gaaattaatacgactcactataggGCGTGCCCAGGGAAGGGCAAgttttagagctagaaatagc	
LmxM.04.0130	Hyp0130::mNG	DF	GTCTGCGTTGTCGCCGCCCTCTATGCCTTTggttctggtagtggttccgg	Puro
		DR	GACGACGCGCACCGGCGTTGCCCACGACCAccaatttgagagacctgtgc	
		3sg	gaaattaatacgactcactataggGAGTGCGTGGTTGATGGTCGgttttagagctagaaatagc	
LmxM.33.0140	mMDH::mNG	DF	ATCAAGAAGGGCATCGAGCTCGGCAACTGGggttctggtagtggttccgg	Puro
		DR	TTGCAGCTGCGTGCCTGTAAAACACCGTCGccaatttgagagacctgtgc	
		3sg	gaaattaatacgactcactataggCATCATCGAATAGCTTCCGAgttttagagctagaaatagc	
LmxM.27.0090	CYP450::mNG	DF	GTGCGGGGCACACCGAACAAGCTGTTCATGggttctggtagtggttccgg	Puro
		DR	CGGAGCGCTGTCCTTCTCTTCTCACCCACCccaatttgagagacctgtgc	
		3sg	gaaattaatacgactcactataggCCTCTCTCTTCTGCGGGTGGgttttagagctagaaatagc	
LmxM.33.0070	APX::mNG	DF	AACCTTCACAAAGCACCCGCGTCGGGGAGCggttctggtagtggttccgg	Puro
		DR	AGAAGGTGGGGGAGAGGAGGATAACAACCAccaatttgagagacctgtgc	
		3sg	gaaattaatacgactcactataggAAAGTGAACGTAGCGCGCTTgttttagagctagaaatagc	
LmxM.03.0600	NMT::mNG	DF	ACCTCGGGCACCTATTACTACCAGTCCTACggttctggtagtggttccgg	Puro
		DR	ACACACGCATGTGCGTCGCTGCACCATCCCccaatttgagagacctgtgc	
		3sg	gaaattaatacgactcactataggTCAAGGATGTGAAGGGGAAGgttttagagctagaaatagc	
LmxM.27.1710	eRF::mNG	DF	GAGGAATTCGACTTCGACGACGACTTCATGggttctggtagtggttccgg	Puro
		DR	CAGACATTGACGCGTCCCGTCCCCCACCCCccaatttgagagacctgtgc	
		3sg	gaaattaatacgactcactataggCTCGCCTACACTCTGAAGAGgttttagagctagaaatagc	
LmxM.31.1870	CatEff::mNG	DF	GCACCTCACAGTGCAACCTATGACCACGTGggttctggtagtggttccgg	Puro
		DR	AAAAATGACGAGAAGTCGACATGTGAGCCAccaatttgagagacctgtgc	
		3sg	gaaattaatacgactcactataggGCCACGTTGAGAGAGCATTGgttttagagctagaaatagc	

LmxM.28.1930	ZIP3::mNG	DF	GGCGTGATGGCGATGATTGGGAAGTGGCTGggttctggtagtggttccgg	Puro
		DR	AAGCGCGACCCATTGCAGCAGCAGCCACCTccaatttgagagacctgtgc	
		3sg	gaaattaatacgactcactataggTCCTGCGCGAGTATGTGGCTgttttagagctagaaatagc	
LmxM.24.1210	mNG::eIF1	UF	TTGCCACGCCCTCGATAAGCAGTGGATCCGgtataatgcagacctgctgc	Puro
		UR	GTTCACAATGGCCTCGACGGTGTCCTCCATactacccgatcctgatccag	
		5sg	gaaattaatacgactcactataggCCTTGTACGGTTAGGGTATGgttttagagctagaaatagc	
LmxM.30.3060-70	mNG::LIT1	UF	CTCCAGTCCGCTTCCGCTTTTTCCAGGCCCgtataatgcagacctgctgc	Puro
		UR	CGCCTCCACGCTCAGTTTCGCCGGCTCCATactacccgatcctgatccag	
		5sg	gaaattaatacgactcactataggAACGGTAGCTGCGGAGGTGTgttttagagctagaaatagc	
LmxM.04.0130	ΔHyp0130	UF	ACCGTGTATACGCGACGGAAAAGATGACCCgtataatgcagacctgctgc	Puro + Blast
		DR	GACGACGCGCACCGGCGTTGCCCACGACCAccaatttgagagacctgtgc	
		5sg	gaaattaatacgactcactataggCGTGGAGCGGGGGAGGATATgttttagagctagaaatagc	
		3sg	gaaattaatacgactcactataggGAGTGCGTGGTTGATGGTCGgttttagagctagaaatagc	
LmxM.33.0140	ΔmMDH	UF	CCACTCTGAGCACATACACCCACATTCCCAgtataatgcagacctgctgc	Puro + Neo
		DR	TTGCAGCTGCGTGCCTGTAAAACACCGTCGccaatttgagagacctgtgc	
		5sg	gaaattaatacgactcactataggAAAGACCGCAAAAGAAAATGgttttagagctagaaatagc	
		3sg	gaaattaatacgactcactataggCATCATCGAATAGCTTCCGAgttttagagctagaaatagc	
LmxM.33.0070	ΔAPX	UF	CAAGAGAAAAAGAGACCCAAATAAGACCGCgtataatgcagacctgctgc	Puro + Blast
		DR	AGAAGGTGGGGGAGAGGAGGATAACAACCAccaatttgagagacctgtgc	
		5sg	gaaattaatacgactcactataggACGCAACGAAGGACTCTACGgttttagagctagaaatagc	
		3sg	gaaattaatacgactcactataggAAAGTGAACGTAGCGCGCTTgttttagagctagaaatagc	
LmxM.30.3060-70	ΔLIT1*	UF	TCGCACACCACCGCAGCGCACAGTGGGCGCgtataatgcagacctgctgc	Puro + Neo + Blast
		DR	GGGAACCGCCCATGGGGCTCAATGTCGAGCccaatttgagagacctgtgc	
		5sg	gaaattaatacgactcactataggACGGCAGCAAAGAAACACACgttttagagctagaaatagc	
		3sg	gaaattaatacgactcactataggAAAAAGCCCTTGAACAAGCTgttttagagctagaaatagc	

LmxM.31.1870	ΔCatEff	UF	GATTCGCGGCCTCGCCGTTTCAGTTCACCGgtataatgcagacctgctgc	Puro + Neo
		DR	AAAAATGACGAGAAGTCGACATGTGAGCCAccaatttgagagacctgtgc	
		5sg	gaaattaatacgactcactataggGAGCGAGGGAGAGAAAGGGGgttttagagctagaaatagc	
		3sg	gaaattaatacgactcactataggGCCACGTTGAGAGAGCATTGgttttagagctagaaatagc	
LmxM.28.1930	ΔZIP3**	UF	TTTCATCTGGCATGTTCGGGTCAGCGTCCCgtataatgcagacctgctgc	Puro + Neo
		DR	GTGGGCGATGAGGACGGGGAGGGCGTGCGCccaatttgagagacctgtgc	
		5sg	gaaattaatacgactcactataggGAGCTGGTTCCCATGAACTGgttttagagctagaaatagc	
		3sg	gaaattaatacgactcactataggGGTGCGGGTAAGTTGGGCGGgttttagagctagaaatagc	
		G00	aaaagcaccgactcggtgccacttttcaagttgataacggactagccttattttaacttgctatttctagctctaaaac	

UF = upstream forward, UR = upstream reverse, DF = downstream forward, DR = downstream reverse 5sg = 5' sgRNA, 3sg = 3' sgRNA.

* primers designed to delete genes: LmxM379c.30.1390425 and LmxM379c.30.1399774 (just upstream and downstream from LmxM379c.30.3060-70) from annotated genome sequence of *Leishmania mexicana* MNYC/BZ/62/M379 expressing Cas9 and T7 RNA polymerase.[525]

**primers designed to delete regions just upstream and downstream from LmxM379c.28.1930, from annotated genome sequence of *Leishmania mexicana* MNYC/BZ/62/M379 expressing Cas9 and T7 RNA polymerase.[525]

7.3.2 Primer sequences used for PCR validation of deletion mutant cell lines

Table 22. Primer sequences used for PCR validation of target ORF deletion in deletion mutant cell lines

Gene ID	Shorthand	Primer Sequence
LmxM.04.0130	ΔHyp0130	CGACTGTGTCCTTCCTCAACCT
		CGAGTTGTACTTGGGGAGGGAG
LmxM.33.0140	ΔmMDH	TCTCAGGCATCCTTCTTCCGTG
		CTGGGGTGTAGATGTGGGAGAG
LmxM.33.0070	ΔAPX	GACGCCTCAAAGATGCAAGGTC
		ACGTCAGTGGGAAGCATCATCA
LmxM.30.3060-70	ΔLIT1	TATGTGTTCTCCGTGGCGAAGT
		GCAATCAGGGCAAGCAAGAAGT
LmxM.31.1870	ΔCatEff	CGTTGGAGTGTCTAGTGGCTGA
		GCTGAGCTTGCGACGTATGTTT
LmxM.28.1930	ΔZIP3	CTTGTGTTCTCGTTCTCTGCGC
		CTTCCCAATCATCGCCATCACG
LmxM.20.1400	PF16	TGATGATCTGGATGGACTCGGC
		CCAGCACTGTGTCTACCTACCC

7.3.3 Agarose gels for visualising validation of deletion mutant cell lines

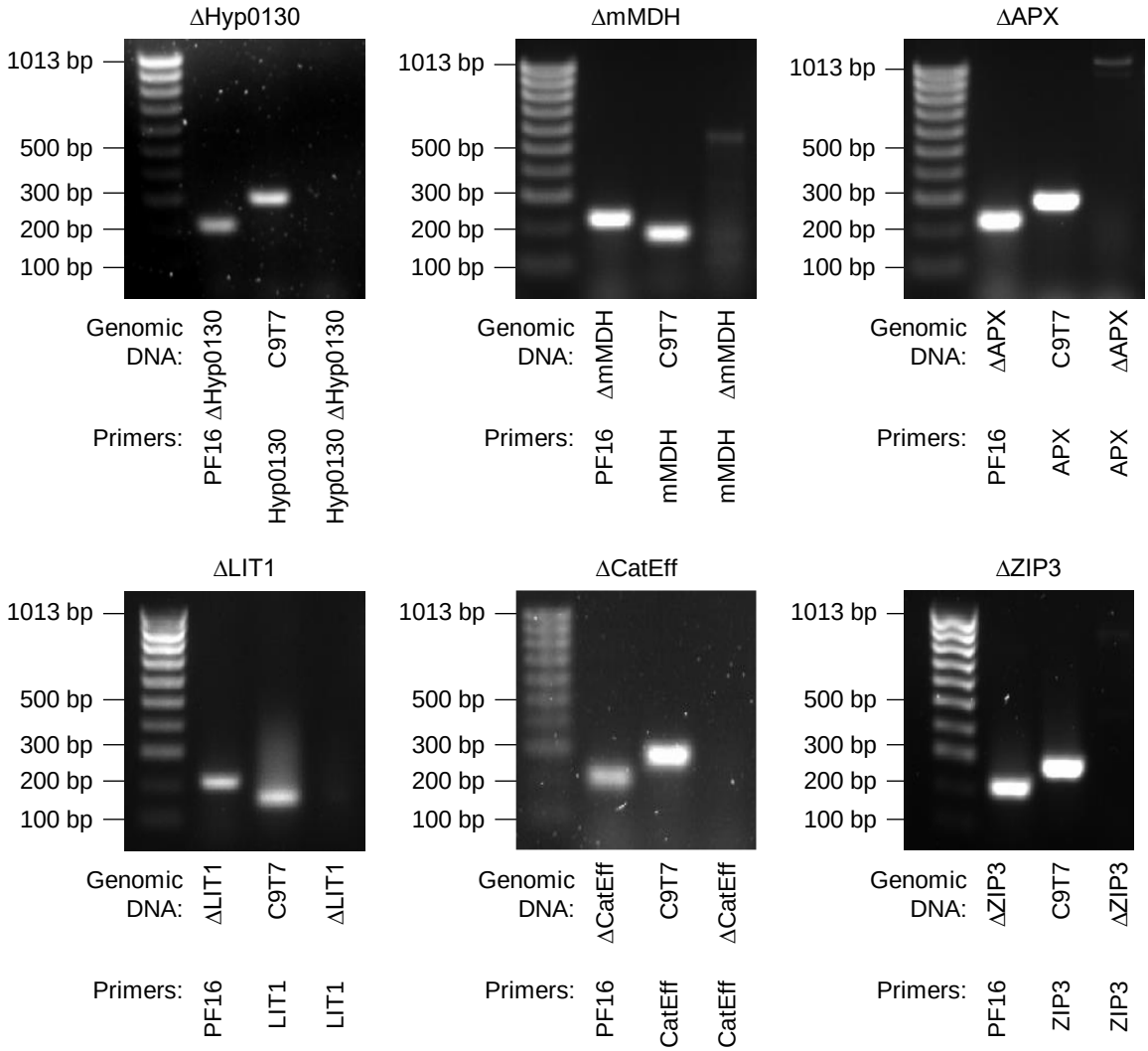

Figure 67. PCR confirmation of target ORF deletion. PCR products were separated by agarose gel electrophoresis and visualised by ethidium bromide DNA labelling. For each cell line, the genomic DNA and ORF to which the primers anneal are indicated. Absence of a DNA band in the third column indicates deletion of the desired ORF. ΔLIT1 is a deletion of both LmxM.30.3060 and LmxM.30.3070 in tandem.

7.4 Chemistry methods

7.4.1 Chemistry general experimental considerations

Materials/procedures: Dichloromethane (CH_2Cl_2), dioxane, tetrahydrofuran (THF), and *N*,*N*-dimethylformamide (DMF) were dried by passing through an activated alumina column under argon in an MBraun SPS-800 solvent dispenser. All other reagents were used as received. Caesium

carbonate and copper(I) chloride were weighed out in a glove box under a nitrogen atmosphere. Brine refers to a saturated aqueous solution of NaCl. All air-sensitive or moisture-sensitive reactions were carried out with anhydrous solvents in heated glassware using a heat gun under an inert nitrogen atmosphere. For reactions that require heating, an oil bath was employed and the temperature monitored *via* a temperature probe plugged into the stirrer plate.

Chromatography: Thin-layer chromatography was performed on pre-coated aluminium-backed plates (Merck Kieselgel 60 F_{254} plates), which were visualised with UV fluorescence (254 nm) and/or staining with potassium(VII) manganate, vanillin, phosphomolybdic acid or ninhydrin followed by heating with a heat gun. Column chromatography refers to normal phase column chromatography unless otherwise specified and was performed manually using Geduran® Silica gel 60 (40-63 μm) under a positive pressure of nitrogen, with the solvent system used in parentheses. Retention factors (R_f) are reported with the solvent system in parentheses.

Infrared spectroscopy: Infrared spectra were recorded on a Bruker Tensor 27 Fourier transform spectrometer, using material applied as a thin film on a diamond PIKE Miracle ATR module. Wavelengths of maximum absorbance (ν_{max}) are quoted in cm^{-1}. Only selected, characteristic IR absorption data are provided for each compound.

NMR spectroscopy: Proton (^1H) and carbon (^{13}C) NMR spectra were recorded on a Bruker AVII HD 400 (400 MHz) or AVII 500 (500 MHz) spectrometer. Chemical shifts (δH and δC) are expressed in parts per million (ppm), referenced to the residual solvent peak of $CDCl_3$ (7.26/77.16 ppm). Coupling constants (*J*) are reported to the nearest 0.1 Hz. Spectra are assigned based on chemical shifts, coupling constants, COSY, HSQC and HMBC data and/or comparison with similar compounds. Splitting patterns are described using the following abbreviations: s (singlet), d (doublet), dd (doublet of doublets), ddt (doublet of doublet of triplets), dt (doublet of triplets), t (triplet), q (quartet), m (multiplet) and br (broad).

Mass spectrometry: Low-resolution mass spectra were recorded on a Micromass LCT Premier Open Access using electrospray ionisation (ESI). High-resolution mass spectra (HRMS) were

recorded by the University of Oxford Departmental Mass Spectrometry Service on a Thermo Scientific Exactive Mass Spectrometer (using a Waters Equity autosampler and pump) for electrospray ionisation (ESI). High resolution values are calculated to 4 decimal places from the molecular formula, and all values are within a tolerance of 5 ppm.

7.4.2 Synthetic schemes

The majority of synthetic routes were shown in Scheme 1, Scheme 2, Scheme 3, and Scheme 4. In addition, the coupling partner for the Ullmann cross-coupling (Section 2.2.1) was synthesised in one step, and linkers for the modification of **DDB-1** to allow further functionalisation were synthesised as shown in Scheme 5.

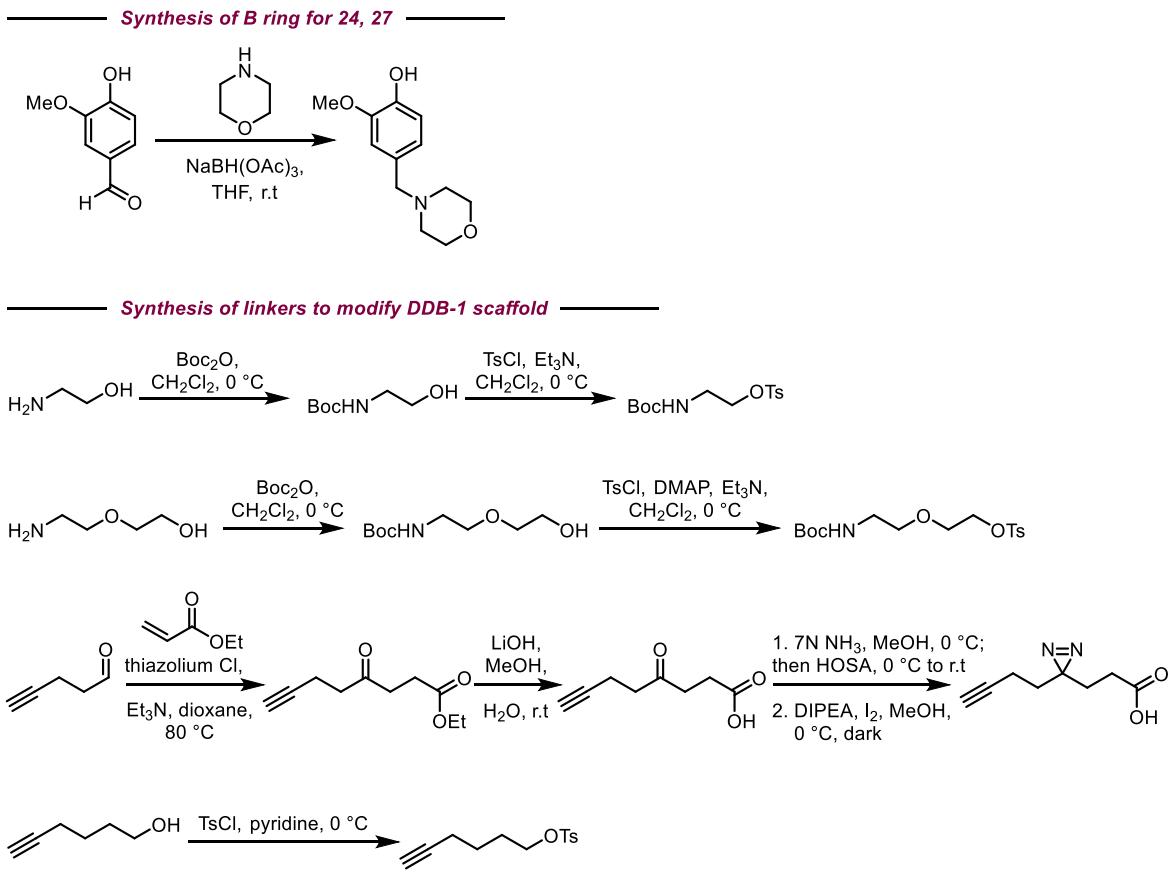

Scheme 5. Synthesis of the B ring coupling partner for the Ullmann cross-coupling, and linkers to further modify the **DDB-1** scaffold.

7.4.3 Chemistry experimental procedures

4-Allyl-2-methoxy-1-(methoxymethoxy)benzene

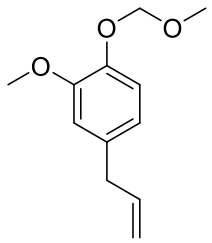

To a solution of eugenol (0.94 mL, 6.1 mmol, 1.0 equiv.) in anhydrous CH_2Cl_2 (40 mL) at 0 °C was added chloromethyl methyl ether (0.68 mL, 9.2 mmol, 1.5 equiv.), followed by *N*,*N*-diisopropylethylamine (2.1 mL, 12 mmol, 2.0 equiv.) dropwise. The resulting solution was allowed to warm to room temperature and stirred until the reaction was complete (24 h). The reaction mixture was washed successively with aqueous 0.5 M HCl, H_2O, aqueous 1 M NaOH, and brine, dried over $MgSO_4$, and evaporated to dryness. Purification *via* column chromatography (19:1 pentane/EtOAc) afforded **4-allyl-2-methoxy-1-(methoxymethoxy)benzene** (1.11 g, 5.33 mmol, 87%) as a colourless oil.

R_f 0.33 (19:1 pentane/EtOAc).

^{1}H NMR (400 MHz, $CDCl_3$) δ 7.07 (d, *J* = 8.0 Hz, 1H), 6.76 – 6.65 (m, 2H), 5.96 (ddt, *J* = 16.8, 10.0, 6.6 Hz, 1H), 5.20 (s, 2H), 5.14 – 5.01 (m, 2H), 3.87 (s, 3H), 3.51 (s, 3H), 3.34 (dt, *J* = 6.6, 1.5 Hz, 2H).

^{13}C NMR (101 MHz, $CDCl_3$) δ 149.7, 144.8, 137.5, 134.5, 120.6, 116.7, 115.7, 112.3, 95.7, 56.1, 55.8, 39.9.

Spectroscopic data is in accordance with the literature.[318]

5-Allyl-1-iodo-3-methoxy-2-(methoxymethoxy)benzene

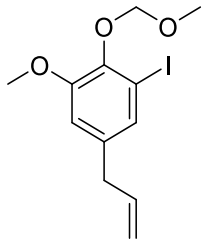

To a solution of 4-allyl-2-methoxy-1-(methoxymethoxy)benzene (2.00 g, 9.60 mmol, 1.0 equiv.) in anhydrous THF (20 mL) was added tetramethylethylenediamine (2.6 mL, 17 mmol, 1.8 equiv.). The solution was cooled to −78 °C then *sec*-butyllithium solution (1.4 M in hexane, 12 mL, 17 mmol, 1.8 equiv.) was added dropwise and stirred for 30 min. Iodine (4.40 g, 17.3 mmol, 1.8 equiv.) was added slowly as a solution in anhydrous THF (5 mL), and after 10 mins, the solution was allowed to warm to room temperature and stirred until the reaction was complete (1 h). The resulting solution was quenched with $Na_2S_2O_3$ (aq., sat), diluted with H_2O, EtOAc (30 mL) and the layers separated. The aqueous layer was extracted with EtOAc (20 mL × 2), the combined organic extracts washed with NH_4Cl (aq., sat), brine, dried over $MgSO_4$ and evaporated to dryness. Purification *via* column chromatography (19:1 pentane/EtOAc) afforded **5-allyl-1-iodo-3-methoxy-2-(methoxymethoxy)benzene** (1.93 g, 5.78 mmol, 60%) as a colourless oil.

R_f 0.38 (19:1 pentane/EtOAc).

^{1}H NMR (400 MHz, $CDCl_3$) δ 7.20 (d, *J* = 1.9 Hz, 1H), 6.70 (d, *J* = 1.9 Hz, 1H), 5.98 – 5.84 (m, 1H), 5.13 (s, 2H), 5.12 – 5.07 (m, 2H), 3.82 (s, 3H), 3.67 (s, 3H), 3.33 – 3.26 (m, 2H).

^{13}C NMR (101 MHz, $CDCl_3$) δ 152.1, 144.2, 138.2, 136.6, 130.7, 116.5, 113.3, 98.7, 92.6, 58.4, 56.1, 39.4.

Spectroscopic data is in accordance with the literature.[318]

4-Allyl-2-iodo-6-methoxyphenol

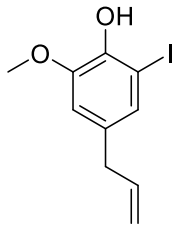

To a solution of 5-allyl-1-iodo-3-methoxy-2-(methoxymethoxy)benzene (2.67 g, 8.00 mmol, 1.0 equiv.) in MeOH (200 mL) was added aqueous 1 M HCl (20 mL) and left stirring until the reaction was complete (24 h). The reaction mixture was basified to pH 5 with aqueous 1 M NaOH, diluted with EtOAc (50 mL) and the layers separated. The aqueous layer was extracted with EtOAc (50 mL × 2), combined organic extracts washed with brine, dried over $MgSO_4$ and evaporated to dryness to afford **4-allyl-2-iodo-6-methoxyphenol** (2.30 g, 7.93 mmol, 99%) as a yellow oil which was used without further purification.

R_f 0.40 (19:1 pentane/EtOAc).

^{1}H NMR (400 MHz, $CDCl_3$) δ 7.12 (d, *J* = 1.8 Hz, 1H), 6.65 (d, *J* = 1.8 Hz, 1H), 5.95 (s, 1H), 5.96 – 5.84 (m, 1H), 5.12 – 5.05 (m, 2H), 3.87 (s, 3H), 3.30 – 3.25 (m, 2H).

^{13}C NMR (101 MHz, $CDCl_3$) δ 146.0, 144.0, 137.1, 133.7, 130.2, 116.2, 111.3, 81.2, 56.2, 39.4.

Spectroscopic data is in accordance with the literature.[318]

5-Allyl-1-iodo-3-methoxy-2-((4-methoxybenzyl)oxy)benzene

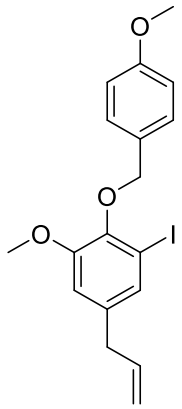

To a solution of 4-allyl-2-iodo-6-methoxyphenol (1.17 g, 4.03 mmol, 1.0 equiv.) and K_2CO_3 (1.39 g, 10.1 mmol, 2.5 equiv.) in DMF (12 mL) was added 4-methoxybenzyl chloride (0.66 mL, 4.8 mmol, 1.2 equiv.) and heated to 80 °C while stirring until complete (1 h). The reaction mixture was diluted with EtOAc (50 mL), H_2O and separated. The organic extract was washed with H_2O, brine, dried over $MgSO_4$ and evaporated to dryness. Purification *via* column chromatography (19:1 pentane/EtOAc) afforded **5-allyl-1-iodo-3-methoxy-2-((4-methoxybenzyl)oxy)benzene** (1.54 g, 3.75 mmol, 93%) as a colourless oil.

R_f 0.73 (19:1 pentane/EtOAc).

^{1}H NMR (400 MHz, $CDCl_3$) δ 7.52 – 7.47 (m, 2H), 7.19 (d, *J* = 1.9 Hz, 1H), 6.94 – 6.88 (m, 2H), 6.72 (d, *J* = 1.9 Hz, 1H), 5.99 – 5.87 (m, 1H), 5.14 – 5.07 (m, 2H), 4.92 (s, 2H), 3.85 (s, 3H), 3.82 (s, 3H), 3.32 – 3.28 (m, 2H).

^{13}C NMR (101 MHz, $CDCl_3$) δ 159.6, 152.7, 146.1, 138.1, 136.7, 130.4, 130.3, 129.4, 116.5, 113.7, 113.4, 93.1, 74.3, 56.0, 55.3, 39.5.

Spectroscopic data is in accordance with the literature.[318]

2-Methoxy-4-(morpholinomethyl)phenol

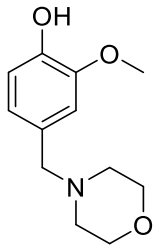

To a solution of vanillin (3.00 g, 19.7 mmol, 1.0 equiv.) and morpholine (1.71 mL, 19.7 mmol, 1.0 equiv.) in anhydrous THF (130 mL) was added sodium triacetoxyborohydride (6.24 g, 29.6 mmol, 1.5 equiv.) and left stirring until the reaction was complete (24 h). The solution was quenched with $NaHCO_3$ (aq., 10%), extracted with Et_2O (80 mL × 3), combined organic extracts washed with brine, dried over Na_2SO_4 and evaporated to dryness to afford **2-methoxy-4-(morpholinomethyl)phenol** (4.28 g, 19.2 mmol, 97%) as a clear gum which was used without further purification.

R_f 0.05 (3:2 EtOAc/pentane).

^{1}H NMR (400 MHz, $CDCl_3$) δ 6.79 (d, *J* = 1.9 Hz, 1H), 6.75 (d, *J* = 7.8 Hz, 1H), 6.70 (dd, *J* = 7.8, 1.9 Hz, 1H), 3.78 (s, 3H), 3.66 – 3.62 (m, 4H), 3.35 (s, 2H), 2.40 – 2.33 (m, 4H).

^{13}C NMR (101 MHz, $CDCl_3$) δ 146.6, 144.9, 129.4, 122.2, 114.0, 111.7, 67.0, 63.4, 55.9, 53.6.

Spectroscopic data is in accordance with the literature.[526]

4-(4-(5-Allyl-3-methoxy-2-((4-methoxybenzyl)oxy)phenoxy)-3-methoxybenzyl)morpholine, DDB-1, 24

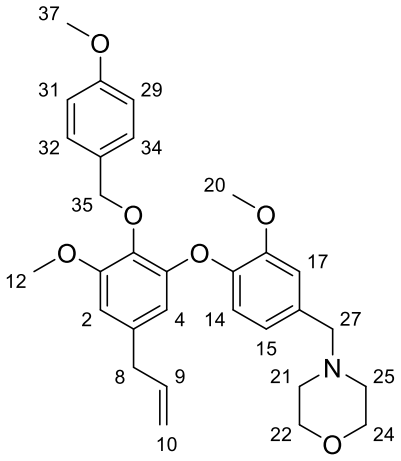

A vial containing 5-allyl-1-iodo-3-methoxy-2-((4-methoxybenzyl)oxy)benzene (1.50 g, 3.70 mmol, 1.0 equiv.), CuCl (178 mg, 1.85 mmol, 0.5 equiv.) and caesium carbonate (2.38 g, 7.40 mmol, 2.0 equiv.) was sealed with a rubber septum then evacuated and backfilled with N_2 (×3). To this was added 2-methoxy-4-(morpholinomethyl)phenol (1.65 g, 7.40 mmol, 2.0 equiv.), *N*-methyl-2-pyrrolidone (3.75 mL) and 2,2,6,6-tetramethyl-3,5-heptanedione (375 µL, 1.85 mmol, 0.5 equiv.) *via* syringe, then the vial was evacuated and backfilled with N_2 (×3) before addition of de-gassed distilled 1,4-dioxane (7.5 mL). The vial was capped and the reaction mixture heated to 80 °C until complete (72 h). The solution was diluted with Et_2O (30 mL), washed with 35% ammonia solution, brine, dried over Na_2SO_4 and evaporated to dryness. Purification *via* column chromatography (1:1 pentane/EtOAc, column prewashed with 1% Et_3N in pentane) afforded **4-(4-(5-allyl-3-methoxy-2-((4-methoxybenzyl)oxy)phenoxy)-3-methoxybenzyl)morpholine** (1.04 g, 2.06 mmol, 56%) as a yellow oil.

R_f 0.42 (EtOAc).

IR (thin film, ν_{max} / cm^{-1}) 2936, 2851, 1585, 1508, 1455, 1420, 1232, 1116, 1091.

^{1}H NMR (400 MHz, $CDCl_3$) δ 7.32 – 7.24 (m, 2H, H32, H34), 6.97 (d, *J* = 1.9 Hz, 1H, H17), 6.82 – 6.77 (m, 2H, H29, H31), 6.76 (dd, *J* = 8.1, 1.9 Hz, 1H, H15), 6.72 (d, *J* = 8.1 Hz, 1H, H14), 6.50

(d, *J* = 2.0 Hz, 1H, H2), 6.36 (d, *J* = 2.0 Hz, 1H, H4), 5.90 (ddt, *J* = 17.5, 9.5, 6.6 Hz, 1H, H9), 5.08 – 5.00 (m, 2H, H10), 4.95 (s, 2H, H35), 3.85 (s, 3H, O-CH_3), 3.83 (s, 3H, O-CH_3), 3.78 (s, 3H, O-CH_3), 3.71 (t, *J* = 4.7 Hz, 4H, H22, H24), 3.45 (s, 2H, H27), 3.26 (dt, *J* = 6.6, 1.5 Hz, 2H, H8), 2.43 (t, *J* = 4.7 Hz, 4H, H21, H25).

^{13}C NMR (101 MHz, $CDCl_3$) δ 159.2, 154.0, 150.3, 150.2, 145.5, 137.2, 137.1, 135.7, 133.2, 130.1, 130.0, 121.5, 118.2, 115.9, 113.4, 113.3, 112.3, 107.9, 74.6, 67.1, 63.2, 56.1, 56.1, 55.2, 53.6, 40.1, 14.2.

HRMS (ESI+) calc. for $C_{30}H_{35}NO_6$ $[M+H]^+$ 506.2532 found 506.2537.

4-(3-Methoxy-4-(3-methoxy-2-((4-methoxybenzyl)oxy)-5-(morpholinomethyl)phenoxy) benzyl)morpholine, 27

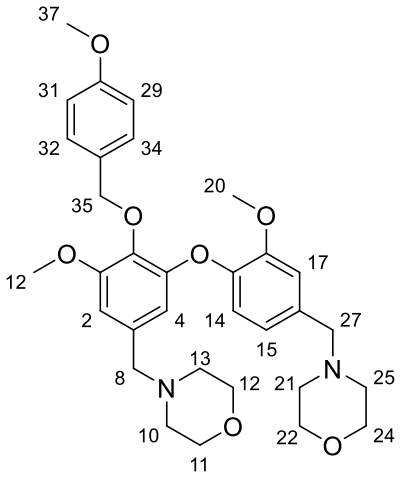

A vial containing 4-(3-iodo-5-methoxy-4-((4-methoxybenzyl)oxy)benzyl)morpholine* (80 mg, 0.17 mmol, 1.0 equiv.), CuCl (8 mg, 0.09 mmol, 0.5 equiv.) and caesium carbonate (110 mg, 0.340 mmol, 2.0 equiv.) was sealed with a rubber septum then evacuated and backfilled with N_2 (×3). To this was added 2-methoxy-4-(morpholinomethyl)phenol (60 mg, 0.26 mmol, 1.5 equiv.), *N*-methyl-2-pyrrolidone (0.17 mL) and 2,2,6,6-tetramethyl-3,5-heptanedione (17 µL, 0.085 mmol, 0.5 equiv.), then the vial was evacuated and backfilled with N_2 (×3) before addition of de-gassed distilled 1,4-dioxane (0.35 mL). The vial was capped and the reaction mixture heated to 120 °C until complete (96 h). The solution was diluted with Et_2O (3 mL), washed with 35% ammonia solution, brine, dried over Na_2SO_4 and evaporated to dryness. Purification *via* column chromatography (9:1 EtOAc/MeOH, column prewashed with 1% Et_3N in EtOAc) afforded **4-(3-methoxy-4-(3-methoxy-2-((4-methoxybenzyl)oxy)-5-(morpholinomethyl)phenoxy)benzyl) morpholine** (10 mg, 0.018 mmol, 11%) as a colourless oil.

R_f 0.20 (19:1 EtOAc/MeOH).

IR (thin film, ν_{max} / cm^{-1}) 2956, 2807, 2764, 1710, 1610, 1587, 1454, 1423, 1350, 1268, 1249, 1219, 1116, 1092, 1035.

^{1}H NMR (500 MHz, $CDCl_3$) δ 7.28 – 7.25 (m, 2H, H32, H34), 7.00 (s, 1H, H17), 6.82 – 6.76 (m, 2H, H29, H31), 6.76 (dd, *J* = 8.1, 1.9 Hz, 1H, H15), 6.71 – 6.68 (m, 2H, H14, H2 or H4), 6.51 (d, *J* = 2.0 Hz, 1H, H2 or H4), 4.96 (s, 2H, H35), 3.85 (s, 3H, O-CH_3), 3.85 (s, 3H, O-CH_3), 3.77 (s, 3H, O-CH_3), 3.71 (s, 4H, morpholine 2 × O-CH_2), 3.68 (t, *J* = 4.7 Hz, 4H, morpholine 2 × O-CH_2), 3.49 (s, 2H, H8 or H27), 3.38 (s, 2H, H8 or H27), 2.46 (s, 4H, morpholine 2 × N-CH_2), 2.40 (s, 4H, morpholine 2 × N-CH_2).

^{13}C NMR (101 MHz, $CDCl_3$) δ 159.3, 154.1, 150.1, 150.0, 150.0, 145.6, 138.0, 130.0, 130.0, 121.6, 117.9, 113.6, 113.4, 113.3, 112.9, 108.2, 74.6, 67.0, 66.9, 63.2, 63.1, 56.2, 56.0, 55.3, 53.5, 53.5.

HRMS (ESI+) calc. for $C_{32}H_{40}N_2O_7$ $[M+H]^+$ 565.2908 found 565.2907.

*Synthesised by Dr. Snigdha Singh in two steps from commercially available starting materials.[337]

4-(3-Methoxy-5-(2-methoxy-4-propylphenoxy)-4-((4-methoxybenzyl)oxy)benzyl)morpholine, 28

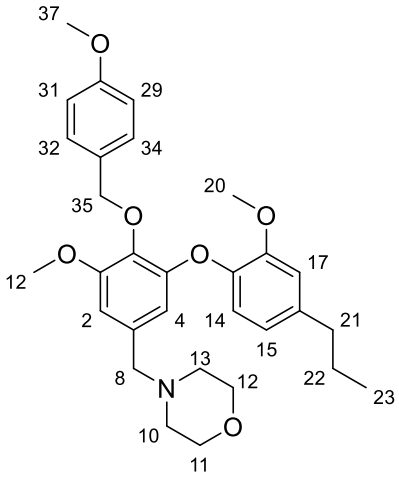

A vial containing 4-(3-iodo-5-methoxy-4-((4-methoxybenzyl)oxy)benzyl)morpholine* (350 mg, 0.745 mmol, 1.0 equiv.), CuCl (36 mg, 0.37 mmol, 0.5 equiv.) and caesium carbonate (480 mg, 1.49 mmol, 2.0 equiv.) was sealed with a rubber septum then evacuated and backfilled with N_2 (×3). To this was added 2-methoxy-4-propylphenol** (238 µL, 1.49 mmol, 2.0 equiv.), *N*-methyl-2-pyrrolidone (0.75 mL) and 2,2,6,6-tetramethyl-3,5-heptanedione (77 µL, 0.37 mmol, 0.5 equiv.), then the vial was evacuated and backfilled with N_2 (×3) before addition of de-gassed distilled 1,4-dioxane (1.5 mL). The vial was capped and the reaction mixture heated to 120 °C until complete (48 h). The solution was diluted with Et_2O (6 mL), washed with 35% ammonia solution, brine, dried over Na_2SO_4 and evaporated to dryness. Purification *via* column chromatography (1:1 pentane/EtOAc, column prewashed with 1% Et_3N in pentane) afforded **4-(3-methoxy-5-(2-methoxy-4-propylphenoxy)-4-((4-methoxybenzyl)oxy)benzyl)morpholine** (292 mg, 0.575 mmol, 77%) as a colourless oil.

R_f 0.36 (EtOAc).

IR (thin film, ν_{max} / cm^{-1}) 2957, 2934, 2360, 2341, 1610, 1587, 1510, 1454, 1423, 1266, 1248, 1216, 1117, 1092, 1035, 982.

^{1}H NMR (400 MHz, $CDCl_3$) δ 7.34 – 7.26 (m, 2H, H32, H34), 6.83 – 6.76 (m, 3H, H29, H31, H17), 6.72 (d, *J* = 8.1 Hz, 1H, H14), 6.66 (dd, *J* = 8.1, 1.9 Hz, 2H, H15, H2 or H4), 6.45 (d, *J* = 1.9 Hz, 1H, H2 or H4), 4.99 (s, 2H, H35), 3.84 (s, 3H, O-CH_3), 3.81 (s, 3H, O-CH_3), 3.78 (s, 3H, O-CH_3), 3.67 (t, *J* = 4.6 Hz, 4H, H11, H12), 3.36 (s, 2H, H8), 2.56 (t, *J* = 7.3 Hz, 2H, H21), 2.39 (t, *J* = 4.6 Hz, 4H, H10, H13), 1.72 – 1.58 (m, 2H, H22), 0.96 (t, *J* = 7.3 Hz, 3H, H23).

^{13}C NMR (101 MHz, $CDCl_3$) δ 159.3, 154.0, 150.6, 150.2, 144.0, 138.5, 137.7, 133.4, 130.2, 130.1, 120.6, 118.9, 113.4, 113.0, 112.2, 107.7, 74.6, 67.0, 63.1, 56.2, 55.9, 55.2, 53.5, 37.8, 24.7, 13.8.

HRMS (ESI+) calc. for $C_{30}H_{37}NO_6$ $[M+H]^+$ 508.2694 found 508.2695.

*Synthesised by Dr. Snigdha Singh in two steps from commercially available starting materials.[337]

** Synthesised by Dr. Snigdha Singh in one step from commercially available starting material.[318]

2-Methoxy-6-(2-methoxy-4-propylphenoxy)-4-(morpholinomethyl)phenol

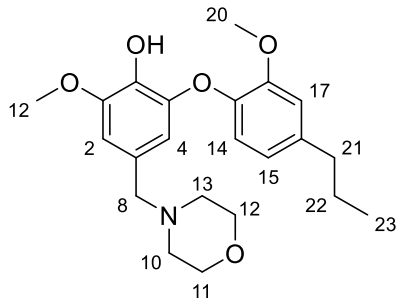

To a solution of 4-(3-methoxy-5-(2-methoxy-4-propylphenoxy)-4-((4-methoxybenzyl)oxy)benzyl) morpholine (140 mg, 0.276 mmol, 1.0 equiv.) in EtOH (9.5 mL) was added aqueous 1 M HCl (4.5 mL) and heated to 80 °C while stirring until the reaction was complete (4 h). The solution was basified to pH 7 with aqueous 1 M NaOH, extracted with EtOAc (5 mL × 3), combined organic extracts washed with brine, dried over Na_2SO_4 and evaporated to dryness. Purification *via* column chromatography (1:4 to 1:0 EtOAc/pentane, column prewashed with 1% Et_3N in pentane) afforded **2-methoxy-6-(2-methoxy-4-propylphenoxy)-4-(morpholinomethyl)phenol** (46 mg, 0.12 mmol, 43%).

R_f 0.18 (EtOAc).

IR (thin film, ν_{max} / cm^{-1}) 2961, 2922, 2361, 2341, 1608, 1595, 1510, 1457, 1432, 1265, 1213, 1155, 1116, 1087, 866.

^{1}H NMR (400 MHz, $CDCl_3$) δ 6.86 (d, *J* = 8.1 Hz, 1H, H14), 6.78 (d, *J* = 1.9 Hz, 1H, H2 or H4), 6.69 (dd, *J* = 8.1, 1.9 Hz, 1H, H15), 6.67 (d, *J* = 1.9 Hz, 1H, H17), 6.53 (d, *J* = 1.9 Hz, 1H, H2 or H4), 3.89 (s, 3H, O-CH_3), 3.85 (s, 3H, O-CH_3), 3.70 – 3.63 (m, 4H, H11, H12), 3.34 (s, 2H, H8), 2.57 (t, *J* = 7.4 Hz, 2H, H21), 2.41 – 2.32 (m, 4H, H10, H13), 1.71 – 1.57 (m, 2H, H22), 0.95 (t, *J* = 7.3 Hz, 3H, H23).

^{13}C NMR (101 MHz, $CDCl_3$) δ 152.3, 147.9, 143.9, 139.3, 136.0, 128.8, 120.7, 119.4, 112.9, 112.5, 111.6, 107.6, 67.0, 63.2, 56.3, 56.0, 53.5, 37.8, 24.6, 13.8.

HRMS (ESI+) calc. for $C_{22}H_{29}NO_5$ $[M+H]^+$ 388.2118 found 388.2119.

4-(3-Methoxy-5-(2-methoxy-4-propylphenoxy)-4-((4-(trifluoromethyl)benzyl)oxy)benzyl) morpholine, 29

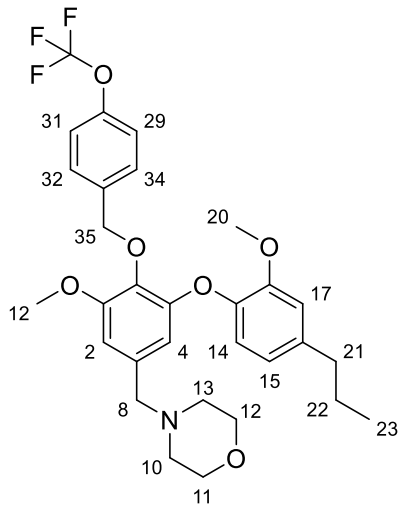

To a solution of 2-methoxy-6-(2-methoxy-4-propylphenoxy)-4-(morpholinomethyl)phenol (20 mg, 0.052 mmol, 1.0 equiv.) and K_2CO_3 (18 mg, 0.13 mmol, 2.5 equiv.) in DMF (0.5 mL) was added 4-(trifluoromethyl)benzyl chloride (9 µL, 0.06 mmol, 1.2 equiv.). The reaction was heated to 80 °C and stirred until complete (18 h). The solution was diluted with EtOAc (3 mL), organic phase was washed with H_2O, brine, dried over $MgSO_4$ and evaporated to dryness. Purification *via* column chromatography (1:0 to 3:1 pentane/EtOAc, column prewashed with 1% Et_3N in pentane) afforded **4-(3-methoxy-5-(2-methoxy-4-propylphenoxy)-4-((4-(trifluoromethyl)benzyl)oxy)benzyl) morpholine** (13 mg, 0.024 mmol, 46%) as a colourless oil.

R_f 0.29 (EtOAc).

^{1}H NMR (400 MHz, $CDCl_3$) δ 7.58 – 7.44 (m, 4H,H29, H31, H32, H34), 6.75 (d, *J* = 1.9 Hz, 1H, H17), 6.71 (d, *J* = 8.1 Hz, 1H, H14), 6.69 – 6.62 (m, 2H, H15, H2 or H4), 6.48 (d, *J* = 1.9 Hz, 1H, H2 or H4), 5.11 (s, 2H, H35), 3.85 (s, 3H, O-CH_3), 3.77 (s, 3H, O-CH_3), 3.67 (t, *J* = 4.6 Hz, 4H, H11, H12), 3.37 (s, 2H, H8), 2.57 (t, *J* = 7.6 Hz, 2H, H21), 2.39 (t, *J* = 4.6 Hz, 4H, H10, H13), 1.71 – 1.56 (m, 2H, H22), 0.95 (t, *J* = 7.3 Hz, 3H, H23).

^{13}C NMR (101 MHz, $CDCl_3$) δ 153.7, 150.4, 150.1, 143.9, 142.1, 138.7, 137.5, 133.9, 128.0, 127.2, 124.9, 120.6, 118.6, 112.8, 112.3, 107.7, 74.0, 67.0, 63.1, 56.1, 55.8, 53.5, 37.8, 24.7, 13.8

HRMS (ESI+) calc. for $C_{30}H_{34}FNO_5$ $[M+H]^+$ 546.2462 found 546.2455.

4-(3-Methoxy-5-(2-methoxy-4-propylphenoxy)-4-((3,4,5-trimethoxybenzyl)oxy)benzyl) morpholine, 30

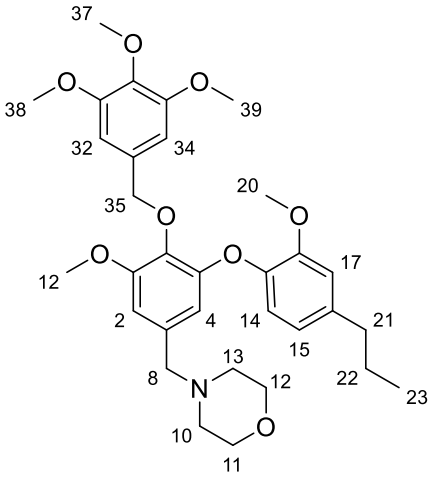

To a solution of 2-methoxy-6-(2-methoxy-4-propylphenoxy)-4-(morpholinomethyl)phenol (20 mg, 0.052 mmol, 1.0 equiv.) and K_2CO_3 (18 mg, 0.13 mmol, 2.5 equiv.) in DMF (0.5 mL) was added 3,4,5-trimethoxybenzyl chloride (13 mg, 0.060 mmol, 1.2 equiv.). The reaction was heated to 80 °C and stirred until complete (18 h). The solution was diluted with EtOAc (3 mL), organic phase was washed with H_2O, brine, dried over $MgSO_4$ and evaporated to dryness. Purification *via* column chromatography (1:0 to 2:3 pentane/EtOAc, column prewashed with 1% Et_3N in pentane) afforded **4-(3-methoxy-5-(2-methoxy-4-propylphenoxy)-4-((3,4,5-trimethoxybenzyl)oxy)benzyl) morpholine** (18 mg, 0.033 mmol, 61%) as a colourless oil.

R_f 0.15 (EtOAc).

^{1}H NMR (400 MHz, $CDCl_3$) δ 6.77 (d, *J* = 1.9 Hz, 1H, Ar-H), 6.73 (d, *J* = 8.1 Hz, 1H, H14), 6.69 – 6.64 (m, 4H, 4 × Ar-H), 6.46 (d, *J* = 1.8 Hz, 1H, Ar-H), 5.02 (s, 2H, H35), 3.87 (s, 3H, O-CH_3), 3.80 (s, 3H, O-CH_3), 3.79 (s, 3H, O-CH_3), 3.76 (s, 6H, 2 × O-CH_3), 3.67 (t, *J* = 4.6 Hz, 4H, H11, H12), 3.36 (s, 2H, H8), 2.55 (t, *J* = 7.5 Hz, 2H, H21), 2.38 (t, *J* = 4.7 Hz, 4H, H10, H13), 1.70 – 1.57 (m, 2H, H22), 0.95 (t, *J* = 7.3 Hz, 3H, H23).

^{13}C NMR (101 MHz, $CDCl_3$) δ 153.8, 152.9, 150.5, 150.1, 147.0, 143.9, 138.6, 137.9, 137.4, 133.7, 120.6, 118.8, 112.8, 112.3, 107.7, 105.3, 75.3, 67.0, 63.1, 60.8, 56.2, 55.9, 55.9, 53.5, 37.8, 24.7, 13.8.

HRMS (ESI+) calc. for $C_{32}H_{41}NO_8$ $[M+H]^+$ 568.2905 found 568.2900.

4-Allyl-2-methoxy-6-(2-methoxy-4-(morpholinomethyl)phenoxy)phenol

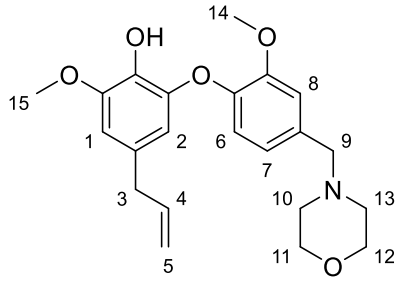

To a solution of 4-(4-(5-allyl-3-methoxy-2-((4-methoxybenzyl)oxy)phenoxy)-3-methoxybenzyl) morpholine (1.45 g, 2.88 mmol, 1.0 equiv.) in EtOH (100 mL) was added aqueous 1 M HCl (50 mL) and heated to 80 °C while stirring until the reaction was complete (24 h). The solution was basified to pH 7 with aqueous 1 M NaOH, extracted with EtOAc (50 mL × 3), combined organic extracts washed with brine, dried over Na_2SO_4 and evaporated to dryness. Purification *via* column chromatography (1:9 to 1:0 EtOAc/pentane) afforded **4-allyl-2-methoxy-6-(2-methoxy-4-(morpholinomethyl)phenoxy) phenol** (758 mg, 1.98 mmol, 69%) as a yellow oil.

R_f 0.20 (EtOAc).

IR (thin film, ν_{max} / cm^{-1}) 3054, 1592, 15122, 1435, 1267, 1189, 1145, 1120, 1085, 736.

^{1}H NMR (400 MHz, $CDCl_3$) δ 6.98 (d, *J* = 1.9 Hz, 1H, H8), 6.86 (d, *J* = 8.1 Hz, 1H, H6), 6.80 (dd, *J* = 8.1, 1.9 Hz, 1H, H7), 6.50 (d, *J* = 1.8 Hz, 1H, H1), 6.41 (d, *J* = 1.8 Hz, 1H, H2), 5.96 – 5.80 (m, 1H, H4), 5.07 – 4.97 (m, 2H, H5), 3.88 (s, 3H, O-CH_3), 3.87 (s, 3H, O-CH_3), 3.73 – 3.68 (m, 4H, H11, H12), 3.45 (s, 2H, H9), 3.24 (dt, *J* = 7.0, 1.5 Hz, 2H, H3), 2.47 – 2.40 (m, 4H, H10, H13).

^{13}C NMR (101 MHz, $CDCl_3$) δ 150.3, 148.0, 145.2, 144.2, 137.4, 135.4, 134.0, 131.1, 121.5, 118.8, 115.7, 113.3, 112.2, 107.4, 67.0, 63.2, 56.2, 56.1, 53.6, 39.9.

HRMS (ESI+) calc. for $C_{22}H_{27}NO_5$ $[M+H]^+$ 386.1967 found 386.1963.

***tert*-Butyl (2-hydroxyethyl)carbamate**

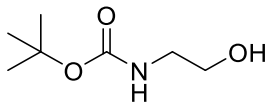

To a solution of 2-aminoethan-1-ol (1.98 mL, 32.8 mmol, 1.0 equiv.) in CH_2Cl_2 (40 mL) at 0 °C was added di-*tert*-butyl dicarbonate (7.50 g, 34.3 mmol, 1.1 equiv.) portion-wise then allowed to warm to room temperature. The reaction was stirred until complete (24 h). The resulting solution was diluted with CH_2Cl_2 (40 mL), washed with $NaHCO_3$ (aq., sat), brine, dried over Na_2SO_4 and evaporated to dryness. Purification *via* column chromatography (1:1 EtOAc/pentane) afforded *tert*-butyl (2-hydroxyethyl)carbamate (4.11 g, 1.98 mmol, 78%) as a pale yellow oil.

R_f 0.58 (EtOAc).

^{1}H NMR (400 MHz, $CDCl_3$) δ 5.01 (s, 1H), 3.68 (p, *J* = 4.6 Hz, 2H), 3.27 (p, *J* = 4.6 Hz, 2H), 1.46 – 1.41 (m, 9H).

^{13}C NMR (101 MHz, $CDCl_3$) δ 156.9, 79.7, 62.6, 43.2, 28.4.

Spectroscopic data is in accordance with the literature.[527]

2-((*tert*-Butoxycarbonyl)amino)ethyl 4-methylbenzenesulfonate

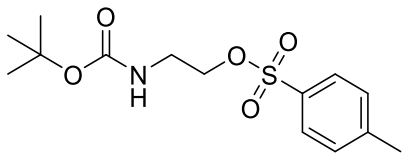

To a solution of *tert*-butyl (2-hydroxyethyl)carbamate (2.00 g, 12.4 mmol, 1.0 equiv.) in CH_2Cl_2 (18 mL) at 0 °C, was added Et_3N (4.0 mL, 29 mmol, 2.3 equiv.) dropwise. A solution of 4-toluenesulfonyl chloride (2.60 g, 13.6 mmol, 1.1 equiv.) in CH_2Cl_2 (18 mL) was added dropwise, then the reaction allowed to warm to room temperature and left stirring until complete (24 h). The resulting solution was diluted with CH_2Cl_2 (18 mL), washed with aqueous 0.1 M HCl, brine, dried over Na_2SO_4 and evaporated to dryness. Purification *via* column chromatography (1:4 EtOAc/pentane) afforded 2-((*tert*-butoxycarbonyl)amino)ethyl 4-methylbenzenesulfonate (3.80 g, 12.0 mmol, 97%) as a pale yellow oil.

R_f 0.70 (1:1 EtOAc/pentane).

^{1}H NMR (400 MHz, $CDCl_3$) δ 7.86 – 7.76 (m, 2H), 7.42 – 7.32 (m, 2H), 4.87 (s, 1H), 4.08 (s, 2H), 3.39 (s, 2H), 2.51 – 2.43 (m, 3H), 1.48 – 1.37 (m, 9H).

^{13}C NMR (101 MHz, $CDCl_3$) δ 155.6, 145.0, 132.7, 130.0, 127.9, 79.8, 69.5, 39.8, 28.3, 21.7.

Spectroscopic data is in accordance with the literature.[528]

***tert*-Butyl(2-(4-allyl-2-methoxy-6-(2-methoxy-4-(morpholinomethyl)phenoxy)phenoxy)ethyl) carbamate**

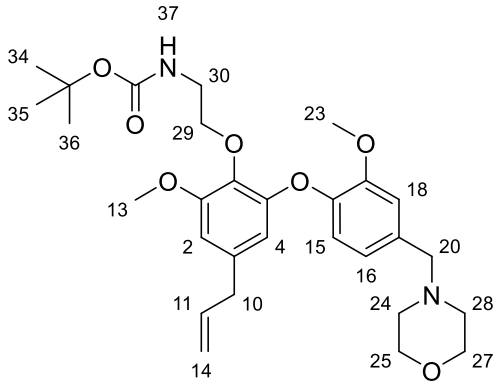

To a solution of 4-allyl-2-methoxy-6-(2-methoxy-4-(morpholinomethyl)phenoxy)phenol (300 mg, 0.780 mmol, 1.1 equiv.) and K_2CO_3 (322 mg, 2.33 mmol, 3.0 equiv.) in DMF (2.5 mL) was added 2-((*tert*-butoxycarbonyl)amino)ethyl 4-methylbenzenesulfonate (271 mg, 0.860 mmol, 1.0 equiv.) as a solution in DMF (2.5 mL). The reaction was heated to 75 °C and stirred until complete (3 h). The solution was diluted with EtOAc (30 mL), organic phase was washed with aqueous LiCl (aq., 5%), brine, dried over Na_2SO_4 and evaporated to dryness. Purification *via* column chromatography (1:1 to 1:0 EtOAc/pentane, column prewashed with 1% Et_3N in pentane) afforded ***tert*-butyl(2-(4-allyl-2-methoxy-6-(2-methoxy-4-(morpholinomethyl)phenoxy)phenoxy)ethyl)carbamate** (159 mg, 0.301 mmol, 35%) as a yellow oil.

R_f 0.26 (EtOAc).

IR (thin film, ν_{max} / cm^{-1}) 3394, 2932, 2853, 1713, 1587, 1507, 1454, 1426, 1270, 1212, 1117, 1091, 1069, 867.

^{1}H NMR (400 MHz, $CDCl_3$) δ 6.98 (d, *J* = 1.6 Hz, 1H, Ar-H), 6.84 – 6.75 (m, 2H, 2 × Ar-H), 6.49 (d, *J* = 1.9 Hz, 1H, Ar-H), 6.30 (d, *J* = 1.9 Hz, 1H, Ar-H), 5.92 – 5.81 (m, 1H, H11), 5.03 (m, 2H, H14), 4.11 (t, *J* = 4.7 Hz, 2H, H29), 3.87 (s, 3H, O-CH_3), 3.85 (s, 3H, O-CH_3), 3.76 – 3.68 (m, 4H,

H25, H27), 3.46 (s, 2H, H20), 3.33 (t, *J* = 4.7 Hz, 2H, H30), 3.27 – 3.22 (m, 2H, H10), 2.45 (t, *J* = 4.7 Hz, 4H, H24, H28), 1.40 (s, 9H, H34, H35, H36).

^{13}C NMR (101 MHz, $CDCl_3$) δ 156.1, 153.4, 150.5, 150.3, 144.6, 136.9, 136.3, 136.0, 133.7, 121.4, 118.7, 116.1, 113.2, 111.4, 107.4, 78.7, 73.1, 67.0, 63.2, 56.0, 55.9, 53.6, 40.6, 40.1, 28.4.

HRMS (ESI+) calc. for $C_{29}H_{40}N_2O_7$ $[M+H]^+$ 529.2906 found 529.2908.

2-(4-Allyl-2-methoxy-6-(2-methoxy-4-(morpholinomethyl)phenoxy)phenoxy)ethan-1-amine

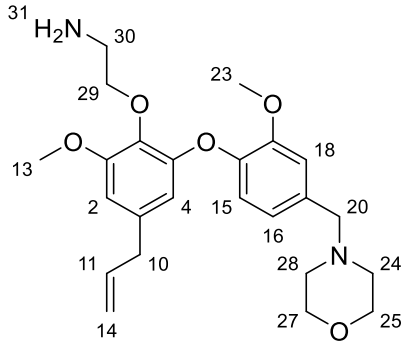

To a solution of *tert*-butyl(2-(4-allyl-2-methoxy-6-(2-methoxy-4-(morpholinomethyl)phenoxy) phenoxy)ethyl)carbamate (159 mg, 0.300 mmol, 1.0 equiv.) in CH_2Cl_2 (2.5 mL) was added trifluoroacetic acid (2.50 mL, 32.7 mmol, 110 equiv.) and stirred until the reaction was complete (1 h). The solution was evaporated to dryness, then dissolved in CH_2Cl_2 (10 mL). The organic phase was diluted with H_2O, basified to pH 14 with aqueous 1 M NaOH and the layers separated. The aqueous phase was extracted with CH_2Cl_2 (10 mL × 3), combined organic extracts washed with brine, dried over Na_2SO_4 and evaporated to afford **2-(4-allyl-2-methoxy-6-(2-methoxy-4-(morpholinomethyl)phenoxy)phenoxy) ethan-1-amine** (91 mg, 0.21 mmol, 70%) as an oil which was used without further purification.

R_f 0.14 (EtOAc).

IR (thin film, ν_{max} / cm^{-1}) 2981, 2889, 1741, 1588, 1508, 1454, 1426, 1268, 1240, 1048.

^{1}H NMR (400 MHz, $CDCl_3$) δ 6.97 (d, *J* = 1.8 Hz, 1H, H18), 6.79 (dd, *J* = 8.2, 1.8 Hz, 1H, H16), 6.76 (d, *J* = 8.2 Hz, 1H, H15), 6.50 (d, *J* = 1.9 Hz, 1H, H2 or H4), 6.32 (d, *J* = 1.9 Hz, 1H, H2 or H4), 5.95 – 5.78 (m, 1H, H11), 5.09 – 4.96 (m, 2H, H14), 4.09 (t, *J* = 4.9 Hz, 2H, H29), 3.85 (s, 3H, O-CH_3), 3.85 (s, 3H, O-CH_3), 3.71 (t, *J* = 4.7 Hz, 4H, H25, H27), 3.44 (s, 2H, H20), 3.27 – 3.20 (m, 2H, H10), 2.91 (s, br, 2H, H30), 2.77 (s, br, 2H, H31), 2.43 (t, *J* = 4.7 Hz, 4H, H24, H28).

^{13}C NMR (101 MHz, $CDCl_3$) δ 153.6, 150.1, 150.1, 144.9, 136.9, 136.6, 136.0, 133.7, 121.4, 118.2, 116.1, 113.2, 111.9, 107.7, 75.1, 67.0, 63.2, 56.1, 56.0, 53.6, 41.8, 40.1.

HRMS (ESI+) calc. for $C_{24}H_{32}N_2O_5$ $[M+H]^+$ 429.2383 found 429.2384.

Pent-4-ynal

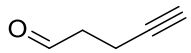

To a stirred solution of oxalyl chloride (5.0 mL, 59 mmol, 1.1 equiv.) in CH_2Cl_2 (100 mL) at −78 °C was added a solution of dimethyl sulfoxide (9.0 mL, 0.13 mol, 2.4 equiv.) in CH_2Cl_2 (20 mL) dropwise over 20 min. After 1.5 h, a solution of 4-pentyn-1-ol (5.0 mL, 54 mmol, 1.0 equiv.) in CH_2Cl_2 (30 mL) was added dropwise. After 1 h, Et_3N (40 mL) was added dropwise and left stirring at −78 °C for 1 h before being allowed to warm to room temperature and stirred for 3 h. The reaction mixture was diluted with CH_2Cl_2 (50 mL), washed with aqueous 1 M HCl, $NaHCO_3$ (aq., sat), brine, and dried over Na_2SO_4. Solvent was carefully removed under reduced pressure then blown off under nitrogen to afford **pent-4-ynal** (3.62 g, 44.1 mmol, 82%) as an orange oil which was used without further purification.

$\mathbf{R_f}$ 0.55 (4:1 CH_2Cl_2/pentane).

^{1}H NMR (400 MHz, $CDCl_3$) δ 9.80 (s, 1H), 2.74 – 2.64 (m, 2H), 2.56 – 2.47 (m, 2H), 1.99 (t, *J* = 2.7 Hz, 1H).

^{13}C NMR (101 MHz, $CDCl_3$) δ 200.1, 82.3, 69.3, 42.4, 11.7.

Spectroscopic data is in accordance with the literature.[529]

Ethyl 4-oxooct-7-ynoate

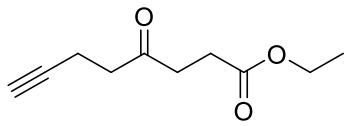

A solution of freshly synthesised pent-4-ynal (3.62 g, 44.1 mmol, 1.0 equiv.) and ethyl acrylate (9.3 mL, 88 mmol, 2 equiv.) in dioxane (40 mL) was added dropwise over 30 min to a suspension of 3-benzyl-5-(2-hydroxyethyl)-4-methylthiazolium chloride (8.09 g, 30.9 mmol, 0.7 equiv.), Et_3N (4.3 mL, 31 mmol, 0.7 equiv.) and ethyl acrylate (10 mL, 95 mmol, 2.2 equiv.) in dioxane (60 mL) at 80 °C. The mixture was left stirring until complete (72 h) and then evaporated to dryness. The residue was resuspended in CH_2Cl_2 (100 mL) and washed with aqueous 1 M H_2SO_4, $NaHCO_3$ (aq., sat), brine (50 mL), dried over Na_2SO_4 and evaporated to dryness. Purification *via* column chromatography (9:1 pentane/EtOAc) afforded **ethyl 4-oxooct-7-ynoate** (1.80 g, 0.220 mmol, 22%) as a brown oil.

R_f 0.39 (4:1 pentane/EtOAc).

^{1}H NMR (400 MHz, $CDCl_3$) δ 4.12 (q, *J* = 7.2 Hz, 2H), 2.79 – 2.64 (m, 4H), 2.64 – 2.56 (m, 2H), 2.51 – 2.43 (m, 2H), 1.94 (t, *J* = 2.7 Hz, 1H), 1.25 (t, *J* = 7.2 Hz, 3H).

^{13}C NMR (101 MHz, $CDCl_3$) δ 206.6, 172.6, 83.0, 68.7, 60.7, 41.4, 37.1, 27.9, 14.2, 12.9.

Spectroscopic data is in accordance with the literature.[256]

4-Oxooct-7-ynoic acid

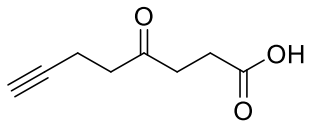

To a solution of ethyl 4-oxooct-7-ynoate (1.79 g, 9.80 mmol, 1.0 equiv.) in MeOH (75 mL), was added LiOH (1.17 g, 49.0 mmol, 5.0 equiv.) and H_2O (0.90 mL, 54 mmol, 5.5 equiv.). The solution was stirred at room temperature until the reaction was complete (15 h), followed by slow acidification with aqueous 6 M HCl to pH 3. The resulting solution was extracted with CH_2Cl_2 (100 mL × 3), the combined organic extracts were dried over Na_2SO_4 and evaporated to dryness, affording **4-oxooct-7-ynoic acid** (1.37 g, 8.90 mmol, 90%) as a brown solid which was used without further purification.

^{1}H NMR (400 MHz, $CDCl_3$) δ 2.78 – 2.62 (m, 6H), 2.49 – 2.43 (m, 2H), 1.95 (t, *J* = 2.7 Hz, 1H).

^{13}C NMR (101 MHz, $CDCl_3$) δ 206.4, 178.5, 82.8, 68.8, 41.3, 36.8, 27.7, 12.9.

Spectroscopic data is in accordance with the literature.[256]

3-(3-(But-3-yn-1-yl)-3H-diazirin-3-yl)propanoic acid

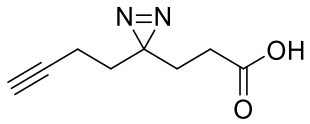

To a dried round bottom flask containing 4-oxooct-7-ynoic acid (300 mg, 1.95 mmol, 1.0 equiv.) cooled to 0 °C was added 7 N NH_3 in MeOH (18 mL) and left stirring for 3 h. Hydroxylamine-O-sulfonic acid (308 mg, 2.72 mmol, 1.4 equiv.) was added portion-wise and the resulting solution stirred at 0 °C for 30 min then allowed to warm to room temperature and stirred for 14 h. The resulting suspension was evaporated to dryness then resuspended in MeOH (20 mL). The solid was filtered under vacuum and washed several times with MeOH. The combined filtrate was evaporated to dryness and resuspended in anhydrous MeOH (18 mL) under an inert atmosphere, then cooled to 0 °C (protected from light). Diisopropylethylamine (0.75 mL, 4.3 mmol, 2.2 equiv.) was added dropwise, followed by iodine (portion-wise), until a dark brown colour persisted for more than 30 min. The solution was diluted with EtOAc (20 mL), washed with aqueous 1 M HCl (20 mL), $Na_2S_2O_3$ (aq., sat), brine, dried over Na_2SO_4 and evaporated to dryness. Purification *via* column chromatography (1:9 to 1:4 EtOAc/hexane) afforded **3-(3-(but-3-yn-1-yl)-3H-diazirin-3-yl)propanoic acid** (31 mg, 0.19 mmol, 10%) as a colourless oil.

R_f 0.44 (1:1 EtOAc/pentane).

^{1}H NMR (400 MHz, $CDCl_3$) δ 2.21 – 2.15 (m, 2H), 2.06 – 1.97 (m, 3H), 1.84 – 1.77 (m, 2H), 1.66 (t, *J* = 7.2 Hz, 2H).

^{13}C NMR (101 MHz, $CDCl_3$) δ 178.2, 82.5, 69.3, 32.2, 28.2, 27.8, 27.4, 13.2.

Spectroscopic data is in accordance with the literature.[244]

***N*-(2-(4-Allyl-2-methoxy-6-(2-methoxy-4-(morpholinomethyl)phenoxy)phenoxy)ethyl)-3-(3-(but-3-yn-1-yl)-3H-diazirin-3-yl)propenamide, DDB-PAL**

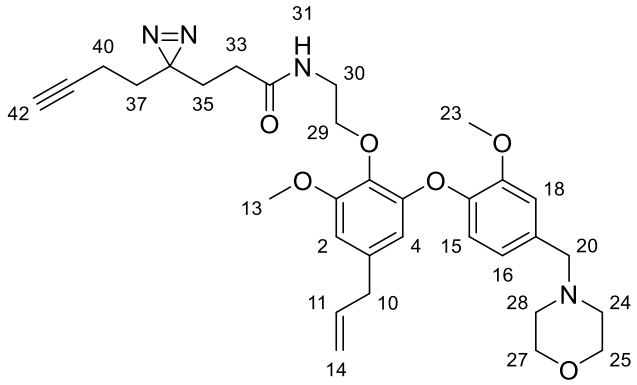

To a solution of 3-(3-(but-3-yn-1-yl)-3H-diazirin-3-yl)propanoic acid (7.5 mg, 0.045 mmol, 1.0 equiv.) in CH_2Cl_2 (0.5 mL) was added a solution of 2-(4-allyl-2-methoxy-6-(2-methoxy-4-(morpholinomethyl) phenoxy)phenoxy)ethan-1-amine (21 mg, 0.050 mmol, 1.1 equiv.) in CH_2Cl_2 (0.5 mL), *N*-(3-dimethylaminopropyl)-*N′*-ethylcarbodiimide hydrochloride (13 mg, 0.068 mmol, 1.5 equiv.), and 1-hydroxybenzotriazole hydrate (9.1 mg, 0.068 mmol, 1.5 equiv.), and stirred until the reaction was complete (1 h). The resulting solution was diluted with CH_2Cl_2 (3.5 mL), organic phase washed with NH_4Cl (aq., sat), $NaHCO_3$ (aq., sat), dried over Na_2SO_4 and evaporated to dryness. Purification *via* column chromatography (1:19 MeOH/CH_2Cl_2) afforded ***N*-(2-(4-allyl-2-methoxy-6-(2-methoxy-4-(morpholinomethyl)phenoxy)phenoxy)ethyl)-3-(3-(but-3-yn-1-yl)-3H-diazirin-3-yl)propanamide** (23 mg, 0.40 mmol, 88%) as a yellow oil.

R_f 0.71 (1:19 MeOH/CH_2Cl_2).

IR (thin film, ν_{max} / cm^{-1}) 3395, 3296, 2958, 2854, 1674, 1587, 1507, 1269, 1212, 1117.

^{1}H NMR (400 MHz, $CDCl_3$) δ 7.03 (s, 1H, H18), 6.83 (dd, *J* = 8.1, 1.8 Hz, 1H, H16), 6.77 (d, *J* = 8.1 Hz, 1H, H15), 6.51 (d, *J* = 1.9 Hz, 1H, H2 or H4), 6.29 (d, *J* = 1.9 Hz, 1H, H2 or H4), 5.93 – 5.81 (m, 1H, H11), 5.06 – 5.02 (m, 1H, H14), 5.02 – 4.98 (m, 1H, H14), 4.12 (t, *J* = 4.9 Hz, 2H, H29), 3.87 (s, 6H, H13, H23), 3.75 – 3.70 (m, 4H, H25, H27), 3.48 (s, 2H, H20), 3.47 – 3.41 (m,

2H, H30), 3.28 – 3.21 (m, 2H, H10), 2.46 (t, *J* = 4.7 Hz, 4H, H24, H28), 1.99 – 1.93 (m, 3H, H40, H42), 1.87 – 1.81 (m, 2H, H33), 1.78 – 1.71 (m, 2H, H35), 1.61 – 1.54 (m, 2H, H37).

^{13}C NMR (101 MHz, $CDCl_3$) δ 171.1, 153.5, 150.1, 144.7, 136.8, 136.3, 134.9, 121.7, 118.5, 116.2, 113.6, 111.4, 107.7, 82.7, 72.7, 69.2, 66.9, 63.1, 56.1, 53.6, 40.1, 39.4, 32.3, 30.2, 28.4, 27.8, 13.3.

HRMS (ESI+) calc. for $C_{32}H_{40}N_4O_6$ $[M+H]^+$ 577.3026 found 577.3021.

Hex-5-yn-1-yl 4-methylbenzenesulfonate

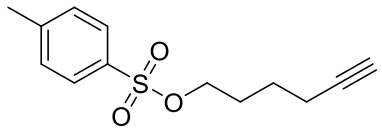

To a solution of hex-5-yn-1-ol (1.12 mL, 10.2 mmol, 1.0 equiv.) and pyridine (1.61 mL, 20.4 mmol, 2.0 equiv.) in CH_2Cl_2 (10 mL) at 0 °C was added 4-methylbenzenesulfonyl chloride (2.92 g, 15.3 mmol, 1.5 equiv.). The solution was stirred at 0 °C for 1 h then warmed to room temperature and stirred for an additional 4.5 h. $NaHCO_3$ (aq., sat) was added and stirred for 10 mins, before the aqueous phase was extracted with Et_2O (50 mL). The organic extract was washed with H_2O, aqueous 1 M HCl, $NaHCO_3$ (aq., sat.), brine, dried over $MgSO_4$ and evaporated to dryness. Purification *via* column chromatography (9:1 pentane/Et_2O) afforded **hex-5-yn-1-yl 4-methylbenzenesulfonate** (2.37 g, 9.38 mmol, 92%) as a colourless oil.

R_f 0.30 (9:1 pentane/Et_2O)

^{1}H NMR (400 MHz, $CDCl_3$) δ 7.83 – 7.75 (m, 2H), 7.39 – 7.31 (m, 2H), 4.05 (t, *J* = 6.3 Hz, 2H), 2.45 (s, 3H), 2.16 (td, *J* = 7.0, 2.6 Hz, 2H), 1.92 (t, *J* = 2.6 Hz, 1H), 1.83 – 1.72 (m, 2H), 1.61 – 1.49 (m, 2H).

^{13}C NMR (101 MHz, $CDCl_3$) δ 144.8, 133.1, 129.9, 127.9, 83.4, 69.9, 69.0, 27.8, 24.2, 21.6, 17.7.

Spectroscopic data is in accordance with the literature.[530]

4-(4-(5-Allyl-2-(hex-5-yn-1-yloxy)-3-methoxyphenoxy)-3-methoxybenzyl)morpholine, DDB-yne

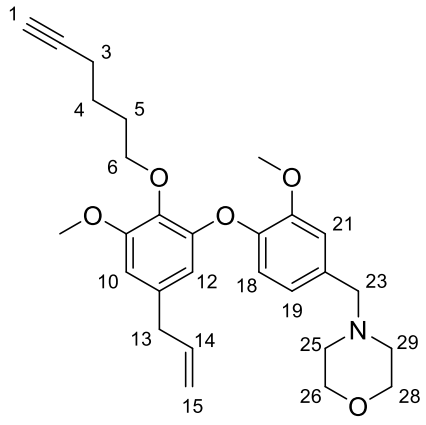

To a suspension of 4-allyl-2-methoxy-6-(2-methoxy-4-(morpholinomethyl)phenoxy)phenol (300 mg, 0.780 mmol, 1.0 equiv.), tetrabutylammonium iodide (30 mg, 0.078 mmol, 0.1 equiv.) and K_2CO_3 (322 mg, 2.33 mmol, 3.0 equiv.) in DMF (5 mL) was added hex-5-yn-1-yl 4-methylbenzenesulfonate (295 mg, 1.17 mmol, 1.5 equiv.). The suspension was stirred at 75 °C until the reaction was complete (7 h). The solution was diluted with H_2O and EtOAc (40 mL), and separated. The organic phase was washed with LiCl (aq., 5%), brine, dried over Na_2SO_4 and evaporated to dryness. Purification *via* column chromatography (1:1 pentane/EtOAc, column prewashed with 1% Et_3N in pentane) afforded **4-(4-(5-allyl-2-(hex-5-yn-1-yloxy)-3-methoxyphenoxy)-3-methoxybenzyl) morpholine** (248 mg, 0.530 mmol, 68%) as a colourless oil.

R_f 0.22 (1:1 pentane/EtOAc).

IR (thin film, ν_{max} / cm^{-1}) 3384, 3299, 2939, 2840, 1584, 1507, 1455, 1424, 1117, 1021.

^{1}H NMR (400 MHz, $CDCl_3$) δ 6.97 (d, *J* = 1.9 Hz, 1H, H21), 6.77 (dd, *J* = 8.2, 1.9 Hz, 1H, H19), 6.71 (d, *J* = 8.2 Hz, 1H, H18), 6.51 (d, *J* = 2.0 Hz, 1H, H10 or H12), 6.35 (d, *J* = 2.0 Hz, 1H, H10 or H12), 5.89 (ddt, *J* = 18.0, 9.3, 6.6 Hz, 1H, H14), 5.09 – 4.97 (m, 2H, H15), 3.99 (t, *J* = 6.2 Hz, 2H, H6), 3.88 (s, 3H, O-CH_3), 3.84 (s, 3H, O-CH_3), 3.72 (t, *J* = 4.7 Hz, 4H, H26, H28), 3.45 (s, 2H, H23),

3.29 – 3.22 (m, 2H, H13), 2.44 (t, *J* = 4.7 Hz, 4H, H25, H29), 2.15 (td, *J* = 7.1, 2.7 Hz, 2H, H3), 1.89 (t, *J* = 2.7 Hz, 1H, H1), 1.79 – 1.68 (m, 2H, H5), 1.66 – 1.54 (m, 2H, H4).

^{13}C NMR (101 MHz, $CDCl_3$) δ 153.8, 150.0, 150.0, 145.6, 137.6, 137.1, 135.6, 133.0, 121.4, 117.7, 116.0, 113.2, 112.5, 107.9, 84.6, 72.7, 68.2, 67.0, 63.2, 56.1, 56.0, 53.6, 40.1, 29.1, 24.8, 18.0.

HRMS (ESI+) calc. for $C_{28}H_{35}NO_5$ $[M+H]^+$ 466.2593 found 466.2594.

***tert*-Butyl (2-(2-hydroxyethoxy)ethyl)carbamate**

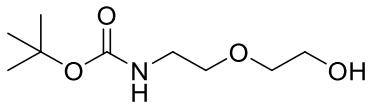

To a solution of diethylene glycol amine (1.43 mL, 14.3 mmol, 1.0 equiv.) in CH_2Cl_2 (10 mL) at 0 °C was added di-*tert*-butyl dicarbonate (3.28 g, 15.0 mmol, 1.1 equiv.) as a solution in CH_2Cl_2 (10 mL) drop-wise. The reaction was stirred at 0 °C for 30 min, then allowed to warm to room temperature and stirred until complete (24 h). The resulting solution was washed with H_2O, the aqueous extracted with CH_2Cl_2 (10 mL × 3), combined organic extracts washed with brine, dried over $MgSO_4$ and evaporated to dryness to afford ***tert*-butyl (2-(2-hydroxyethoxy)ethyl)carbamate** (2.92 g, 14.2 mmol, 99%) as a colourless oil which was used without further purification.

R_f 0.42 (EtOAc).

^{1}H NMR (400 MHz, $CDCl_3$) δ 4.91 (br, s, 1H), 3.78 – 3.70 (m, 2H), 3.61 – 3.52 (m, 4H), 3.37 – 3.29 (m, 2H), 2.12 (s, 1H), 1.45 (s, 9H).

^{13}C NMR (101 MHz, $CDCl_3$) δ 156.1, 79.4, 72.2, 70.3, 61.8, 40.4, 28.4.

Spectroscopic data is in accordance with the literature.[531]

2-(2-((*tert*-Butoxycarbonyl)amino)ethoxy)ethyl 4-methylbenzenesulfonate

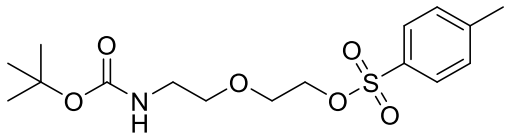

To a solution of *tert*-butyl (2-(2-hydroxyethoxy)ethyl)carbamate (800 mg, 3.90 mmol, 1.0 equiv.) in CH_2Cl_2 (13 mL) at 0 °C was added Et_3N (1.63 mL, 11.7 mmol, 3.0 equiv.) dropwise. 4-Toluenesulfonyl chloride (1.11 g, 5.84 mmol, 1.5 equiv.) and 4-dimethylaminopyridine (48 mg, 0.38 mmol, 0.1 equiv.) were each added portion-wise, the reaction allowed to warm to room temperature and stirred until complete (3 h). The resulting solution was diluted with CH_2Cl_2 (30 mL), washed with aqueous 0.1 M HCl, brine, dried over $MgSO_4$ and evaporated to dryness. Purification *via* column chromatography (1:1 EtOAc/pentane) afforded **2-(2-((*tert*-butoxycarbonyl) amino)ethoxy)ethyl 4-methylbenzene sulfonate** (1.20 g, 3.33 mmol, 85%) as a pale yellow oil.

R_f 0.22 (1:4 EtOAc/pentane).

^{1}H NMR (400 MHz, $CDCl_3$) δ 7.80 (d, *J* = 8.0 Hz, 2H), 7.35 (d, *J* = 8.0 Hz, 2H), 4.79 (s, 1H), 4.19 – 4.12 (m, 2H), 3.66 – 3.59 (m, 2H), 3.44 (t, *J* = 5.1 Hz, 2H), 3.28 – 3.19 (m, 2H), 2.45 (s, 3H), 1.45 (s, 9H).

^{13}C NMR (101 MHz, $CDCl_3$) δ 155.9, 144.9, 133.0, 129.8, 128.0, 79.4, 70.4, 69.1, 68.4, 40.2, 28.4, 21.7.

Spectroscopic data is in accordance with the literature.[532]

***tert*-Butyl (2-(2-(4-allyl-2-methoxy-6-(2-methoxy-4-(morpholinomethyl)phenoxy)phenoxy) ethoxy)ethyl)carbamate**

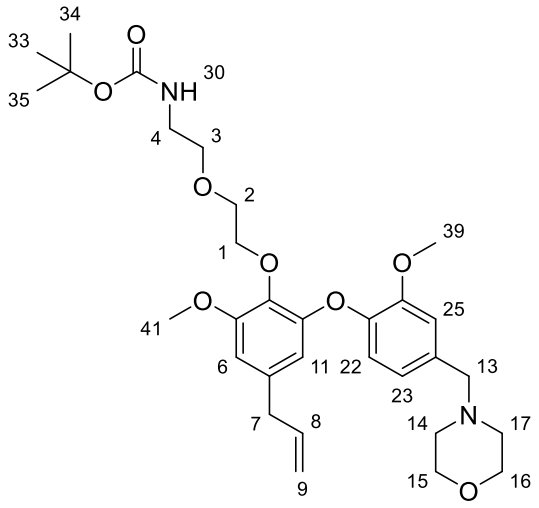

To a solution of 4-allyl-2-methoxy-6-(2-methoxy-4-(morpholinomethyl)phenoxy)phenol (75 mg, 0.19 mmol, 1.1 equiv.) and K_2CO_3 (37 mg, 0.27 mmol, 1.5 equiv.) in DMF (0.5 mL) was added a solution of 2-(2-((*tert*-butoxycarbonyl)amino) ethoxy)ethyl 4-methylbenzenesulfonate (65 mg, 0.18 mmol, 1.0 equiv.) in DMF (0.5 mL). The reaction mixture was heated to 75 °C and left stirring until the reaction was complete (72 h). The solution was diluted with EtOAc (30 mL), H_2O and the layers separated. The organic extract was washed with H_2O, brine, dried over $MgSO_4$ and evaporated to dryness to afford ***tert*-butyl (2-(2-(4-allyl-2-methoxy-6-(2-methoxy-4-(morpholinomethyl) phenoxy)phenoxy)ethoxy)ethyl)carbamate** (69 mg, 0.12 mmol, 63%) as a pale yellow oil which was used without further purification.

R_f 0.15 (EtOAc).

IR (thin film, ν_{max} / cm^{-1}) 2972, 2934, 1711, 1587, 1507, 1454, 1425, 1269, 1117.

^{1}H NMR (400 MHz, $CDCl_3$) δ 6.97 (d, *J* = 1.6 Hz, 1H, H25), 6.79 – 6.75 (m, 2H H22, H23), 6.50 (d, *J* = 1.9 Hz, 1H, H6 or H11), 6.31 (d, *J* = 1.9 Hz, 1H, H6 or H11), 5.97 – 5.80 (m, 1H, H8), 5.10 (s, 1H, H30), 5.07 – 4.97 (m, 2H, H9), 4.19 – 4.12 (m, 2H, H1), 3.86 (s, 3H, O-CH_3), 3.85 (s, 3H, O-CH_3), 3.73 – 3.69 (m, 4H, H15, H16), 3.68 – 3.64 (m, 2H, H2), 3.50 (t, *J* = 5.1 Hz, 2H, H3), 3.45

(s, 2H, H13), 3.28 – 3.20 (m, 4H, H4, H7), 2.44 (t, *J* = 4.7 Hz, 4H, H14, H17), 1.42 (s, 9H, H33, H34, H35).

^{13}C NMR (101 MHz, $CDCl_3$) δ 156.1, 153.6, 150.3, 150.2, 145.2, 137.2, 137.0, 135.8, 133.5, 121.5, 118.5, 116.0, 113.3, 111.9, 107.7, 78.9, 72.4, 70.2, 70.1, 67.0, 63.2, 56.1, 56.0, 53.6, 40.5, 40.1, 28.4.

HRMS (ESI+) calc. for $C_{31}H_{45}N_2O_8$ $[M+H]^+$ 573.3170 found 573.3165.

2-(2-(4-Allyl-2-methoxy-6-(2-methoxy-4-(morpholinomethyl)phenoxy)phenoxy)ethoxy)ethan-1-amine, DDB-NH_2

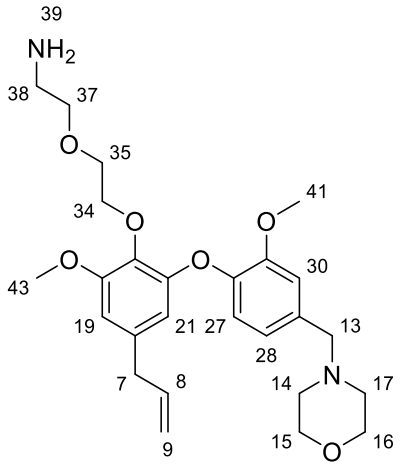

To a solution of *tert*-butyl (2-(2-(4-allyl-2-methoxy-6-(2-methoxy-4-(morpholinomethyl)phenoxy) phenoxy)ethoxy)ethyl)carbamate (68 mg, 0.12 mmol, 1.0 equiv.) in CH_2Cl_2 (2.4 mL) was added trifluoroacetic acid (2.4 mL) and left stirring until the reaction was complete (3 h). The solution was evaporated to dryness, the crude re-dissolved in CH_2Cl_2 (5 mL) and basified to pH 14 with aqueous 1 M NaOH. The layers were separated and the aqueous extracted with CH_2Cl_2 (5 mL × 3), combined organic extracts dried over $MgSO_4$, and evaporated to dryness resulting in **2-(2-(4-allyl-2-methoxy-6-(2-methoxy-4-(morpholinomethyl)phenoxy)phenoxy)ethoxy)ethan-1-amine** (42 mg, 0.090 mmol, 74%) as an orange oil which was used without further purification.

R_f 0.38 (19:1 CH_2Cl_2/7 N ammonia in MeOH).

IR (thin film, ν_{max} / cm^{-1}) 2934, 2854, 1586, 1506, 1454, 1425, 1268, 1232, 1211, 1116, 1091.

^{1}H NMR (400 MHz, $CDCl_3$) δ 6.97 (d, *J* = 1.6 Hz, 1H, H30), 6.82 – 6.75 (m, 2H, H27, H28), 6.49 (d, *J* = 1.9 Hz, 1H, H19 or H21), 6.30 (d, *J* = 1.9 Hz, 1H, H10 or H21), 5.95 – 5.80 (m, 1H, H8), 5.07 – 4.97 (m, 2H, H9), 4.17 (t, *J* = 4.9 Hz, 2H, H34), 3.85 (s, 6H, H41, H43), 3.74 – 3.65 (m, 6H, H15, H16, H35), 3.48 (t, *J* = 5.1 Hz, 2H, H37), 3.45 (s, 2H, H13), 3.24 (d, *J* = 6.7 Hz, 2H, H7), 2.79 (t, *J* = 5.1 Hz, 2H, H38), 2.44 (t, *J* = 4.6 Hz, 4H, H14, H17).

HRMS (ESI+) calc. for $C_{26}H_{36}N_2O_6$ $[M+H]^+$ 473.2652, found 473.2646.

8 References

(1) Leishman, W. B. On the possibility of the occurrence of trypanosomiasis in India. *British Medical Journal* **1903**, *1*, 1252-1254.
(2) Donovan, C. A Possible Cause of Kala-Azar. *Indian Medical Gazette* **1903**, *38*, 478.
(3) Ross, R. Note on the bodies recently described by Leishman and Donovan. *British Medical Journal* **1903**, *2*, 1261-1262.
(4) Berman, J. D. Chemotherapy for Leishmaniasis: Biochemical Mechanisms, Clinical Efficacy, and Future Strategies. *Reviews of Infectious Diseases* **1988**, *10* (3), 560-586.
(5) Davidson, R. N.; Croft, S. L. Recent advances in the treatment of visceral leishmaniasis. *Transactions of The Royal Society of Tropical Medicine and Hygiene* **1993**, *87* (2), 130-131.
(6) Olliaro, P. L.; Bryceson, A. D. M. Practical progress and new drugs for changing patterns of leishmaniasis. *Parasitology Today* **1993**, *9* (9), 323-328.
(7) Akhoundi, M.; Kuhls, K.; Cannet, A.; Votýpka, J.; Marty, P.; Delaunay, P.; Sereno, D. A Historical Overview of the Classification, Evolution, and Dispersion of *Leishmania* Parasites and Sandflies. *PLOS Neglected Tropical Diseases* **2016**, *10* (3), e0004349.
(8) Vickerman, K. The diversity of the kinetoplastid flagellates. In *Biology of the kinetoplastida*, W.H.R. Lumsden, D. A. E. Ed.; Vol. 1; London: Academic Press, 1976; pp 1-34.
(9) Lewis, D. J. Phlebotomid sandflies. *Bulletin of the World Health Organization* **1971**, *44* (4), 535-551.
(10) Rogers, M. E.; Hajmová, M.; Joshi, M. B.; Sadlova, J.; Dwyer, D. M.; Volf, P.; Bates, P. A. *Leishmania* chitinase facilitates colonization of sand fly vectors and enhances transmission to mice. *Cellular Microbiology* **2008**, *10* (6), 1363-1372.
(11) Ilg, T.; Stierhof, Y.-D.; Craik, D.; Simpson, R.; Handman, E.; Bacic, A. Purification and Structural Characterization of a Filamentous, Mucin-like Proteophosphoglycan Secreted by *Leishmania* Parasites. *Journal of Biological Chemistry* **1996**, *271* (35), 21583-21596.
(12) Rogers, M. E.; Chance, M. L.; Bates, P. A. The role of promastigote secretory gel in the origin and transmission of the infective stage of *Leishmania mexicana* by the sandfly *Lutzomyia longipalpis*. *Parasitology* **2002**, *124* (5), 495-507.
(13) Stierhof, Y.-D.; Bates, P. A.; Jacobson, R. L.; Rogers, M. E.; Schlein, Y.; Handman, E.; Ilg, T. Filamentous proteophosphoglycan secreted by *Leishmania* promastigotes forms gel-like three-dimensional networks that obstruct the digestive tract of infected sandfly vectors. *European Journal of Cell Biology* **1999**, *78* (10), 675-689.
(14) Rogers, M. E.; Bates, P. A. *Leishmania* Manipulation of Sand Fly Feeding Behavior Results in Enhanced Transmission. *PLOS Pathogens* **2007**, *3* (6), e91.
(15) Rogers, M. E.; Ilg, T.; Nikolaev, A. V.; Ferguson, M. A. J.; Bates, P. A. Transmission of cutaneous leishmaniasis by sand flies is enhanced by regurgitation of fPPG. *Nature* **2004**, *430* (6998), 463-467.
(16) Almeida, M. C. d.; Vilhena, V.; Barral, A.; Barral-Netto, M. *Leishmanial* infection: analysis of its first steps. A review. *Memórias do Instituto Oswaldo Cruz* **2003**, *98*.
(17) Bates, P. A.; Tetley, L. *Leishmania mexicana*: Induction of Metacyclogenesis by Cultivation of Promastigotes at Acidic pH. *Experimental Parasitology* **1993**, *76* (4), 412-423.
(18) Alcolea, P. J.; Alonso, A.; Gómez, M. J.; Sánchez-Gorostiaga, A.; Moreno-Paz, M.; González-Pastor, E.; Toraño, A.; Parro, V.; Larraga, V. Temperature increase prevails over acidification in gene expression modulation of amastigote differentiation in *Leishmania infantum*. *BMC Genomics* **2010**, *11* (1), 31.
(19) Shapira, M.; McEwen, J. G.; Jaffe, C. L. Temperature effects on molecular processes which lead to stage differentiation in *Leishmania*. *The EMBO Journal* **1988**, *7* (9), 2895-2901-2901.

(20) Antoine, J.-C.; Prina, E.; Lang, T.; Courret, N. The biogenesis and properties of the parasitophorous vacuoles that harbour *Leishmania* in murine macrophages. *Trends in Microbiology* **1998**, *6* (10), 392-401.
(21) Antoine, J. C.; Prina, E.; Jouanne, C.; Bongrand, P. Parasitophorous vacuoles of *Leishmania amazonensis*-infected macrophages maintain an acidic pH. *Infection and Immunity* **1990**, *58* (3), 779-787.
(22) Carrera, L.; Gazzinelli, R. T.; Badolato, R.; Hieny, S.; Muller, W.; Kuhn, R.; Sacks, D. L. *Leishmania* promastigotes selectively inhibit interleukin 12 induction in bone marrow-derived macrophages from susceptible and resistant mice. *Journal of Experimental Medicine* **1996**, *183* (2), 515-526.
(23) Reiner, S. L.; Zheng, S.; Wang, Z. E.; Stowring, L.; Locksley, R. M. *Leishmania* promastigotes evade interleukin 12 (IL-12) induction by macrophages and stimulate a broad range of cytokines from CD4+ T cells during initiation of infection. *Journal of Experimental Medicine* **1994**, *179* (2), 447-456.
(24) Belkaid, Y.; Butcher, B.; Sacks, D. L. Analysis of cytokine production by inflammatory mouse macrophages at the single-cell level: selective impairment of IL-12 induction in *Leishmania*-infected cells. *European Journal of Immunology* **1998**, *28* (4), 1389-1400.
(25) Weinheber, N.; Wolfram, M.; Harbecke, D.; Aebischer, T. Phagocytosis of *Leishmania mexicana* amastigotes by macrophages leads to a sustained suppression of IL-12 production. *European Journal of Immunology* **1998**, *28* (8), 2467-2477.
(26) Liew, F. Y.; Millott, S.; Parkinson, C.; Palmer, R. M.; Moncada, S. Macrophage killing of *Leishmania* parasite *in vivo* is mediated by nitric oxide from L-arginine. *The Journal of Immunology* **1990**, *144* (12), 4794-4797.
(27) Kane, M. M.; Mosser, D. M. The Role of IL-10 in Promoting Disease Progression in Leishmaniasis. *The Journal of Immunology* **2001**, *166* (2), 1141-1147.
(28) Barral, A.; Barral-Netto, M.; Yong, E. C.; Brownell, C. E.; Twardzik, D. R.; Reed, S. G. Transforming growth factor beta as a virulence mechanism for *Leishmania braziliensis*. *Proceedings of the National Academy of Sciences* **1993**, *90* (8), 3442-3446.
(29) Nandan, D.; Reiner, N. E. Attenuation of gamma interferon-induced tyrosine phosphorylation in mononuclear phagocytes infected with *Leishmania donovani*: selective inhibition of signaling through *Janus* kinases and Stat1. *Infection and Immunity* **1995**, *63* (11), 4495-4500.
(30) Gregory, D. J.; Olivier, M. Subversion of host cell signalling by the protozoan parasite *Leishmania*. *Parasitology* **2005**, *130* (S1), S27-S35.
(31) Sunter, J.; Gull, K. Shape, form, function and *Leishmania* pathogenicity: from textbook descriptions to biological understanding. *Open Biology* **2017**, *7* (9), 170165.
(32) Leishman, W. B.; Statham, J. C. B. The Development of the Leishman body in Cultivation. *Journal of the Royal Army Medical Corps* **1905**, *4* (3), 321.
(33) Bates, P. A. Complete developmental cycle of *Leishmania mexicana* in axenic culture. *Parasitology* **1994**, *108* (1), 1-9.
(34) Hendricks, L. D.; Wood, D. E.; Hajduk, M. E. Haemoflagellates: commercially available liquid media for rapid cultivation. *Parasitology* **1978**, *76* (3), 309-316.
(35) Pan, A. A. *Leishmania mexicana*: Serial cultivation of intracellular stages in a cell-free medium. *Experimental Parasitology* **1984**, *58* (1), 72-80.
(36) Saraiva, E. M.; Pinto-da-Silva, L. H.; Wanderley, J. L. M.; Bonomo, A. C.; Barcinski, M. A.; Moreira, M. E. C. Flow cytometric assessment of *Leishmania* spp metacyclic differentiation: Validation by morphological features and specific markers. *Experimental Parasitology* **2005**, *110* (1), 39-47.
(37) Gossage, S. M.; Rogers, M. E.; Bates, P. A. Two separate growth phases during the development of *Leishmania* in sand flies: implications for understanding the life cycle. *International Journal for Parasitology* **2003**, *33* (10), 1027-1034.

(38) Pan, A. A.; Duboise, S. M.; Eperon, S.; Rivas, L.; Hodgkinson, V.; Traub-Cseko, Y.; McMahon-Pratt, D. Developmental Life Cycle of *Leishmania*—Cultivation and Characterization of Cultured Extracellular Amastigotes. *Journal of Eukaryotic Microbiology* **1993**, *40* (2), 213-223.
(39) Bates, P. A.; Robertson, C. D.; Tetley, L.; Coombs, G. H. Axenic cultivation and characterization of *Leishmania mexicana* amastigote-like forms. *Parasitology* **1992**, *105* (2), 193-202.
(40) Saar, Y.; Ransford, A.; Waldman, E.; Mazareb, S.; Amin-Spector, S.; Plumblee, J.; Turco, S. J.; Zilberstein, D. Characterization of developmentally-regulated activities in axenic amastigotes of *Leishmania donovani*. *Molecular and Biochemical Parasitology* **1998**, *95* (1), 9-20.
(41) Gupta, N.; Goyal, N.; Rastogi, A. K. *In vitro* cultivation and characterization of axenic amastigotes of *Leishmania*. *Trends in Parasitology* **2001**, *17* (3), 150-153.
(42) Gupta, N.; Goyal, N.; Singha, U. K.; Bhakuni, V.; Roy, R.; Rastogi, A. K. Characterization of intracellular metabolites of axenic amastigotes of *Leishmania donovani* by ^{1}H NMR spectroscopy. *Acta Tropica* **1999**, *73* (2), 121-133.
(43) Vickerman, K. Developmental Cycles and Biology of Pathogenic Trypanosomes. *British Medical Bulletin* **1985**, *41* (2), 105-114.
(44) Halliday, C.; Billington, K.; Wang, Z.; Madden, R.; Dean, S.; Sunter, J. D.; Wheeler, R. J. Cellular landmarks of *Trypanosoma brucei* and *Leishmania mexicana*. *Molecular and Biochemical Parasitology* **2019**, *230*, 24-36.
(45) Aleman, C. Finestructure of cultured *Leishmania brasiliensis*. *Experimental Parasitology* **1969**, *24* (2), 259-264.
(46) Rudzinska, M. A.; D'Alesandro, P. A.; Trager, W. The Fine Structure of *Leishmania donovani* and the Role of the Kinetoplast in the *Leishmania*-Leptomonad Transformation. *The Journal of Protozoology* **1964**, *11* (2), 166-191.
(47) Pan, A. A.; Pan, S. C. *Leishmania mexicana*: Comparative fine structure of amastigotes and promastigotes *in vitro* and *in vivo*. *Experimental Parasitology* **1986**, *62* (2), 254-265.
(48) Robinson, D. R.; Gull, K. Basal body movements as a mechanism for mitochondrial genome segregation in the trypanosome cell cycle. *Nature* **1991**, *352* (6337), 731-733.
(49) Ogbadoyi, E. O.; Robinson, D. R.; Gull, K. A High-Order Trans-Membrane Structural Linkage Is Responsible for Mitochondrial Genome Positioning and Segregation by Flagellar Basal Bodies in Trypanosomes. *Molecular Biology of the Cell* **2003**, *14* (5), 1769-1779.
(50) Gluenz, E.; Ginger, M. L.; McKean, P. G. Flagellum assembly and function during the *Leishmania* life cycle. *Current Opinion in Microbiology* **2010**, *13* (4), 473-479.
(51) Wheeler, R. J.; Gluenz, E.; Gull, K. The cell cycle of *Leishmania*: morphogenetic events and their implications for parasite biology. *Molecular Microbiology* **2011**, *79* (3), 647-662.
(52) Overath, P.; Engstler, M. Endocytosis, membrane recycling and sorting of GPI-anchored proteins: *Trypanosoma brucei* as a model system. *Molecular Microbiology* **2004**, *53* (3), 735-744.
(53) Waller, R. F.; McConville, M. J. Developmental changes in lysosome morphology and function *Leishmania* parasites. *International Journal for Parasitology* **2002**, *32* (12), 1435-1445.
(54) McConville, M., J.; Mullin, K., A.; Ilgoutz, S., C.; Teasdale, R., D. Secretory Pathway of Trypanosomatid Parasites. *Microbiology and Molecular Biology Reviews* **2002**, *66* (1), 122-154.
(55) Mullin, K. A.; Foth, B. J.; Ilgoutz, S. C.; Callaghan, J. M.; Zawadzki, J. L.; McFadden, G. I.; McConville, M. J. Regulated Degradation of an Endoplasmic Reticulum Membrane Protein in a Tubular Lysosome in *Leishmania mexicana*. *Molecular Biology of the Cell* **2001**, *12* (8), 2364-2377.
(56) Weise, F.; Stierhof, Y.-D.; Kühn, C.; Wiese, M.; Overath, P. Distribution of GPI-anchored proteins in the protozoan parasite *Leishmania*, based on an improved ultrastructural description using high-pressure frozen cells. *Journal of Cell Science* **2000**, *113* (24), 4587-4603.
(57) Ghedin, E.; Debrabant, A.; Engel, J. C.; Dwyer, D. M. Secretory and Endocytic Pathways Converge in a Dynamic Endosomal System in a Primitive Protozoan. *Traffic* **2001**, *2* (3), 175-188.
(58) Langreth, S. G.; Balber, A. E. Protein Uptake and Digestion in Bloodstream and Culture Forms of *Trypanosoma brucei*. *The Journal of Protozoology* **1975**, *22* (1), 40-53.

(59) Paulin, J. J. Conformation of a Single Mitochondrion in the Trypomastigote Stage of *Trypanosoma cruzi*. *The Journal of Parasitology* **1983**, *69* (1), 242-244.
(60) Paulin, J. J. The chondriome of selected trypanosomatids. A three-dimensional study based on serial thick sections and high voltage electron microscopy. *Journal of Cell Biology* **1975**, *66* (2), 404-413.
(61) Newberry, L. B.; Paulin, J. J. Reconstruction of the Chondriome of the Amastigote Form of *Trypanosoma cruzi*. *The Journal of Parasitology* **1989**, *75* (4), 649-652.
(62) de Souza, W.; Attias, M.; Rodrigues, J. C. F. Particularities of mitochondrial structure in parasitic protists (Apicomplexa and Kinetoplastida). *The International Journal of Biochemistry & Cell Biology* **2009**, *41* (10), 2069-2080.
(63) Vickerman, K. Polymorphism and Mitochondrial Activity In Sleeping Sickness Trypanosomes. *Nature* **1965**, *208* (5012), 762-766.
(64) Halliday, C.; Dean, S.; Sunter, J.; Wheeler, R. Subcellular protein localisation of *Trypanosoma brucei* bloodstream form-upregulated proteins maps stage-specific adaptations. *Wellcome Open Research* **2023**, *8* (46).
(65) Jakob, M.; Hoffmann, A.; Amodeo, S.; Peitsch, C.; Zuber, B.; Ochsenreiter, T. Mitochondrial growth during the cell cycle of *Trypanosoma brucei* bloodstream forms. *Scientific Reports* **2016**, *6* (1), 36565.
(66) Simpson, L. The Kinetoplast of the Hernoflagellates. In *International Review of Cytology*, Bourne, G. H., Danielli, J. F., Jeon, K. W. Eds.; Vol. 32; Academic Press, 1972; pp 139-207.
(67) Borst, P.; Van der Ploeg, M.; Van Hoek, J. F. M.; Tas, J.; James, J. On the DNA content and ploidy of trypanosomes. *Molecular and Biochemical Parasitology* **1982**, *6* (1), 13-23.
(68) Simpson, L.; Neckelmann, N.; de la Cruz, V. F.; Simpson, A. M.; Feagin, J. E.; Jasmer, D. P.; Stuart, J. E. Comparison of the maxicircle (mitochondrial) genomes of *Leishmania tarentolae* and *Trypanosoma brucei* at the level of nucleotide sequence. *Journal of Biological Chemistry* **1987**, *262* (13), 6182-6196.
(69) Bolender, N.; Sickmann, A.; Wagner, R.; Meisinger, C.; Pfanner, N. Multiple pathways for sorting mitochondrial precursor proteins. *EMBO reports* **2008**, *9* (1), 42-49-49.
(70) Verner, Z.; Čermáková, P.; Škodová, I.; Kováčová, B.; Lukeš, J.; Horváth, A. Comparative analysis of respiratory chain and oxidative phosphorylation in *Leishmania tarentolae*, *Crithidia fasciculata*, *Phytomonas serpens* and procyclic stage of *Trypanosoma brucei*. *Molecular and Biochemical Parasitology* **2014**, *193* (1), 55-65.
(71) Bermúdez, R.; Dagger, F.; D'Aquino, J. A.; Benaim, G.; Dawidowicz, K. Characterization of mitochondrial electron-transfer in *Leishmania mexicana*. *Molecular and Biochemical Parasitology* **1997**, *90* (1), 43-54.
(72) Chaudhuri, M.; Ajayi, W.; Hill, G. C. Biochemical and molecular properties of the *Trypanosoma brucei* alternative oxidase. *Molecular and Biochemical Parasitology* **1998**, *95* (1), 53-68.
(73) Taleva, G.; Husová, M.; Panicucci, B.; Hierro-Yap, C.; Pineda, E.; Biran, M.; Moos, M.; Šimek, P.; Butter, F.; Bringaud, F.*; et al.* Mitochondrion of the *Trypanosoma brucei* long slender bloodstream form is capable of ATP production by substrate-level phosphorylation. *PLOS Pathogens* **2023**, *19* (10), e1011699.
(74) Zíková, A. Mitochondrial adaptations throughout the *Trypanosoma brucei* life cycle. *Journal of Eukaryotic Microbiology* **2022**, *69* (6), e12911.
(75) Wheeler, R. J.; Gull, K.; Sunter, J. D. Coordination of the Cell Cycle in Trypanosomes. *Annual review of microbiology* **2019**, *73* (1), 133-154.
(76) Sherwin, T.; Gull, K.; Vickerman, K. The cell division cycle of *Trypanosoma brucei brucei*: timing of event markers and cytoskeletal modulations. *Philosophical Transactions of the Royal Society of London. B, Biological Sciences* **1997**, *323* (1218), 573-588.
(77) Woodward, R.; Gull, K. Timing of nuclear and kinetoplast DNA replication and early morphological events in the cell cycle of *Trypanosoma brucei*. *Journal of Cell Science* **1990**, *95* (1), 49-57.

(78) Ivens, A. C.; Peacock, C. S.; Worthey, E. A.; Murphy, L.; Aggarwal, G.; Berriman, M.; Sisk, E.; Rajandream, M.-A.; Adlem, E.; Aert, R.*; et al.* The Genome of the Kinetoplastid Parasite, *Leishmania major*. *Science* **2005**, *309* (5733), 436-442.
(79) Berriman, M.; Ghedin, E.; Hertz-Fowler, C.; Blandin, G.; Renauld, H.; Bartholomeu, D. C.; Lennard, N. J.; Caler, E.; Hamlin, N. E.; Haas, B.*; et al.* The Genome of the African Trypanosome *Trypanosoma brucei*. *Science* **2005**, *309* (5733), 416-422.
(80) El-Sayed, N. M.; Myler, P. J.; Bartholomeu, D. C.; Nilsson, D.; Aggarwal, G.; Tran, A.-N.; Ghedin, E.; Worthey, E. A.; Delcher, A. L.; Blandin, G.*; et al.* The Genome Sequence of *Trypanosoma cruzi*, Etiologic Agent of Chagas Disease. *Science* **2005**, *309* (5733), 409-415.
(81) Peacock, C. S.; Seeger, K.; Harris, D.; Murphy, L.; Ruiz, J. C.; Quail, M. A.; Peters, N.; Adlem, E.; Tivey, A.; Aslett, M.*; et al.* Comparative genomic analysis of three *Leishmania* species that cause diverse human disease. *Nature Genetics* **2007**, *39* (7), 839-847.
(82) Rogers, M. B.; Hilley, J. D.; Dickens, N. J.; Wilkes, J.; Bates, P. A.; Depledge, D. P.; Harris, D.; Her, Y.; Herzyk, P.; Imamura, H.*; et al.* Chromosome and gene copy number variation allow major structural change between species and strains of *Leishmania*. *Genome research* **2011**, *21* (12), 2129-2142.
(83) Cantacessi, C.; Dantas-Torres, F.; Nolan, M. J.; Otranto, D. The past, present, and future of *Leishmania* genomics and transcriptomics. *Trends in Parasitology* **2015**, *31* (3), 100-108.
(84) Downing, T.; Imamura, H.; Decuypere, S.; Clark, T. G.; Coombs, G. H.; Cotton, J. A.; Hilley, J. D.; de Doncker, S.; Maes, I.; Mottram, J. C.*; et al.* Whole genome sequencing of multiple *Leishmania donovani* clinical isolates provides insights into population structure and mechanisms of drug resistance. *Genome research* **2011**, *21* (12), 2143-2156.
(85) Britto, C.; Ravel, C.; Bastien, P.; Blaineau, C.; Pagès, M.; Dedet, J.-P.; Wincker, P. Conserved linkage groups associated with large-scale chromosomal rearrangements between Old World and New World *Leishmania* genomes. *Gene* **1998**, *222* (1), 107-117.
(86) Wincker, P.; Ravel, C.; Blaineau, C.; Pages, M.; Jauffret, Y.; Dedet, J.-P.; Bastien, P. The *Leishmania* Genome Comprises 36 Chromosomes Conserved Across Widely Divergent Human Pathogenic Species. *Nucleic Acids Research* **1996**, *24* (9), 1688-1694.
(87) Black, J. A.; Reis-Cunha, J. L.; Cruz, A. K.; Tosi, L. R. O. Life in plastic, it's fantastic! How *Leishmania* exploit genome instability to shape gene expression. *Frontiers in Cellular and Infection Microbiology* **2023**, *13*.
(88) Sterkers, Y.; Lachaud, L.; Crobu, L.; Bastien, P.; Pagès, M. FISH analysis reveals aneuploidy and continual generation of chromosomal mosaicism in *Leishmania major*. *Cellular Microbiology* **2011**, *13* (2), 274-283.
(89) Negreira, G. H.; Monsieurs, P.; Imamura, H.; Maes, I.; Kuk, N.; Yagoubat, A.; Van den Broeck, F.; Sterkers, Y.; Dujardin, J.-C.; Domagalska, Malgorzata A. High throughput single-cell genome sequencing gives insights into the generation and evolution of mosaic aneuploidy in *Leishmania donovani*. *Nucleic Acids Research* **2022**, *50* (1), 293-305.
(90) Clayton, C. E. Gene expression in Kinetoplastids. *Current Opinion in Microbiology* **2016**, *32*, 46-51.
(91) Martínez-Calvillo, S.; Yan, S.; Nguyen, D.; Fox, M.; Stuart, K.; Myler, P. J. Transcription of *Leishmania major* Friedlin Chromosome 1 Initiates in Both Directions within a Single Region. *Molecular Cell* **2003**, *11* (5), 1291-1299.
(92) Michaeli, S. Trans-Splicing in Trypanosomes: Machinery and Its Impact on the Parasite Transcriptome. *Future Microbiology* **2011**, *6* (4), 459-474.
(93) Clayton, C. Regulation of gene expression in trypanosomatids: living with polycistronic transcription. *Open Biology* **2019**, *9* (6), 190072.
(94) Fernández-Moya, S. M.; Estévez, A. M. Posttranscriptional control and the role of RNA-binding proteins in gene regulation in trypanosomatid protozoan parasites. *WIREs RNA* **2010**, *1* (1), 34-46.
(95) Haile, S.; Papadopoulou, B. Developmental regulation of gene expression in trypanosomatid parasitic protozoa. *Current Opinion in Microbiology* **2007**, *10* (6), 569-577.

(96) Clayton, C.; Shapira, M. Post-transcriptional regulation of gene expression in trypanosomes and leishmanias. *Molecular and Biochemical Parasitology* **2007**, *156* (2), 93-101.
(97) De Gaudenzi, J. G.; Noé, G.; Campo, V. A.; Frasch, A. C.; Cassola, A. Gene expression regulation in trypanosomatids. *Essays in Biochemistry* **2011**, *51*, 31-46.
(98) Palenchar, J. B.; Bellofatto, V. Gene transcription in trypanosomes. *Molecular and Biochemical Parasitology* **2006**, *146* (2), 135-141.
(99) Daniels, J.-P.; Gull, K.; Wickstead, B. Cell Biology of the Trypanosome Genome. *Microbiology and Molecular Biology Reviews* **2010**, *74* (4), 552-569.
(100) Ngô, H.; Tschudi, C.; Gull, K.; Ullu, E. Double-stranded RNA induces mRNA degradation in *Trypanosoma brucei*. *Proceedings of the National Academy of Sciences* **1998**, *95* (25), 14687-14692.
(101) Robinson, K. A.; Beverley, S. M. Improvements in transfection efficiency and tests of RNA interference (RNAi) approaches in the protozoan parasite *Leishmania*. *Molecular and Biochemical Parasitology* **2003**, *128* (2), 217-228.
(102) Lye, L.-F.; Owens, K.; Shi, H.; Murta, S. M. F.; Vieira, A. C.; Turco, S. J.; Tschudi, C.; Ullu, E.; Beverley, S. M. Retention and Loss of RNA Interference Pathways in Trypanosomatid Protozoans. *PLOS Pathogens* **2010**, *6* (10), e1001161.
(103) Hannon, G. J. RNA interference. *Nature* **2002**, *418* (6894), 244-251.
(104) Müller, A.; Montoya, A.; Escacena, C.; de la Cruz, M.; Junco, A.; Iriso, A.; Marino, E.; Fúster, F.; Miró, G. *Leishmania infantum* infection serosurveillance in stray dogs inhabiting the Madrid community: 2007–2018. *Parasites & Vectors* **2022**, *15* (1), 96.
(105) Alvar, J.; Canavate, C.; Molina, R.; Moreno, J.; Nieto, J. Canine leishmaniasis. *Advances in parasitology* **2004**, *57* (3), 1-88.
(106) Burza, S.; Croft, S. L.; Boelaert, M. Leishmaniasis. *The Lancet* **2018**, *392* (10151), 951-970.
(107) Alvar, J.; Vélez, I. D.; Bern, C.; Herrero, M.; Desjeux, P.; Cano, J.; Jannin, J.; den Boer, M.; WHO Leishmaniasis Control Team. Leishmaniasis worldwide and global estimates of its incidence. *PloS one* **2012**, *7* (5), e35671-e35671.
(108) Ready, P. D. Epidemiology of visceral leishmaniasis. *Clinical Epidemiology* **2014**, *6* (null), 147-154.
(109) Mock, D. J.; Hollenbaugh, J. A.; Daddacha, W.; Overstreet, M. G.; Lazarski, C. A.; Fowell, D. J.; Kim, B. *Leishmania* Induces Survival, Proliferation and Elevated Cellular dNTP Levels in Human Monocytes Promoting Acceleration of HIV Co-Infection. *PLOS Pathogens* **2012**, *8* (4), e1002635.
(110) Pintado, V.; Martín-Rabadán, P.; Rivera, M. L.; Moreno, S.; Bouza, E. Visceral Leishmaniasis in Human Immunodeficiency Virus (HIV)-Infected and Non-HIV-Infected Patients: A Comparative Study. *Medicine* **2001**, *80* (1).
(111) Zijlstra, E. E.; Musa, A. M.; Khalil, E. A. G.; El Hassan, I. M.; El-Hassan, A. M. Post-kala-azar dermal leishmaniasis. *The Lancet Infectious Diseases* **2003**, *3* (2), 87-98.
(112) Gedda, M. R.; Singh, B.; Kumar, D.; Singh, A. K.; Madhukar, P.; Upadhyay, S.; Singh, O. P.; Sundar, S. Post kala-azar dermal leishmaniasis: A threat to elimination program. *PLOS Neglected Tropical Diseases* **2020**, *14* (7), e0008221.
(113) Gurel, M. S.; Tekin, B.; Uzun, S. Cutaneous leishmaniasis: A great imitator. *Clinics in Dermatology* **2020**, *38* (2), 140-151.
(114) Sangueza, O. P.; Sangueza, J. M.; Stiller, M. J.; Sangueza, P. Mucocutaneous leishmaniasis: A clinicopathologic classification. *Journal of the American Academy of Dermatology* **1993**, *28* (6), 927-932.
(115) David, C. V.; Craft, N. Cutaneous and mucocutaneous leishmaniasis. *Dermatologic Therapy* **2009**, *22* (6), 491-502.
(116) Naghavi, M.; Mestrovic, T.; Gray, A.; Gershberg Hayoon, A.; Swetschinski, L. R.; Robles Aguilar, G.; Davis Weaver, N.; Ikuta, K. S.; Chung, E.; Wool, E. E.*; et al.* Global burden associated with 85 pathogens in 2019: a systematic analysis for the Global Burden of Disease Study 2019. *The Lancet Infectious Diseases* **2024**, *24* (8), 868-895.

(117) Murray, C. J.; Lopez, A. D. *The global burden of disease: a comprehensive assessment of mortality and disability from diseases, injuries, and risk factors in 1990 and projected to 2020, Summary*; The Harvard School of Public Health on behalf of the World Health Organization and the World Bank, 1996.
(118) Boelaert, M.; Verdonck, K.; Menten, J.; Sunyoto, T.; van Griensven, J.; Chappuis, F.; Rijal, S. Rapid tests for the diagnosis of visceral leishmaniasis in patients with suspected disease. *Cochrane Database of Systematic Reviews* **2014**, (6).
(119) Chappuis, F.; Rijal, S.; Soto, A.; Menten, J.; Boelaert, M. A meta-analysis of the diagnostic performance of the direct agglutination test and rK39 dipstick for visceral leishmaniasis. *British Medical Journal* **2006**, *333* (7571), 723.
(120) Harith, A. E.; Kolk, A. H. J.; Kager, P. A.; Leeuwenburg, J.; Muigai, R.; Kiugu, S.; Kiugu, S.; Laarman, J. J. A simple and economical direct agglutination test for serodiagnosis and sero-epidemiological studies of visceral leishmaniasis. *Transactions of The Royal Society of Tropical Medicine and Hygiene* **1986**, *80* (4), 583-586.
(121) Adams, E. R.; Schoone, G. J.; Ageed, A. F.; Safi, S. E.; Schallig, H. D. F. H. Development of a Reverse Transcriptase Loop-Mediated Isothermal Amplification (LAMP) Assay for the Sensitive Detection of *Leishmania* Parasites in Clinical Samples. *The American Society of Tropical Medicine and Hygiene* **2010**, *82* (4), 591-596.
(122) Vallur, A. C.; Tutterrow, Y. L.; Mohamath, R.; Pattabhi, S.; Hailu, A.; Abdoun, A. O.; Ahmed, A. E.; Mukhtar, M.; Salam, M. A.; Almeida, M. L.*; et al.* Development and comparative evaluation of two antigen detection tests for Visceral Leishmaniasis. *BMC Infectious Diseases* **2015**, *15* (1), 384.
(123) Gillespie, P. M.; Beaumier, C. M.; Strych, U.; Hayward, T.; Hotez, P. J.; Bottazzi, M. E. Status of vaccine research and development of vaccines for leishmaniasis. *Vaccine* **2016**, *34* (26), 2992-2995.
(124) Kaye, P. M.; Matlashewski, G.; Mohan, S.; Le Rutte, E.; Mondal, D.; Khamesipour, A.; Malvolti, S. Vaccine value profile for leishmaniasis. *Vaccine* **2023**, *41*, S153-S175.
(125) Aronson, N.; Herwaldt, B. L.; Libman, M.; Pearson, R.; Lopez-Velez, R.; Weina, P.; Carvalho, E.; Ephros, M.; Jeronimo, S.; Magill, A. Diagnosis and Treatment of Leishmaniasis: Clinical Practice Guidelines by the Infectious Diseases Society of America (IDSA) and the American Society of Tropical Medicine and Hygiene (ASTMH). *The American journal of tropical medicine and hygiene* **2017**, *96* (1), 24-45.
(126) McGwire, B. S.; Satoskar, A. R. Treatment Options for Leishmaniasis. *Current Clinical Microbiology Reports* **2016**, *3* (4), 198-203.
(127) WHO Control of Neglected Tropical Diseases. *Technical Report Series, Control of the leishmaniases: Report of a meeting of the WHO Expert Committee on the Control of Leishmaniases*; 2010.
(128) Alves, F.; Bilbe, G.; Blesson, S.; Goyal, V.; Monnerat, S.; Mowbray, C.; Muthoni Ouattara, G.; Pécoul, B.; Rijal, S.; Rode, J.*; et al.* Recent Development of Visceral Leishmaniasis Treatments: Successes, Pitfalls, and Perspectives. *Clinical Microbiology Reviews* **2018**, *31* (4), 10.1128/cmr.00048-00018.
(129) Bryceson, A. A policy for leishmaniasis with respect to the prevention and control of drug resistance. *Tropical Medicine & International Health* **2001**, *6* (11), 928-934.
(130) Diro, E.; Blesson, S.; Edwards, T.; Ritmeijer, K.; Fikre, H.; Admassu, H.; Kibret, A.; Ellis, S. J.; Bardonneau, C.; Zijlstra, E. E.*; et al.* A randomized trial of AmBisome monotherapy and AmBisome and miltefosine combination to treat visceral leishmaniasis in HIV co-infected patients in Ethiopia. *PLOS Neglected Tropical Diseases* **2019**, *13* (1), e0006988.
(131) Musa, A. M.; Mbui, J.; Mohammed, R.; Olobo, J.; Ritmeijer, K.; Alcoba, G.; Muthoni Ouattara, G.; Egondi, T.; Nakanwagi, P.; Omollo, T.*; et al.* Paromomycin and Miltefosine Combination as an Alternative to Treat Patients With Visceral Leishmaniasis in Eastern Africa: A Randomized, Controlled, Multicountry Trial. *Clinical Infectious Diseases* **2023**, *76* (3), e1177-e1185.
(132) Croft, S.; Sundar, S.; Fairlamb, A. Drug Resistance in Leishmaniasis. *Clinical Microbiology Reviews* **2006**, *19* (1), 111-126.

(133) Sundar, S.; More, D. K.; Singh, M. K.; Singh, V. P.; Sharma, S.; Makharia, A.; Kumar, P. C. K.; Murray, H. W. Failure of Pentavalent Antimony in Visceral Leishmaniasis in India: Report from the Center of the Indian Epidemic. *Clinical Infectious Diseases* **2000**, *31* (4), 1104-1107.
(134) Lira, R.; Sundar, S.; Makharia, A.; Kenney, R.; Gam, A.; Saraiva, E.; Sacks, D. Evidence that the High Incidence of Treatment Failures in Indian Kala-Azar Is Due to the Emergence of Antimony-Resistant Strains of *Leishmania donovani*. *The Journal of Infectious Diseases* **1999**, *180* (2), 564-567.
(135) Abdo, M. G.; Elamin, W. M.; Khalil, E. A. G.; Mukhtar, M. M. Antimony-resistant *Leishmania donovani* in eastern Sudan: incidence and *in vitro* correlation. *Eastern Mediterranean Health Journal* **2003**, *9* (4), 837-843.
(136) Sundar, S.; Singh, A.; Rai, M.; Prajapati, V. K.; Singh, A. K.; Ostyn, B.; Boelaert, M.; Dujardin, J.-C.; Chakravarty, J. Efficacy of Miltefosine in the Treatment of Visceral Leishmaniasis in India After a Decade of Use. *Clinical Infectious Diseases* **2012**, *55* (4), 543-550.
(137) Carnielli, J. B. T.; Monti-Rocha, R.; Costa, D. L.; Molina Sesana, A.; Pansini, L. N. N.; Segatto, M.; Mottram, J. C.; Costa, C. H. N.; Carvalho, S. F. G.; Dietze, R. Natural Resistance of *Leishmania infantum* to Miltefosine Contributes to the Low Efficacy in the Treatment of Visceral Leishmaniasis in Brazil. *The American journal of tropical medicine and hygiene* **2019**, *101* (4), 789-794.
(138) Ferreira, B. A.; Coser, E. M.; de la Roca, S.; Aoki, J. I.; Branco, N.; Soares, G. H. C.; Lima, M. I. S.; Coelho, A. C. Amphotericin B resistance in *Leishmania amazonensis*: *In vitro* and *in vivo* characterization of a Brazilian clinical isolate. *PLOS Neglected Tropical Diseases* **2024**, *18* (5), e0012175.
(139) Purkait, B.; Kumar, A.; Nandi, N.; Sardar Abul, H.; Das, S.; Kumar, S.; Pandey, K.; Ravidas, V.; Kumar, M.; De, T.*; et al.* Mechanism of Amphotericin B Resistance in Clinical Isolates of *Leishmania donovani*. *Antimicrobial Agents and Chemotherapy* **2012**, *56* (2), 1031-1041.
(140) Mano, C.; Kongkaew, A.; Tippawangkosol, P.; Somboon, P.; Roytrakul, S.; Pescher, P.; Späth, G. F.; Uthaipibull, C.; Tantiworawit, A.; Siriyasatien, P.*; et al.* Amphotericin B resistance correlates with increased fitness *in vitro* and *in vivo* in *Leishmania* (*Mundinia*) *martiniquensis*. *Frontiers in Microbiology* **2023**, *14*, 1156061.
(141) Teklemariam, S.; Hiwot, A. G.; Frommel, D.; Miko, T. L.; Ganlov, G.; Bryceson, A. Aminosidine and its combination with sodium stibogluconate in the treatment of diffuse cutaneous leishmaniasis caused by *Leishmania aethiopica*. *Transactions of The Royal Society of Tropical Medicine and Hygiene* **1994**, *88* (3), 334-339.
(142) Fairlamb, A. H.; Gow, N. A. R.; Matthews, K. R.; Waters, A. P. Drug resistance in eukaryotic microorganisms. *Nature Microbiology* **2016**, *1* (7), 16092.
(143) Pradhan, S.; Schwartz, R. A.; Patil, A.; Grabbe, S.; Goldust, M. Treatment options for leishmaniasis. *Clinical and Experimental Dermatology* **2022**, *47* (3), 516-521.
(144) Badaro, R.; Falcoff, E.; Badaro Fernando, S.; Carvalho Edgar, M.; Pedral-Sampaio, D.; Barral, A.; Carvalho Jose, S.; Barral-Netto, M.; Brandely, M.; Silva, L.*; et al.* Treatment of Visceral Leishmaniasis with Pentavalent Antimony and Interferon Gamma. *New England Journal of Medicine* **1990**, *322* (1), 16-21.
(145) Eberle, C.; Lauber, B. S.; Fankhauser, D.; Kaiser, M.; Brun, R.; Krauth-Siegel, R. L.; Diederich, F. Improved Inhibitors of Trypanothione Reductase by Combination of Motifs: Synthesis, Inhibitory Potency, Binding Mode, and Antiprotozoal Activities. *ChemMedChem* **2011**, *6* (2), 292-301.
(146) Mottram, J. C.; Brooks, D. R.; Coombs, G. H. Roles of cysteine proteinases of trypanosomes and *Leishmania* in host-parasite interactions. *Current Opinion in Microbiology* **1998**, *1* (4), 455-460.
(147) Balaña-Fouce, R.; Redondo, C. M.; Pérez-Pertejo, Y.; Díaz-González, R.; Reguera, R. M. Targeting atypical trypanosomatid DNA topoisomerase I. *Drug discovery today* **2006**, *11* (15), 733-740.
(148) Eder, J.; Sedrani, R.; Wiesmann, C. The discovery of first-in-class drugs: origins and evolution. *Nature Reviews Drug Discovery* **2014**, *13* (8), 577-587.
(149) Croston, G. E. The utility of target-based discovery. *Expert Opinion on Drug Discovery* **2017**, *12* (5), 427-429.

(150) Swinney, D. C.; Anthony, J. How were new medicines discovered? *Nature Reviews Drug Discovery* **2011**, *10* (7), 507-519.
(151) Nühs, A.; De Rycker, M.; Manthri, S.; Comer, E.; Scherer, C. A.; Schreiber, S. L.; Ioset, J.-R.; Gray, D. W. Development and Validation of a Novel *Leishmania donovani* Screening Cascade for High-Throughput Screening Using a Novel Axenic Assay with High Predictivity of Leishmanicidal Intracellular Activity. *PLOS Neglected Tropical Diseases* **2015**, *9* (9), e0004094.
(152) Peña, I.; Pilar Manzano, M.; Cantizani, J.; Kessler, A.; Alonso-Padilla, J.; Bardera, A. I.; Alvarez, E.; Colmenarejo, G.; Cotillo, I.; Roquero, I.*; et al.* New Compound Sets Identified from High Throughput Phenotypic Screening Against Three Kinetoplastid Parasites: An Open Resource. *Scientific Reports* **2015**, *5* (1), 8771.
(153) de Koning, H. P. Drug resistance in protozoan parasites. *Emerging Topics in Life Sciences* **2017**, *1* (6), 627-632.
(154) De Koning, H. P. Uptake of Pentamidine in *Trypanosoma brucei brucei* is Mediated by Three Distinct Transporters: Implications for Cross-Resistance with Arsenicals. *Molecular Pharmacology* **2001**, *59* (3), 586.
(155) Wyllie, S.; Patterson, S.; Stojanovski, L.; Simeons, F. R. C.; Norval, S.; Kime, R.; Read, K. D.; Fairlamb, A. H. The Anti-Trypanosome Drug Fexinidazole Shows Potential for Treating Visceral Leishmaniasis. *Science Translational Medicine* **2012**, *4* (119), 119re111-119re111.
(156) Phase II Proof of Concept Trial to Determine Efficacy of Fexinidazole in Visceral Leishmaniasis Patients in Sudan. https://clinicaltrials.gov/study/NCT01980199 (accessed (02/09/2024).
(157) van de Waterbeemd, H.; Gifford, E. ADMET in silico modelling: towards prediction paradise? *Nature Reviews Drug Discovery* **2003**, *2* (3), 192-204.
(158) Waring, M. J.; Arrowsmith, J.; Leach, A. R.; Leeson, P. D.; Mandrell, S.; Owen, R. M.; Pairaudeau, G.; Pennie, W. D.; Pickett, S. D.; Wang, J.*; et al.* An analysis of the attrition of drug candidates from four major pharmaceutical companies. *Nature Reviews Drug Discovery* **2015**, *14* (7), 475-486.
(159) Kar, S.; Leszczynski, J. Open access *in silico* tools to predict the ADMET profiling of drug candidates. *Expert Opinion on Drug Discovery* **2020**, *15* (12), 1473-1487.
(160) Cummins, C. L.; Jacobsen, W.; Benet, L. Z. Unmasking the Dynamic Interplay between Intestinal P-Glycoprotein and CYP3A4. *Journal of Pharmacology and Experimental Therapeutics* **2002**, *300* (3), 1036.
(161) A Phase II, Multicentre, Randomized, Two-arm Blinded Study to Assess the Efficacy and Safety of Two LXE408 Regimens for Treatment of Patients With Primary Visceral Leishmaniasis. National Library of Medicine: ClinicalTrials.gov, 2022.
(162) Drugs for Neglected Diseases initiative. *LXE408 Novartis*. https://dndi.org/research-development/portfolio/novartis-lxe408/ (accessed 25/09/2024).
(163) Drugs for Neglected Diseases initiative DND*i*. *Research & Development portfolio June 2024*. 2024. https://dndi.org/research-development/portfolio/ (accessed 25/09/2024).
(164) Thacker, S. G.; McWilliams, I. L.; Bonnet, B.; Halie, L.; Beaucage, S.; Rachuri, S.; Dey, R.; Duncan, R.; Modabber, F.; Robinson, S.*; et al.* CpG ODN D35 improves the response to abbreviated low-dose pentavalent antimonial treatment in non-human primate model of cutaneous leishmaniasis. *PLOS Neglected Tropical Diseases* **2020**, *14* (2), e0008050.
(165) A Phase I, double-blind, randomised, single-centre, parallel-group, single ascending dose, placebo-controlled study of the safety, tolerability, pharmacokinetics, and pharmacodynamics of CpG ODN D35 after subcutaneous administration in healthy male subjects. BioMed Central: ISRCTN registry, 2021.
(166) Drugs for Neglected Diseases initiative. *DNDI-0690*. https://dndi.org/research-development/portfolio/dndi-0690/ (accessed 25/09/2024).
(167) Drugs for Neglected Diseases initiative. *DNDI-6148*. https://dndi.org/research-development/portfolio/dndi-6148/ (accessed 25/09/2024).

(168) Betu Kumeso, V. K.; Kalonji, W. M.; Rembry, S.; Valverde Mordt, O.; Ngolo Tete, D.; Prêtre, A.; Delhomme, S.; Ilunga Wa Kyhi, M.; Camara, M.; Catusse, J.*; et al.* Efficacy and safety of acoziborole in patients with human African trypanosomiasis caused by *Trypanosoma brucei gambiense*: a multicentre, open-label, single-arm, phase 2/3 trial. *The Lancet Infectious Diseases* **2023**, *23* (4), 463-470.
(169) Rakotomanga, M.; Blanc, S.; Gaudin, K.; Chaminade, P.; Loiseau, P. M. Miltefosine Affects Lipid Metabolism in *Leishmania donovani* Promastigotes. *Antimicrobial Agents and Chemotherapy* **2007**, *51* (4), 1425-1430.
(170) Ramos, H.; Valdivieso, E.; Gamargo, M.; Dagger, F.; Cohen, B. E. Amphotericin B Kills Unicellular Leishmanias by Forming Aqueous Pores Permeable to Small Cations and Anions. *The Journal of Membrane Biology* **1996**, *152* (1), 65-75.
(171) El-Dirany, R.; Shahrour, H.; Dirany, Z.; Abdel-Sater, F.; Gonzalez-Gaitano, G.; Brandenburg, K.; Martinez de Tejada, G.; Nguewa, P. A. Activity of Anti-Microbial Peptides (AMPs) against *Leishmania* and Other Parasites: An Overview. *Biomolecules* **2021**, *11* (7), 984.
(172) Rodrigues, J. C. F.; Concepcion, J. L.; Rodrigues, C.; Caldera, A.; Urbina, J. A.; de Souza, W. *In Vitro* Activities of ER-119884 and E5700, Two Potent Squalene Synthase Inhibitors, against *Leishmania amazonensis*: Antiproliferative, Biochemical, and Ultrastructural Effects. *Antimicrobial Agents and Chemotherapy* **2008**, *52* (11), 4098-4114.
(173) Rodrigues, J. C. F.; Bernardes, C. F.; Visbal, G.; Urbina, J. A.; Vercesi, A. E.; de Souza, W. Sterol Methenyl Transferase Inhibitors Alter the Ultrastructure and Function of the *Leishmania amazonensis* Mitochondrion Leading to Potent Growth Inhibition. *Protist* **2007**, *158* (4), 447-456.
(174) Rodrigues, J., C. F.; Attias, M.; Rodriguez, C.; Urbina, J., A.; de Souza, W. Ultrastructural and Biochemical Alterations Induced by 22,26-Azasterol, a Δ24(25)-Sterol Methyltransferase Inhibitor, on Promastigote and Amastigote Forms of *Leishmania amazonensis*. *Antimicrobial Agents and Chemotherapy* **2002**, *46* (2), 487-499.
(175) Shapiro, T. A. Inhibition of topoisomerases in African trypanosomes. *Acta Tropica* **1993**, *54* (3), 251-260.
(176) Yang, G.; Choi, G.; No, J. H. Antileishmanial Mechanism of Diamidines Involves Targeting Kinetoplasts. *Antimicrobial Agents and Chemotherapy* **2016**, *60* (11), 6828-6836.
(177) Vercesi, A. E.; Docampo, R. Ca^{2+} transport by digitonin-permeabilized *Leishmania donovani*. Effects of Ca^{2+}, pentamidine and WR-6026 on mitochondrial membrane potential *in situ*. *Biochemical Journal* **1992**, *284* (2), 463-467.
(178) Ortiz, D.; Forquer, I.; Boitz, J.; Soysa, R.; Elya, C.; Fulwiler, A.; Nilsen, A.; Polley, T.; Riscoe Michael, K.; Ullman, B.*; et al.* Targeting the Cytochrome bc_1 Complex of *Leishmania* Parasites for Discovery of Novel Drugs. *Antimicrobial Agents and Chemotherapy* **2016**, *60* (8), 4972-4982.
(179) Carvalho, L.; Luque-Ortega, J. R.; Manzano, J. I.; Castanys, S.; Rivas, L.; Gamarro, F. Tafenoquine, an Antiplasmodial 8-Aminoquinoline, Targets *Leishmania* Respiratory Complex III and Induces Apoptosis. *Antimicrobial Agents and Chemotherapy* **2010**, *54* (12), 5344-5351.
(180) Braillard, S.; Keenan, M.; Breese, K. J.; Heppell, J.; Abbott, M.; Islam, R.; Shackleford, D. M.; Katneni, K.; Crighton, E.; Chen, G.*; et al.* DNDI-6174 is a preclinical candidate for visceral leishmaniasis that targets the cytochrome bc_1. *Science Translational Medicine* **2023**, *15* (726), eadh9902.
(181) Luque-Ortega, J. R.; Reuther, P.; Rivas, L.; Dardonville, C. New Benzophenone-Derived Bisphosphonium Salts as Leishmanicidal Leads Targeting Mitochondria through Inhibition of Respiratory Complex II. *Journal of Medicinal Chemistry* **2010**, *53* (4), 1788-1798.
(182) Alkhaldi, A. A. M.; Martinek, J.; Panicucci, B.; Dardonville, C.; Zíková, A.; de Koning, H. P. Trypanocidal action of bisphosphonium salts through a mitochondrial target in bloodstream form *Trypanosoma brucei*. *International Journal for Parasitology: Drugs and Drug Resistance* **2016**, *6* (1), 23-34.
(183) Patterson, S.; Fairlamb, H. A. Current and Future Prospects of Nitro-compounds as Drugs for Trypanosomiasis and Leishmaniasis. *Current Medicinal Chemistry* **2019**, *26* (23), 4454-4475.

(184) Peterson, F. J.; Mason, R. P.; Hovsepian, J.; Holtzman, J. L. Oxygen-sensitive and -insensitive nitroreduction by *Escherichia coli* and rat hepatic microsomes. *Journal of Biological Chemistry* **1979**, *254* (10), 4009-4014.
(185) McCalla, D. R.; Reuvers, A.; Kaiser, C. Breakage of Bacterial DNA by Nitrofuran Derivatives. *Cancer Research* **1971**, *31* (12), 2184-2188.
(186) Hall, B. S.; Bot, C.; Wilkinson, S. R. Nifurtimox Activation by Trypanosomal Type I Nitroreductases Generates Cytotoxic Nitrile Metabolites. *Journal of Biological Chemistry* **2011**, *286* (15), 13088-13095.
(187) Kubata, B. K.; Kabututu, Z.; Nozaki, T.; Munday, C. J.; Fukuzumi, S.; Ohkubo, K.; Lazarus, M.; Maruyama, T.; Martin, S. K.; Duszenko, M.*; et al.* A Key Role for Old Yellow Enzyme in the Metabolism of Drugs by *Trypanosoma cruzi*. *Journal of Experimental Medicine* **2002**, *196* (9), 1241-1252.
(188) Montenegro, M.; Cuervo, C.; Cardenas, C.; Duarte, S.; Díaz, J. R.; Thomas, M. C.; Lopez, M. C.; Puerta, C. J. Identification of a type I nitroreductase gene in non-virulent *Trypanosoma rangeli*. *Memórias do Instituto Oswaldo Cruz* **2017**, *112* (7), 504-509.
(189) Voak, A. A.; Gobalakrishnapillai, V.; Seifert, K.; Balczo, E.; Hu, L.; Hall, B. S.; Wilkinson, S. R. An Essential Type I Nitroreductase from *Leishmania major* Can Be Used to Activate Leishmanicidal Prodrugs. *Journal of Biological Chemistry* **2013**, *288* (40), 28466-28476.
(190) Mason, R. P.; Holtzman, J. L. Mechanism of microsomal and mitochondrial nitroreductase. Electron spin resonance evidence for nitroaromatic free radical intermediates. *Biochemistry* **1975**, *14* (8), 1626-1632.
(191) Docampo, R.; Mason, R. P.; Mottley, C.; Muniz, R. P. Generation of free radicals induced by nifurtimox in mammalian tissues. *Journal of Biological Chemistry* **1981**, *256* (21), 10930-10933.
(192) Wilkinson, S. R.; Taylor, M. C.; Horn, D.; Kelly, J. M.; Cheeseman, I. A mechanism for cross-resistance to nifurtimox and benznidazole in trypanosomes. *Proceedings of the National Academy of Sciences* **2008**, *105* (13), 5022-5027.
(193) Wyllie, S.; Roberts, A. J.; Norval, S.; Patterson, S.; Foth, B. J.; Berriman, M.; Read, K. D.; Fairlamb, A. H. Activation of Bicyclic Nitro-drugs by a Novel Nitroreductase (NTR2) in *Leishmania*. *PLOS Pathogens* **2016**, *12* (11), e1005971.
(194) Hall, B. S.; Wilkinson, S. R. Activation of Benznidazole by Trypanosomal Type I Nitroreductases Results in Glyoxal Formation. *Antimicrobial Agents and Chemotherapy* **2012**, *56* (1), 115-123.
(195) Wyllie, S.; Cunningham, M. L.; Fairlamb, A. H. Dual Action of Antimonial Drugs on Thiol Redox Metabolism in the Human Pathogen *Leishmania donovani*. *Journal of Biological Chemistry* **2004**, *279* (38), 39925-39932.
(196) Pinto-Martinez Andrea, K.; Rodriguez-Durán, J.; Serrano-Martin, X.; Hernandez-Rodriguez, V.; Benaim, G. Mechanism of Action of Miltefosine on *Leishmania donovani* Involves the Impairment of Acidocalcisome Function and the Activation of the Sphingosine-Dependent Plasma Membrane Ca^{2+} Channel. *Antimicrobial Agents and Chemotherapy* **2017**, *62* (1), 10.1128/aac.01614-01617.
(197) Fernández, M. M.; Malchiodi, E. L.; Algranati, I. D. Differential Effects of Paromomycin on Ribosomes of *Leishmania mexicana* and Mammalian Cells. *Antimicrobial Agents and Chemotherapy* **2011**, *55* (1), 86-93.
(198) Wyllie, S.; Brand, S.; Thomas, M.; De Rycker, M.; Chung, C.-w.; Pena, I.; Bingham, R. P.; Bueren-Calabuig, J. A.; Cantizani, J.; Cebrian, D.*; et al.* Preclinical candidate for the treatment of visceral leishmaniasis that acts through proteasome inhibition. *Proceedings of the National Academy of Sciences* **2019**, *116* (19), 9318-9323.
(199) Nagle, A.; Biggart, A.; Be, C.; Srinivas, H.; Hein, A.; Caridha, D.; Sciotti, R. J.; Pybus, B.; Kreishman-Deitrick, M.; Bursulaya, B.*; et al.* Discovery and Characterization of Clinical Candidate LXE408 as a Kinetoplastid-Selective Proteasome Inhibitor for the Treatment of Leishmaniases. *Journal of Medicinal Chemistry* **2020**, *63* (19), 10773-10781.
(200) Drugs for Neglected Diseases initiative. *S07 series*. https://dndi.org/research-development/portfolio/s07-series/ (accessed 25/09/2024).

(201) Wyllie, S.; Thomas, M.; Patterson, S.; Crouch, S.; De Rycker, M.; Lowe, R.; Gresham, S.; Urbaniak, M. D.; Otto, T. D.; Stojanovski, L.*; et al.* Cyclin-dependent kinase 12 is a drug target for visceral leishmaniasis. *Nature* **2018**, *560* (7717), 192-197.
(202) Thomas, J. A.; Baker, N.; Hutchinson, S.; Dominicus, C.; Trenaman, A.; Glover, L.; Alsford, S.; Horn, D. Insights into antitrypanosomal drug mode-of-action from cytology-based profiling. *PLOS Neglected Tropical Diseases* **2018**, *12* (11), e0006980.
(203) Mittra, B.; Andrews, N. W. IRONy OF FATE: role of iron-mediated ROS in *Leishmania* differentiation. *Trends in Parasitology* **2013**, *29* (10), 489-496.
(204) Mittra, B.; Cortez, M.; Haydock, A.; Ramasamy, G.; Myler, P. J.; Andrews, N. W. Iron uptake controls the generation of *Leishmania* infective forms through regulation of ROS levels. *Journal of Experimental Medicine* **2013**, *210* (2), 401-416.
(205) Oteiza, P. I. Zinc and the modulation of redox homeostasis. *Free Radical Biology and Medicine* **2012**, *53* (9), 1748-1759.
(206) Bray, T. M.; Bettger, W. J. The physiological role of zinc as an antioxidant. *Free Radical Biology and Medicine* **1990**, *8* (3), 281-291.
(207) Paradela, L. d. S. Drug target deconvolution in *Leishmania donovani*. University of Dundee, Doctorol Thesis Portal, 2022.
(208) Wall, R. J.; Moniz, S.; Thomas, M. G.; Norval, S.; Ko, E.-J.; Marco, M.; Miles, T. J.; Gilbert, I. H.; Horn, D.; Fairlamb, A. H.*; et al.* Antitrypanosomal 8-Hydroxy-Naphthyridines Are Chelators of Divalent Transition Metals. *Antimicrobial Agents and Chemotherapy* **2018**, *62* (8), 10.1128/aac.00235-00218.
(209) Hendrickx, S.; Reis-Cunha, J. L.; Forrester, S.; Jeffares, D. C.; Caljon, G. Experimental Selection of Paromomycin Resistance in *Leishmania donovani* Amastigotes Induces Variable Genomic Polymorphisms. *Microorganisms* **2021**, *9* (8), 1546.
(210) Patino, L. H.; Imamura, H.; Cruz-Saavedra, L.; Pavia, P.; Muskus, C.; Méndez, C.; Dujardin, J. C.; Ramírez, J. D. Major changes in chromosomal somy, gene expression and gene dosage driven by Sb^{III} in *Leishmania braziliensis* and *Leishmania panamensis*. *Scientific Reports* **2019**, *9* (1), 9485.
(211) Coelho, A. C.; Boisvert, S.; Mukherjee, A.; Leprohon, P.; Corbeil, J.; Ouellette, M. Multiple Mutations in Heterogeneous Miltefosine-Resistant *Leishmania major* Population as Determined by Whole Genome Sequencing. *PLOS Neglected Tropical Diseases* **2012**, *6* (2), e1512.
(212) Mukherjee, A.; Padmanabhan, P. K.; Sahani, M. H.; Barrett, M. P.; Madhubala, R. Roles for mitochondria in pentamidine susceptibility and resistance in *Leishmania donovani*. *Molecular and Biochemical Parasitology* **2006**, *145* (1), 1-10.
(213) Hefnawy, A.; Berg, M.; Dujardin, J.-C.; De Muylder, G. Exploiting Knowledge on *Leishmania* Drug Resistance to Support the Quest for New Drugs. *Trends in Parasitology* **2017**, *33* (3), 162-174.
(214) Basselin, M.; Denise, H.; Coombs Graham, H.; Barrett Michael, P. Resistance to Pentamidine in *Leishmania mexicana* Involves Exclusion of the Drug from the Mitochondrion. *Antimicrobial Agents and Chemotherapy* **2002**, *46* (12), 3731-3738.
(215) Castanys-Muñoz, E.; Pérez-Victoria José, M.; Gamarro, F.; Castanys, S. Characterization of an ABCG-Like Transporter from the Protozoan Parasite *Leishmania* with a Role in Drug Resistance and Transbilayer Lipid Movement. *Antimicrobial Agents and Chemotherapy* **2008**, *52* (10), 3573-3579.
(216) Tulloch, L. B.; Tinti, M.; Wall, R. J.; Weidt, S. K.; Corpas- Lopez, V.; Dey, G.; Smith, T. K.; Fairlamb, A. H.; Barrett, M. P.; Wyllie, S. Sterol 14-alpha demethylase (CYP51) activity in *Leishmania donovani* is likely dependent upon cytochrome P450 reductase 1. *PLOS Pathogens* **2024**, *20* (7), e1012382.
(217) Kolb, H. C.; Finn, M. G.; Sharpless, K. B. Click Chemistry: Diverse Chemical Function from a Few Good Reactions. *Angewandte Chemie International Edition* **2001**, *40* (11), 2004-2021.
(218) Best, M. D. Click Chemistry and Bioorthogonal Reactions: Unprecedented Selectivity in the Labeling of Biological Molecules. *Biochemistry* **2009**, *48* (28), 6571-6584.
(219) Sletten, E. M.; Bertozzi, C. R. Bioorthogonal Chemistry: Fishing for Selectivity in a Sea of Functionality. *Angewandte Chemie International Edition* **2009**, *48* (38), 6974-6998.

(220) The Nobel Prize in Chemistry 2022. The Royal Swedish Academy of Sciences: NobelPrize.org, 2022.
(221) Huisgen, R. Kinetics and Mechanism of 1,3-Dipolar Cycloadditions. *Angewandte Chemie International Edition in English* **1963**, *2* (11), 633-645.
(222) Rostovtsev, V. V.; Green, L. G.; Fokin, V. V.; Sharpless, K. B. A Stepwise Huisgen Cycloaddition Process: Copper(I)-Catalyzed Regioselective "Ligation" of Azides and Terminal Alkynes. *Angewandte Chemie International Edition* **2002**, *41* (14), 2596-2599.
(223) Tornøe, C. W.; Christensen, C.; Meldal, M. Peptidotriazoles on Solid Phase: [1,2,3]-Triazoles by Regiospecific Copper(I)-Catalyzed 1,3-Dipolar Cycloadditions of Terminal Alkynes to Azides. *The Journal of Organic Chemistry* **2002**, *67* (9), 3057-3064.
(224) Soares, E. V.; Hebbelinck, K.; Soares, H. M. V. M. Toxic effects caused by heavy metals in the yeast *Saccharomyces cerevisiae*: a comparative study. *Canadian Journal of Microbiology* **2003**, *49* (5), 336-343.
(225) Agard, N. J.; Baskin, J. M.; Prescher, J. A.; Lo, A.; Bertozzi, C. R. A Comparative Study of Bioorthogonal Reactions with Azides. *ACS Chemical Biology* **2006**, *1* (10), 644-648.
(226) Agard, N. J.; Prescher, J. A.; Bertozzi, C. R. A Strain-Promoted [3 + 2] Azide–Alkyne Cycloaddition for Covalent Modification of Biomolecules in Living Systems. *Journal of the American Chemical Society* **2004**, *126* (46), 15046-15047.
(227) Baskin, J. M.; Prescher, J. A.; Laughlin, S. T.; Agard, N. J.; Chang, P. V.; Miller, I. A.; Lo, A.; Codelli, J. A.; Bertozzi, C. R. Copper-free click chemistry for dynamic in vivo imaging. *Proceedings of the National Academy of Sciences* **2007**, *104* (43), 16793-16797.
(228) Saxon, E.; Bertozzi, C. R. Cell Surface Engineering by a Modified Staudinger Reaction. *Science* **2000**, *287* (5460), 2007-2010.
(229) Staudinger, H.; Meyer, J. Über neue organische phosphorverbindungen III. Phosphinmethylenderivate und phosphinimine. *Helvetica Chimica Acta* **1919**, *2* (1), 635-646.
(230) Nilsson, B. L.; Kiessling, L. L.; Raines, R. T. Staudinger Ligation: A Peptide from a Thioester and Azide. *Organic Letters* **2000**, *2* (13), 1939-1941.
(231) Nilsson, B. L.; Kiessling, L. L.; Raines, R. T. High-Yielding Staudinger Ligation of a Phosphinothioester and Azide To Form a Peptide. *Organic Letters* **2001**, *3* (1), 9-12.
(232) Saxon, E.; Armstrong, J. I.; Bertozzi, C. R. A "Traceless" Staudinger Ligation for the Chemoselective Synthesis of Amide Bonds. *Organic Letters* **2000**, *2* (14), 2141-2143.
(233) Lin, F. L.; Hoyt, H. M.; van Halbeek, H.; Bergman, R. G.; Bertozzi, C. R. Mechanistic Investigation of the Staudinger Ligation. *Journal of the American Chemical Society* **2005**, *127* (8), 2686-2695.
(234) Speers, A. E.; Adam, G. C.; Cravatt, B. F. Activity-Based Protein Profiling *in Vivo* Using a Copper(I)-Catalyzed Azide-Alkyne [3 + 2] Cycloaddition. *Journal of the American Chemical Society* **2003**, *125* (16), 4686-4687.
(235) Jeffery, D. A.; Bogyo, M. Chemical proteomics and its application to drug discovery. *Current Opinion in Biotechnology* **2003**, *14* (1), 87-95.
(236) Cisar, J. S.; Cravatt, B. F. Fully Functionalized Small-Molecule Probes for Integrated Phenotypic Screening and Target Identification. *Journal of the American Chemical Society* **2012**, *134* (25), 10385-10388.
(237) Singh, A.; Thornton, E. R.; Westheimer, F. H. The Photolysis of Diazoacetylchymotrypsin. *Journal of Biological Chemistry* **1962**, *237* (9), PC3006-PC3008.
(238) A. Fleming, S. Chemical reagents in photoaffinity labeling. *Tetrahedron* **1995**, *51* (46), 12479-12520.
(239) Gritsan, N. P.; Yuzawa, T.; Platz, M. S. Direct Observation of Singlet Phenylnitrene and Measurement of Its Rate of Rearrangement. *Journal of the American Chemical Society* **1997**, *119* (21), 5059-5060.
(240) Schnapp, K. A.; Poe, R.; Leyva, E.; Soundararajan, N.; Platz, M. S. Exploratory photochemistry of fluorinated aryl azides. Implications for the design of photoaffinity labeling reagents. *Bioconjugate Chemistry* **1993**, *4* (2), 172-177.

(241) Dorman, G.; Prestwich, G. D. Benzophenone Photophores in Biochemistry. *Biochemistry* **1994**, *33* (19), 5661-5673.
(242) Eirich, J.; Burkhart, J. L.; Ullrich, A.; Rudolf, G. C.; Vollmar, A.; Zahler, S.; Kazmaier, U.; Sieber, S. A. Pretubulysin derived probes as novel tools for monitoring the microtubule network *via* activity-based protein profiling and fluorescence microscopy. *Molecular BioSystems* **2012**, *8* (8), 2067-2075.
(243) Sakurai, K.; Ozawa, S.; Yamada, R.; Yasui, T.; Mizuno, S. Comparison of the Reactivity of Carbohydrate Photoaffinity Probes with Different Photoreactive Groups. *ChemBioChem* **2014**, *15* (10), 1399-1403.
(244) Li, Z.; Hao, P.; Li, L.; Tan, C. Y. J.; Cheng, X.; Chen, G. Y. J.; Sze, S. K.; Shen, H.-M.; Yao, S. Q. Design and Synthesis of Minimalist Terminal Alkyne-Containing Diazirine Photo-Crosslinkers and Their Incorporation into Kinase Inhibitors for Cell- and Tissue-Based Proteome Profiling. *Angewandte Chemie International Edition* **2013**, *52* (33), 8551-8556.
(245) Chang, C.-F.; Mfuh, A.; Gao, J.; Wu, H.-Y.; Woo, C. M. Synthesis of an electronically-tuned minimally interfering alkynyl photo-affinity label to measure small molecule–protein interactions. *Tetrahedron* **2018**, *74* (26), 3273-3277.
(246) West, A. V.; Amako, Y.; Woo, C. M. Design and Evaluation of a Cyclobutane Diazirine Alkyne Tag for Photoaffinity Labeling in Cells. *Journal of the American Chemical Society* **2022**, *144* (46), 21174-21183.
(247) Dubinsky, L.; Krom, B. P.; Meijler, M. M. Diazirine based photoaffinity labeling. *Bioorganic & Medicinal Chemistry* **2012**, *20* (2), 554-570.
(248) Smith, R. A. G.; Knowles, J. R. Aryldiazirines. Potential reagents for photolabeling of biological receptor sites. *Journal of the American Chemical Society* **1973**, *95* (15), 5072-5073.
(249) Das, J. Aliphatic Diazirines as Photoaffinity Probes for Proteins: Recent Developments. *Chemical Reviews* **2011**, *111* (8), 4405-4417.
(250) Wright, M. H.; Sieber, S. A. Chemical proteomics approaches for identifying the cellular targets of natural products. *Natural Product Reports* **2016**, *33* (5), 681-708.
(251) Hashimoto, M.; Hatanaka, Y. Recent Progress in Diazirine-Based Photoaffinity Labeling. *European Journal of Organic Chemistry* **2008**, *2008* (15), 2513-2523.
(252) Conway, L. P.; Jadhav, A. M.; Homan, R. A.; Li, W.; Rubiano, J. S.; Hawkins, R.; Lawrence, R. M.; Parker, C. G. Evaluation of fully-functionalized diazirine tags for chemical proteomic applications. *Chemical Science* **2021**, *12* (22), 7839-7847.
(253) Shi, H.; Cheng, X.; Sze, S. K.; Yao, S. Q. Proteome profiling reveals potential cellular targets of staurosporine using a clickable cell-permeable probe. *Chemical Communications* **2011**, *47* (40), 11306-11308.
(254) Su, Y.; Pan, S.; Li, Z.; Li, L.; Wu, X.; Hao, P.; Sze, S. K.; Yao, S. Q. Multiplex Imaging and Cellular Target Identification of Kinase Inhibitors *via* an Affinity-Based Proteome Profiling Approach. *Scientific Reports* **2015**, *5* (1), 7724.
(255) Pan, S.; Jang, S.-Y.; Wang, D.; Liew, S. S.; Li, Z.; Lee, J.-S.; Yao, S. Q. A Suite of "Minimalist" Photo-Crosslinkers for Live-Cell Imaging and Chemical Proteomics: Case Study with BRD4 Inhibitors. *Angewandte Chemie International Edition* **2017**, *56* (39), 11816-11821.
(256) Parker, C. G.; Galmozzi, A.; Wang, Y.; Correia, B. E.; Sasaki, K.; Joslyn, C. M.; Kim, A. S.; Cavallaro, C. L.; Lawrence, R. M.; Johnson, S. R.*; et al.* Ligand and Target Discovery by Fragment-Based Screening in Human Cells. *Cell* **2017**, *168* (3), 527-541.e529.
(257) Gao, J.; Mfuh, A.; Amako, Y.; Woo, C. M. Small Molecule Interactome Mapping by Photoaffinity Labeling Reveals Binding Site Hotspots for the NSAIDs. *Journal of the American Chemical Society* **2018**, *140* (12), 4259-4268.
(258) Ngo, J. T.; Adams, S. R.; Deerinck, T. J.; Boassa, D.; Rodriguez-Rivera, F.; Palida, S. F.; Bertozzi, C. R.; Ellisman, M. H.; Tsien, R. Y. Click-EM for imaging metabolically tagged nonprotein biomolecules. *Nature chemical biology* **2016**, *12* (6), 459-465.

(259) Jao, C. Y.; Roth, M.; Welti, R.; Salic, A. Metabolic labeling and direct imaging of choline phospholipids *in vivo*. *Proceedings of the National Academy of Sciences* **2009**, *106* (36), 15332-15337.
(260) Kaur, G.; Rajput, B. Comparative Analysis of the Omics Technologies Used to Study Antimonial, Amphotericin B, and Pentamidine Resistance in *Leishmania*. *Journal of Parasitology Research* **2014**, *2014* (1), 726328.
(261) Fairlamb, A. H.; Wyllie, S. The critical role of mode of action studies in kinetoplastid drug discovery. *Frontiers in Drug Discovery* **2023**, *3*.
(262) Jones, D. C.; Foth, B. J.; Urbaniak, M. D.; Patterson, S.; Ong, H. B.; Berriman, M.; Fairlamb, A. H. Genomic and Proteomic Studies on the Mode of Action of Oxaboroles against the African Trypanosome. *PLOS Neglected Tropical Diseases* **2015**, *9* (12), e0004299.
(263) Bhattacharya, A.; Bigot, S.; Padmanabhan, P. K.; Mukherjee, A.; Coelho, A.; Leprohon, P.; Papadopoulou, B.; Ouellette, M. New insights in the mode of action of anti-leishmanial drugs by using chemical mutagenesis screens coupled to next-generation sequencing. *Microbial cell (Graz, Austria)* **2020**, *7* (2), 59-61.
(264) Corpas-Lopez, V.; Wyllie, S. Utilizing thermal proteome profiling to identify the molecular targets of anti-leishmanial compounds. *STAR Protocols* **2021**, *2* (3), 100704.
(265) Creek, D. J.; Barrett, M. P. Determination of antiprotozoal drug mechanisms by metabolomics approaches. *Parasitology* **2014**, *141* (1), 83-92.
(266) Vincent, I. M.; Barrett, M. P. Metabolomic-Based Strategies for Anti-Parasite Drug Discovery. *Journal of Biomolecular Screening* **2014**, *20* (1), 44-55.
(267) Bhattacharya, A.; Corbeil, A.; do Monte-Neto, R. L.; Fernandez-Prada, C. Of Drugs and Trypanosomatids: New Tools and Knowledge to Reduce Bottlenecks in Drug Discovery. *Genes* **2020**, *11* (7).
(268) Leprohon, P.; Fernandez-Prada, C.; Gazanion, É.; Monte-Neto, R.; Ouellette, M. Drug resistance analysis by next generation sequencing in *Leishmania*. *International Journal for Parasitology: Drugs and Drug Resistance* **2015**, *5* (1), 26-35.
(269) Beneke, T.; Madden, R.; Makin, L.; Valli, J.; Sunter, J.; Gluenz, E. A CRISPR Cas9 high-throughput genome editing toolkit for kinetoplastids. *Royal Society Open Science* **2017**, *4* (5), 170095.
(270) Jones, N. G.; Catta-Preta, C. M. C.; Lima, A. P. C. A.; Mottram, J. C. Genetically Validated Drug Targets in *Leishmania*: Current Knowledge and Future Prospects. *ACS Infectious Diseases* **2018**, *4* (4), 467-477.
(271) Cohen, A.; Azas, N. Challenges and Tools for *In Vitro Leishmania* Exploratory Screening in the Drug Development Process: An Updated Review. In *Pathogens*, 2021; Vol. 10.
(272) Duncan, S. M.; Jones, N. G.; Mottram, J. C. Recent advances in *Leishmania* reverse genetics: Manipulating a manipulative parasite. *Molecular and Biochemical Parasitology* **2017**, *216*, 30-38.
(273) Minet, C.; Thévenon, S.; Chantal, I.; Solano, P.; Berthier, D. Mini-review on CRISPR-Cas9 and its potential applications to help controlling neglected tropical diseases caused by Trypanosomatidae. *Infection, Genetics and Evolution* **2018**, *63*, 326-331.
(274) Yasur-Landau, D.; Jaffe, C. L.; David, L.; Doron-Faigenboim, A.; Baneth, G. Resistance of *Leishmania infantum* to allopurinol is associated with chromosome and gene copy number variations including decrease in the S-adenosylmethionine synthetase (METK) gene copy number. *International Journal for Parasitology: Drugs and Drug Resistance* **2018**, *8* (3), 403-410.
(275) Alpizar-Sosa, E. A.; Ithnin, N. R. B.; Wei, W.; Pountain, A. W.; Weidt, S. K.; Donachie, A. M.; Ritchie, R.; Dickie, E. A.; Burchmore, R. J. S.; Denny, P. W.*; et al.* Amphotericin B resistance in *Leishmania mexicana*: Alterations to sterol metabolism and oxidative stress response. *PLOS Neglected Tropical Diseases* **2022**, *16* (9), e0010779.
(276) Paradela, L. S.; Wall, R. J.; Carvalho, S.; Chemi, G.; Corpas-Lopez, V.; Moynihan, E.; Bello, D.; Patterson, S.; Güther, M. L. S.; Fairlamb, A. H.*; et al.* Multiple unbiased approaches identify

oxidosqualene cyclase as the molecular target of a promising anti-leishmanial. *Cell Chemical Biology* **2021**, *28* (5), 711-721.e718.
(277) Rosa-Teijeiro, C.; Wagner, V.; Corbeil, A.; d'Annessa, I.; Leprohon, P.; do Monte-Neto, R. L.; Fernandez-Prada, C. Three different mutations in the DNA topoisomerase 1B in *Leishmania infantum* contribute to resistance to antitumor drug topotecan. *Parasites & Vectors* **2021**, *14* (1), 438.
(278) Hefnawy, A.; Negreira, G.; Jara, M.; Cotton James, A.; Maes, I.; D'Haenens, E.; Imamura, H.; Cuypers, B.; Monsieurs, P.; Mouchtoglou, C.*; et al.* Genomic and Phenotypic Characterization of Experimentally Selected Resistant *Leishmania donovani* Reveals a Role for Dynamin-1-Like Protein in the Mechanism of Resistance to a Novel Antileishmanial Compound. *mBio* **2022**, *13* (1), e03264-03221.
(279) Robins, W. P.; Faruque, S. M.; Mekalanos, J. J. Coupling mutagenesis and parallel deep sequencing to probe essential residues in a genome or gene. *Proceedings of the National Academy of Sciences* **2013**, *110* (9), E848-E857.
(280) Bhattacharya, A.; Leprohon, P.; Bigot, S.; Padmanabhan, P. K.; Mukherjee, A.; Roy, G.; Gingras, H.; Mestdagh, A.; Papadopoulou, B.; Ouellette, M. Coupling chemical mutagenesis to next generation sequencing for the identification of drug resistance mutations in *Leishmania*. *Nature Communications* **2019**, *10* (1), 5627.
(281) Laffitte, M.-C. N.; Leprohon, P.; Papadopoulou, B.; Ouellette, M. Plasticity of the *Leishmania* genome leading to gene copy number variations and drug resistance. *F1000Research* **2016**, *5*, 2350.
(282) Begolo, D.; Erben, E.; Clayton, C. Drug Target Identification Using a Trypanosome Overexpression Library. *Antimicrobial Agents and Chemotherapy* **2014**, *58* (10), 6260-6264.
(283) Gazanion, É.; Fernández-Prada, C.; Papadopoulou, B.; Leprohon, P.; Ouellette, M. Cos-Seq for high-throughput identification of drug target and resistance mechanisms in the protozoan parasite *Leishmania*. *Proceedings of the National Academy of Sciences* **2016**, *113* (21), E3012-E3021.
(284) Corpas-Lopez, V.; Moniz, S.; Thomas, M.; Wall, R. J.; Torrie, L. S.; Zander-Dinse, D.; Tinti, M.; Brand, S.; Stojanovski, L.; Manthri, S.*; et al.* Pharmacological Validation of *N*-Myristoyltransferase as a Drug Target in *Leishmania donovani*. *ACS Infectious Diseases* **2019**, *5* (1), 111-122.
(285) Wall, R. J.; Rico, E.; Lukac, I.; Zuccotto, F.; Elg, S.; Gilbert, I. H.; Freund, Y.; Alley, M. R. K.; Field, M. C.; Wyllie, S.*; et al.* Clinical and veterinary trypanocidal benzoxaboroles target CPSF3. *Proceedings of the National Academy of Sciences* **2018**, *115* (38), 9616-9621.
(286) Fairlamb, A. H. Genomics decodes drug action. *Nature* **2012**, *482* (7384), 167-169.
(287) Wang, Z.; Morris, J. C.; Drew, M. E.; Englund, P. T. Inhibition of *Trypanosoma brucei* Gene Expression by RNA Interference Using an Integratable Vector with Opposing T7 Promoters. *Journal of Biological Chemistry* **2000**, *275* (51), 40174-40179.
(288) Shi, H.; Djikeng, A.; Mark, T.; Wirtz, E.; Tschudi, C.; Ullu, E. Genetic interference in *Trypanosoma brucei* by heritable and inducible double-stranded RNA. *RNA* **2000**, *6* (7), 1069-1076.
(289) Motyka, S. A.; Englund, P. T. RNA interference for analysis of gene function in trypanosomatids. *Current Opinion in Microbiology* **2004**, *7* (4), 362-368.
(290) Alsford, S.; Turner, D. J.; Obado, S. O.; Sanchez-Flores, A.; Glover, L.; Berriman, M.; Hertz-Fowler, C.; Horn, D. High-throughput phenotyping using parallel sequencing of RNA interference targets in the African trypanosome. *Genome research* **2011**, *21* (6), 915-924.
(291) Alsford, S.; Eckert, S.; Baker, N.; Glover, L.; Sanchez-Flores, A.; Leung, K. F.; Turner, D. J.; Field, M. C.; Berriman, M.; Horn, D. High-throughput decoding of antitrypanosomal drug efficacy and resistance. *Nature* **2012**, *482* (7384), 232-236.
(292) Patino, L. H.; Ramírez, J. D. RNA-seq in kinetoplastids: A powerful tool for the understanding of the biology and host-pathogen interactions. *Infection, Genetics and Evolution* **2017**, *49*, 273-282.
(293) Cruz, A. K.; Freitas-Castro, F. Genome and transcriptome analyses of *Leishmania* spp.: opening Pandora's box. *Current Opinion in Microbiology* **2019**, *52*, 64-69.
(294) Mosquillo, M. F.; Smircich, P.; Lima, A.; Gehrke, S. A.; Scalese, G.; Machado, I.; Gambino, D.; Garat, B.; Pérez-Díaz, L. High Throughput Approaches to Unravel the Mechanism of Action of a New

Vanadium-Based Compound against *Trypanosoma cruzi*. *Bioinorganic Chemistry and Applications* **2020**, *2020* (1), 1634270.
(295) Do Monte-Neto, R. L.; Coelho, A. C.; Raymond, F.; Légaré, D.; Corbeil, J.; Melo, M. N.; Frézard, F.; Ouellette, M. Gene Expression Profiling and Molecular Characterization of Antimony Resistance in *Leishmania amazonensis*. *PLOS Neglected Tropical Diseases* **2011**, *5* (5), e1167.
(296) Vacchina, P.; Norris-Mullins, B.; Abengózar, M. A.; Viamontes, C. G.; Sarro, J.; Stephens, M. T.; Pfrender, M. E.; Rivas, L.; Morales, M. A. Genomic Appraisal of the Multifactorial Basis for *In Vitro* Acquisition of Miltefosine Resistance in *Leishmania donovani*. *Antimicrobial Agents and Chemotherapy* **2016**, *60* (7), 4089-4100.
(297) Rastrojo, A.; García-Hernández, R.; Vargas, P.; Camacho, E.; Corvo, L.; Imamura, H.; Dujardin, J.-C.; Castanys, S.; Aguado, B.; Gamarro, F.*; et al.* Genomic and transcriptomic alterations in *Leishmania donovani* lines experimentally resistant to antileishmanial drugs. *International Journal for Parasitology: Drugs and Drug Resistance* **2018**, *8* (2), 246-264.
(298) Wang, Z.; Gerstein, M.; Snyder, M. RNA-Seq: a revolutionary tool for transcriptomics. *Nature Reviews Genetics* **2009**, *10* (1), 57-63.
(299) Salloum, T.; Tokajian, S.; Hirt, R. P. Advances in Understanding *Leishmania* Pathobiology: What Does RNA-Seq Tell Us? *Frontiers in Cell and Developmental Biology* **2021**, *9*.
(300) Ziegler, S.; Pries, V.; Hedberg, C.; Waldmann, H. Target Identification for Small Bioactive Molecules: Finding the Needle in the Haystack. *Angewandte Chemie International Edition* **2013**, *52* (10), 2744-2792.
(301) Meissner, F.; Geddes-McAlister, J.; Mann, M.; Bantscheff, M. The emerging role of mass spectrometry-based proteomics in drug discovery. *Nature Reviews Drug Discovery* **2022**, *21* (9), 637-654.
(302) Sato, S.-i.; Murata, A.; Shirakawa, T.; Uesugi, M. Biochemical Target Isolation for Novices: Affinity-Based Strategies. *Chemistry & Biology* **2010**, *17* (6), 616-623.
(303) Rix, U.; Superti-Furga, G. Target profiling of small molecules by chemical proteomics. *Nature chemical biology* **2009**, *5* (9), 616-624.
(304) Smith, A.; Wall, R. J.; Patterson, S.; Rowan, T.; Rico Vidal, E.; Stojanovski, L.; Huggett, M.; Hampton, S. E.; Thomas, M. G.; Corpas Lopez, V.*; et al.* Repositioning of a Diaminothiazole Series Confirmed to Target the Cyclin-Dependent Kinase CRK12 for Use in the Treatment of African Animal Trypanosomiasis. *Journal of Medicinal Chemistry* **2022**.
(305) Shanmugasundram, A.; Starns, D.; Böhme, U.; Amos, B.; Wilkinson, P. A.; Harb, O. S.; Warrenfeltz, S.; Kissinger, J. C.; McDowell, M. A.; Roos, D. S.*; et al.* TriTrypDB: An integrated functional genomics resource for kinetoplastida. *PLOS Neglected Tropical Diseases* **2023**, *17* (1), e0011058.
(306) Sanchiz, Á.; Morato, E.; Rastrojo, A.; Camacho, E.; González-de la Fuente, S.; Marina, A.; Aguado, B.; Requena, J. M. The Experimental Proteome of *Leishmania infantum* Promastigote and Its Usefulness for Improving Gene Annotations. In *Genes*, 2020; Vol. 11, p 1036.
(307) Pawar, H.; Kulkarni, A.; Dixit, T.; Chaphekar, D.; Patole, M. S. A bioinformatics approach to reanalyze the genome annotation of kinetoplastid protozoan parasite *Leishmania donovani*. *Genomics* **2014**, *104* (6, Part B), 554-561.
(308) Newman, D. J.; Cragg, G. M. Natural Products as Sources of New Drugs over the Nearly Four Decades from 01/1981 to 09/2019. *Journal of Natural Products* **2020**.
(309) Fernández-Álvaro, E.; Hong, W. D.; Nixon, G. L.; O'Neill, P. M.; Calderón, F. Antimalarial Chemotherapy: Natural Product Inspired Development of Preclinical and Clinical Candidates with Diverse Mechanisms of Action. *Journal of Medicinal Chemistry* **2016**, *59* (12), 5587-5603.
(310) Ungogo, M. A.; Ebiloma, G. U.; Ichoron, N.; Igoli, J. O.; de Koning, H. P.; Balogun, E. O. A Review of the Antimalarial, Antitrypanosomal, and Antileishmanial Activities of Natural Compounds Isolated From Nigerian Flora. *Frontiers in Chemistry* **2020**, *8*, Review.

(311) Cortes, S.; Bruno de Sousa, C.; Morais, T.; Lago, J.; Campino, L. Potential of the natural products against leishmaniasis in Old World - a review of *in-vitro* studies. *Pathogens and global health* **2020**, *114* (4), 170-182.
(312) Nweze, J. A.; Mbaoji, F. N.; Li, Y.-M.; Yang, L.-Y.; Huang, S.-S.; Chigor, V. N.; Eze, E. A.; Pan, L.-X.; Zhang, T.; Yang, D.-F. Potentials of marine natural products against malaria, leishmaniasis, and trypanosomiasis parasites: a review of recent articles. *Infectious Diseases of Poverty* **2021**, *10* (1), 9.
(313) Costa-Silva, T. A. d.; Grecco, S. S.; de Sousa, F. S.; Lago, J. H. G.; Martins, E. G. A.; Terrazas, C. A.; Varikuti, S.; Owens, K. L.; Beverley, S. M.; Satoskar, A. R.*; et al.* Immunomodulatory and Antileishmanial Activity of Phenylpropanoid Dimers Isolated from *Nectandra leucantha*. *Journal of Natural Products* **2015**, *78* (4), 653-657.
(314) Grecco, S. S.; Costa-Silva, T. A.; Jerz, G.; de Sousa, F. S.; Alves Conserva, G. A.; Mesquita, J. T.; Galuppo, M. K.; Tempone, A. G.; Neves, B. J.; Andrade, C. H.*; et al.* Antitrypanosomal activity and evaluation of the mechanism of action of dehydrodieugenol isolated from *Nectandra leucantha* (Lauraceae) and its methylated derivative against *Trypanosoma cruzi*. *Phytomedicine* **2017**, *24*, 62-67.
(315) Grecco, S. S.; Costa-Silva, T. A.; Jerz, G.; de Sousa, F. S.; Londero, V. S.; Galuppo, M. K.; Lima, M. L.; Neves, B. J.; Andrade, C. H.; Tempone, A. G.*; et al.* Neolignans from leaves of *Nectandra leucantha* (Lauraceae) display *in vitro* antitrypanosomal activity *via* plasma membrane and mitochondrial damages. *Chemico-Biological Interactions* **2017**, *277*, 55-61.
(316) Grecco, S. S.; Costa-Silva, T. A.; Sousa, F. S.; Cargnelutti, S. B.; Umehara, E.; Mendonça, P. S.; Tempone, A. G.; Lago, J. H. G. Neolignans isolated from twigs of *Nectandra leucantha* Ness & Mart (Lauraceae) displayed *in vitro* antileishmanial activity. *Journal of Venomous Animals and Toxins including Tropical Diseases* **2018**, *24* (1), 27.
(317) Ferreira, D. D.; Sousa, F. S.; Costa-Silva, T. A.; Reimão, J. Q.; Torrecilhas, A. C.; Johns, D. M.; Sear, C. E.; Honorio, K. M.; Lago, J. H. G.; Anderson, E. A.*; et al.* Dehydrodieugenol B derivatives as antiparasitic agents: Synthesis and biological activity against *Trypanosoma cruzi*. *European Journal of Medicinal Chemistry* **2019**, *176*, 162-174.
(318) Sear, C. E.; Pieper, P.; Amaral, M.; Romanelli, M. M.; Costa-Silva, T. A.; Haugland, M. M.; Tate, J. A.; Lago, J. H. G.; Tempone, A. G.; Anderson, E. A. Synthesis and Structure–Activity Relationship of Dehydrodieugenol B Neolignans against *Trypanosoma cruzi*. *ACS Infectious Diseases* **2020**, *6* (11), 2872-2878.
(319) Amaral, M.; de Sousa, F. S.; Silva, T. A. C.; Junior, A. J. G.; Taniwaki, N. N.; Johns, D. M.; Lago, J. H. G.; Anderson, E. A.; Tempone, A. G. A semi-synthetic neolignan derivative from dihydrodieugenol B selectively affects the bioenergetic system of *Leishmania infantum* and inhibits cell division. *Scientific Reports* **2019**, *9* (1), 6114.
(320) Amaral, M.; Romanelli, M. M.; Asiki, H.; Bicker, J.; Lage, D. P.; Freitas, C. S.; Taniwaki, N. N.; Lago, J. H. G.; Coelho, E. A. F.; Falcão, A.*; et al.* Synthesis of a dehydrodieugenol B derivative as a lead compound for visceral leishmaniasis—mechanism of action and *in vivo* pharmacokinetic studies. *Antimicrobial Agents and Chemotherapy* **2024**, *68* (11), e00831-00824.
(321) Sharma, V.; Sharma, P. C.; Kumar, V. A mini review on pyridoacridines: Prospective lead compounds in medicinal chemistry. *Journal of Advanced Research* **2015**, *6* (1), 63-71.
(322) Dassonneville, L.; Wattez, N.; Baldeyrou, B.; Mahieu, C.; Lansiaux, A.; Banaigs, B.; Bonnard, I.; Bailly, C. Inhibition of topoisomerase II by the marine alkaloid ascididemin and induction of apoptosis in leukemia cells. *Biochemical Pharmacology* **2000**, *60* (4), 527-537.
(323) Kobayash, J. i.; Cheng, J.-f.; Nakamura, H.; Ohizumi, Y.; Hirata, Y.; Sasaki, T.; Ohta, T.; Nozoe, S. Ascididemin, a novel pentacyclic aromatic alkaloid with potent antileukemic activity from the okinawan tunicate *didemnum* sp. *Tetrahedron Letters* **1988**, *29* (10), 1177-1180.
(324) Lindsay, B. S.; Christiansen, H. C.; Copp, B. R. Structural Studies of Cytotoxic Marine Alkaloids: Synthesis of Novel Ring-E Analogues of Ascididemin and their *in vitro* and *in vivo* Biological Evaluation. *Tetrahedron* **2000**, *56* (3), 497-505.

(325) Feng, Y.; Davis, R. A.; Sykes, M. L.; Avery, V. M.; Carroll, A. R.; Camp, D.; Quinn, R. J. Antitrypanosomal pyridoacridine alkaloids from the Australian ascidian *Polysyncraton echinatum*. *Tetrahedron Letters* **2010**, *51* (18), 2477-2479.
(326) Copp, B. R.; Kayser, O.; Brun, R.; Kiderlen, A. F. Antiparasitic activity of marine pyridoacridone alkaloids related to the asciddemins. *Planta Medica* **2003**, *69* (6), 527-531.
(327) Weber, C.; Opatz, T. Chapter One - Bisbenzylisoquinoline Alkaloids. In *The Alkaloids: Chemistry and Biology*, Knölker, H.-J. Ed.; Vol. 81; Academic Press, 2019; pp 1-114.
(328) Otshudi, A. L.; Apers, S.; Pieters, L.; Claeys, M.; Pannecouque, C.; De Clercq, E.; Van Zeebroeck, A.; Lauwers, S.; Frédérich, M.; Foriers, A. Biologically active bisbenzylisoquinoline alkaloids from the root bark of *Epinetrum villosum*. *Journal of Ethnopharmacology* **2005**, *102* (1), 89-94.
(329) Lv, J.-J.; Xu, M.; Wang, D.; Zhu, H.-T.; Yang, C.-R.; Wang, Y.-F.; Li, Y.; Zhang, Y.-J. Cytotoxic Bisbenzylisoquinoline Alkaloids from *Stephania epigaea*. *Journal of Natural Products* **2013**, *76* (5), 926-932.
(330) Kumar, A.; Chowdhury, S. R.; Sarkar, T.; Chakrabarti, T.; Majumder, H. K.; Jha, T.; Mukhopadhyay, S. A new bisbenzylisoquinoline alkaloid isolated from *Thalictrum foliolosum*, as a potent inhibitor of DNA topoisomerase IB of *Leishmania donovani*. *Fitoterapia* **2016**, *109*, 25-30.
(331) Camacho, M. d. R.; Phillipson, J. D.; Croft, S. L.; Rock, P.; Marshall, S. J.; Schiff Jr, P. L. *In vitro* activity of *Triclisia patens* and some bisbenzylisoquinoline alkaloids against *Leishmania donovani* and *Trypanosoma brucei brucei*. *Phytotherapy Research* **2002**, *16* (5), 432-436.
(332) Naman, C. B.; Gupta, G.; Varikuti, S.; Chai, H.; Doskotch, R. W.; Satoskar, A. R.; Kinghorn, A. D. Northalrugosidine Is a Bisbenzyltetrahydroisoquinoline Alkaloid from *Thalictrum alpinum* with *in Vivo* Antileishmanial Activity. *Journal of Natural Products* **2015**, *78* (3), 552-556.
(333) Fournet, A.; Muñoz, V.; Manjon, A. M.; Angelo, A.; Hocquemiller, R.; Cortes, D.; Cave, A.; Bruneton, J. Activité antiparasitaire d'alcaloïdes bisbenzylisoquinoleiques. I: activité *in vitro* sur des promastigotes de trois souches de *Leishmania*. *Journal of Ethnopharmacology* **1988**, *24* (2), 327-335.
(334) Fournet, A.; Manjon, A. M.; Muñoz, V.; Angelo, A.; Bruneton, J.; Hocquemiller, R.; Cortes, D.; Cavé, A. Activité antiparasitaire d'alcaloïdes bisbenzylisoquinoléiques. II: Activité *in vitro* sur des epimastigotes de trois souches typifiees de *Trypanosoma cruzi*. *Journal of Ethnopharmacology* **1988**, *24* (2), 337-343.
(335) Sozanschi, A.; Asiki, H.; Amaral, M.; de Castro Levatti, E. V.; Tempone, A. G.; Wheeler, R. J.; Anderson, E. A. Synthesis and Evaluation of (Bis)benzyltetrahydroisoquinoline Alkaloids as Antiparasitic Agents. *JACS Au* **2024**, *4* (2), 847-854.
(336) Scientists praised for pulling plug on a drug. WCAIR: Wellcome centre anti-infectives research - news, 2018.
(337) Amaral, M.; Asiki, H.; Sear, C. E.; Singh, S.; Pieper, P.; Haugland, M. M.; Anderson, E. A.; Tempone, A. G. Biological activity and structure–activity relationship of dehydrodieugenol B analogues against visceral leishmaniasis. *RSC Medicinal Chemistry* **2023**, *14* (7), 1344-1350.
(338) Süleymanoğlu, N.; Ustabaş, R.; Direkel, Ş.; Alpaslan, Y. B.; Ünver, Y. 1,2,4-triazole derivatives with morpholine; DFT study and antileishmanial activity. *Canadian Journal of Physics* **2017**, *96* (7), 719-723.
(339) Khan, K. M.; Khan, M. Z.; Taha, M.; Maharvi, G. M.; Saify, Z. S.; Parveen, S.; Choudhary, M. I. Leishmanicidal potential of N-substituted morpholine derivatives: Synthesis and structure–activity relationships. *Natural Product Research* **2009**, *23* (5), 479-484.
(340) Kumari, A.; Singh, R. K. Morpholine as ubiquitous pharmacophore in medicinal chemistry: Deep insight into the structure-activity relationship (SAR). *Bioorganic Chemistry* **2020**, *96*, 103578.
(341) Selassie, C. D.; Kapur, S.; Verma, R. P.; Rosario, M. Cellular Apoptosis and Cytotoxicity of Phenolic Compounds: A Quantitative Structure−Activity Relationship Study. *Journal of Medicinal Chemistry* **2005**, *48* (23), 7234-7242.

(342) Xiong, G.; Wu, Z.; Yi, J.; Fu, L.; Yang, Z.; Hsieh, C.; Yin, M.; Zeng, X.; Wu, C.; Lu, A.*; et al.* ADMETlab 2.0: an integrated online platform for accurate and comprehensive predictions of ADMET properties. *Nucleic Acids Research* **2021**, *49* (W1), W5-W14.
(343) Dulsat, J.; López-Nieto, B.; Estrada-Tejedor, R.; Borrell, J. I. Evaluation of Free Online ADMET Tools for Academic or Small Biotech Environments. *Molecules (Basel, Switzerland)* **2023**, *28* (2), 776.
(344) Lipinski, C. A.; Lombardo, F.; Dominy, B. W.; Feeney, P. J. Experimental and computational approaches to estimate solubility and permeability in drug discovery and development settings. *Advanced Drug Delivery Reviews* **1997**, *23* (1), 3-25.
(345) Zheng, W. Neurotoxicology of the Brain Barrier System: New Implications. *Journal of Toxicology: Clinical Toxicology* **2001**, *39* (7), 711-719.
(346) Kirchmair, J.; Göller, A. H.; Lang, D.; Kunze, J.; Testa, B.; Wilson, I. D.; Glen, R. C.; Schneider, G. Predicting drug metabolism: experiment and/or computation? *Nature Reviews Drug Discovery* **2015**, *14* (6), 387-404.
(347) Garrido, A.; Lepailleur, A.; Mignani, S. M.; Dallemagne, P.; Rochais, C. hERG toxicity assessment: Useful guidelines for drug design. *European Journal of Medicinal Chemistry* **2020**, *195*, 112290.
(348) Recanatini, M.; Poluzzi, E.; Masetti, M.; Cavalli, A.; De Ponti, F. QT prolongation through hERG K+ channel blockade: Current knowledge and strategies for the early prediction during drug development. *Medicinal Research Reviews* **2005**, *25* (2), 133-166.
(349) Katsuno, K.; Burrows, J. N.; Duncan, K.; Van Huijsduijnen, R. H.; Kaneko, T.; Kita, K.; Mowbray, C. E.; Schmatz, D.; Warner, P.; Slingsby, B. T. Hit and lead criteria in drug discovery for infectious diseases of the developing world. *Nature Reviews Drug Discovery* **2015**, *14* (11), 751-758.
(350) Don, R. O. B.; Ioset, J.-R. Screening strategies to identify new chemical diversity for drug development to treat kinetoplastid infections. *Parasitology* **2014**, *141* (1), 140-146.
(351) O'Brien, J.; Wilson, I.; Orton, T.; Pognan, F. Investigation of the Alamar Blue (resazurin) fluorescent dye for the assessment of mammalian cell cytotoxicity. *European Journal of Biochemistry* **2000**, *267* (17), 5421-5426.
(352) Räz, B.; Iten, M.; Grether-Bühler, Y.; Kaminsky, R.; Brun, R. The Alamar Blue® assay to determine drug sensitivity of African trypanosomes (*T.b. rhodesiense* and *T.b. gambiense*) *in vitro*. *Acta Tropica* **1997**, *68* (2), 139-147.
(353) Jones, D. C.; Hallyburton, I.; Stojanovski, L.; Read, K. D.; Frearson, J. A.; Fairlamb, A. H. Identification of a κ-opioid agonist as a potent and selective lead for drug development against human African trypanosomiasis. *Biochemical Pharmacology* **2010**, *80* (10), 1478-1486.
(354) Zangger, H.; Mottram, J. C.; Fasel, N. Cell death in *Leishmania* induced by stress and differentiation: programmed cell death or necrosis? *Cell Death & Differentiation* **2002**, *9* (10), 1126-1139.
(355) Moreira, M. E. C.; Del Portillo, H. A.; Milder, R. V.; Balanco, J. M. F.; Barcinski, M. A. Heat shock induction of apoptosis in promastigotes of the unicellular organism *Leishmania* (*Leishmania*) *amazonensis*. *Journal of Cellular Physiology* **1996**, *167* (2), 305-313.
(356) Ambit, A.; Woods, K. L.; Cull, B.; Coombs, G. H.; Mottram, J. C. Morphological Events during the Cell Cycle of *Leishmania major*. *Eukaryotic Cell* **2011**, *10* (11), 1429-1438.
(357) Mukherjee, A.; Sasikala, W. D. Chapter One - Drug–DNA Intercalation: From Discovery to the Molecular Mechanism. In *Advances in Protein Chemistry and Structural Biology*, Karabencheva-Christova, T. Ed.; Vol. 92; Academic Press, 2013; pp 1-62.
(358) Inoue, N.; Terabayashi, T.; Takiguchi-Kawashima, Y.; Fujinami, D.; Matsuoka, S.; Kawano, M.; Tanaka, K.; Tsumura, H.; Ishizaki, T.; Narahara, H.*; et al.* The benzylisoquinoline alkaloids, berberine and coptisine, act against camptothecin-resistant topoisomerase I mutants. *Scientific Reports* **2021**, *11* (1), 7718.
(359) Matsumoto, S. S.; Biggs, J.; Copp, B. R.; Holden, J. A.; Barrows, L. R. Mechanism of Ascididemin-Induced Cytotoxicity. *Chemical Research in Toxicology* **2003**, *16* (2), 113-122.

(360) Bennett, C. B.; Westmoreland, T. J.; Snipe, J. R.; Resnick, M. A. A Double-Strand Break within a Yeast Artificial Chromosome (YAC) Containing Human DNA Can Result in YAC Loss, Deletion, or Cell Lethality. *Molecular and Cellular Biology* **1996**, *16* (8), 4414-4425.
(361) Cannan, W. J.; Pederson, D. S. Mechanisms and Consequences of Double-Strand DNA Break Formation in Chromatin. *Journal of Cellular Physiology* **2016**, *231* (1), 3-14.
(362) da Silva, M. S. DNA Double-Strand Breaks: A Double-Edged Sword for Trypanosomatids. *Frontiers in Cell and Developmental Biology* **2021**, *9*, Review.
(363) Lyles, M. B.; Cameron, I. L. Interactions of the DNA intercalator acridine orange, with itself, with caffeine, and with double stranded DNA. *Biophysical Chemistry* **2002**, *96* (1), 53-76.
(364) Wilhelm, M.; Mukherjee, A.; Bouvier, B.; Zakrzewska, K.; Hynes, J. T.; Lavery, R. Multistep Drug Intercalation: Molecular Dynamics and Free Energy Studies of the Binding of Daunomycin to DNA. *Journal of the American Chemical Society* **2012**, *134* (20), 8588-8596.
(365) McKean, P. G.; Keen, J. K.; Smith, D. F.; Benson, F. E. Identification and characterisation of a RAD51 gene from *Leishmania major*. *Molecular and Biochemical Parasitology* **2001**, *115* (2), 209-216.
(366) Passos-Silva, D. G.; Rajão, M. A.; Nascimento De Aguiar, P. H.; Vieira-Da-Rocha, J. P.; Machado, C. R.; Furtado, C. Overview of DNA repair in *Trypanosoma cruzi, Trypanosoma brucei,* and *Leishmania major*. *Journal of Nucleic Acids* **2010**, *2010*, Review.
(367) Genois, M. M.; Paquet, E. R.; Laffitte, M. C. N.; Maity, R.; Rodrigue, A.; Ouellette, M.; Massona, J. Y. DNA repair pathways in trypanosomatids: From DNA repair to drug resistance. *Microbiology and Molecular Biology Reviews* **2014**, *78* (1), 40-73.
(368) Genois, M.-M.; Plourde, M.; Éthier, C.; Roy, G.; Poirier, G. G.; Ouellette, M.; Masson, J.-Y. Roles of Rad51 paralogs for promoting homologous recombination in *Leishmania infantum*. *Nucleic Acids Research* **2015**, *43* (5), 2701-2715.
(369) Proudfoot, C.; McCulloch, R. Distinct roles for two RAD51-related genes in *Trypanosoma brucei* antigenic variation. *Nucleic Acids Research* **2005**, *33* (21), 6906-6919.
(370) Glover, L.; McCulloch, R.; Horn, D. Sequence homology and microhomology dominate chromosomal double-strand break repair in African trypanosomes. *Nucleic Acids Research* **2008**, *36* (8), 2608-2618.
(371) Moore, C. W. Cleavage of Cellular and Extracellular *Saccharomyces cerevisiae* DNA by Bleomycin and Phleomycin. *Cancer Research* **1989**, *49* (24 Part 1), 6935-6940.
(372) Mondal, S.; Roy, J. J.; Bera, T. Generation of adenosine tri-phosphate in *Leishmania donovani* amastigote forms. *Acta Parasitologica* **2014**, *59* (1), 11-16.
(373) Castro, J.; Bittner, C. X.; Humeres, A.; Montecinos, V. P.; Vera, J. C.; Barros, L. F. A cytosolic source of calcium unveiled by hydrogen peroxide with relevance for epithelial cell death. *Cell Death & Differentiation* **2004**, *11* (4), 468-478.
(374) Benaim, G.; Bermudez, R.; Urbina, J. A. Ca^{2+} transport in isolated mitochondrial vesicles from *Leishmania braziliensis* promastigotes. *Molecular and Biochemical Parasitology* **1990**, *39* (1), 61-68.
(375) Mukherjee, S. B.; Das, M.; Sudhandiran, G.; Shaha, C. Increase in Cytosolic Ca^{2+} Levels through the Activation of Non-selective Cation Channels Induced by Oxidative Stress Causes Mitochondrial Depolarization Leading to Apoptosis-like Death in *Leishmania donovani* Promastigotes. *Journal of Biological Chemistry* **2002**, *277* (27), 24717-24727.
(376) Forman, H. J.; Zhang, H.; Rinna, A. Glutathione: Overview of its protective roles, measurement, and biosynthesis. *Molecular Aspects of Medicine* **2009**, *30* (1), 1-12.
(377) Romão, P. R. T.; Tovar, J.; Fonseca, S. G.; Moraes, R. H.; Cruz, A. K.; Hothersall, J. S.; Noronha-Dutra, A. A.; Ferreira, S. H.; Cunha, F. Q. Glutathione and the redox control system trypanothione/trypanothione reductase are involved in the protection of *Leishmania* spp. against nitrosothiol-induced cytotoxicity. *Brazilian Journal of Medical and Biological Research* **2006**, *39* (3), 355-363.

(378) ThermoFisherScientific. *Technical Resources, Media Formulation - 31100 - Medium 199, powder*. https://www.thermofisher.com/uk/en/home/technical-resources/media-formulation.90.html (accessed 2024).
(379) Elmore, S. Apoptosis: A Review of Programmed Cell Death. *Toxicologic Pathology* **2007**, *35* (4), 495-516.
(380) Ploubidou, A.; Robinson, D. R.; Docherty, R. C.; Ogbadoyi, E. O.; Gull, K. Evidence for novel cell cycle checkpoints in trypanosomes: kinetoplast segregation and cytokinesis in the absence of mitosis. *Journal of Cell Science* **1999**, *112* (24), 4641-4650.
(381) McDonald, L. A.; Eldredge, G. S.; Barrows, L. R.; Ireland, C. M. Inhibition of Topoisomerase II Catalytic Activity by Pyridoacridine Alkaloids from a *Cystodytes* sp. Ascidian: A Mechanism for the Apparent Intercalator-Induced Inhibition of Topoisomerase II. *Journal of Medicinal Chemistry* **1994**, *37* (22), 3819-3827.
(382) McConville, M. J.; Naderer, T. Metabolic pathways required for the intracellular survival of *Leishmania*. *Annual review of microbiology* **2011**, *65*, 543-561.
(383) Hart, D. T.; Coombs, G. H. *Leishmania mexicana*: Energy metabolism of amastigotes and promastigotes. *Experimental Parasitology* **1982**, *54* (3), 397-409.
(384) Nolan, D. P.; Voorheis, H. P. The mitochondrion in bloodstream forms of *Trypanosoma brucei* is energized by the electrogenic pumping of protons catalysed by the F_1F_0-ATPase. *European Journal of Biochemistry* **1992**, *209* (1), 207-216.
(385) Schnaufer, A.; Clark-Walker, G. D.; Steinberg, A. G.; Stuart, K. The F_1-ATP synthase complex in bloodstream stage trypanosomes has an unusual and essential function. *The EMBO Journal* **2005**, *24* (23), 4029-4040.
(386) Gahura, O.; Hierro-Yap, C.; Zíková, A. Redesigned and reversed: architectural and functional oddities of the trypanosomal ATP synthase. *Parasitology* **2021**, *148* (10), 1151-1160.
(387) Nicholls, D. G. The Non-Ohmic Proton Leak—25 Years On. *Bioscience Reports* **1997**, *17* (3), 251-257.
(388) Brookes, P. S. Mitochondrial H^+ leak and ROS generation: An odd couple. *Free Radical Biology and Medicine* **2005**, *38* (1), 12-23.
(389) Skulachev, V. P. Role of uncoupled and non-coupled oxidations in maintenance of safely low levels of oxygen and its one-electron reductants. *Quarterly Reviews of Biophysics* **1996**, *29* (2), 169-202.
(390) Bonnard, I.; Bontemps, N.; Lahmy, S.; Banaigs, B.; Combaut, G.; Francisco, C.; Colson, P.; Houssier, C.; Waring, M. J.; Bailly, C. Binding to DNA and cytotoxic evaluation of ascididemin, the major alkaloid from the Mediterranean ascidian *Cystodytes dellechiajei*. *Anti-cancer drug design* **1995**, *10* (4), 333-346.
(391) Glisson, B. S.; Ross, W. E. DNA topoisomerase II: A primer on the enzyme and its unique role as a multidrug target in cancer chemotherapy. *Pharmacology & Therapeutics* **1987**, *32* (2), 89-106.
(392) Liu, L. F. DNA topoisomerase poisons as antitumor drugs. *Annual Review of Biochemistry* **1989**, *58* (Volume 58, 1989), 351-375.
(393) Wang, H.-K.; Morris-Natschke, S. L.; Lee, K.-H. Recent advances in the discovery and development of topoisomerase inhibitors as antitumor agents. *Medicinal Research Reviews* **1997**, *17* (4), 367-425.
(394) Matsumoto, S. S.; Sidford, M. H.; Holden, J. A.; Barrows, L. R.; Copp, B. R. Mechanism of action studies of cytotoxic marine alkaloids: ascididemin exhibits thiol-dependent oxidative DNA cleavage. *Tetrahedron Letters* **2000**, *41* (10), 1667-1670.
(395) Mahdi, F.; Morgan, J. B.; Liu, W.; Agarwal, A. K.; Jekabsons, M. B.; Liu, Y.; Zhou, Y.-D.; Nagle, D. G. Sampangine (a Copyrine Alkaloid) Exerts Biological Activities through Cellular Redox Cycling of Its Quinone and Semiquinone Intermediates. *Journal of Natural Products* **2015**, *78* (12), 3018-3023.
(396) Southey, M. W. Y.; Brunavs, M. Introduction to small molecule drug discovery and preclinical development. *Frontiers in Drug Discovery* **2023**, *3*, Mini Review.

(397) Ghosh, B.; Jones, L. H. Target validation using in-cell small molecule clickable imaging probes. *Medicinal Chemistry Communications* **2014**, *5*, 247-254.
(398) Yang, P.-Y.; Wang, M.; Liu, K.; Ngai, M. H.; Sheriff, O.; Lear, M. J.; Sze, S. K.; He, C. Y.; Yao, S. Q. Parasite-Based Screening and Proteome Profiling Reveal Orlistat, an FDA-Approved Drug, as a Potential Anti *Trypanosoma brucei* Agent. *Chemistry – A European Journal* **2012**, *18* (27), 8403-8413.
(399) Yang, P.-Y.; Wang, M.; Li, L.; Wu, H.; He, C. Y.; Yao, S. Q. Design, Synthesis and Biological Evaluation of Potent Azadipeptide Nitrile Inhibitors and Activity-Based Probes as Promising Anti-*Trypanosoma brucei* Agents. *Chemistry – A European Journal* **2012**, *18* (21), 6528-6541.
(400) Yang, P.-Y.; Wang, M.; He, C. Y.; Yao, S. Q. Proteomic profiling and potential cellular target identification of K11777, a clinical cysteine protease inhibitor, in *Trypanosoma brucei*. *Chemical Communications* **2012**, *48* (6), 835-837.
(401) Speers, A. E.; Cravatt, B. F. Profiling Enzyme Activities *In Vivo* Using Click Chemistry Methods. *Chemistry & Biology* **2004**, *11* (4), 535-546.
(402) Salic, A.; Mitchison, T. J. A chemical method for fast and sensitive detection of DNA synthesis *in vivo*. *Proceedings of the National Academy of Sciences* **2008**, *105* (7), 2415-2420.
(403) Swedlow, J. R. Chapter 17 - Quantitative Fluorescence Microscopy and Image Deconvolution. In *Methods in Cell Biology*, Sluder, G., Wolf, D. E. Eds.; Vol. 114; Academic Press, 2013; pp 407-426.
(404) Dean, S.; Sunter, J. D.; Wheeler, R. J. TrypTag.org: A Trypanosome Genome-wide Protein Localisation Resource. *Trends in Parasitology* **2017**, *33*, 80-82.
(405) Billington, K.; Halliday, C.; Madden, R.; Dyer, P.; Barker, A. R.; Moreira-Leite, F. F.; Carrington, M.; Vaughan, S.; Hertz-Fowler, C.; Dean, S.*; et al.* Genome-wide subcellular protein map for the flagellate parasite *Trypanosoma brucei*. *Nature Microbiology* **2023**, *8* (3), 533-547.
(406) Aaron, J. S.; Taylor, A. B.; Chew, T.-L. Image co-localization – co-occurrence versus correlation. *Journal of Cell Science* **2018**, *131* (3), jcs211847.
(407) Shaner, N. C.; Lambert, G. G.; Chammas, A.; Ni, Y.; Cranfill, P. J.; Baird, M. A.; Sell, B. R.; Allen, J. R.; Day, R. N.; Israelsson, M.*; et al.* A bright monomeric green fluorescent protein derived from *Branchiostoma lanceolatum*. *Nature Methods* **2013**, *10* (5), 407-409.
(408) Bolte, S.; Cordelières, F. P. A guided tour into subcellular colocalization analysis in light microscopy. *Journal of Microscopy* **2006**, *224* (3), 213-232.
(409) Bourge, M.; Fort, C.; Soler, M. N.; Satiat-Jeunemaître, B.; Brown, S. C. A pulse-chase strategy combining click-EdU and photoconvertible fluorescent reporter: tracking Golgi protein dynamics during the cell cycle. *New Phytologist* **2015**, *205* (2), 938-950.
(410) Manders, E. M. M.; Verbeek, F. J.; Aten, J. A. Measurement of co-localization of objects in dual-colour confocal images. *Journal of Microscopy* **1993**, *169* (3), 375-382.
(411) Los, G. V.; Wood, K. The HaloTag™. In *High Content Screening: A Powerful Approach to Systems Cell Biology and Drug Discovery*, Taylor, D. L., Haskins, J. R., Giuliano, K. A. Eds.; Humana Press, 2006; pp 195-208.
(412) Pyrih, J.; Hammond, M.; Alves, A.; Dean, S.; Sunter, J. D.; Wheeler, R. J.; Gull, K.; Lukeš, J. Comprehensive sub-mitochondrial protein map of the parasitic protist *Trypanosoma brucei* defines critical features of organellar biology. *Cell Reports* **2023**, *42* (9), 113083.
(413) da Silva, M. S.; Muñoz, P. A. M.; Armelin, H. A.; Elias, M. C. Differences in the Detection of BrdU/EdU Incorporation Assays Alter the Calculation for G1, S, and G2 Phases of the Cell Cycle in Trypanosomatids. *Journal of Eukaryotic Microbiology* **2017**, *64* (6), 756-770.
(414) Skepper, J. N.; Powell, J. M. Immunogold Staining of London Resin (LR) White Sections for Transmission Electron Microscopy (TEM). *Cold Spring Harbour Protocols* (1559-6095).
(415) Skepper, J. N.; Powell, J. M. Immunogold Staining of Epoxy Resin Sections for Transmission Electron Microscopy (TEM). *Cold Spring Harbour Protocols* (1559-6095).
(416) Möbius, W.; Posthuma, G. Sugar and ice: Immunoelectron microscopy using cryosections according to the Tokuyasu method. *Tissue and Cell* **2019**, *57*, 90-102.

(417) Tokuyasu, K. T. A technique for ultracryotomy of cell suspensions and tissues. *Journal of Cell Biology* **1973**, *57* (2), 551-565.
(418) Maslov, D. A.; Opperdoes, F. R.; Kostygov, A. Y.; Hashimi, H.; Lukeš, J.; Yurchenko, V. Recent advances in trypanosomatid research: genome organization, expression, metabolism, taxonomy and evolution. *Parasitology* **2019**, *146* (1), 1-27.
(419) Hair, M.; Yanase, R.; Moreira-Leite, F.; Wheeler, R. J.; Sádlová, J.; Volf, P.; Vaughan, S.; Sunter, J. D. Whole cell reconstructions of *Leishmania mexicana* through the cell cycle. *PLOS Pathogens* **2024**, *20* (2), e1012054.
(420) Jares-Erijman, E. A.; Jovin, T. M. FRET imaging. *Nature Biotechnology* **2003**, *21* (11), 1387-1395.
(421) Kelso, G. F.; Porteous, C. M.; Coulter, C. V.; Hughes, G.; Porteous, W. K.; Ledgerwood, E. C.; Smith, R. A. J.; Murphy, M. P. Selective Targeting of a Redox-active Ubiquinone to Mitochondria within Cells. *Journal of Biological Chemistry* **2001**, *276* (7), 4588-4596.
(422) Antonenko, Y. N.; Avetisyan, A. V.; Bakeeva, L. E.; Chernyak, B. V.; Chertkov, V. A.; Domnina, L. V.; Ivanova, O. Y.; Izyumov, D. S.; Khailova, L. S.; Klishin, S. S.*; et al.* Mitochondria-targeted plastoquinone derivatives as tools to interrupt execution of the aging program. 1. Cationic plastoquinone derivatives: Synthesis and *in vitro* studies. *Biochemistry* **2008**, *73* (12), 1273-1287.
(423) Szeto, H. H.; Schiller, P. W. Novel Therapies Targeting Inner Mitochondrial Membrane—From Discovery to Clinical Development. *Pharmaceutical Research* **2011**, *28* (11), 2669-2679.
(424) Arbon, D.; Ženíšková, K.; Šubrtová, K.; Mach, J.; Štursa, J.; Machado, M.; Zahedifard, F.; Leštinová, T.; Hierro-Yap, C.; Neuzil, J.*; et al.* Repurposing of MitoTam: Novel Anti-Cancer Drug Candidate Exhibits Potent Activity against Major Protozoan and Fungal Pathogens. *Antimicrobial Agents and Chemotherapy* **2022**, *66* (8), e00727-00722.
(425) Fantin, V. R.; Berardi, M. J.; Scorrano, L.; Korsmeyer, S. J.; Leder, P. A novel mitochondriotoxic small molecule that selectively inhibits tumor cell growth. *Cancer Cell* **2002**, *2* (1), 29-42.
(426) Sandes, J. M.; de Figueiredo, R. C. B. Q. The endoplasmic reticulum of trypanosomatids: An unrevealed road for chemotherapy. *Frontiers in Cellular and Infection Microbiology* **2022**, *12*, Review.
(427) Pimenta, P. F. P.; De Souza, W. Fine structure and cytochemistry of the endoplasmic reticulum and its association with the plasma membrane of *Leishmania mexicana amazonensis*. *Journal of submicroscopic cytology* **1985**, *17* (3), 413-419.
(428) Rastogi, R.; Verma, J. K.; Kapoor, A.; Langsley, G.; Mukhopadhyay, A. Rab5 Isoforms Specifically Regulate Different Modes of Endocytosis in *Leishmania*. *Journal of Biological Chemistry* **2016**, *291* (28), 14732-14746.
(429) Bucci, C.; Parton, R. G.; Mather, I. H.; Stunnenberg, H.; Simons, K.; Hoflack, B.; Zerial, M. The small GTPase rab5 functions as a regulatory factor in the early endocytic pathway. *Cell* **1992**, *70* (5), 715-728.
(430) Mathis, A. M.; Holman, J. L.; Sturk, L. M.; Ismail, M. A.; Boykin, D. W.; Tidwell, R. R.; Hall, J. E. Accumulation and Intracellular Distribution of Antitrypanosomal Diamidine Compounds DB75 and DB820 in African Trypanosomes. *Antimicrobial Agents and Chemotherapy* **2006**, *50* (6), 2185-2191.
(431) Espada, C. R.; Magalhães, R. M.; Cruz, M. C.; Machado, P. R.; Schriefer, A.; Carvalho, E. M.; Hornillos, V.; Alves, J. M.; Cruz, A. K.; Coelho, A. C.*; et al.* Investigation of the pathways related to intrinsic miltefosine tolerance in *Leishmania (Viannia) braziliensis* clinical isolates reveals differences in drug uptake. *International Journal for Parasitology: Drugs and Drug Resistance* **2019**, *11*, 139-147.
(432) Wang, Z.; Wheeler, R. J.; Sunter, J. D. Lysosome assembly and disassembly changes endocytosis rate through the *Leishmania* cell cycle. *MicrobiologyOpen* **2020**, *9* (2), e969.
(433) Shannon, D. A.; Weerapana, E. Covalent protein modification: the current landscape of residue-specific electrophiles. *Current Opinion in Chemical Biology* **2015**, *24*, 18-26.
(434) Rishton, G. M. Reactive compounds and *in vitro* false positives in HTS. *Drug discovery today* **1997**, *2* (9), 382-384.

(435) Boike, L.; Henning, N. J.; Nomura, D. K. Advances in covalent drug discovery. *Nature Reviews Drug Discovery* **2022**, *21* (12), 881-898.
(436) Lypaczewski, P.; Hoshizaki, J.; Zhang, W.-W.; McCall, L.-I.; Torcivia-Rodriguez, J.; Simonyan, V.; Kaur, A.; Dewar, K.; Matlashewski, G. A complete *Leishmania donovani* reference genome identifies novel genetic variations associated with virulence. *Scientific Reports* **2018**, *8* (1), 16549.
(437) Beilstein, S.; El Phil, R.; Sahraoui, S. S.; Scapozza, L.; Kaiser, M.; Mäser, P. Laboratory Selection of Trypanosomatid Pathogens for Drug Resistance. *Pharmaceuticals* **2022**, *15* (2), 135.
(438) Wiedemar, N.; Graf, F. E.; Zwyer, M.; Ndomba, E.; Kunz Renggli, C.; Cal, M.; Schmidt, R. S.; Wenzler, T.; Mäser, P. Beyond immune escape: a variant surface glycoprotein causes suramin resistance in *Trypanosoma brucei*. *Molecular Microbiology* **2018**, *107* (1), 57-67.
(439) Kaur, K.; Coons, T.; Emmett, K.; Ullman, B. Methotrexate-resistant *Leishmania donovani* genetically deficient in the folate-methotrexate transporter. *Journal of Biological Chemistry* **1988**, *263* (15), 7020-7028.
(440) Tulloch Lindsay, B.; Carvalho, S.; Lima, M.; Wall Richard, J.; Tinti, M.; Pinto Erika, G.; MacLean, L.; Wyllie, S. RES-Seq—a barcoded library of drug-resistant *Leishmania donovani* allowing rapid assessment of cross-resistance and relative fitness. *mBio* **2023**, *14* (6), e01803-01823.
(441) Doyle, M. A.; Macrae, J. I.; De Souza, D. P.; Saunders, E. C.; Mcconville, M. J.; Likić, V. A. LeishCyc: a biochemical pathways database for *Leishmania major*. *BMC Systems Biology* **2009**, *3* (1), 57.
(442) Leroux, A.; Fleming-Canepa, X.; Aranda, A.; Maugeri, D.; Cazzulo, J. J.; Sánchez, M. A.; Nowicki, C. Functional characterization and subcellular localization of the three malate dehydrogenase isozymes in *Leishmania* spp. *Molecular and Biochemical Parasitology* **2006**, *149* (1), 74-85.
(443) Tripodi, K. E. J.; Buttigliero, L. V.; Altabe, S. G.; Uttaro, A. D. Functional characterization of front-end desaturases from trypanosomatids depicts the first polyunsaturated fatty acid biosynthetic pathway from a parasitic protozoan. *FEBS Journal* **2006**, *273* (2), 271-280.
(444) Paape, D.; Lippuner, C.; Schmid, M.; Ackermann, R.; Barrios-Llerena, M. E.; Zimny-Arndt, U.; Brinkmann, V.; Arndt, B.; Pleissner, K. P.; Jungblut, P. R.*; et al.* Transgenic, Fluorescent *Leishmania mexicana* Allow Direct Analysis of the Proteome of Intracellular Amastigotes. *Molecular & Cellular Proteomics* **2008**, *7* (9), 1688-1701.
(445) Adak, S.; Datta, K., Alok. *Leishmania major* encodes an unusual peroxidase that is a close homologue of plant ascorbate peroxidase: a novel role of the transmembrane domain. *Biochemical Journal* **2005**, *390* (2), 465-474.
(446) Laranjeira-Silva, M. F.; Hamza, I.; Pérez-Victoria, J. M. Iron and Heme Metabolism at the *Leishmania*–Host Interface. *Trends in Parasitology* **2020**, *36* (3), 279-289.
(447) Carvalho, S.; Barreira da Silva, R.; Shawki, A.; Castro, H.; Lamy, M.; Eide, D.; Costa, V.; Mackenzie, B.; Tomás, A. M. *Li*ZIP3 is a cellular zinc transporter that mediates the tightly regulated import of zinc in *Leishmania infantum* parasites. *Molecular Microbiology* **2015**, *96* (3), 581-595.
(448) Roscoe, R. B. Characterising kinetoplastid pantothenate kinase, a multifunctional enzyme of the CoA biosynthesis pathway. University of London, Doctorol Thesis Portal LSHTM Research Online, 2023.
(449) Leonardi, R.; Jackowski, S. Biosynthesis of Pantothenic Acid and Coenzyme A. *EcoSal Plus* **2007**, *2* (2), 10.1128.
(450) Rastrojo, A.; Corvo, L.; Lombraña, R.; Solana, J. C.; Aguado, B.; Requena, J. M. Analysis by RNA-seq of transcriptomic changes elicited by heat shock in *Leishmania major*. *Scientific Reports* **2019**, *9* (1), 6919.
(451) Hughes, T. R.; Marton, M. J.; Jones, A. R.; Roberts, C. J.; Stoughton, R.; Armour, C. D.; Bennett, H. A.; Coffey, E.; Dai, H.; He, Y. D.*; et al.* Functional Discovery *via* a Compendium of Expression Profiles. *Cell* **2000**, *102* (1), 109-126.
(452) Kühl, I.; Miranda, M.; Atanassov, I.; Kuznetsova, I.; Hinze, Y.; Mourier, A.; Filipovska, A.; Larsson, N.-G. Transcriptomic and proteomic landscape of mitochondrial dysfunction reveals secondary coenzyme Q deficiency in mammals. *eLife* **2017**, *6*, e30952.

(453) Elstner, M.; Turnbull, D. M. Transcriptome analysis in mitochondrial disorders. *Brain Research Bulletin* **2012**, *88* (4), 285-293.
(454) Dolai, S.; Yadav, R. K.; Datta, A. K.; Adak, S. Effect of thiocyanate on the peroxidase and pseudocatalase activities of *Leishmania major* ascorbate peroxidase. *Biochimica et Biophysica Acta (BBA) - General Subjects* **2007**, *1770* (2), 247-256.
(455) Dolai, S.; Yadav Rajesh, K.; Pal, S.; Adak, S. Overexpression of Mitochondrial *Leishmania major* Ascorbate Peroxidase Enhances Tolerance to Oxidative Stress-Induced Programmed Cell Death and Protein Damage. *Eukaryotic Cell* **2009**, *8* (11), 1721-1731.
(456) Saxena, A.; Lahav, T.; Holland, N.; Aggarwal, G.; Anupama, A.; Huang, Y.; Volpin, H.; Myler, P. J.; Zilberstein, D. Analysis of the *Leishmania donovani* transcriptome reveals an ordered progression of transient and permanent changes in gene expression during differentiation. *Molecular and Biochemical Parasitology* **2007**, *152* (1), 53-65.
(457) Kumar, A.; Das, S.; Purkait, B.; Sardar Abul, H.; Ghosh Ayan, K.; Dikhit Manas, R.; Abhishek, K.; Das, P. Ascorbate Peroxidase, a Key Molecule Regulating Amphotericin B Resistance in Clinical Isolates of *Leishmania donovani*. *Antimicrobial Agents and Chemotherapy* **2014**, *58* (10), 6172-6184.
(458) Dolai, S.; Yadav, R. K.; Pal, S.; Adak, S. *Leishmania major* ascorbate peroxidase overexpression protects cells against reactive oxygen species-mediated cardiolipin oxidation. *Free Radical Biology and Medicine* **2008**, *45* (11), 1520-1529.
(459) Kashif, M.; Paladhi, A.; Singh, R.; Bhattacharyya, S.; Hira Sumit, K.; Manna Partha, P. Leishmanicidal Activity of an *In Silico*-Screened Novel Inhibitor against Ascorbate Peroxidase of *Leishmania donovani*. *Antimicrobial Agents and Chemotherapy* **2020**, *64* (7), 01766-01719.
(460) Martínez-Reyes, I.; Chandel, N. S. Mitochondrial TCA cycle metabolites control physiology and disease. *Nature Communications* **2020**, *11* (1), 102.
(461) Saunders, E. C.; Ng, W. W.; Chambers, J. M.; Ng, M.; Naderer, T.; Krömer, J. O.; Likić, V. A.; McConville, M. J. Isotopomer Profiling of *Leishmania mexicana* Promastigotes Reveals Important Roles for Succinate Fermentation and Aspartate Uptake in Tricarboxylic Acid Cycle (TCA) Anaplerosis, Glutamate Synthesis, and Growth. *Journal of Biological Chemistry* **2011**, *286* (31), 27706-27717.
(462) Gietl, C. Malate dehydrogenase isoenzymes: Cellular locations and role in the flow of metabolites between the cytoplasm and cell organelles. *Biochimica et Biophysica Acta (BBA) - Bioenergetics* **1992**, *1100* (3), 217-234.
(463) Springer, Amy L.; Agrawal, S.; Chang, Eric P. Malate dehydrogenase in parasitic protozoans: roles in metabolism and potential therapeutic applications. *Essays in Biochemistry* **2024**, *68* (2), 253-251.
(464) Kane, D. A. Lactate oxidation at the mitochondria: a lactate-malate-aspartate shuttle at work. *Frontiers in Neuroscience* **2014**, *8*, Perspective.
(465) Traven, A.; Wong, J. M. S.; Xu, D.; Sopta, M.; Ingles, C. J. Interorganellar Communication: Altered nuclear gene expression profiles in a yeast mitochondrial DNA mutant. *Journal of Biological Chemistry* **2001**, *276* (6), 4020-4027.
(466) Kloehn, J.; Saunders, E. C.; O'Callaghan, S.; Dagley, M. J.; McConville, M. J. Characterization of Metabolically Quiescent *Leishmania* Parasites in Murine Lesions Using Heavy Water Labeling. *PLOS Pathogens* **2015**, *11* (2), e1004683.
(467) Jara, M.; Maes, I.; Imamura, H.; Domagalska, M. A.; Dujardin, J. C.; Arevalo, J. Tracking of quiescence in *Leishmania* by quantifying the expression of GFP in the ribosomal DNA locus. *Scientific Reports* **2019**, *9* (1), 18951.
(468) Mandell, M. A.; Beverley, S. M. Continual renewal and replication of persistent *Leishmania major* parasites in concomitantly immune hosts. *Proceedings of the National Academy of Sciences* **2017**, *114* (5), E801-E810.

(469) Jara, M.; Barrett, M.; Maes, I.; Regnault, C.; Imamura, H.; Domagalska, M. A.; Dujardin, J.-C. Transcriptional Shift and Metabolic Adaptations during *Leishmania* Quiescence Using Stationary Phase and Drug Pressure as Models. *Microorganisms* **2022**, *10* (1), 97.
(470) Ouellette, M.; Hettema, E.; Wüst, D.; Fase-Fowler, F.; Borst, P. Direct and inverted DNA repeats associated with P-glycoprotein gene amplification in drug resistant *Leishmania*. *The EMBO Journal* **1991**, *10* (4), 1009-1016.
(471) García-Hernández, R.; Manzano, J. I.; Castanys, S.; Gamarro, F. *Leishmania donovani* Develops Resistance to Drug Combinations. *PLOS Neglected Tropical Diseases* **2012**, *6* (12), e1974.
(472) Alkhaldi, A. A. M.; Creek, D. J.; Ibrahim, H.; Kim, D.-H.; Quashie, N. B.; Burgess, K. E.; Changtam, C.; Barrett, M. P.; Suksamrarn, A.; de Koning, H. P. Potent Trypanocidal Curcumin Analogs Bearing a Monoenone Linker Motif Act on *Trypanosoma brucei* by Forming an Adduct with Trypanothione. *Molecular Pharmacology* **2015**, *87* (3), 451.
(473) Huynh, C.; Sacks, D. L.; Andrews, N. W. A *Leishmania amazonensis* ZIP family iron transporter is essential for parasite replication within macrophage phagolysosomes. *Journal of Experimental Medicine* **2006**, *203* (10), 2363-2375.
(474) Flannery, A. R.; Renberg, R. L.; Andrews, N. W. Pathways of iron acquisition and utilization in *Leishmania*. *Current Opinion in Microbiology* **2013**, *16* (6), 716-721.
(475) Wyllie, S.; Foth, B. J.; Kelner, A.; Sokolova, A. Y.; Berriman, M.; Fairlamb, A. H. Nitroheterocyclic drug resistance mechanisms in *Trypanosoma brucei*. *Journal of Antimicrobial Chemotherapy* **2016**, *71* (3), 625-634.
(476) Wyllie, S.; Patterson, S.; Fairlamb Alan, H. Assessing the Essentiality of *Leishmania donovani* Nitroreductase and Its Role in Nitro Drug Activation. *Antimicrobial Agents and Chemotherapy* **2013**, *57* (2), 901-906.
(477) Rau, J.; Stolz, A. Oxygen-Insensitive Nitroreductases NfsA and NfsB of *Escherichia coli* Function under Anaerobic Conditions as Lawsone-Dependent Azo Reductases. *Applied and Environmental Microbiology* **2003**, *69* (6), 3448-3455.
(478) Valiauga, B.; Williams, E. M.; Ackerley, D. F.; Čėnas, N. Reduction of quinones and nitroaromatic compounds by *Escherichia coli* nitroreductase A (NfsA): Characterization of kinetics and substrate specificity. *Archives of Biochemistry and Biophysics* **2017**, *614*, 14-22.
(479) Hall, B. S.; Meredith, E. L.; Wilkinson, S. R. Targeting the Substrate Preference of a Type I Nitroreductase To Develop Antitrypanosomal Quinone-Based Prodrugs. *Antimicrobial Agents and Chemotherapy* **2012**, *56* (11), 5821-5830.
(480) Ighodaro, O. M.; Akinloye, O. A. First line defence antioxidants-superoxide dismutase (SOD), catalase (CAT) and glutathione peroxidase (GPX): Their fundamental role in the entire antioxidant defence grid. *Alexandria Journal of Medicine* **2018**, *54* (4), 287-293.
(481) Alishvandi, M.; Bahrami, S.; Rashidi, S.; Hatam, G. Isoenzyme characterization of *Leishmania infantum* toward checking the antioxidant activity of superoxide dismutase and glutathione peroxidase. *BMC Infectious Diseases* **2024**, *24* (1), 208.
(482) Amiri-Dashatan, N.; Koushki, M.; Rezaei-tavirani, M.; Ahmadi, N. Stage-Specific Differential Gene Expression of Glutathione Peroxidase in *Leishmania Major* and *Leishmania Tropica*. *Reports of Biochemistry and Molecular Biology* **2020**, *9* (3), 324-330.
(483) Gibbs, P. N. B.; Gore, M. G.; Jordan, P. M. Investigation of the effect of metal ions on the reactivity of thiol groups in human 5-aminolaevulinate dehydratase. *Biochemical Journal* **1985**, *225* (3), 573-580.
(484) Zago, M. P.; Oteiza, P. I. The antioxidant properties of zinc: interactions with iron and antioxidants. *Free Radical Biology and Medicine* **2001**, *31* (2), 266-274.
(485) Cortese, M. M.; Suschek, C. V.; Wetzel, W.; Kröncke, K.-D.; Kolb-Bachofen, V. Zinc protects endothelial cells from hydrogen peroxide via Nrf2-dependent stimulation of glutathione biosynthesis. *Free Radical Biology and Medicine* **2008**, *44* (12), 2002-2012.

(486) Kumari, A.; Singh, K. P.; Mandal, A.; Paswan, R. K.; Sinha, P.; Das, P.; Ali, V.; Bimal, S.; Lal, C. S. Intracellular zinc flux causes reactive oxygen species mediated mitochondrial dysfunction leading to cell death in *Leishmania donovani*. *PloS one* **2017**, *12* (6), e0178800.
(487) Saini, S.; Bharati, K.; Shaha, C.; Mukhopadhyay, C. K. Zinc depletion promotes apoptosis-like death in drug-sensitive and antimony-resistance *Leishmania donovani*. *Scientific Reports* **2017**, *7* (1), 10488.
(488) Ponte-Sucre, A.; Gamarro, F.; Dujardin, J.-C.; Barrett, M. P.; López-Vélez, R.; García-Hernández, R.; Pountain, A. W.; Mwenechanya, R.; Papadopoulou, B. Drug resistance and treatment failure in leishmaniasis: A 21st century challenge. *PLOS Neglected Tropical Diseases* **2017**, *11* (12), e0006052.
(489) Khare, S.; Nagle, A. S.; Biggart, A.; Lai, Y. H.; Liang, F.; Davis, L. C.; Barnes, S. W.; Mathison, C. J. N.; Myburgh, E.; Gao, M.-Y.*; et al.* Proteasome inhibition for treatment of leishmaniasis, Chagas disease and sleeping sickness. *Nature* **2016**, *537* (7619), 229-233.
(490) Thompson, A. M.; O'Connor, P. D.; Marshall, A. J.; Yardley, V.; Maes, L.; Gupta, S.; Launay, D.; Braillard, S.; Chatelain, E.; Franzblau, S. G.*; et al.* 7-Substituted 2-Nitro-5,6-dihydroimidazo[2,1-b][1,3]oxazines: Novel Antitubercular Agents Lead to a New Preclinical Candidate for Visceral Leishmaniasis. *Journal of Medicinal Chemistry* **2017**, *60* (10), 4212-4233.
(491) Mowbray, C. E.; Braillard, S.; Glossop, P. A.; Whitlock, G. A.; Jacobs, R. T.; Speake, J.; Pandi, B.; Nare, B.; Maes, L.; Yardley, V.*; et al.* DNDI-6148: A Novel Benzoxaborole Preclinical Candidate for the Treatment of Visceral Leishmaniasis. *Journal of Medicinal Chemistry* **2021**, *64* (21), 16159-16176.
(492) Kamiński, D. M. Recent progress in the study of the interactions of amphotericin B with cholesterol and ergosterol in lipid environments. *European Biophysics Journal* **2014**, *43* (10), 453-467.
(493) Thomas, M.; Brand, S.; De Rycker, M.; Zuccotto, F.; Lukac, I.; Dodd, P. G.; Ko, E.-J.; Manthri, S.; McGonagle, K.; Osuna-Cabello, M.*; et al.* Scaffold-Hopping Strategy on a Series of Proteasome Inhibitors Led to a Preclinical Candidate for the Treatment of Visceral Leishmaniasis. *Journal of Medicinal Chemistry* **2021**, *64* (9), 5905-5930.
(494) Jumper, J.; Evans, R.; Pritzel, A.; Green, T.; Figurnov, M.; Ronneberger, O.; Tunyasuvunakool, K.; Bates, R.; Žídek, A.; Potapenko, A.*; et al.* Highly accurate protein structure prediction with AlphaFold. *Nature* **2021**, *596* (7873), 583-589.
(495) Baek, M.; DiMaio, F.; Anishchenko, I.; Dauparas, J.; Ovchinnikov, S.; Lee, G. R.; Wang, J.; Cong, Q.; Kinch, L. N.; Schaeffer, R. D.*; et al.* Accurate prediction of protein structures and interactions using a three-track neural network. *Science* **2021**, *373* (6557), 871-876.
(496) Wall, R. J.; Carvalho, S.; Milne, R.; Bueren-Calabuig, J. A.; Moniz, S.; Cantizani-Perez, J.; MacLean, L.; Kessler, A.; Cotillo, I.; Sastry, L.*; et al.* The Q_i Site of Cytochrome *b* is a Promiscuous Drug Target in *Trypanosoma cruzi* and *Leishmania donovani*. *ACS Infectious Diseases* **2020**, *6* (3), 515-528.
(497) MacLean, L. M.; Thomas, J.; Lewis, M. D.; Cotillo, I.; Gray, D. W.; De Rycker, M. Development of *Trypanosoma cruzi in vitro* assays to identify compounds suitable for progression in Chagas' disease drug discovery. *PLOS Neglected Tropical Diseases* **2018**, *12* (7), e0006612.
(498) Tuon, F. F.; Amato Neto, V.; Sabbaga Amato, V. *Leishmania*: origin, evolution and future since the Precambrian. *FEMS Immunology & Medical Microbiology* **2008**, *54* (2), 158-166.
(499) Ishikawa, M.; Hashimoto, Y. Improvement in Aqueous Solubility in Small Molecule Drug Discovery Programs by Disruption of Molecular Planarity and Symmetry. *Journal of Medicinal Chemistry* **2011**, *54* (6), 1539-1554.
(500) Strovel, J.; Sittampalam, S.; Coussens, N. P.; Hughes, M.; Inglese, J.; Kurtz, A.; Andalibi, A.; Patton, L.; Austin, C.; Baltezor, M.*; et al.* Early Drug Discovery and Development Guidelines: For Academic Researchers, Collaborators, and Start-up Companies. In *Assay Guidance Manual*, Sarine Markossian, Abigail Grossman, Michelle Arkin, Douglas Auld, Chris Austin, Jonathan Baell, Kyle

Brimacombe, Thomas D.Y. Chung, Nathan P. Coussens, Jayme L. Dahlin*, et al.* Eds.; Bethesda (MD): Eli Lilly & Company and the National Center for Advancing Translational Sciences, 2012.
(501) Graf, F. E.; Ludin, P.; Arquint, C.; Schmidt, R. S.; Schaub, N.; Kunz Renggli, C.; Munday, J. C.; Krezdorn, J.; Baker, N.; Horn, D.*; et al.* Comparative genomics of drug resistance in *Trypanosoma brucei rhodesiense*. *Cellular and Molecular Life Sciences* **2016**, *73* (17), 3387-3400.
(502) Van Den Kerkhof, M.; Sterckx, Y.; Leprohon, P.; Maes, L.; Caljon, G. Experimental Strategies to Explore Drug Action and Resistance in Kinetoplastid Parasites. *Microorganisms* **2020**, *8* (6), 950.
(503) Zhang, Z.; Tang, W. Drug metabolism in drug discovery and development. *Acta Pharmaceutica Sinica B* **2018**, *8* (5), 721-732.
(504) Fueyo González, F. J.; Ebiloma, G. U.; Izquierdo García, C.; Bruggeman, V.; Sánchez Villamañán, J. M.; Donachie, A.; Balogun, E. O.; Inaoka, D. K.; Shiba, T.; Harada, S.*; et al.* Conjugates of 2,4-Dihydroxybenzoate and Salicylhydroxamate and Lipocations Display Potent Antiparasite Effects by Efficiently Targeting the *Trypanosoma brucei* and *Trypanosoma congolense* Mitochondrion. *Journal of Medicinal Chemistry* **2017**, *60* (4), 1509-1522.
(505) Brun, R.; Schönenberger, M. Cultivation and *in vitro* cloning of procyclic culture forms of *Trypanosoma brucei* in a semi-defined medium: Short communication. *Acta Tropica* **1979**, (36), 289-292.
(506) Hirumi, H.; Hirumi, K. Continuous Cultivation of *Trypanosoma brucei* Blood Stream Forms in a Medium Containing a Low Concentration of Serum Protein without Feeder Cell Layers. *The Journal of Parasitology* **1989**, *75* (6), 985-989.
(507) Goyard, S.; Segawa, H.; Gordon, J.; Showalter, M.; Duncan, R.; Turco, S. J.; Beverley, S. M. An *in vitro* system for developmental and genetic studies of *Leishmania donovani* phosphoglycans. *Molecular and Biochemical Parasitology* **2003**, *130* (1), 31-42.
(508) Beneke, T.; Gluenz, E. LeishGEdit: A Method for Rapid Gene Knockout and Tagging Using CRISPR-Cas9. In *Leishmania: Methods and Protocols*, Clos, J. Ed.; Springer New York, 2019; pp 189-210.
(509) Dean, S.; Sunter, J.; Wheeler, R. J.; Hodkinson, I.; Gluenz, E.; Gull, K. A toolkit enabling efficient, scalable and reproducible gene tagging in trypanosomatids. *Open Biology* **2015**, *5* (1), 140197.
(510) Peng, D.; Tarleton, R. EuPaGDT: a web tool tailored to design CRISPR guide RNAs for eukaryotic pathogens. *Microbial Genomics* **2015**, *1* (4).
(511) Edwards, B. F. L.; Wheeler, R. J.; Barker, A. R.; Moreira-Leite, F. F.; Gull, K.; Sunter, J. D. Direction of flagellum beat propagation is controlled by proximal/distal outer dynein arm asymmetry. *Proceedings of the National Academy of Sciences* **2018**, *115* (31), E7341-E7350.
(512) Schumann Burkard, G.; Jutzi, P.; Roditi, I. Genome-wide RNAi screens in bloodstream form trypanosomes identify drug transporters. *Molecular and Biochemical Parasitology* **2011**, *175* (1), 91-94.
(513) Schindelin, J.; Arganda-Carreras, I.; Frise, E.; Kaynig, V.; Longair, M.; Pietzsch, T.; Preibisch, S.; Rueden, C.; Saalfeld, S.; Schmid, B.*; et al.* Fiji: an open-source platform for biological-image analysis. *Nature Methods* **2012**, *9* (7), 676-682.
(514) Dougherty, R. Extensions of DAMAS and Benefits and Limitations of Deconvolution in Beamforming. In *11th AIAA/CEAS Aeroacoustics Conference*, Aeroacoustics Conferences, American Institute of Aeronautics and Astronautics, 2005.
(515) Cordelières, F. P.; Bolte, S. JACoP v 2 . 0 : improving the user experience with co-localization studies. In *2nd ImageJ user and developer conference*, 2008; pp 6-7.
(516) Manders, E. M. M.; Stap, J.; Brakenhoff, G. J.; Driel, R. V.; Aten, J. A. Dynamics of three-dimensional replication patterns during the S-phase, analysed by double labelling of DNA and confocal microscopy. *Journal of Cell Science* **1992**, *103* (3), 857-862.
(517) Costes, S. V.; Daelemans, D.; Cho, E. H.; Dobbin, Z.; Pavlakis, G.; Lockett, S. Automatic and Quantitative Measurement of Protein-Protein Colocalization in Live Cells. *Biophysical Journal* **2004**, *86* (6), 3993-4003.

(518) Reynolds, E. S. The use of lead citrate at high pH as an electron-opaque stain in electron microscopy. *Journal of Cell Biology* **1963**, *17* (1), 208-212.
(519) Schork, K.; Podwojski, K.; Turewicz, M.; Stephan, C.; Eisenacher, M. Important Issues in Planning a Proteomics Experiment: Statistical Considerations of Quantitative Proteomic Data. In *Quantitative Methods in Proteomics*, Marcus, K., Eisenacher, M., Sitek, B. Eds.; Springer US, 2021; pp 1-20.
(520) Li, H.; Durbin, R. Fast and accurate long-read alignment with Burrows–Wheeler transform. *Bioinformatics* **2010**, *26* (5), 589-595.
(521) Li, H.; Handsaker, B.; Wysoker, A.; Fennell, T.; Ruan, J.; Homer, N.; Marth, G.; Abecasis, G.; Durbin, R. The Sequence Alignment/Map format and SAMtools. *Bioinformatics* **2009**, *25* (16), 2078-2079.
(522) Walker, B. J.; Abeel, T.; Shea, T.; Priest, M.; Abouelliel, A.; Sakthikumar, S.; Cuomo, C. A.; Zeng, Q.; Wortman, J.; Young, S. K.*; et al.* Pilon: An Integrated Tool for Comprehensive Microbial Variant Detection and Genome Assembly Improvement. *PloS one* **2014**, *9* (11), e112963.
(523) Glover, L.; Alsford, S.; Baker, N.; Turner, D. J.; Sanchez-Flores, A.; Hutchinson, S.; Hertz-Fowler, C.; Berriman, M.; Horn, D. Genome-scale RNAi screens for high-throughput phenotyping in bloodstream-form African trypanosomes. *Nature Protocols* **2015**, *10* (1), 106-133.
(524) Wagner, G. P.; Kin, K.; Lynch, V. J. Measurement of mRNA abundance using RNA-seq data: RPKM measure is inconsistent among samples. *Theory in Biosciences* **2012**, *131* (4), 281-285.
(525) Beneke, T.; Dobramysl, U.; Catta-Preta, C.; Mottram, J.; Gluenz, E.; Wheeler, R. Genome sequence of *Leishmania mexicana* MNYC/BZ/62/M379 expressing Cas9 and T7 RNA polymerase. *Wellcome Open Research* **2023**, *7* (294).
(526) Yoder, R. J.; Zhuang, Q.; Beck, J. M.; Franjesevic, A.; Blanton, T. G.; Sillart, S.; Secor, T.; Guerra, L.; Brown, J. D.; Reid, C.*; et al.* Study of para-Quinone Methide Precursors toward the Realkylation of Aged Acetylcholinesterase. *ACS Medicinal Chemistry Letters* **2017**, *8* (6), 622-627.
(527) Mattingly, P. G. Mono-Protected Diamines. Nα-tert-Butoxycarbonyl α,ω-Alkanediamine Hydrochlorides from Amino alcohols. *Synthesis* **1990**, *1990*, 366-368.
(528) Moon, H.; Jung, Y.; Kim, Y.; Kim, B. W.; Choi, J. G.; Kim, N. H.; Oh, M. S.; Park, S.; Kim, B. M.; Kim, D. High Stability of a Donor–Acceptor Type Oxazepine-Containing Fluorophore and Its Applications in Cellular Imaging and Two-Photon Deep Tissue Imaging. *Organic Letters* **2019**, *21* (11), 3891-3894.
(529) Adams, T. C.; Dupont, A. C.; Carter, J. P.; Kachur, J. F.; Guzewska, M. E.; Rzeszotarski, W. J.; Farmer, S. G.; Noronha-Blob, L.; Kaiser, C. Aminoalkynyldithianes. A new class of calcium channel blockers. *Journal of Medicinal Chemistry* **1991**, *34* (5), 1585-1593.
(530) Davison, E. C.; Fox, M. E.; Holmes, A. B.; Roughley, S. D.; Smith, C. J.; Williams, G. M.; Davies, J. E.; Raithby, P. R.; Adams, J. P.; Forbes, I. T.*; et al.* Nitrone dipolar cycloaddition routes to piperidines and indolizidines. Part 9. Formal synthesis of (−)-pinidine and total synthesis of (−)-histrionicotoxin, (+)-histrionicotoxin and (−)-histrionicotoxin 235A. *Journal of the Chemical Society, Perkin Transactions 1* **2002**, (12), 1494-1514.
(531) Budhadev, D.; Poole, E.; Nehlmeier, I.; Liu, Y.; Hooper, J.; Kalverda, E.; Akshath, U. S.; Hondow, N.; Turnbull, W. B.; Pöhlmann, S.*; et al.* Glycan-Gold Nanoparticles as Multifunctional Probes for Multivalent Lectin–Carbohydrate Binding: Implications for Blocking Virus Infection and Nanoparticle Assembly. *Journal of the American Chemical Society* **2020**, *142* (42), 18022-18034.
(532) Tamura, T.; Tsukiji, S.; Hamachi, I. Native FKBP12 Engineering by Ligand-Directed Tosyl Chemistry: Labeling Properties and Application to Photo-Cross-Linking of Protein Complexes *in Vitro* and in Living Cells. *Journal of the American Chemical Society* **2012**, *134* (4), 2216-2226.